TURBULENCE AND PARTICLE DYNAMICS IN DENSE CRYSTAL SLURRIES

A numerical study by means of
lattice-Boltzmann simulations

TURBULENCE AND PARTICLE DYNAMICS IN DENSE CRYSTAL SLURRIES

A numerical study by means of lattice-Boltzmann simulations

PROEFSCHRIFT

ter verkrijging van de graad van doctor
aan de Technische Universiteit Delft,
op gezag van de Rector Magnificus prof. dr. ir. J. T. Fokkema,
voorzitter van het College voor Promoties,
in het openbaar te verdedigen op
maandag 11 november 2002 om 10.30 uur

door

Andreas TEN CATE

scheikundig ingenieur
geboren te Amsterdam

Dit proefschrift is goedgekeurd door de promotoren:
Prof. dr. ir. H. E. A. van den Akker
Prof. dr. ir. G. M. van Rosmalen

Samenstelling promotiecommissie:

Rector Magnificus, voorzitter	
Prof. dr. ir. H. E. A. van den Akker,	Technische Universiteit Delft, promotor
Prof. dr. ir. G. M. van Rosmalen,	Technische Universiteit Delft, promotor
Dr. ir. J. J. Derksen,	Technische Universiteit Delft
Prof. ir. J. Grievink,	Technische Universiteit Delft
Prof. dr. ir. G. Ooms,	Technische Universiteit Delft
Prof. dr. S. Sundaresan,	Princeton University (Verenigde Staten van Amerika)
Prof. dr. C. D. Rielly,	Loughborough University (Verenigd Koninkrijk)

This research was one of the projects in "Mastering the Molecules in Manufacturing", abbreviated as M3, a Delft Interdisciplinary Research Center approved by the university board of Delft University of Technology.

Published and distributed by: DUP Science
DUP Science is an imprint of
Delft University Press
P.O. Box 98
2600 MG Delft
The Netherlands
Telephone: +31 15 27 85 678
Telefax: +31 15 27 85 706
E-mail: Info@Library.TUDelft.NL

ISBN 90-407-2324-9

Keywords: Suspension, Crystallisation, lattice-Boltzmann

Printed in The Netherlands

AAN MIJN OUDERS

Contents

Summary

In industrial crystallisation processes, solid crystals are produced in a dense crystal slurry which is operated under highly turbulent conditions to maintain a well mixed homogeneous suspension. The slurry in a typical crystallisation process contains approximately 20 vol % solids with a particle size in the range between 100 and 2000 μm. It has been recognised in literature that the hydrodynamics of the crystallisation process plays a crucial role in the dynamics of the crystallisation process. Due to the action of the turbulent flow, crystals will collide with equipment internals or amongst each other, which may lead to secondary nucleation, the formation of new crystals from crystal fragments. Secondary nuclei may have a strong effect on the dynamic behaviour of the crystallisation process and accordingly on the quality of the solid product. This process may have a large impact on *e.g.* the scale-up of crystallisation processes.

The objective of this thesis was to study the mechanism of fragmentation and secondary nucleation due to crystal-crystal collisions for solid particles in a turbulent flow field, based on the direct numerical simulation of freely moving particles.

To determine the hydrodynamic conditions for such simulations, first a detailed large-eddy simulation of the internal flow of a pilot scale draft-tube baffled crystalliser was carried out. In this simulation, it was assumed that a single phase large eddy simulation (LES) could represent the behaviour of the fluid flow of a dense solid-liquid suspension. The LES was performed at a Reynolds number of 240,000, using a lattice-Boltzmann scheme with a Smagorinsky sub-grid scale turbulence model (c_s was 0.11). From the simulation results, the microscopic turbulent length scales were estimated to become upto one order of magnitude smaller than the mean particle size in the crystallisation process.

Since the Kolmogorov length scale was estimated to be of the order of the particle size or smaller, and since the particle and fluid motion in a dense solid-liquid suspension are closely coupled, a simulation method had to be developed where the flow field surrounding the particles was fully resolved, with full coupling of the motion of the particle phase and the fluid phase. For this purpose, a simulation method for freely moving particles in a turbulent flow field was developed based on the lattice-Boltzmann method. Two aspects of this approach that required further research where the implementation of the particle boundary condition, and the method for generation of sustained turbulent fluid motion.

The adaptive force-field method was used for implementing the no-slip particle boundary condition. Since this method has not previously been applied in simulations of freely moving particles, validation of this method was required. A comparison was made between experiments and simulations on a single sphere settling in a box. The box

dimensions were chosen such that the full domain could be captured in the simulations, including the no-slip boundary conditions of the box. Cross-correlation particle imaging velocimetry (PIV) measurements were carried out at particle Reynolds numbers ranging from 1.5 to 31.9. The particle Stokes number varied from 0.2 to 4 and at bottom impact no rebound was observed. Detailed data of the flow field induced by the settling sphere were obtained, along with time series of the sphere's trajectory and velocity during acceleration, steady fall and deceleration at bottom approach. Lattice-Boltzmann simulations proved to capture the full transient behaviour of both the sphere motion and the fluid motion. The experimental data were used to assess the effect of spatial resolution in the simulations over a range of 2 to 8 grid nodes per sphere radius. The quality of the flow field predictions depended on the Reynolds number. Application of a lubrication force to compensate for the lack of spatial resolution in the simulations when the sphere is very close to the bottom of the container, has been studied.

For the generation of sustained turbulent conditions, a spectral forcing scheme has been implemented in the lattice-Boltzmann framework. With this scheme, a turbulent flow field with *a priori* set conditions is generated. It was demonstrated that pre-defined properties such as the Kolmogorov length scale, the integral length scale and the integral time scale are well recovered. A specific feature of the forcing scheme is that it allows to control the power input by eliminating the force-velocity correlation. It is demonstrated that this feature can be used in the lattice-Boltzmann simulations.

Turbulent suspension simulations with accurately prescribed conditions have been realised by combining the particle simulations with the turbulent forcing algorithm. In these simulations, the particle diameter measured 8 grid points, the volume concentration was varied between 2 and 10 % and the particle to fluid density ratio between 1.15 and 1.73. The Taylor scale Reynolds number was 61. Lubrication force was used to account for sub-grid hydrodynamic interaction between approaching particles. Results were presented on the influence of the particle phase on the turbulent energy spectrum and on the behaviour of the particle phase with respect to particle collisions.

The simulations showed that the presence of the particles reduces the kinetic energy by facilitating the rate of energy dissipation. Fluid motion is generated at length scales in the range of the particle size, which results in a strong increase in the rate of energy dissipation at the small length scales. The simulation results on the energy transfer in the turbulent suspension flows confirmed earlier findings in literature on two-way coupled DNS of point particles in turbulence.

Collision data indicated that two separate collision mechanisms occur in the simulations. Collisions due to uncorrelated particle motion are observed (primary collisions), and collision frequencies obtained for this phenomenon are in agreement with theory on inertial particle collisions. In contrast to this, also a large quantity of collisions at high frequency (secondary collisions) was encountered. These so-called secondary collisions are due to accumulation of particles, due to the correlated motion of particles that results from the short-range hydrodynamic interaction between the particles, due to the spatial correlation of the velocities in the turbulent flow field at short separations and due to the implementation of the method for lubrication forces and particle collisions in the simulations. The image of two separate types of collision behaviour occurring in the turbulent suspension is supported by an analysis of the particle phase based on

the distribution of the relative particle velocities at close separation and on the spatial correlation functions of the particle velocities.

Finally, crystal-crystal collisions in the turbulent suspension simulations were evaluated to obtain a measure for the rate of fragmentation of ammonium sulphate crystals in the simulated turbulent flow field. A minimum impact velocity at which fragmentation occurs was determined from the minimum energy of fragmentation and therefore depended on the particle size. The impact velocities of the particles in the suspension simulations were evaluated based on the distribution of the radial velocity near contact. This distribution demonstrated that the probability for higher impact velocities decreases. Therefore only a small fraction of the collisions, *i.e.* for which the impact energy exceeds the minimum energy of fragmentation, will result in fragmentation. The part of the distribution where the velocity exceeds the minimum energy of fragmentation could be related to a rate constant of fragmentation, based on a theoretical collision model. Values of the fragmentation kernel obtained via this theoretical route correspond well to the values obtained from the collisions registered during the suspension simulations. This indicated that the developed simulation approach provides a consistent method for estimation of crystal fragmentation frequencies, and thus provides a perspective for generating models to predict fragmentation in turbulent crystal suspension flows.

Preface

Just like so many things one undertakes in life, writing this thesis has very much been like undertaking a long trip. Now that I come to the end of it, I want to use this place to look back on my period in Delft and to share with you some of the experiences that I gained while doing my PhD work.

I started my PhD in the fall of 1997. I recall clearly that I had no clue as to where to begin and look for a position, since many fields of research attracted my interest. At that same time my good friend and roommate Bart Henstra, who also was looking around for a PhD position, told me that an interesting new project was started named the DIOC, and that I should talk to professor Johan Grievink about this. I went to his office and had a very inspiring afternoon, which resulted in me starting my PhD in October of that year in both his group and that of professor Gerda van Rosmalen.

Then, the first hub in the road appeared. I knew I was going to work in the field of crystallisation and in the field of process modelling, but what I didn't know was what the questions were that were of interest to this field. I had all liberty to choose a direction, which in academic sense is great, but for a rookie in the field is quite a big task. I read the DIOC project description, and again, and again, but it didn't make sense to me. I decided to go and talk to my supervisors, and the idea came up that using discrete particle simulations could be of interest to industrial crystallisation. I looked into that and reasoned that if one wants to study anythiing on individual crystals, then the first thing one needs to know is the motion of these crystals. I went into the library and soon came up with a paper by a certain Mr. Ladd, saying basically that if one wants to look at the motion of particles in fluid, a novel and by far the best way to study this is by means of the lattice-Boltzmann method. Later, looking into the motio of particles was was extended to looking into collisions of individual crystals, which then became formally the subject of my thesis.

So, enthusiastically I started to work. "Great!", I thought, "lets go!...but how does this lattice-Boltzmann method work?" Many hours later the paper of Ladd still didn't make much sense to me and I decided that I needed advise from someone who knows this method. I looked around, and coincidentally ran into Jos Derksen, who happened to be using the method, and who offered me to use some of his programs. During the summer and fall of 1998, I started working with this method and soon I had sorted out my whole research program. I was first to do particle simulations, from that we would learn about collisions and then in the second part of my thesis I would do complete integrated process design of industrial crystalliser with.....yeah...dream on! Very much as a rookie, I had a million idea's of where I would take my thesis, but I stil had to learn a lot. I had to learn mostly how much work one can realise during a period of about four

years. It seems endless at the beginning, it seems almost nothing at the end. I decided that if I were to succeed in the ambitious plans I had, I needed both the supervision and dedication to my project of someone who knows his way around fluid mechanics, and so I asked Jos Derksen if he could be involved in my project more formally. This was very much supported by both Gerda van Rosmalen and Johan Grievink.

In December 1998, Jos suggested that I should work for a few months at the Kramers Laboratorium, because there I would be across the hall from him and it would much speed up my work. I got introduced to the lab as, 'Hi, this is Andreas, he will be here, say, typically for the next three months'. At that moment I didn't know yet that this would be a major change of my PhD project. Harrie van den Akker was both program leader of the DIOC and the director of the Kramers Laboratorium, and since I was member of the DIOC, this facilitated very much my move to the Kramers Laboratorium. Before I knew what was happening, the next change came up. Since I was focussing more and more on fluid mechanics, it would make sense that my primary advisor would be in this field. Very courteously, Johan Grievink himself suggested that he would move away from my project and let Harrie be my promotor. And so, three months became three years.

Ever since I took off and worked hard to finish my PhD thesis, the result of which lies in front of you. I learned about compartmental modelling and population balances of crystallisation processes, I learned about the Navier-Stokes equations and about turbulence, I learned about the behaviour of suspensions and about collisions of particles, and I learned about many other things in life. Much of this is reflected in the following pages, much more of what I learned isn't, simply because it is impossible to capture in pages. I hope that for you as a reader, reading and using this book will be as usefull as many other theses have been to me, and will be as much of a pleasure to read and use as it has been for me writing it.

Andreas ten Cate,
Delft 2002.

Chapter 1

Introduction

1.1 Industrial Crystallisation

Crystallisation is the formation of solid crystals from a clear solution. It is used in a wide range of applications, ranging from a bench scale purification step in chemical laboratory work to obtain highly purified chemicals (Laarhoven (1932)), to a full sized industrial scale unit operation (Myerson (1993)) for the large scale production and separation of pure solids from impure solutions. Crystallisation on large scales dates back to the beginning of civilisation for the production of household products such as salt or sugar. In current days it has developed into an industrial process for the production of organic and inorganic solids as intermediate or end product for both the consumer market and the chemical industry. One of the major advantages of crystallisation is that it is capable of producing solids at high purity at a low energy consumption compared to other separation processes such as distillation, while yielding a product with often good handling properties.

From the early 20-th century on, a growing demand for large scale products led to the development of advanced crystallisation units such as the forced-circulation (FC) crystalliser, an early example of which is given in figure 1.1, and the draft-tube (DT) crystalliser. In the FC crystalliser, the crystal slurry is kept in suspension by a pump that circulates the slurry via a heat exchanger to a vessel where solvent is evaporated. The DT crystalliser consists of a vessel provided with a marine type impeller that circulates the crystal slurry through a vertical riser tube in order to maintain the crystal slurry suspended and well mixed. At the surface, vacuum is applied to generate a boiling slurry at moderate temperature. Both crystalliser types are called evaporation crystallisers since supersaturation, the driving force for nucleation and crystal growth, is generated by evaporation of the solvent.

Application of crystallisation in the process industry requires large scale equipment. With the scale-up of crystallisation processes from a pilot scale size of the order of 1 m^3 to full sized industrial scale processes of the order of 100 m^3, the behaviour of the crystallisation process often changes drastically.

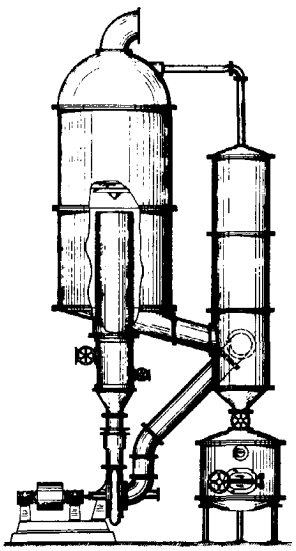

Figure 1.1: Example of a forced-circulation crystalliser anno 1932. (From Bennet (1984))

The complex behaviour of large scale industrial crystallisation processes is clearly reflected in the following quote (Bennet (1993));

> Crystallisation has long been considered an art rather than a science, although recent theoretical discoveries and new analytical techniques have produced a change in this historic position. It is also true that the mechanical design of the crystalliser has a significant influence on the nucleation rate due to contact nucleation, which is that caused by contact of the crystals with each other or with the pump impeller or propeller when suspended in a supersaturated solution. This phenomenon yields varying rates of nucleation on scale-up and differences in nucleation rate when the same piece of equipment is used to crystallise different materials.

This quote clearly indicates the complexity of crystallisation processes. An often highly turbulent boiling suspension is circulated in a crystalliser. The residence time for the crystals is of the order of hours to assure that crystals grow sufficiently large to obtain a product with a desired crystal size. At the same time, kinetic processes occur that influence the condition of a crystallisation process at a time scale of minutes (see also figure 1.3). The kinetic processes are summarised in the scheme of figure 1.2 and comprise,

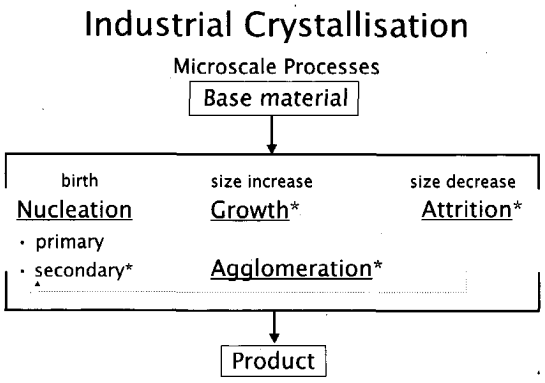

Figure 1.2: Kinetic mechanisms in industrial crystallisation processes. A * indicates processes dominated by hydrodynamics.

- nucleation; the formation of new crystals,

  primary nucleation; the (spontaneous) formation of new crystals from a supersaturated liquid

  secondary nucleation; the formation of new crystals from fragments generated by crystal collisions in a supersaturated suspension

- crystal growth; the increase in crystal size from deposition of solute from the supersaturated liquid on the crystal surface,

- agglomeration; the glueing of crystals that collide in a supersaturated liquid,

- attrition; the abrasion or breakage of crystals due to contacts or collisions of the crystals with internal parts of the crystalliser or with neighbour crystals.

For design, scale-up, and control purposes, much attention has been paid to modelling crystallisation processes (Myerson (1993), Mullin (2001)). Traditionally, population balance models play a large role in this field of research. These models describe the evolution of a population of crystals as a function of process conditions, compound and solvent properties and crystalliser type and layout. In the first propositions the crystalliser is considered to be an ideally mixed vessel, designated as the Mixed Slurry Mixed Product Removal (MSMPR) crystalliser (Garside (1985)). Parameters for these models are determined typically from lab-scale reactors of a few liters volume. A highly desirable feature for population balance models would be to use parameters obtained from laboratory experiments to model processes accurately at an industrial scale.

One major issue that raises difficulties in proposing adequate population balance models is that the relation between crystalliser design, scale, operation, compound properties and the resulting product is highly non-linear in nature. For instance, a typical expression for describing the rate of secondary nucleation B_0 in a population balance is

the empirical power law (Bermingham *et al.* (1997))

$$B_0 = k_N N^h G^i M_T^j \tag{1.1}$$

where k_N is a constant, G is the linear growth rate, N the impeller revolution and M_T the crystal mass of the slurry. In this expression, the constants h, i and j are parameters that need to be determined experimentally. Experimental values vary substantially, such as $1.8 < h < 2.1$, $0.5 < i < 3$ while $j = 1$ for describing crystal-impeller collisions and $j = 2$ for crystal-crystal collisions. In equation 1.1 a large number of properties of the crystalliser setup are lumped into the exponential parameters and constants. These parameters should capture the effects of the physical properties of the compound involved, the hydrodynamic regime, the crystal slurry circulation time, the slurry settling properties, the crystalliser layout and the impeller type on the rate of nucleation. The predictive value of such an approach is limited to the specific crystallisation process for which the parameters have been determined.

Recently, models were proposed that describe secondary nucleation from a first-principles basis. Gahn & Mersmann (1997) presented a fracture model that predicts the formation of secondary nuclei due to the collision of a crystal with a much harder object such as an impeller. The model is based on the mechanical properties of the crystalline material, that can be determined *a priori* at lab scale. With this approach, a step has been set in the direction of isolating the many fundamental mechanisms that contribute to the nonlinear behaviour of crystallisation processes.

An important characteristic of the kinetic mechanisms given in figure 1.2 is that most of them are driven by the hydrodynamics of the process (Garside (1985)). The hydrodynamics determine the transport and circulation of the slurry inside the crystalliser on the large scales (scale of the process equipment). Although from a modeling point of view the crystalliser is assumed homogeneous, inhomogeneities of the local conditions may occur in industrial scale crystallisers due to *e.g.* the spread in residence time of the slurry in different zones of the crystalliser. The impact that inhomogeneities inside a crystalliser may have on the resulting product is clearly demonstrated in Hollander *et al.* (2001). These authors studied the effects of hydrodynamics on the scale-up of precipitation reactors in which agglomeration represents the main growth mechanism. To capture the inhomogeneous distribution of properties such as the crystal mass the supersaturation or the hydrodynamic regime inside the crystalliser, a compartmentisation of the population balance model that corresponds to the crystalliser layout has been proposed (*e.g.* by Bermingham *et al.* (1998)). A simulation result of such a model is given in figure 1.3, where the compartment structure was based on a highly detailed flow simulation (Ten Cate *et al.* ((2000)). The large difference between both simulation results demonstrates that this type of models raises new questions, *e.g.* as to how to design an accurate compartment structure.

At smaller scales (around the crystal size), the flow field affects the mass transfer at the crystal surface and dominates crystal-equipment and crystal-crystal collisions. The microscopic hydrodynamic conditions are generated by the large scale flow structure which in its turn depends on equipment design and operating conditions. The complex nonlinear behaviour obtained in the equation for the rate of nucleation (eq. 1.1) and hinted at in the above citation (Bennet (1993)) originates from these dependencies.

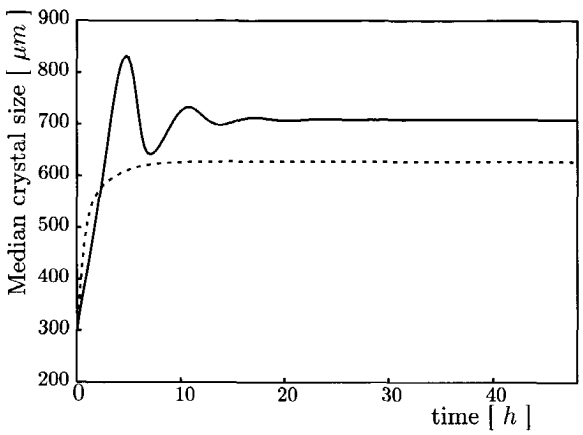

Figure 1.3: Simulated time series of the startup behaviour of a crystallisation process. Influence of turbulent back mixing in a 21-compartment model (dotted line with back-mixing, continuous line without back mixing) (Ten Cate *et al.* ((2000)).

1.2 Approach

In this thesis, the issue of secondary nucleation due to crystal-crystal collisions is addressed. In many studies on secondary nucleation, the contribution of these collisions has been ignored under the assumption that their contribution is negligble compared to the contribution of crystal-impeller collisions (*e.g.* Gahn & Mersmann (1999*b*)). Although this assumption may be valid for bench or pilot scale crystallisers, with an increase in equipment size the frequency at which crystals will pass the impeller will decrease and the ratio of crystal-impeller to crystal-crystal collisions to the contribution of secondary nucleation may shift towards the latter. This behaviour severly complicates modeling the scale up behaviour of crystallisers.

Secondary nucleation due to crystal-crystal collisions is typically expected to become important in dense crystal suspensions (*i.e.* with high solids volume fractions), operated under highly turbulent conditions. The turbulent fluid motion will cause particles to have sufficient relative velocity to undergo collisions that lead to fragmentation. Although it is recognized that hydrodymamics play a key role in the dynamic behaviour of the crystallisation process, little knowledge on the exact behaviour of crystal particles in a dense turbulent suspension has been available to the crystallisation community. Recent studies of Gahn & Mersmann (1999*b*), focussing on secondary nucleation due to crystal-impeller collisions, present an example. In this work, impact efficiencies are predicted based on the passage of the crystals through the impeller-swept volume, while the flow field of the suspension near the impeller is approximated as potential flow. Nevertheless, important aspects such as the turbulent fluctuations of the flow field and the high volume fraction of particles in the suspension that strongly modifies the fluid behaviour are disregarded in this work.

A field of research where in recent years large progress has been made in the under-

standing of particle motion in turbulent suspensions is the area of modeling and computational fluid dynamics of multi-phase or suspension flow. In this area, research has focussed on many different fundamental aspects of suspension flows, both theoretically and numerically. Droplets suspended in turbulent air and agglomerating into raindrops have inspired Saffman & Turner (1956) to develop models that describe the collisions of fine particles in turbulent flow fields. Based on this work, both theoretical and numerical studies have been employed to understand the influence of physical parameters such as the particle-fluid density ratio or the flow field Reynolds number on phenomena such as the particle collision rates (Sundaram & Collins (1997); Wang *et al.* (2000)) or the inhomogeneous distribution of particles in turbulent flow fields (Squires & Eaton (1990); Reade & Collins (2000)). To study the effect of particles on the development of turbulent flow fields, numerical studies have been carried out where the interaction between the flow field and the particle phase are coupled (Squires & Eaton (1990)). The latter type studies focus on suspensions of particles that are much smaller than the microscopic length scales of the flow field, where the particle volume concentration is very low but where the mass loading can be considerable and where the particles are approximated as point particles.

Again a different direction in multi-phase hydrodynamic studies is the research field of dense solid-liquid suspensions. This branch has gained increasing attention over the last decade with the upcome of efficient numerical schemes to solve the Navier-Stokes equations and availability of cheap computational power. For instance, the sedimentation of suspensions is studied via direct simulation of the full flow field of the individual particles, with complete hydrodynamic interaction between the particles and the fluid phase. The basis for this field of research was set out by Ladd (1994*a*).

In this thesis, an effort is made to bring the two different worlds of industrial crystallisation research and multi-phase flow research closer together. Insights from the above three different fields of research are combined to obtain a greater understanding of collision behaviour and fragmentation of particles in a dense suspension under the action of a turbulent flow field. This led to the following approach:

- the first step is to assess the turbulent flow field of a crystalliser on the basis of a large eddy simulation, assuming that the flow can be represented using a pseudo single-phase simulation. This simulation is used to estimate characteristic turbulent properties of the crystalliser flow field such as the locally occuring rate of energy dissipation and fluctuating fluid velocities.

- the second step is to perform detailed simulations of fully resolved suspensions in a fully periodic turbulent box, which is assumed to represent the local conditions in a small section (typically 1 cm^3) of a turbulent crystalliser flow field. In crystallisation processes, a suspension typically contains between 10 and 30 vol % solids at a low density ratio, which indicates the need for full simulation of the suspension. The conditions of these simulations are chosen such that they correspond to the turbulent conditions observed locally in the crystalliser simulation. In these detailed simulations, turbulence-particle interactions and particle-particle collision behaviour is studied.

1.3 Outline of the thesis

The proposed research approach is reflected in the outline of this thesis:

In **chapter 2**, a detailed large eddy simulation of the internal flow field of a pilot scale 1100 l crystalliser is presented where the slurry is assumed to behave as a single phase. This simulation is used in a feasibility study to estimate the requirements for direct simulation of a turbulent suspension. Macroscopic and microscopic length scales of the turbulent flow field were calculated from the LES simulation to determine the relation between the equipment length scales, the turbulence length scales and the particle length scales.

For the purpose of validating direct simulations of suspensions, a study is presented in **chapter 3** on the transient motion of a single particle settling towards the bottom of a square vessel. The simulation approach is based on the lattice-Boltzmann scheme proposed by Eggels & Somers ((1995), while using boundary conditions for the particle based on an adaptive force field scheme (Derksen & Van den Akker ((1999)). This approach differs from the one presented by Ladd (1994a). To establish the accuracy of the method (experimental) validation is required. To this end, simulation results are compared with experimental results on both the particle trajectory and the flow field, which was measured by use of particle image velocimetry (PIV).

To obtain turbulent conditions in the computational domain, the spectral forcing scheme proposed by Alvelius (1999) is used. This method is generally applied to simulations of sustained homogeneous turbulence in a periodic domain, where the Navier-Stokes equations are solved using a (pseudo-) spectral scheme. In **chapter 4**, the forcing scheme is applied to the lattice-Boltzmann method and a number of cases is presented to demonstrate that turbulent conditions with pre-defined properties are accurately recovered via this approach.

In **chapter 5**, the particle simulations of chapter 3 are combined with the forcing scheme presented in chapter 4 to obtain direct simulations of suspensions with *a priori* determined conditions. In this chapter the numerical setup is presented and results on 5 simulations are discussed, in which the particle volume concentration and particle density were varied. The influence of the particle phase on the development of the turbulent flow field is discussed and compared with results presented in literature on two-way coupled simulations. Particle-particle collisions are analysed and the relative velocity distribution of the particles is studied to gain understanding of the observed collision behaviour.

Chapter 6 returns to crystallisation. First, the collision behaviour of approaching particles is studied, where the particle relative motion is dominated by lubrication forces. Then, an interpretation is given of the particle-particle collisions observed in the suspension simulations of chapter 5, which are now assumed to represent crystal-crystal collisions in a crystallisation process. A method is given to estimate the rate of fragmentation of crystals as a source for secondary nucleation.

Finally, in **Chapter 7** the general conclusions of this thesis are presented and an outlook for future implications of this work is given.

Chapters 2 to 5 of this thesis have appeared in literature or have been or will be submitted for publication. As a result, some parts in the chapters may appear double.

The choice of notation throughout this thesis is conform the requirements of the various journals and therefore varies from chapter to chapter. For clarity, a list of symbols is added to the end of each chapter.

1.4 Industrial Crystallisation research at Delft University of Technology

Crystallisation research at Delft University of Technology has traditionally been carried out by the chair for separation processes, situated at the Laboratory for Process Equipment. Two research projects of this laboratory have provided a basis for the research on crystallisation and precitipation presented in this thesis.

A project for the study of industrial crystallisation, named UNIAK, has been running since 1984. The original focus of this project has been on instrumentation and control of industrial evaporation crystallisers. In the early 1980's, the idea was that, with upcoming techniques such as laser devices for in-line measuring of particle size and advanced controller equipment, on-line control and model-based predictive control of crystallisation equipment should come within reach. These viewpoints formed the basis for three phases of the UNIAK project running from 1984 up to 2002. The UNIAK research project formed the basis for the industrial crystallisation aspects of the research presented in this thesis. At the start of the project of this thesis, the third phase of UNIAK was half way. At this moment, this phase has lead to the PhD thesis of Neumann (2001).

Around the same time, research into precipitating systems was carried out in the PREMIX project, which focussed on the role of hydrodynamics and mixing in precipitation processes. In this type of crystallisation processes, supersaturation is created instantaneously by a chemical reaction. This project formed a collaboration between the Laboratory for Process Equipment and the Kramers Laboratorium voor Fysische Technology, and resulted in the thesis of Leeuwen (1998).

1.5 DIOC 6: Mastering the Molecules in Manufacturing

In the early nineties of the last century, the buzz-word in academia was 'inter-disciplinary'. In 1996, Delft University of Technology took the initiative to promote inter-disciplinary research at the university by starting the so-called Delft Interfacultary Research Centers (DIOC). These DIOC's were invoked to stimulate new research at the intersection between well-established traditional mono-disciplines. 12 DIOC research programs were selected and approved.

This thesis is supported by the DIOC 6 program named 'Mastering the Molecules in Manufacturing', abbreviated as M3. This program started on April 1, 1997, and aimed at Precision Process Technology, *i.e.* improving process technology by means of optimal design and control of chemical production processes, with a central role for process modelling. The program contained research fields from chemical process

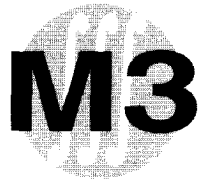

Figure 1.4: Mastering the Molecules in Manufacturing.

industry as diverse as industrial catalysis; biotechnology; conceptual process design, control and safety; hydrodynamics of multiphase processes; industrial crystallisation and precipitation. The rationale of the program is that any chemical process, whether bulk-, fine- or biochemistry, passes through a stage of process design and optimisation. Using the commonalities between the different disciplines, one can develop a general methodology for process design for any type of industrial process.

The first phase of M3, consisted of 6 projects with a total of 12 PhD students, divided over as many as five different faculties. To stimulate the multi-disciplinary character, each PhD student participating in M3 had the difficult task to manage his or her project while working in two different research groups, often distributed over two different faculties. This thesis contributes to project 3 of M3, *Optimal Design and Product Control in Crystallisation and Precipitation.* Two PhD students participated in this project which formed a collaboration between the groups of Process Systems Engineering Group of DelftChemTech, the Laboratory for Process Equipment and the Kramers Laboratorium voor Fysische Technologie. One part of the project, the subject of the thesis of colleague PhD student Elco Hollander, focussed on the relation between hydrodynamics and agglomeration in precipitating systems, while the other is the subject of this thesis. Currently, M3 is in the stage of finalising phase 1, with most participating PhD students finishing their theses (Zhu (2001),Overkamp (2002),Roubos (2002),Hollander (2002)).

Chapter 2

The microscopic modelling of hydrodynamics in industrial crystallisers

In this chapter a method for the calculation of crystal-crystal collisions in the flow field of an industrial crystalliser is proposed. The method consists of two steps. The first step is to simulate the internal flow of the crystalliser as a whole. For this purpose, the simulation of the internal flow of an 1100 l draft tube baffled crystalliser at a Reynolds number of 240,000 is presented. This simulation was done with a lattice-Boltzmann scheme with a Smagorinsky sub grid-scale turbulence model (c_s was 0.11) on approximately $35.5 \cdot 10^6$ grid nodes. The second step of the method consists of simulating individual crystals in a fully periodic box with turbulent conditions that represent the conditions in a point of the crystalliser. Thus collision frequencies and intensities of the crystals under the local hydrodynamic regime can be obtained. In this contribution a feasibility study of this second step is described. A theoretical framework is established to identify the key parameters that determine the relationship between the crystalliser flow and the box simulations. Based on this framework, conditions for box simulations representing three monitor points in the simulated crystalliser are calculated. Finally, to demonstrate the method of predicting the motion of individual particles, sedimentation and consecutive collision of a single sphere with a solid wall is simulated.

Key words: crystallisation, lattice-Boltzmann, collision rate, large eddy simulation, discrete particle simulation, turbulence

Parts of this chapter have been published in Chem. Eng. Sci. **56**, 2495-2509 (2001).

2.1 Introduction

The design and scale-up of industrial crystallisers requires predictive models that describe the evolution of the crystal size distribution (CSD) as a function of process con-

ditions, crystalliser layout and type of crystallisation process. Generally, these models are based on population balances, mass balances and energy balances and treat the crystalliser as a single ideally mixed vessel (MSMPR-models). For evaporation crystallisation, these models generally contain strongly nonlinear kinetic expressions for crystal growth, secondary or contact nucleation and agglomeration (Gahn & Mersmann (1999*b*)). The model parameters are based on the volume averaged behaviour of the entire crystalliser. However, an industrial crystalliser is far from homogeneous in terms of the physical and thermodynamic conditions. With varying crystalliser dimensions, modes of operation or types of crystalliser, these models therefore require different model parameters.

A detailed approach to modelling crystallisation processes should be able to capture the geometry of the crystalliser on the one hand and contain geometry independent kinetic models on the other. This approach has been presented by Kramer *et al.* (1999) who propose to divide the crystalliser in a number of well defined regions in which supersaturation, rate of energy dissipation, solids concentration and CSD are more or less uniformly distributed. With such an approach, kinetic parameters for these models can be obtained from lab-scale experiments or can be estimated from simulation techniques while model simulations on industrial scale are able to predict the performance of the full-scale crystallisation process.

One of the key aspects in the (dynamic) behaviour of a crystallisation process is the role of hydrodynamics. On a macroscopic scale the hydrodynamic conditions control the crystal residence time and circulation time in the crystalliser. On a microscopic scale key processes such as crystal collisions (source for secondary nucleation and agglomeration) and mass transfer for crystal growth are largely determined by the smallest scale flow phenomena. One of the main difficulties in correctly capturing the effect of the crystalliser hydrodynamics on the evolution of the crystal product is that the length and time scales in a crystallisation process vary widely. At one end of the spectrum there are the crystalliser length and time scales, which lie in ranges of meters and hours. At the other end, one can consider the individual crystals in the turbulent flow field. Here dominating length scales are in the range of 100-1000 μm for the crystals and 10-100 μm for the smallest fluid eddies. Time scales are of the order of milliseconds. The main question is how to integrate these widely varying scales and formulate a consistent method for estimating the influence of the small-scale phenomena on the overall performance of the crystalliser.

In this chapter a method is proposed to solve part of the above posed question. The crystal-crystal collision rate is an important parameter in describing both agglomeration and the formation of attrition fragments and thus plays an important role in the crystalliser behaviour. The crystal motion is directly related to the local hydrodynamic conditions. Therefore, a relationship between the macroscopic and microscopic hydrodynamic conditions needs to be established to predict collision rates in the crystalliser accurately. In this contribution, a two step method is proposed.

The first step of our method is to perform computational fluid dynamics (CFD) simulations of a given crystallisation process. From these simulations, characteristic flow data are obtained that describe the local hydrodynamic conditions of the crystalliser. The fluid phase (typically containing 10 to 20 vol% solids) is treated as a single phase

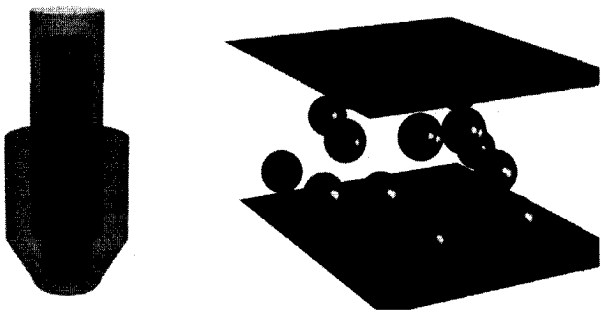

Figure 2.1: Two scales of fluid motion. The macroscopic scale (crystalliser) and microscopic scale (individual particles).

with a homogeneous density and viscosity, characteristic for the crystal slurry. This approach limits the method. It can only be applied to simulations of crystalliser flow with a virtually homogeneous slurry concentration, *i.e.* to crystallisers at lab to pilot scale at high Reynolds numbers. This assumption can be relieved by taking into account the particle transport, for instance by solving a particle dispersion equation (*e.g.* Liu (1999)) and coupling back of the particle concentration to a subgrid scale model that locally modifies the fluid viscosity, comparable to subgrid scale turbulence modelling. Typical parameters that are obtained from these simulations are rates of energy dissipation, turbulent kinetic energy and fluid velocity. These parameters are obtained at the resolution of the CFD simulation, which is at least one order of magnitude larger than the particle size of the crystallisation process.

The second step of our method is to focus on the individual crystals in the crystalliser. A transition is made from a pseudo single phase simulation to an explicit two phase simulation and thus, a transition is made from crystalliser flow simulations to highly detailed CFD simulations of individually suspended particles (see fig. 2.1). The simulated particles are implemented at high resolution with respect to the CFD grid and therefore typically occupy a number of grid nodes. The crystalliser slurry consist of high inertia particles (*i.e.* particles that do not follow the streamlines of the turbulent fluid motion) at high volume concentrations. CFD simulations of colliding particles under turbulent fluid motion are reported by for instance Sundaram & Collins (1997) and Chen *et al.* (1998*c*), but these systems are typically investigated at (very) low particle volume concentrations which do not require a coupling between the particle and fluid motion. At high volume concentrations, particles will continuously hinder each other. Therefore, in order to accurately simulate the particle motion, a direct coupling between the fluid motion and the particle motion is required.

The basic concept to resolve the second step is to design a box with fully periodic boundaries that contains a large number of particles. In this box turbulence is generated by forcing the fluid motion on the large scales. The turbulent flow is simulated up to the smallest occurring scales (*i.e.* direct numerical simulation (DNS) of the tur-

bulent flow). The conditions in this periodic box are related to the crystalliser flow via a number of key parameters. These parameters are the turbulence characteristics obtained from the crystalliser CFD and the slurry characteristics (particle size, viscosity and density). From these so-called box simulations, the collision frequency and energy can be monitored. Collision data obtained in this way can be used in models predicting the rate of secondary nucleation and attrition (Gahn & Mersmann (1999*a*)) or agglomeration in crystallisers. Since the fluid phase in the crystalliser is currently assumed to be a homogeneous slurry, no back-coupling of the results from the microscopic particle simulations (*e.g.* streak formation of particles and turbulence modification) to the macroscopic crystalliser simulations is taken into account.

The numerical method chosen to simulate both the full-scale crystalliser flow and the suspended particles is the lattice-Boltzmann method. This method is chosen because it has a number of favourable properties. First, the method is efficient and numerically stable. Second, it has an excellent performance on parallel computers. This is an important feature, because both the equipment flow simulations and the discrete particle simulations require large computational resources. Third, the method is inherently time dependent, which makes it suitable for the implementation of a sub grid-scale (SGS) turbulence model for large eddy simulations (LES). Turbulence modelling is required for simulation of the highly turbulent crystalliser flow. Fourth, the method can treat arbitrarily shaped boundaries which makes it suited for simulating fluid flow in irregular shaped geometries such as a crystalliser or a cluster of moving particles. Simulations of generated isotropic turbulence are frequently done with spectral methods. Turbulence in the lattice-Boltzmann schemes can be generated by agitating the fluid at varying time and length scales with fluctuating force fields. In section 2.2 the background of the lattice-Boltzmann method is discussed along with the implementation of the LES model and the treatment of the boundary conditions.

The main objective of this chapter is to establish the relationship between the two steps of the simulation methodology and to investigate the feasibility of the proposed method. For the first step, in section 2.3, the CFD simulation of a pilot scale 1100 l draft tube baffled crystalliser is reported and results are presented. Then, in section 2.4 an analysis is given of the hydrodynamic length and time scales that occur in the turbulent crystalliser flow and that characterise the crystalliser flow at the microscopic scale. These parameters are then used to explain how to calculate the parameters that set the scene for a representative box simulation. It is shown what the requirements of box-simulations that represent three chosen monitor points in the crystalliser will be with respect to computational parameters such as the domain size and computational time for a given particle size. The box-simulations are currently still under construction and therefore no results of these simulations are reported here. However, as a first example of a detailed suspended particle simulation, the lattice-Boltzmann simulation of a single particle settling towards and colliding with a solid wall is presented in section 2.5. In section 2.6 conclusions are drawn regarding the obtained framework.

2.2 The lattice-Boltzmann method

The lattice-Boltzmann method has been developed during the last decade and stems from the lattice gas cellular automata techniques that date back to the seventies and eighties. The concept of the lattice-Boltzmann method is based on the premise that the mesoscopic (continuum) behaviour of a fluid is determined by the behaviour of the individual molecules at the microscopic level. In the lattice-Boltzmann approach, the fluid is represented by fluid mass placed on the nodes of an equidistant grid (lattice). At each time cycle, a number of steps are executed; from each grid node, fluid mass moves to the surrounding grid nodes and conversely mass arrives at each grid node. In this way conservation of mass is guaranteed. Arriving mass collides, while collision rules are applied that guarantee conservation of momentum. After the collision step, the mass is redistributed and a cycle is finished. One of the elegant features of the method is that although the collision rules describe the fluid behaviour locally on a grid node, the continuity equation and incompressible Navier-Stokes equations are recovered (Rothman & Zaleski (1997); Chen & Doolen (1998)).

A number of recent developments in the application of the lattice-Boltzmann method clearly demonstrate its versatility. In this contribution a methodology is presented to simulate turbulent slurry flow while resolving the complete hydrodynamic environment of the particles. The first publications in which this approach to slurry flow is described are from Ladd, who applied the method to simulate slurry-flow at the most detailed level (Ladd (1994*a*,*b*)) and calculated sedimentation with up to 32,000 individual particles (Ladd (1997)). Another contribution is this field is given by Heemels (1999). Multi-phase problems have also been addressed by Rothman & Zaleski (1997) (liquid-liquid) or by Sankaranarayanan *et al.* (1999) (liquid-gas). Examples of lattice-Boltzmann studies in which complex and dynamic geometries are combined with mass transfer are simulations of coral growth (Kaandorp *et al.* (1996)) and bio film growth (Picioreanu *et al.* (1999); Picioreanu (1999)). The internal flow of a crystalliser is highly turbulent and requires the incorporation of a sub grid-scale (SGS)turbulence model. Examples in which the method is used to investigate the turbulent fluid flow in a stirred tank are given by Eggels (1996) and Derksen & Van den Akker ((1999). A review on the lattice-Boltzmann method is found in Chen & Doolen (1998).

2.2.1 The lattice-Boltzmann equation

Although different types of lattice-Boltzmann schemes have been developed, the different methods all stem from the evaluation of the same lattice-Boltzmann equation (LBE):

$$f_i(\mathbf{x} + \mathbf{c}_i, t + 1) = f_i(\mathbf{x}, t) + \Omega_i(f_i(\mathbf{x}, t)) \tag{2.1}$$

This equation states that at a position $\mathbf{x}$ and time t, an amount Ω_i is added to f_i and transported to the position $\mathbf{x} + \mathbf{c}_i$ at time $\mathbf{t} + 1$. The subscript indicator i represents the direction of propagation and is determined by the type of grid, $\mathbf{c}_i$ is the discrete velocity at which mass travels from one node to the other, Ω_i is the collision operator which determines the post collision distribution of mass over the M directions on a grid node.

The mass density function f_i and the collision operator Ω_i have the following universal properties;

- summation of f_i over the M directions of the chosen lattice gives the fluid density at position $\mathbf{x}$ and summation of $f_i\mathbf{c}_i$ gives the momentum vector;

$$\sum_{i=1}^{M} f_i(\mathbf{x},t) = \rho \tag{2.2}$$

$$\sum_{i=1}^{M} f_i(\mathbf{x},t)\mathbf{c}_i = \rho\mathbf{u} \tag{2.3}$$

- conservation of mass and momentum are guaranteed by the following equations;

$$\sum_{i=1}^{M} \Omega_i(\mathbf{x},t) = 0 \tag{2.4}$$

$$\sum_{i=1}^{M} \Omega\mathbf{c}_i = \mathbf{f}(\mathbf{x},t) \tag{2.5}$$

where $\mathbf{f}(\mathbf{x},t)$ represents a source of momentum from an external force field. This force field can be homogeneous, as in *e.g.* a gravity field or can be manipulated locally, as in the method for the boundary condtions, which will be explained later.

For the two applications discussed in this chapter, two different schemes for solution of the LBE equation were used. The simulation of the internal flow of an 1100 l DTB crystalliser is based on the method of Somers (1993). Based on this method, a 3D code for large eddy simulations was developed by Derksen & Van den Akker ((1999). For the simulation of settling particles, a single relaxation time scheme is used (Qian *et al.* (1992)). Both schemes obtain the same continuity equation

$$\partial_t\rho + \nabla\cdot\rho\mathbf{u} = 0 \tag{2.6}$$

and momentum equation

$$\partial_t\rho\mathbf{u} + \nabla\cdot\rho\mathbf{u}\mathbf{u} = -\nabla P + \nabla\cdot\nu[\nabla(\rho\mathbf{u}) + (\nabla(\rho\mathbf{u}))^T] + \mathbf{f}. \tag{2.7}$$

In the incompressible limit (*i.e.* for fluid velocities much smaller than the speed of sound,$|\mathbf{u}| \ll u_s$) equation 2.7 corresponds to the incompressible Navier-Stokes equation. The lattice-Boltzmann method is inherently dimension less. Length scales are treated as lattice units (equal to the grid spacing Δ) and time is represented in time steps.

2.2.2 Large Eddy Simulation

For the simulation of flows at industrially relevant Reynolds numbers (*i.e.* at turbulent conditions) direct simulation of the flow is not feasible and turbulence modelling is required. The time dependent character of the lattice-Boltzmann method makes it suitable for the implementation of a sub grid-scale (SGS) model. In this way large-scale motions are explicitly solved, while all small-scale motions, typically smaller than two times the grid spacing, are filtered out. This approach is usually referred to as Large Eddy Simulation (LES). The filtering of small-scale motion is based on the assumption that the motion of the smallest scales is isotropic in nature and that the SGS energy is dissipated via an inertial subrange that has a geometry independent character. Thus, the turbulent flow at the sub grid-scale can be represented by a SGS eddy viscosity (ν_t). The LES-model applied in this research is a standard Smagorinsky model (Smagorinsky ((1963)) where the eddy viscosity is related to the local rate of deformation:

$$\nu_t = l_{mix}^2 \sqrt{S^2} \tag{2.8}$$

where l_{mix} is the mixing length of the sub grid motion. The rate of deformation S^2 is calculated by

$$S^2 = \frac{1}{2}\left(\frac{\partial u_\alpha}{\partial x_\beta} + \frac{\partial u_\beta}{\partial x_\alpha} - \frac{2}{3}\delta_{\alpha\beta}\nabla\cdot\mathbf{u}\right)^2 \tag{2.9}$$

with $\delta_{\alpha\beta}$ the Kronecker delta. The Smagorinsky constant c_s is defined as the ratio between the mixing length and the grid spacing. This constant is related to the cut-off length of the turbulence model l_f. This can be estimated from (Eggels (1994)), assuming isotropic homogeneous turbulence at the sub grid-scale:

$$l_{mix} = c_s\Delta = 0.0825 l_f. \tag{2.10}$$

The cut-off length indicates the length scale in the turbulent energy spectrum, below which all motion is considered homogeneous isotropic turbulence, the contribution of which to the large scale fluid motion is captured by the turbulence model. Implementation of this LES model into the lattice-Boltzmann framework is rather straightforward, because the rate of deformation tensor (equation 2.9) is essentially contained within the method. A local total viscosity ($\nu + \nu_t$) is calculated and applied in the collision step.

2.2.3 Boundary Conditions

Boundary conditions are imposed onto the fluid via the external force vector $\mathbf{f}(\mathbf{x}, t)$ from equation 2.5. A force is applied on a grid node $\mathbf{x}$ in order to manipulate the fluid with the view of obtaining a prescribed velocity at this grid node. Thus, inlet and outlet flows can be imposed, no-slip boundaries at the surface of an object can be imposed, or the fluid can be manipulated to generate velocity fluctuations to simulate turbulent conditions. When imposing the boundary of an object not located at the position of the grid nodes, an interpolation-extrapolation scheme is used. Derksen *et al.* (1997) developed a method of adaptive force fields within the lattice-Boltzmann framework. This method, used for the Somers (1993) type lattice-Boltzmann scheme has been modified for the single relaxation time scheme that is used for the particle simulation presented in section 2.5.

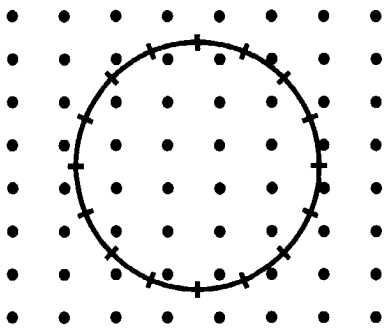

Figure 2.2: Imposing a circle on a 2D lattice. (•) represent lattice nodes and (+) circle points.

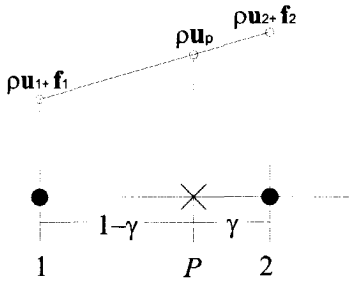

Figure 2.3: Interpolation of the fluid velocity at point P between grid nodes 1 and 2.

The force field technique is best explained by the following example. Suppose one wants to impose no-slip boundary conditions at the circle within the flow-domain (see figure 2.2). The circle is defined by points located in the computational space at the crosses on the circle. These points have a velocity that is determined by the translational and rotational velocity components of the object. A force is applied at the nodes surrounding each of these points to force the fluid to obtain a velocity related to these points. This force is determined in two steps. First, the actual fluid momentum at a point on the circle is determined by first-order Lagrange interpolation from the surrounding grid nodes. Equation 2.11 and figure 2.3 demonstrate this for the one-dimensional case.

$$\rho \mathbf{u}_p = (\rho \mathbf{u}_1 + \mathbf{f}_1) \cdot \gamma + (\rho \mathbf{u}_2 + \mathbf{f_2}) \cdot (1 - \gamma) \tag{2.11}$$

The force applied to the grid node in a previous step is incorporated in the interpolation to account for the effect that two points on the circle may affect the fluid at the same grid node. γ represents the fractional distance between point P and point 2. Now a force is defined at point P that opposes the difference between $\mathbf{u}_p$ and $\mathbf{u}_{set}$. Second, this force $\mathbf{f}_i$, applied on nodes 1 and 2, is calculated by extrapolation of the opposing

force at point P to the grid nodes using the same linear interpolation coefficient γ. For the one-dimensional example this is given by equations 2.12 and 2.13:

$$\mathbf{f}_1' = \mathbf{f}_1 + \gamma \cdot \rho(\mathbf{u}_{set} - \mathbf{u}_p) \tag{2.12}$$

$$\mathbf{f}_2' = \mathbf{f}_2 + (1-\gamma) \cdot \rho(\mathbf{u}_{set} - \mathbf{u}_p) \tag{2.13}$$

This method can be extended to two and three dimensions by linear interpolation and extrapolation over the respective 4 or 8 surrounding nodes of an object surface point and can also be extended to higher order interpolation schemes. The total hydrodynamic force on an object can be determined by summation of the forces applied at the grid nodes surrounding the surface of the object.

2.3 Crystalliser CFD simulations

As a case study, the internal flow of a pilot scale 1100 l DTB crystalliser was simulated. The crystalliser subject of this CFD study has been investigated in many previous crystallisation studies (*e.g.*, Bermingham *et al.* (1998) or Neumann *et al.* (1999)) for characterisation of its dynamic behaviour in crystallising ammonium sulphate and potassium nitrate under varying process conditions. Because of the complex geometry and highly turbulent operating conditions ($Re \geq 4 \cdot 10^5$), a high-resolution CFD simulation is required. The flow data, more specifically the turbulence characteristics, thus obtained will be used as a basis for further studies of colliding particle simulations (see section 2.4).

In the following two sections, the crystalliser setup and operating conditions are presented and the setup of the simulation is described. Instantaneous as well as time averaged results were obtained that are discussed in the final part of this section.

2.3.1 Crystalliser setup and geometry

In figure 2.4, the crystalliser geometry and dimensions are given. The 1100 l DTB crystalliser is equipped with a marine type impeller which is placed at the bottom section inside the draft tube. The impeller revolves in such a way that the flow is directed upward from the bottom of the draft tube to the top section of the crystalliser. The draft tube interior contains four baffles. At the top of the crystalliser, vacuum is applied in order to lower the boiling temperature of the crystal slurry. The crystal slurry is circulated downwards along the outside of the draft tube. The outer shell of the crystalliser, equipped with six baffle skirts and six fines flow outlets, is a settling zone where an upward flow causes classification such that fine crystals are removed from the crystalliser. The flow containing fine crystals is passed through an external heat exchanger for heat input and dissolution of fine crystals and returned to the bottom section of the crystalliser. The bottom of the crystalliser also contains a feed inlet. The operating conditions of the crystalliser are given in table 2.1. Under these operating conditions, the crystalliser produces ammonium sulphate crystals in the size range from 500 to 1000 μm at a slurry density of 10 to 20 vol%.

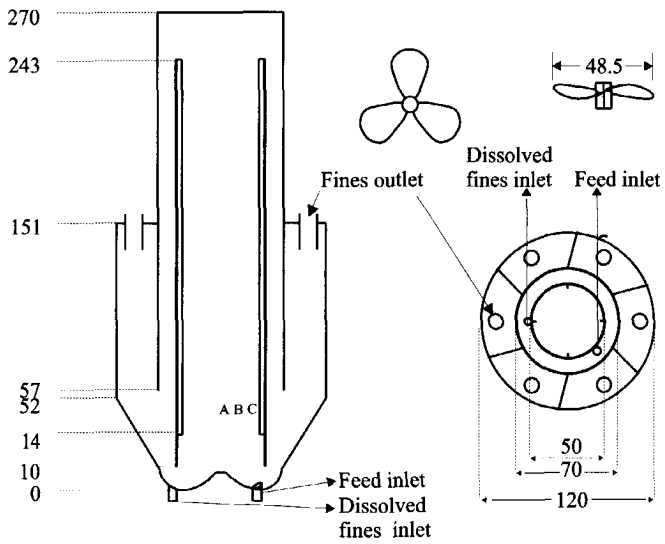

Figure 2.4: Crystalliser and stirrer geometry and dimensions. Side view and top view of the 1100 l DTB crystalliser and the marine type impeller. Dimensions are given in cm. The impeller is placed 12 cm from the bottom of the crystalliser. Points (A), (B) and (C) are monitoring points, placed at (A) the centre of the crystalliser, (B) 15 cm from the centre and (C) 21 cm from the centre, 7.5 cm above the impeller in a vertical plane containing two draft tube baffles.

Table 2.1: Operating conditions and simulation settings of the 1100 l DTB crystalliser. The crystalliser properties were estimated for an ammonium sulfate suspension of 10 vol% solids in a saturated solution at 60^0 C (see also table 2.4).

Physical conditions			Simulation conditions		
Impeller speed	[rpm]	320	Impeller speed	[rp ts]	1/3200
ν	$[m^2/s]$	$2.04{\cdot}10^{-6}$	ν_{lB}	[-]	$1.4{\cdot}10^{-4}$
Re Impeller	[-]	615,000	Re Impeller	[-]	240,000
ϕ_v// feed	[m/s]	0.14	ϕ_v// feed	[lu/ts]	$1.17 \cdot 10^{-3}$
ϕ_v// fines	[m/s]	1.20	ϕ_v// fines	[lu/ts]	$14.6 \cdot 10^{-3}$
			timestep	[μs/ts]	58
			gridspacing Δ	[mm/lu]	5.0

2.3.2 Crystalliser simulation setup

The crystalliser was simulated on a computational domain of 552 x 253 x 253 ($\approx 35.5{\cdot}10^6$) grid nodes. Thus, a spatial resolution of 5.0 mm per lattice unit was obtained. The geometry and stirrer were implemented in the computational domain via a second order adaptive force field technique analogous to the first order method presented in section 2.2. The Smagorinsky constant c_s was set to 0.11. In order to keep the simulation within the constraint of the incompressibility limit, the impeller speed was kept well below the speed of sound of the lattice gas and was set to complete one revolution in 3200 time steps. Table 2.1 contains the simulation settings. The impeller Reynolds number given in table 2.1 is calculated with

$$Re = \frac{ND_{imp}^2}{\nu}. \tag{2.14}$$

The impeller Reynolds number is a function of the slurry viscosity, which is a function of the slurry solids concentration. The slurry viscosity was estimated with Krieger's equation (Liu (1999)),

$$\mu = \mu_f \Big(1 - \frac{\phi}{\phi_{max}}\Big)^{-1.82} \tag{2.15}$$

where ϕ_{max} is the maximum packing limit particle concentration, which was set 0.68. The effect of the particles on the overall slurry viscosity is twofold. In the first place, during operation, the slurry density varies from 10 to 20 vol% This causes the impeller Reynolds number to vary between approximately 800,000 and 400,000 during operation. In the second place, the slurry concentration is not homogeneously distributed throughout the crystalliser. Streaks of high and low solids concentrations will form, influencing the local viscosity throughout the crystalliser.

At the given scale of 1100 l and the given high Reynolds numbers, as a first approach, the slurry density may be considered practically homogeneous. The high Reynolds number of the crystalliser indicates that the assumption of a homogeneous suspension at least on the large scales can be justified. The difference in Reynolds number between the pilot scale crystalliser and the LES will hardly result in a change in the overall obtained flow field. At higher Reynolds numbers the fluid flow will mainly exhibit an increase in motion at the small length scales ($\mathcal{O}(\eta)$). The large scales of fluid motion are limited by the size of the equipment and therefore fixed, while the Kolmogorov scale can be rescaled based on the Reynolds similarity. Furthermore, the small scale motion is not resolved but filtered by the turbulence model, which will further suppress the difference in the flow fields at increasing Reynolds number.

The lattice-Boltzmann/LES code was parallellized by means of domain decomposition. The computational domain was divided in 8 sections. Message passing was performed by the MPI protocol. The total memory requirement for this simulation was approximately 3.0 gigabytes. The simulation was performed on 8 nodes of a parallel cluster of pentiumIII 500 MHz processors. The simulation of one impeller revolution on this system took about 26 hours wall clock time. After development of the turbulent flow field the simulation was continued for another 6.4 impeller revolutions in order to obtain time-averaged data and time-series.

Table 2.2: Operating parameters from the 1100 l DTB crystalliser. Values derived from the high resolution CFD and from literature (Neumann *et al.* (1999))

		From CFD	From literature
Po	$[-]$	0.47	0.40
$\bar{\epsilon}$	$[W/kg]$	1.73	1.48
Pu	$[-]$	0.25-0.30	0.32

2.3.3 Results of the crystalliser LES simulation

In figure 2.5, the velocity field and contour plot of the rate of energy dissipation are presented as found by the LES simulation. The time averaged contour plot of figure 2.5 (a) clearly demonstrates that a wide distribution in the rates of energy dissipation can be observed throughout the crystalliser. Of particular interest is the difference in the rate of energy dissipation between the core of the flow inside the draft tube and the outer zone. Apparently, the pumping activity of the marine type impeller is mainly present at the impeller tip. This is observed in the vector plots of both figures 2.5 (a) and (b). At a larger distance upward from the impeller, the velocity profile becomes more uniform although averaged velocities in the core remain lower. The contour plots of the rate of energy dissipation demonstrate that energy dissipation is highest near the impeller tips and near the draft tube wall and baffles. Figure 2.5 (b) gives an instantaneous realisation of the flow field. In this figure the resolved turbulent structures can be clearly seen, both in the velocity field and in the rate of energy dissipation. An interesting feature is that the rate of energy dissipation in the impeller region is apparently strongly dependent on the impeller position since the contour plot of figure (a) gives a larger high intensity region than that of figure (b).

The difference in flow characteristic at different radial positions in the crystalliser is also clearly seen in the time-series of figure 2.6. At three monitor-points, (A), (B) and (C) a time-series of flow data was stored. Parameters that were determined from these points are presented in table 2.3 and will be discussed more extensively in section 2.4. From point (A) to (C) (from the centre to the outside of the draft tube), the frequency of the fluctuations increases, which indicates a higher degree of turbulence. A periodicity in the temporal behaviour due to the impeller passing is not observed even at this relatively close distance from the impeller. A final remark can be made about the top section of the crystalliser, where the flow enters the down coming region. Apparently, the flow is drawn into the down comer due to the impeller action. This causes both a high degree of turbulence in the top section of the down comer and a short circuit flow at the boiling zone.

In table 2.2, the performance of the crystalliser impeller as determined from the simulations is compared to typical literature values. This table demonstrates that the values obtained are in the same range as those found previously in literature.

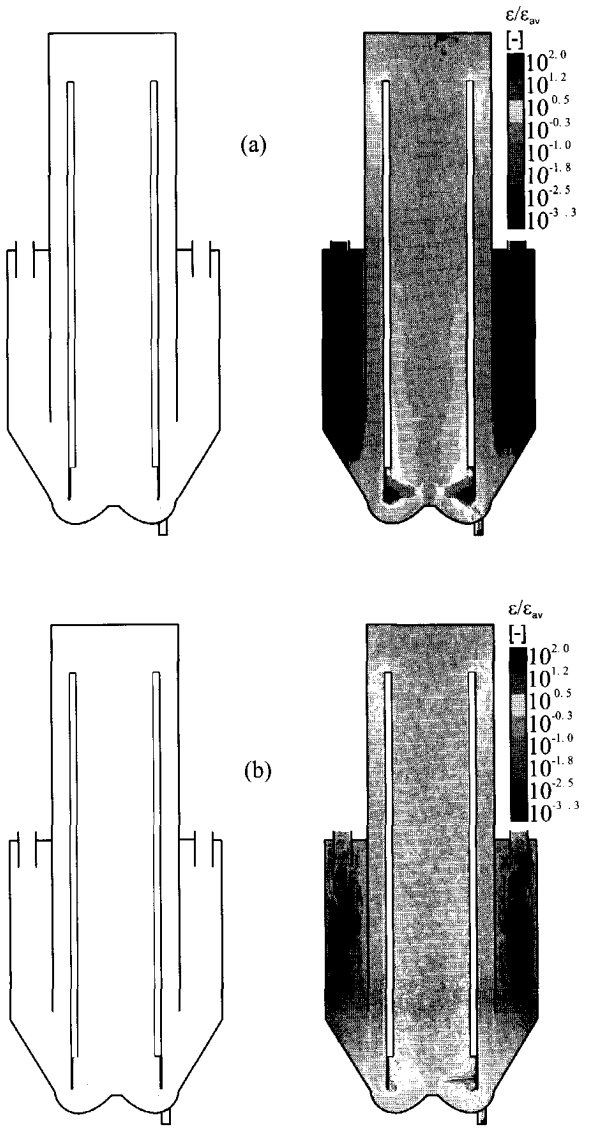

Figure 2.5: Flow field of the 1100 l DTB crystalliser. (a) The time-averaged vector plot (left) and contour plot of the rate of energy dissipation (right). (b) An instantaneous realisation of vector plot (left) and contour plot of the rate of energy dissipation (right).

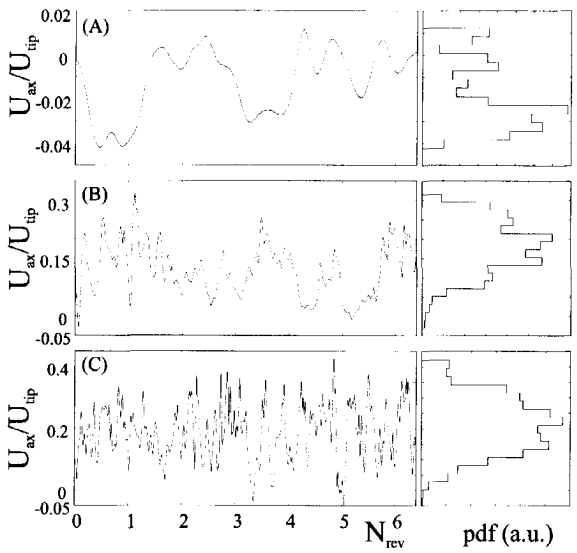

Figure 2.6: Time series (left) and pdf (right) of the axial velocity component inside the draft tube at the three monitor points (A), (B) and (C) (see fig 2.4). The p.d.f. is given in arbitrary units.

2.4 Length scale analysis

The objective of our study is to develop a method to predict collision rates in the turbulent flow field of an industrial crystalliser. The collision rates will be calculated from the direct numerical simulation (DNS) of individual particles in a periodic box. The development of the box simulations with particles is the subject of the following chapters (in section 2.5 a single settling sphere is presented to demonstrate of a moving particle). In this section a length and time scale analysis is given to identify the relationship between the LES simulation of the crystalliser and to explore the feasibility of a DNS-particle simulation. The LES simulations assume a pseudo-homogeneous single phase fluid while the individual particle simulations describe a discrete two phase system. The LES simulation is used to set the scene for the discrete particle simulations and a number of assumptions are made to identify the parameters that determine the relationship between the two types of simulations. The following two sections discuss parameters that characterise the solid phase and the turbulent crystalliser flow. The third section introduces a method to estimate the collision rate of a given type of particles in a given turbulent flow field. This collision rate is used only to estimate the required simulation time to obtain sufficient statistical data on particle collision rates. The theoretical parameters that are obtained in the following three sections are evaluated at the monitor points in the flow field of the crystalliser to demonstrate the evolving dimensions and characteristics of box simulations that represent these three points.

2.4.1 Parameters determined by the particulate phase

The first parameter that can be addressed is the particle size. In the type of industrial crystallisation processes subject of this work, the average particle size varies in a range of 100 to 1000 μm. Under the turbulent conditions of an industrial crystalliser, the Kolmogorov length scale typically ranges from 10 to 100 μm. Thus, the size of the crystals typically exceeds a number of times the Kolmogorov length scales encountered in the crystalliser. The particle diameter is obviously determined by the choice of model system from the crystallisation process. The first approach is to represent the solid phase as mono disperse spheres with a diameter equal to the average particle size of the crystal product. The true crystal product has a CSD starting at sub-Kolmogorov length particles. Nevertheless, this choice can be justified based on the argument that the topic of interest is the collision rate and intensity. To determine attrition, only particles with sufficient inertia will fracture, being typically the larger particles. Particles are implemented at high resolution with respect to the grid spacing (see also section 2.5) and therefore the particle diameter should, as a rule of thumb, cover at least 10 grid units for sufficient resolution. The grid spacing is determined by the hydrodynamic conditions (see section 2.4.2) and therefore after choosing a typical particle size, the particle diameter in lattice units is fixed.

The minimum length of the box size is determined by the length at which the fluid velocities are uncorrelated (see section 2.4.2). One could argue that not only the fluid velocity should be uncorrelated at half the box size, but also the particle interactions. The reason for this is that in order to prevent numerical artifacts, a particle at the centre of the box should not influence its own trajectory via the periodic boundaries of the box. Therefore, a criterion to quantify the distance at which two particles influence each other is determined by the long-range hydrodynamic interaction force. For two identical spheres in the Stokes regime, the leading term of this interaction force decays as 1/R (Kim & Karrila (1991)). A rule of thumb that can be applied here is that the box dimensions should exceed approximately 10 to 20 particle diameters for the interaction force to break down. Furthermore, because of the turbulent fluid field and the expected non-Stokesian regime of the particles, the interaction force will break down stronger than 1/R. Thus, the criterion for the box size determined by the demand of uncorrelated turbulent flow will be strict enough to prevent the particles to be self-correlated.

The particle concentration in the box simulations is a set parameter that is chosen based on the crystal slurry concentration encountered in the crystallisation process under consideration. The main assumption that has been made for the overall crystalliser flow simulation is that the slurry flow is represented as one homogeneous fluid phase. Thus, the solid phase is assumed to be homogeneously spread throughout the crystalliser. When focussing on a small section in the crystalliser a transition is made from a pseudo single-phase simulation to an explicit two phase simulation of fluid with suspended particles. The assumption of a homogeneous suspension is also required for the box simulations because of the limited size of the box and the lack of knowledge on the distribution of the crystals throughout the crystalliser. This is warranted by the fully periodic boundary conditions of the box for both the fluid phase and the particulate phase. Because of the limited size of the box and the limited number of contained particles, at

any position inside the box any particle will experience a practically homogeneous and constant particle concentration.

The particle inertia can be characterised with the particle relaxation time τ_p which is a measure for the response time of a particle subject to external accelerations. For Stokesian particles this relaxation time is given by

$$\tau_p = \frac{(2\rho_p + \rho_f)d_p^2}{36\mu}. \tag{2.16}$$

Although the particles in the turbulent flow field are likely to exhibit Reynolds numbers larger than 1, we use this parameter as an estimate for the order of magnitude of the particle inertia. Two particles coming from two uncorrelated eddies will collide if their inertia is large enough to make them deviate from the streamlines. The relaxation time of the particles can be used as a measure to determine which turbulent scales need to be investigated. The large scale motion of the turbulent fluid flow will cause all particles in a cluster to move simultaneously in the same direction without effective relative motion and thus the contribution of the largest scales to collisions will be small. On the other hand, the smallest scale motion (*i.e.* at the Kolmogorov length scale) is typically one order of magnitude smaller than the average particle size and thus the net contribution of this motion to particle collisions will also be negligible. The scales of fluid motion that contribute most to the particle collisions are probably the scales that are identified with a time scale of the same order of magnitude as the particle relaxation time.

2.4.2 Turbulence length and time scales

In order to have a consistent method to translate the GS and SGS turbulent fluid motion of the crystalliser to a DNS of the fluid flow in a periodic box, the assumptions that are made for LES modelling need to be investigated and the key parameters that characterise the flow conditions at both the GS and the SGS need to be determined.

As discussed in section 2.2.2, the LES modelling approach is based on the assumption that the turbulent motion at the SGS is isotropic. The kinetic energy contained at the grid scale is transported via a cascade of eddies to the smallest length scale or dissipation scale where it is dissipated. The energy spectrum of the cascade of large to small eddies is assumed to behave according to the $k^{-\frac{5}{3}}$-law that characterises the inertial subrange (Eggels (1994)) and can be taken as (Tennekes & Lumley (1973)):

$$E(k) = \alpha_K \epsilon^{\frac{2}{3}} k^{-\frac{5}{3}} \tag{2.17}$$

where α_K is the Kolmogorov constant with an approximate value of 1.6. Thus, the SGS motion of the LES simulation is characterised by the energy that is contained at the GS and SGS and the rate at which energy is locally dissipated. From the LES simulations, the rate of energy dissipation (ϵ) and the energy that is contained by the motion at the GS and the SGS turbulence, E_{GS} and E_{SGS}, are calculated according to the following equations:

$$\epsilon = \nu_t S^2 \tag{2.18}$$

$$E_{GS} = \frac{1}{2}(u'^2 + v'^2 + w'^2) \tag{2.19}$$

where u', v' and w' are the root-mean-square values of the x,y, and z components of the resolved velocity fluctuations. Finally an equation for E_{SGS} (Eggels (1994)) is:

$$E_{SGS} = \frac{\nu_t^2}{0.27 l_{mix}^2} = \frac{l_{mix}^2 S^2}{0.27} \tag{2.20}$$

The total turbulent kinetic energy κ is given by

$$\kappa = E_{GS} + E_{SGS} \tag{2.21}$$

A mean square velocity related to the kinetic energy of a scale i can be calculated with

$$\overline{U_i^2} \equiv \frac{2}{3} E_i \tag{2.22}$$

From the LES simulations a number of characteristic length and time scales can be determined that need to be resolved by the temporal and spatial resolution of a DNS of the turbulent flow. The dissipation scale or Kolmogorov length scale is the smallest length scale encountered in the turbulent flow. This length scale and the time scale associated with this length scale are given by

$$\eta = \left(\frac{\nu^3}{\epsilon}\right)^{\frac{1}{4}} \tag{2.23}$$

$$\tau_k = \left(\frac{\nu}{\epsilon}\right)^{\frac{1}{2}} \tag{2.24}$$

A criterion for good representation of the microscopic length scales is given by the demand that the grid spacing wave number times the occurring Kolmogorov length is greater that unity, *i.e.* $\Delta < \pi\eta$ (Sundaram & Collins (1997)).

A criterion that should be satisfied and determines a minimum box dimension is that the fluid velocities are uncorrelated over a distance of at least half the box length. With the assumption of the existence of an inertial subrange, the correlation coefficient $f_{11}(r)$ can be used to estimate this length. This coefficient describes the correlation of fluid velocities along a line joining two points and for the inertial subrange can be estimated by the following equation(Abrahamson (1975)):

$$f_{11}(r) = 1 - \frac{0.9\epsilon^{\frac{2}{3}} r^{\frac{2}{3}}}{\overline{U_i^2}} \tag{2.25}$$

From this equation, the minimum distance l_0 at which velocities are uncorrelated is given when $f_{11}(r) = 0$:

$$l_0 = \frac{1.2(\overline{U_i^2})^{\frac{3}{2}}}{\epsilon} \tag{2.26}$$

A characteristic integral timescale is given by the eddy turnover time. This timescale is given by the ratio of the kinetic energy of turbulent motion and the rate of energy dissipation:

$$T_e = \frac{\kappa}{\epsilon} \tag{2.27}$$

An integral timescale for the SGS motion is determined by the dissipation of the SGS energy E_{SGS};

$$T_{SGS} = \frac{E_{SGS}}{\epsilon} \tag{2.28}$$

Table 2.3: Parameters obtained from the three monitor points

Position	ϵ [W/kg]	E_{GS} $[m^2/s^2]$	E_{SGS} $[m^2/s^2]$	$l_{0(GS)}$ $[m]$	$l_{0(SGS)}$ $[mm]$	η $[mm]$	T_e $[ms]$	T_{SGS} $[ms]$	τ_k $[ms]$
Point (A)	0.043	0.029	0.003	0.075	2.340	1.503	677.4	66.83	37.45
Point (B)	0.959	0.285	0.020	0.104	1.983	0.692	297.5	21.26	7.930
Point (C)	4.122	0.951	0.054	0.147	2.007	0.480	230.6	13.18	3.826

2.4.3 Collision frequencies

In order to obtain sufficient collision statistics a (large) number of collisions must be obtained during the simulation and this sets a minimum requirement to the simulation time. Thus, to address the feasibility of the proposed simulation approach, an estimate of the collision rate is required. The theoretical framework of Abrahamson (1975) can be used to estimate collision frequencies for given particle and flow conditions. Based on kinetic gas theory, Abrahamson derived an expression for the collision rate for particles with large inertia in isotropic turbulence, which is also the subject of this study. His analysis was based on the correlation between fluid motion and particle motion for particles in turbulent fluid in an inertial subrange that is described by the correlation function in equation 2.25. The mean square velocity of an individual particle is calculated with (Abrahamson (1975)):

$$\frac{\overline{U_p^2}}{\overline{U_i^2}} = \frac{T_i/\tau_p + b^2}{T_i/\tau_p + 1} \tag{2.29}$$

and b is calculated with

$$b = \frac{3\rho_f}{(2\rho_p + \rho_f)}. \tag{2.30}$$

The mean square fluid velocity and timescale that need to be applied in expression 2.29 are estimated from either the GS or the SGS kinetic energy. The expression for the collision rate of mono disperse particles takes the form of:

$$Z = 4\sqrt{\pi} n_p^2 d_p^2 \sqrt{\overline{U_p^2}}. \tag{2.31}$$

The collision rate of equation 2.31 is used in the following section to estimate the duration of the box simulations in order to obtain sufficient collision statistics.

2.4.4 Length scales in the 1100 l DTB crystalliser

The data obtained from the monitor points of the crystalliser simulation is used to estimate the parameters for the box simulations that should represent the conditions at the monitor points. A number of properties is given in table 2.3. This data clearly demonstrates an increase in turbulence towards the outside of the draft tube, as was already observed in section 2.3. In order to estimate crystal collision frequencies, the crystal phase needs to be chosen. The crystalliser of section 2.3 is used to produce ammonium sulphate crystals. In table 2.4 the solid and fluid phase of a typical crystal slurry are given, determined for a saturated ammonium sulphate solution. The data in

Table 2.4: Properties of a typical ammonium sulphate slurry. The fluid properties were determined for a saturated ammonium sulphate solution at 60 ^0C.

d_p	600	$[\mu m]$	n_p	$8.84 \cdot 10^8$	$[\#/m^3]$
ρ_p	1768	$[kg/m^3]$	ρ_f	1250	$[kg/m^3]$
τ_p	24.1	$[ms]$	μ_f	$1.99 \cdot 10^{-3}$	$[kg/(ms)]$
C	0.10	$[m^3/m^3]$			

table 2.3 demonstrates that the Kolmogorov length scale is of the order of the particle size. However, in the actual crystalliser, the Reynolds number is higher than in that of the large-eddy simulation. This may further decrease the actual Kolmogorov length scale in the turbulent suspension by a factor of roughly 0.5.

To estimate the size and resolution for the box simulations, a particle size and box size need to be chosen. If one were to capture the turbulent flow field of the crystalliser in the turbulent box simulations, then these simulations should capture at least the integral length scales $l_{0(GS)}$ of the crystalliser flow. For case A this would mean that a box should capture roughly 7.5^3 cm^3 and accordingly 373.000 particles. A domain size for such a simulation would be approximately 1250^3 grid nodes. These figures are not considered feasible for studies of turbulent suspension simulations. Apart from the feasibility, the characteristics of the turbulent flow field in the crystalliser are also not likely to be isotropic on such a length scale, which is a requirement for the turublent box simulations.

On the other hand, the sub-grid turbulence of the large-eddy simulation is assumed to be isotropic. The integral scale of this turbulent flow is of the order of 2 mm. By choosing the domain as 1 cm^3, a simulation can be set up that contains 880 particles, and where the integral scale of the sub-grid scale turbulent flow is captured a number of times. The resolution should be sufficient to meet the requirement on the Kolmogorov length scale. Therefore the resolution needs to be determined, which is set by choosing the resolution of the particle size. In a typical simulation of resolved particles, a particle is chosen to occupy approximatley 10 gridnodes per particle diameter. This fixes the resolution of the simulations to 60 $\mu m/lu$. At this resolution, the demand that the Kolmogorov length scale should be captured by the computational grid is easily met. A box of 1 cm^3 occupies 167^3 grid nodes, which can be considered a feasible box size.

In this way, a box simulation of a suspension in an isotropic turbulent flow field will correspond to the motion of the particles at the sub-grid scale of the crystalliser flow. The typical particle velocity and particle Reynolds number encountered in this flow field are given in table 2.5. The velocity fixes the temporal resolution of the simulation. The lattice-Boltzmann scheme demands that the maximum velocity in the simulation is maintained well below the speed of sound. Therefore, $\overline{U}_p$ was used as a measure for the maximum velocity, and was set to correspond to a velocity in grid units of 0.01 lu/ts. Due to this requirement, the Kolmogorov time scale is approximately 2000 time steps, which assures that sufficient temporal resolution is warranted to capture the high-frequency motion of the turbulent flow. Table 2.5 gives the particle Reynolds number of the spheres. By use of equations 2.29 and 2.31, the collision rate is determined that is encountered at the monitor points. To obtain sufficient collisions for statistical analysis,

Table 2.5: Estimation of the collision frequencies and particle properties for a DNS simulation of mono disperse solid spheres in a isotropic turbulent flow.

Position	Re_p [-]	$\overline{U_p^2}$ $[m^2/s^2]$	Z $[\#/(m^3 s)]$	t_{sim} [s]	Timestep $[\mu s]$
Point (A)	12.88	0.002	$0.87 \cdot 10^{11}$	1.14	13.71
Point (B)	34.29	0.014	$2.33 \cdot 10^{11}$	0.43	5.15
Point (C)	55.96	0.036	$3.80 \cdot 10^{11}$	0.26	3.15

the time in which 100,000 collisions occur is taken as the simulation time, which for all three simulations is approximately 84.000 time-steps, which can also be considered feasible.

2.5 Sedimentation of a single particle

In this section a single settling particle is presented to demonstrate the method of the lattice-Boltzmann simulation of moving particles. A single sphere settling in a semi-periodic box is presented. A sphere that moves in a cluster of spheres under turbulent conditions will experience a continuously changing environment and will continuously collide with neighbouring particles. The simulation of a single sphere settling under gravity and colliding onto the bottom wall of a box with periodic sidewalls and rigid top and bottom wall is considered a good, first test case for the many-particle box simulations. Although the setup appears relatively simple, a number of complex processes occur that require accurate treatment of the hydrodynamic interaction between the particle and the fluid: (1) simulation of the transient behaviour of the settling sphere requires accurate description of the flow field between the sphere and the surrounding walls and of the developing wake behind the sphere, (2) the head-on collision of the particle with the bottom wall will make the particle reverse instantaneously and requires an accurate and stable simulation technique that can treat such a discontinuity and (3) upon collision, the particle will reverse in direction and move through its own wake. The relatively simple setup of a single settling particle in a box makes this test case also a good option for experimental validation. A recent paper on experiments of settling and collision of a sphere in a closed box is given by Gondret *et al.* (1999).

2.5.1 Setup of the single particle simulation

The simulation of the single settling particle was done with a single relaxation time lattice-Boltzmann scheme (Chen & Doolen (1998)). For the implementation of the no-slip boundary condition of the sphere surface the forcing method as described in section 2.2 was used. The no-slip boundary condition of the box top and bottom was imposed by a so-called bounce back boundary, a standard method for lattice-Boltzmann schemes to impose no-slip boundary conditions. The hydrodynamic force that dictates the motion of the sphere was obtained from the force applied on the grid nodes surrounding the sphere. The particle acceleration was obtained from the momentum balance of the sphere, which

Table 2.6: Setup and derived parameters of the single particle sedimentation simulation.

d_p	10	[l.u.]	Re	3.4	[-]
ρ_p	540	[-]	Ri	0.22	[-]
ρ_f	10.8	[-]	St	38.0	[-]
ν_{lB}	0.067	[-]	$U_{p,m}$	$2.28 \cdot 10^{-2}$	[l.u./t.s.]

was used for integration of the particle trajectory. Integration of the trajectory was done via a leapfrog algorithm (Smit & Frenkel (1996)). The particle is described as a rigid sphere that makes a perfectly elastic collision. The simulation was done on a grid of 60 x 20 x 20 grid nodes with a sphere with a radius of 5 grid nodes and was executed for 4500 time steps. The simulation took 9 minutes on a single pentiumII 450 MHz processor.

2.5.2 Results

In table 2.6, the conditions of the simulation and a number of pertinent parameters are given. The dimensionless numbers governing the particle sedimentation, *viz.* the particle Reynolds number ($Re_p = U_{p,m}d_p/\nu$), Stokes number ($St_p = U_{p,m}d_p\rho_p/9\nu\rho_f$) and Richardson number($Ri = (\rho_s - \rho_f)gd_p/\rho_s U_{p,m}^2$), are given and were calculated from the maximum particle sedimentation velocity ($U_{p,m}$). In figure 2.7 snapshots of the sedimenting sphere are given and in figure 2.8 the sphere's trajectory is presented. Here the position h represents the distance between the bottom apex of the sphere and the bottom of the box. The flow pattern of figure 2.7 clearly shows the development of the circulation flow between the sphere and periodic sidewalls. The periodicity can also be observed by the fluid acceleration at the wall, indicated by the contour plot at $\theta = 1.14$ and further. As the sphere approaches the bottom wall, fluid is clearly squeezed out of the layer between the sphere and the bottom wall. After collision the particle velocity is reversed instantaneously, causing a wave to propagate through the fluid upwards, which is clearly visible at $\theta = 6.38$. This is caused due to the slight compressibility of the lattice-Boltzmann technique. In this picture the post-collision reversed fluid velocity profile around the sphere is also clearly visible.

2.6 Conclusion and outlook

In this chapter a methodology for the calculation of crystal-crystal collision rates in the turbulent flow field of an industrial crystalliser is presented. The collision frequency of crystals in the crystalliser is a complex function of the local hydrodynamic conditions. Therefore, accurate estimation of collision data requires knowledge of the behaviour of the flow field at the scale of the individual crystals. To obtain insight in the relationship between the overall crystalliser hydrodynamics and the motion of individual crystals in the crystalliser, the proposed method consists of simulating the internal flow of the industrial crystalliser as a whole and of simulating the motion of the individual particles suspended in the turbulent flow field in a small sub-domain (box) of the crystalliser. The flow simulations of the crystalliser as a whole can be used to set the scene for the particle

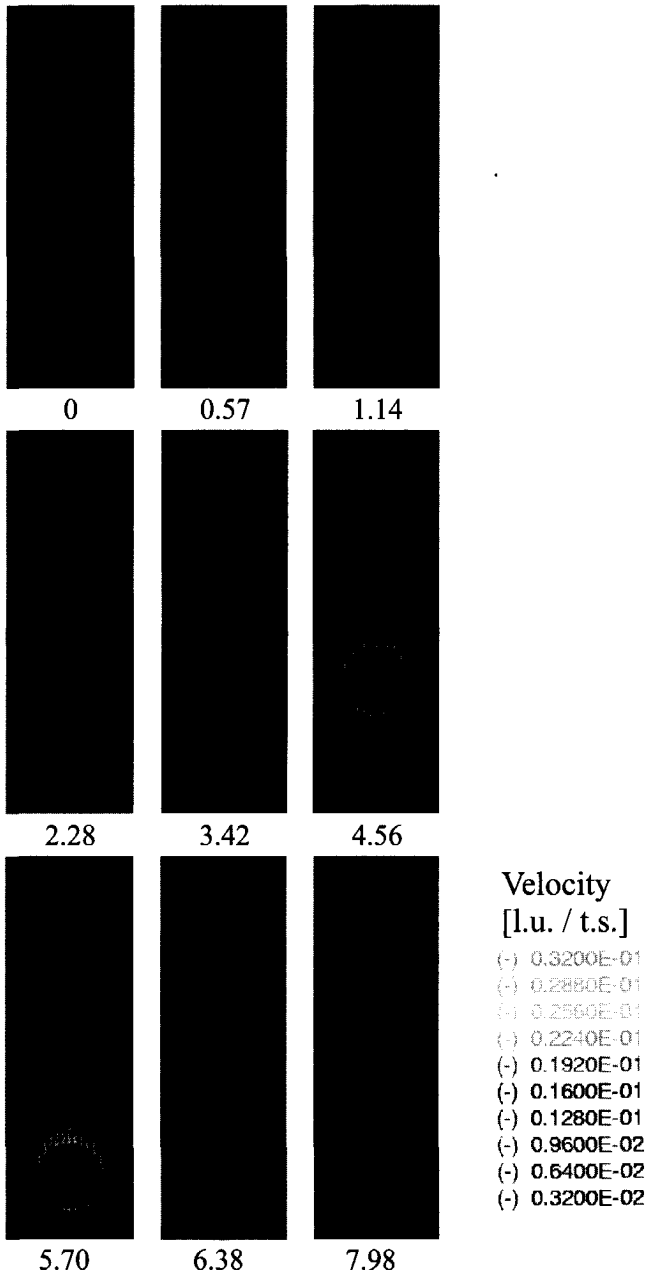

Figure 2.7: Snapshots of the lattice-Boltzmann simulation of a sphere settling under a gravitational force. The contours represent the magnitude, the arrows the direction and magnitude of the fluid velocity. Dimensionless velocity in lattice units per time step and dimensionless time as $\theta = tU_{p,m}/d_p$.

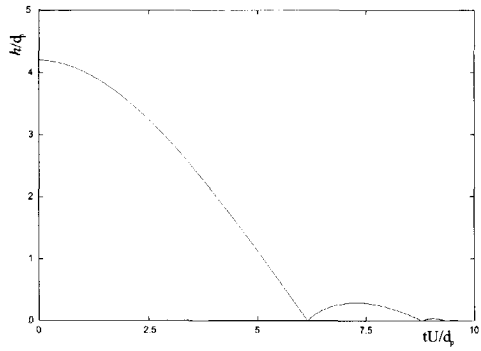

Figure 2.8: The trajectory of a sphere settling under a gravitational force. Dimensionless position (h/d_p) vs. dimensionless time ($\theta = tU_{p,m}/d_p$).

simulations. Back-coupling of results from particle simulations to the crystalliser flow simulation is not considered.

It is demonstrated that the lattice-Boltzmann method combined with a LES type turbulence model can be used as an efficient technique to resolve the complex flow field of the 1100 l DTB crystalliser. High resolution simulations done at a Reynolds number of 240,000 produced detailed information on the turbulence characteristics of the crystalliser. A pseudo single phase simulation was used to represent the two phase slurry flow of the crystalliser. Although this approach sets limitations to simulations where particle dispersion becomes an important factor for the resulting flow field, it is demonstrated that the here performed simulation is in good agreement with previous literature values for global characterising dimensionless numbers (Po and Pu numbers) of the presented crystalliser.

By analysis of the appropriate length and time scales a theoretical framework is established to relate the conditions of the crystalliser to the conditions of the box simulations. A key parameter that identifies the particle phase is the particle relaxation time, a parameter that indicates the particle response to external accelerations. Parameters obtained from the LES simulations that identify the turbulence characteristics are the turbulent kinetic energy at the GS and SGS and the rate of energy dissipation. These determine the integral time scales of fluid motion. The length scale at which fluid motion is uncorrelated sets limitations to the feasible size at which the box size can represent the flow field of the crystalliser. Therefore periodic box simulations can be used to study particle collisions comparable to the motion at the sub-grid scale level of the large-eddy simulation. It is concluded that simulation of individual particles in a periodic box under turbulent conditions is feasible and can be used to simulate the local conditions of the crystalliser.

The many-particle box simulations are currently under development. As a first test case of microscopic particle modelling, the sedimentation and collision of a single sphere towards a solid wall is simulated to demonstrate that the lattice-Boltzmann method is capable of simulating moving and colliding spheres in a confined geometry. Special

attention is required for the accurate treatment of a collision of two particles. Two approaching particles at grid-spacing distance will violate the lattice-Boltzmann framework for an accurate description of the flow in the layer between the particles and which describes the evolving hydrodynamic forces. This requires a sub-grid collision model that gives an accurate treatment of the flow in the layer between the spheres. Available approaches are application of lubrication theory or the use of a collision model along the lines of a method described by Zenit & Hunt (1999). For validation of a collision model, the dynamics of a particle approaching a wall will be experimentally investigated. In our laboratory, an experimental setup is being developed for the sedimentation and collision of a single sphere in a confined geometry. In this experiment the flow field of the sphere upon collision will be measured, using particle image velocimetry.

Future work will further consist of the application of a method to generate turbulent fluid flow in the lattice-Boltzmann framework. When this is achieved, box simulations will be performed in correspondence with the flow conditions and box dimensions estimated in this contribution. The obtained collision frequencies and intensities can be used to calculate agglomeration and attrition rates in crystallisation processes.

List of Symbols

Symbol	**description**	**unit**
$\mathbf{c}_i$	discrete velocity	-
c_s	Smagorinsky constant	
D_{imp}	impeller diameter	m
d_p	particle diameter	m
E	Energy	$m^2\,s^{-2}$
f_i	mass density function	$-$
f_{11}	velocity correlation function	$-$
$\mathbf{f}$	force vector	$-$
h	z-coordinate	m
k	wave number	m^{-1}
l_{mix}	mixing length	m
l_f	cut off length	m
l_0	zero corelation length	m
n_p	particle number concentration	$\#m^{-3}$
N	impeller speed	$rev\,s^{-1}$
N_p	number of particles	$\#m^{-3}$
N_g	number of gridcells	$\#$
N_{ts}	number of timesteps	$\#$
M	lattice directions	$-$
P	pressure	Pa
r	distance	m

S	rate of deformation	s^{-2}
t	time	s
T	Integral time scale	s
u, v, w	velocity components	$m\,s^{-1}$
u_s	speed of sound	$m\,s^{-1}$
$\mathbf{u}$	velocity vector	$m\,s^{-1}$
$\mathbf{x}$	position vector	–
Z	collision rate	$\#m^{-3}s^{-1}$

Greek	**description**	**unit**
Δ	grid spacing	m
$\overline{\epsilon}$	average energy dissipation rate	$m^2\,s^{-3}$
ϵ	energy dissipation rate	$m^2\,s^{-3}$
η	Kolmogorov length scale	m
γ	length ratio	–
κ	turbulent kinetic energy	$m^2\,s^{-2}$
θ	dimensionless time	–
μ	dynamic viscosity	$Pa\,s$
μ_f	dynamic viscosity of pure liquid	$Pa\,s$
ν	kinematic viscosity	$m^2\,s^{-1}$
ν_t	turbulent kinematic viscosity	$m^2\,s^{-1}$
ν_{lB}	kinematic viscosity of lB scheme	–
Ω_i	collision operator	-
ρ	density	$kg\,m^{-3}$
τ_k	Kolmogorov time scale	s
τ_p	particle relaxation time	s
ϕ	volume fraction	–
ϕ_v''	volume flux	m/s

Dim. numbers

Po	Power number
Pu	Pumping number
Re	Reynolds number
Ri	Richardson number
St	Stokes number

Acronyms

CFD	Computational Fluid Dynamics
CSD	Crystal Size Distribution
DNS	Direct Numerical Simulation
DTB	Draft Tube Baffle crystallizer
GS	Grid Scale
LES	Large Eddy Simulation
SGS	Sub-Grid Scale

Chapter 3

PIV experiments and lattice-Boltzmann simulations on a single sphere settling under gravity

A comparison is made between experiments and simulations on a single sphere settling in silicon oil in a box. Cross-correlation particle imaging velocimetry (PIV) measurements were carried out at particle Reynolds numbers ranging from 1.5 to 31.9. The particle Stokes number varied from 0.2 to 4 and at bottom impact no rebound was observed. Detailed data of the flow field induced by the settling sphere were obtained, along with time series of the sphere's trajectory and velocity during acceleration, steady fall and deceleration at bottom approach.

Lattice-Boltzmann simulations prove to capture the full transient behaviour of both the sphere motion and the fluid motion. The experimental data were used to assess the effect of spatial resolution in the simulations over a range of 2 to 8 grid nodes per sphere radius. The quality of the flow field predictions depends on the Reynolds number. When the sphere is very close to the bottom of the container, lubrication theory has been applied to compensate for the lack of spatial resolution in the simulations.

Key words: lattice-Boltzmann, PIV measurement, discrete particle simulation, sedimentation

This chapter has been accepted for publication in Phys. Fluids (2002)

3.1 Introduction

Particle motion and particle collisions play an important role in the performance of many industrial processes involving suspension flow. For instance, in industrial crystallisation, crystal-crystal collisions determine kinetic mechanisms such as agglomeration and nucleation due to crystal fracturing. Presently, we are developing a method to study suspensions under turbulent conditions. For this method, it is attempted to fully resolve

the flow field around the particles and to make a direct coupling between the particle and the fluid motion. To validate the way the particles are represented in the simulation procedure, we compare experimental and numerical results on the motion of a single sphere settling in a closed box. In the experiment, the transient motion of a single sphere and its associated flow field were measured from the moment of release to a steady-state or maximum settling velocity to deceleration and rest at the bottom of the box. For this experiment, the Reynolds number, based on the steady state settling velocity of a sphere in an infinite medium ($Re = \rho_f u_\infty d_p/\mu_f$) was varied between 1.5 and 32. This range of Reynolds numbers was chosen because it corresponds to the range of Reynolds numbers encountered in our sample crystallisation process for production of ammonium sulfate crystals (Ten Cate *et al.* (2001)).

A particle settling towards a wall has been studied previously by Brenner (1961), who derived an analytical solution in the creeping flow regime. However, at the Reynolds numbers studied, the particle is well out of this regime. Recent experimental work in this field has been presented by several authors (Gondret *et al.* (2002, 1999); Zenit & Hunt (1999); Joseph *et al.* (2001)), who studied the wall approach and rebound, to obtain restitution coefficients for submerged particles colliding with a wall. The parameter that determines rebound is the Stokes number ($St = 1/9 Re \rho_p/\rho_f$). Gondret *et al.* (2002) demonstrated that the critical Stokes number above which rebound occurs is approximately 10. In our experiments, the Stokes number was varied between 0.19 and 4.13 and no rebound was observed.

We chose to perform the experiment in a closed container for a number of reasons. Firstly, the box width to particle diameter ratio was kept relatively small, to avoid the need to make assumptions regarding the domain size or the external boundary conditions in the simulations. In this way the full flow field of the box can be simulated, using no-slip boundary conditions for the outer tank walls, while having sufficient resolution to capture the flow field of the particle and still simulate the flow at a moderate computational domain size. In this way, the influence of the container walls on the particle motion is contained both in the experiment and in the numerical simulation. Secondly, the experiment is transient and has a limited time-span. This has the advantage that the transient character of the simulations can be assessed throughout the different stages of acceleration, steady fall and deceleration at bottom approach.

The first objective of this chapter is to present our experimental data on a settling sphere in a confined geometry. The data set consists of the velocity field of the fluid surrounding the settling sphere and the trajectory (*i.e.* position as a function of time). The velocity field has been measured using cross correlation particle image velocimetry (PIV) (Raffel *et al.* (1998)). The PIV experiment is described in the next section.

The second objective is to present our approach to the simulation of freely moving particles based on the lattice-Boltzmann method. This method was chosen because it provides a robust numerical scheme that can efficiently treat the complex geometry of freely moving particles. A further advantage of this method is that it can be parallelised at high computational efficiency. The use of the lattice-Boltzmann scheme for simulation of suspensions has been proposed by Ladd (1994*a*,*b*), who also presented validation of his method. A number of other authors (*e.g.*Behrend (1995); Qi (1999); Aidun *et al.* (1998*b*)) have used the lattice-Boltzmann method to simulate suspended particles. Re-

cent developments on direct simulation of suspensions can also be found in Koch & Hill (2001).

Our approach differs from the method of these authors in two ways. Firstly,we use a scheme for solving the lattice-Boltzmann equation, based on the work of Eggels & Somers ((1995). This scheme explicitly treats the higher order terms in the lattice-Boltzmann equation which improves the stability of the numerical scheme and allows for the use of a low kinematic viscosity. Secondly, we use a fundamentally different method for implementation of the moving no-slip boundary at the surface of the solid particle. In our approach, we apply the adaptive force-field technique that has been used in the work of Derksen & Van den Akker ((1999) to implement both the rotating impeller and the steady vessel walls in the numerical study of the turbulent flow in a stirred vessel. To our knowledge this approach has not been applied previously for simulating freely moving particles. However, based on the good results obtained in previous studies (Derksen & Van den Akker ((1999, 2000)), we had confidence that this approach could also be used to simulate freely moving particles at a relatively low spatial resolution per particle, bearing in mind that the method needs to be applied to simulate many particles ($O(10^3)$) in a turbulent flow.

Therefore, our final objective is to assess and benchmark our numerical method with the flow cases considered in this chapter. In section 3.3, a number of specific details of the setup of our particle simulations are discussed. A comparison between the experimental and numerical results is made in section 3.4.

3.2 Experimental Setup

The objective of the experiment was to accurately measure both the trajectory (*i.e.* the position as a function of time) and the associated flow field of a settling sphere from its moment of release until rest at the bottom of a vessel, where the ratio of the vessel dimensions to sphere radius was kept relatively small, such that the full flow field could be simulated under identical conditions.

As the settling sphere, a precision Nylon ball bearing with a diameter $d_p = 15\ mm$ and density $\rho_p = 1120\ kg/m^3$ was selected. The container dimensions were chosen as $depth \times width \times height = 100 \times 100 \times 160\ mm$ (see Fig. 3.1). Upon start of an experiment, the sphere was released while simultaneously triggering the camera system to start filming. The sphere was hanging 120 mm from the bottom of the tank at the capillary tip of a Pasteur pipette that was connected to a vacuum system. The sphere was released by abruptly opening an electronic valve, thus disconnecting the vacuum from the pipette.

Various types of silicon oil were used as the working fluid, because of their good optical accessibility and weak temperature dependency of the viscosity. The Reynolds number of the settling sphere was based on the sedimentation velocity u_∞ of a sphere in an infinite medium. To determine u_∞, a relation for the drag coefficient due to Abraham (1970) was used.

$$C_d = \frac{24}{(9.06)^2}\left(\frac{9.06}{\sqrt{Re}} + 1\right)^2 \tag{3.1}$$

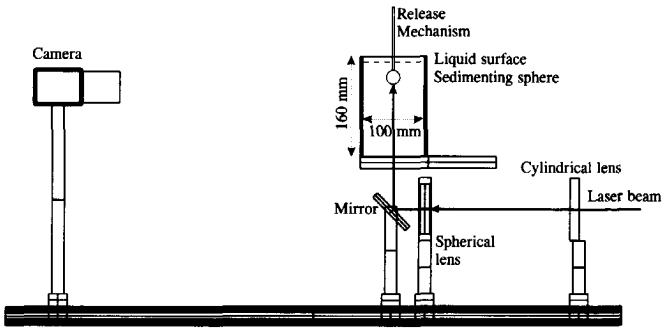

Figure 3.1: Experimental setup for the PIV measurement of a single settling particle in a confined geometry

Table 3.1: Setup of the sedimentation experiments

	ρ_f $[kg/m^3]$	μ_f $[Ns/m^2]$	u_∞ [m/s]	Re [-]	St [-]	Camera frequency $[s^{-1}]$	Resolution [-]
Case E 1	970	373	0.038	1.5	0.19	60	low
Case E 2	965	212	0.060	4.1	0.53	100	low
Case E 3	962	113	0.091	11.6	1.50	170	high
Case E 4	960	58	0.128	31.9	4.13	248	high

The four experimental cases are defined in table 3.1.

The flow field was visualised with seeding particles illuminated with a (laser) light sheet. As the light source, a Spectra-Physics 4W Argon-ion laser (2016-05) operating in all lines mode was used. A cylindrical and a spherical lens converted the laser beam into a sheet of 190 μm thickness. The laser sheet entered the vessel via the bottom. Neutrally buoyant hollow glass spheres approximately 10 μm in size were used as seeding particles. A continuous camera with a frame rate up to 250 Hz and an array size of 512 $\times$ 512 pixels was used to record the experiment. The flow field was measured on a grid of interrogation areas (IA's). An IA typically contained 32 $\times$ 32 pixels. The fluid velocity was determined in each interrogation area by estimating the displacement of the seeding particles between two consecutive frames through cross-correlation (Westerweel (1993)).

The desired spatial resolution and the maximum camera frame rate set a restriction to the maximum fluid velocity that can be accurately measured, as between two frames the tracer particles are not allowed to shift more than $\frac{1}{4}$ part of the linear size of an interrogation area (Raffel *et al.* (1998)). This limits the maximum sedimentation velocity of the sphere, which can be taken as a measure for the maximum fluid velocity during an experiment. The required resolution depends on the Reynolds number of the flow, because at higher Reynolds numbers, the structures in the flow become smaller. The flow was measured at either of the two resolutions given in Fig. 3.2. At the low resolution (Fig. 3.2 (b)), when the array size is chosen to map three sphere diameters, the maximum allowed sphere velocity is 0.18 m/s, which is larger than any of the settling velocities

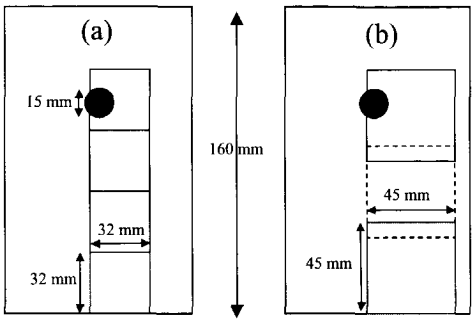

Figure 3.2: Measurement positions at high (a) and low (b) resolution.

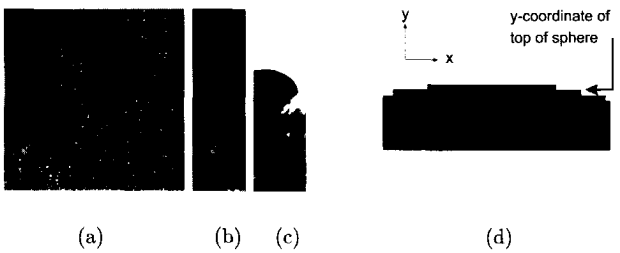

Figure 3.3: Processing steps in detection of sphere position. (a) Raw PIV-recording with sphere. (b) Part of recording after a Kuwahara-filter has been applied. (c) Result of thresholding image b. (d) Magnification of the rear side of the sphere.

of the Nylon sphere as given in table 3.1. At the high resolution (fig. 3.2 (a)), the maximum allowed velocity is 0.13 m/s, which is close to the sedimentation velocity of case $E4$. However, the sphere is expected to move at a velocity that is lower than u_∞ due to hindrance from the container walls. Based on the $\frac{1}{4}$ part displacement rule, the camera frame rate was adjusted for each experiment.

To capture the full trajectory of the particle, three overlapping fields of view (FOV) were used at low resolution (cases $E1$ and $E2$) while the measurements at high resolution (cases $E3$ and $E4$) were done in four FOV's (see figure 3.2). A raw image is given in Fig 3.3 (a). As can be seen, the leading side of the sphere was made dark to prevent overradiation due to reflections at the sphere surface.

In each frame, the sphere position had to be determined accurately for a good interpretation of the flow field. Because the laser sheet enters from the bottom and is blocked by the sedimenting sphere, no fluid velocities could be measured behind the sphere (Fig. 3.5 (a)). The sphere's position was determined from the coloured top of the sphere. The motion blur was removed from the sphere by using an edge-preserving Kuwahara filter (Scilimage (1994)) (Fig. 3.3 (b)) and after having applied a threshold (Fig. 3.3 (c)), the y-position of the sphere was determined at pixel accuracy (Fig. 3.3 (d)). The resulting

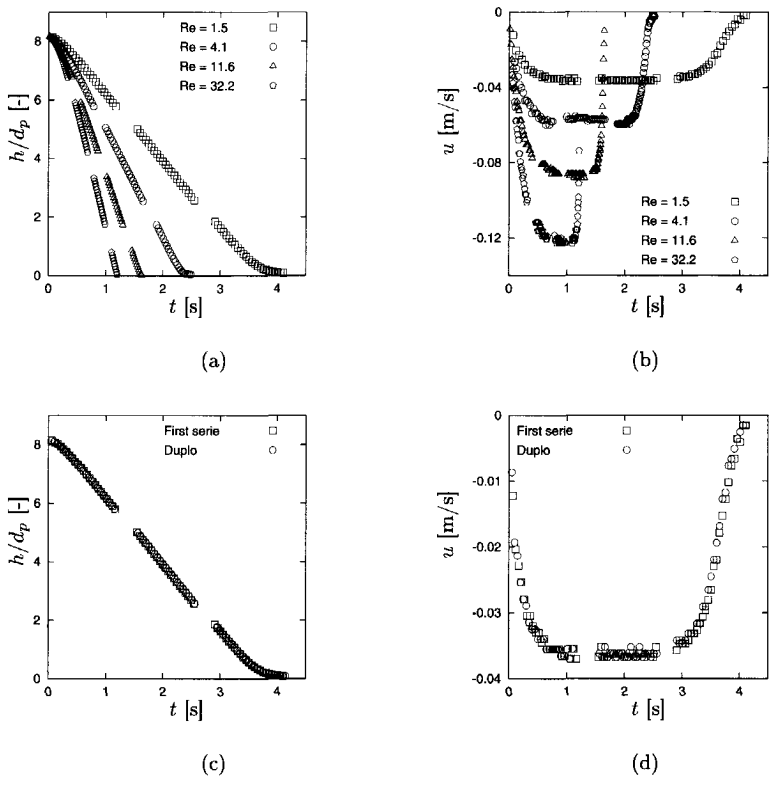

Figure 3.4: Experimental data on sphere trajectory (a) and sedimentation velocity (b) at the four measured Reynolds numbers and comparison of measurement duplication of trajectory (c) and sedimentation velocity (d) at $Re = 1.5$.

sphere trajectories and velocities are given in Fig. 3.4.

A raw vector image of the flow at a particle Reynolds number of 1.5 is given in Fig. 3.5 (a). Interrogation was done with IA's of 32×32 pixels with a 50 % overlap, resulting in a total of 961 vectors per image. After determination of the sphere position, the vectors inside and behind the sphere were removed from the image and (for reference) a sphere was placed in the figure, as can be seen in Fig. 3.5 (b). In this figure, the maximum velocities are found closely underneath the sphere where tracer particle displacements of approximately 7 pixels were found. Velocities far away from the sphere become very low, which gives particle displacements smaller than 0.5 pixel. Sub-pixel displacements were estimated using a Gaussian peak fit estimator (Westerweel (1993)). The accuracy is approximately 0.1 pixel for displacements larger than 0.5 pixel, leading to a relative error of 2 % for the highest velocities, whereas the relative error is approximately 17 % for particle displacements less than 0.5 pixel. After removal of the vectors inside and behind

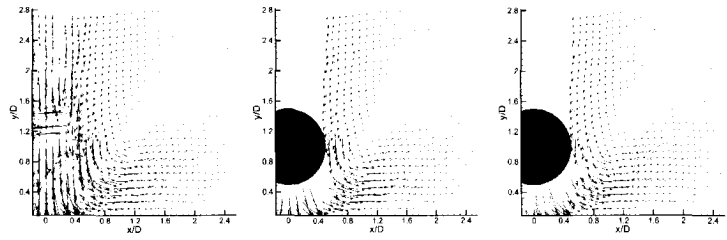

(a) (b) (c)

Figure 3.5: Measurement of the flow field at $Re = 1.5$ ($E1$) at a dimensionless gap height of $h/d_p = 0.5$. Raw flow field (a) and flow field after removal of the vectors at and behind the sphere (b) with a second measurement at the same Reynolds number and sphere position (c).

the sphere, approximately 10 spurious vectors remain per frame. This is about 1% of the total amount of vectors which is low compared to a typical value of 5% encountered in turbulent flow fields (Westerweel (1994)). This is due to the flow being laminar and virtually two-dimensional in the center plane of the sphere, which results in practically no out of plane motion. To test the reproducibility of the experiment, all measurements were done twice. In Figs. 3.4 (c) and (d), the trajectories and sedimentation velocities have been plotted for case $E1$. The two trajectories practically coincide. The measurements at higher Reynolds numbers give comparable results. The flow fields around the sphere of case $E1$ are presented in Fig. 3.5 to demonstrate that the PIV measurements yields an accurately reproducible result here as well.

3.3 Simulation

For computational simulation of the sedimentation experiment, a lattice-Boltzmann scheme (Chen & Doolen (1998)) was used. This scheme exploits a microscopic model for fluid motion on a uniform cubic lattice. Fluid masses propagate on the lattice. Collision rules that conserve mass and momentum guarantee that, in the limit of low Mach numbers, both the continuity equation and the Navier-Stokes equations for incompressible fluid flow are satisfied.

In this section, a number of issues will be addressed that had to be solved to make our simulation method applicable to freely moving particles. First, we explain the implementation of the no-slip boundary condition at the particle surface and then we discuss the issues of (i) treatment of the inertia of the internal fluid that may affect the particle motion in a non-physical manner and (ii) the non-physical dependency of the drag-force on the viscosity. As a consequence of this dependency, if one wants to perform accurate dynamic simulations of particles with a radius of a limited number of grid nodes, (iii) a separate calibration procedure for the particle radius is required. This calibration and scaling procedure of the simulations is discussed and finally (iv) the application of an

additional lubrication force is presented, which is required when the distance between the particle and the wall has reduced to less than one grid spacing.

3.3.1 Boundary conditions

The implementation of (moving) boundary conditions in the lattice-Boltzmann framework has received considerable attention in recent years and constitutes a field of ongoing research (Mei *et al.* (1999); Chen *et al.* (1998*a*); Verberg & Ladd (2000); Rohde *et al.* (2002)). Most of the methods presented in these references are adaptations of the bounce back rule for boundary conditions, as explained by Ladd (1994*a*). In the standard application of the bounce back rule a link between two grid nodes that crosses a no-slip boundary is cut and mass that propagates from the flow domain towards the solid boundary is reflected along the link of its origin. One drawback of this approach is that in the straightforward implementation according to Ladd (1994*a*) curved solid objects are approximated by staircase shaped objects.

In the current application the boundary of the solid sphere is implemented via the so-called adaptive force-field technique, similar to Derksen & Van den Akker ((1999). The scheme is based on a method for implementation of no-slip boundary conditions in spectral simulations (Goldstein *et al.* (1993)). The method locally forces the fluid velocity near the boundary and interferes with the flow field not at the mesoscopic level of the propagating fluid mass but at the macroscopic level of the fluid velocities. An adavantage of the method is that implementation of curved boundary conditions is done via an interpolation-extrapolation scheme which produces a smooth surface instead of a sharply cut staircase shaped surface. Specifically for moving surfaces this is an advantageous feature since it reduces unphysical shape changes of the surface due to its motion with respect to the grid.

The sphere surface is represented by a set of M control points, placed at the sphere's surface, evenly spaced at a resolution slightly higher than the grid spacing. At each control point, the local fluid velocity is forced to the surface velocity of the sphere. The steps in the procedure are as follows; First, the fluid velocity at a control point is determined via first-order Lagrange interpolation from the velocity at the surrounding grid nodes. Then, the deviation between the desired surface velocity $\vec{u}_i$ at control point i and the interpolated fluid velocity $\vec{u}$ is used to determine the force that needs to be applied to the fluid to better approach the local surface velocity. The surface velocity is given by the translational and rotational velocity components

$$\vec{u}_i = \vec{u}_p + \vec{\Omega}_p \times \vec{r}_i \tag{3.2}$$

where $\vec{r}_i$ is the position of the control point relative to the center of mass of the sphere ($\vec{r}_i = \vec{x}_i - \vec{x}_c$). The deviation of the fluid velocity at a control point i is calculated by

$$\vec{d}_i = \vec{u}_i - \sum_j I(\vec{r}_{ij})\vec{u}_j \tag{3.3}$$

where $\vec{u}_j$ is the fluid velocity at grid node j and $I(\vec{r}_{ij})$ is the set of interpolation coefficients, which is a function of the relative distances $\vec{r}_{ij}$ between the surrounding lattice

nodes j and the control point i. The coefficients that were used for interpolation were also used for projection of the force from the control point onto the surrounding grid nodes, where the forces ($\vec{F}_j$) are updated with a relaxation scheme

$$\vec{F}_j(\mathbf{x}, t) = \alpha \vec{F}_j(\mathbf{x}, t-1) + \beta I(\vec{r}_{ij}) \rho \vec{d}(t) \tag{3.4}$$

where t indicates the time step. We move to the next control point and the procedure is repeated until all M control points have been updated. If desired, this procedure can be iterated.

The scheme of equation 3.4 that imposes locally the desired boundary condition is a control scheme that is characterised by the constants α and β. The scheme adjusts the imposed body force $\vec{F}_j(\mathbf{x}, t)$ proportional to the deviation of the local velocity. The dynamic action, accuracy, and stability of the control scheme is determined by the relaxation parameters and the topology of the control points $\vec{x}_i$. The parameters α and β were determined empirically as 0.95 and 1.8 respectively.

After having updated the forces at the grid nodes, we calculate the hydrodynamic force and torque on the sphere according to

$$\vec{F}_p = \sum_j \vec{F}_j(\mathbf{x}, t) \tag{3.5}$$

$$\vec{T}_p = \sum_j \vec{r}_j \times \vec{F}_j(\mathbf{x}, t) \tag{3.6}$$

where r_j is the relative distance between the grid node j and the center of mass of the particle. The summation is over all boundary nodes in both the external and internal regions at the sphere's surface. The force and torque are used to integrate the equations of motion of the sphere. This is done by using an Euler forward integration scheme where the forces are averaged over two time steps to suppress unphysical fluctuations.

3.3.2 Internal mass

The boundary condition scheme requires the objects to have internal fluid. An advantage of this is that when a node shifts from the inside of an object into the exterior, it already contains fluid mass and the state of this node does not need to be changed. For the same reason, Ladd (1994*b*) also has internal mass in his particles. A drawback of keeping internal mass is that its inertia affects the motion of the sphere via a contribution to $\vec{F}_p$ (see Eq. 3.5). Different approaches have been proposed to solve this problem. Ladd (Ladd (1994*b*)) suggests to integrate the equation of motion with a corrected particle mass. Although this is a fair approximation for systems with large solid/fluid density ratios, for solid particles in liquid with a density ratio typically between 1 and 2, numerical instabilities can occur when integrating the equation of motion. Other authors (Aidun *et al.* (1998*b*); Aidun & Lu (1995); Heemels (1999)) have proposed methods to remove the internal mass, but this can not be done for the adaptive force-field technique. Qi (Qi (1999))proposes to compensate the hydrodynamic force $\vec{F}_p$ for contribution from nodes entering or leaving the interior of a particle, which is comparable to our approach.

The force applied to the fluid nodes influences the fluid on both the inside and the outside of the sphere. Hence, the total force that acts on the sphere, as calculated with equation 3.5, is the sum of the internal and external components of the force:

$$\vec{F}_{p,tot} = \vec{F}_{p,int} + \vec{F}_{p,ext} \tag{3.7}$$

When integrating the equation of motion, the only physical contribution to the sphere's motion comes from the external flow field. To determine the external contribution $\vec{F}_{p,ext}$, we calculate the change of momentum of the internal fluid between two successive time steps,

$$\vec{F}(t)_{p,int} = \iiint_{V_{sphere}} \rho\vec{u}_{int}(x,t) - \rho\vec{u}_{int}(x,t-1)\ dV \tag{3.8}$$

and subtract this from the total force $\vec{F}_{p,tot}$. When using this approach the correct physical behaviour is obtained, which allows us to simulate particle motion at a density ratio as low as 1.15, as is demonstrated in section 3.4. A similar correction procedure is applied for the torque.

3.3.3 Low Reynolds number calibration

Results presented by Ladd (Ladd (1994*b*)) indicated that boundary conditions in lattice-Boltzmann schemes based on the bounce back rule suffer from a non-physical dependency of the resulting drag force on the kinematic viscosity. A study by Rohde *et al.* (2002) indicated that also more advanced boundary condition methods that are based on the bounce back rule still exhibit this behaviour. A detailed analysis of this behaviour is given by He *et al.* (1997), who demonstrate that in lattice-Boltzmann methods, the exact position at which the no-slip condition is obtained is a function of the kinematic viscosity. Although there is a fundamental difference between the bounce back boundary condition and our approach, this non-physical dependency is also observed in our current approach.

An explanation for the fact that this behaviour is also observed in our simulations may be that due to the interpolation and extrapolation procedure, the sphere's surface is smeared out and the fluid experiences a sphere that is slightly bigger than the sphere on which the M control points lie. The result of this effect is that the drag force obtained from the simulation is larger than the force that would correspond to the sphere's given input radius.

To compensate for this effect, Ladd (1994*b*) proposed a procedure for estimating the effective sphere radius (hereafter called *hydrodynamic radius*). Ladd demonstrated that the hydrodynamic radius varied with viscosity by approximately one grid node. The calibration procedure is based on an analytic expression of Hasimoto (1959) for the drag force on a fixed sphere in a periodic array of spheres in the creeping flow regime,

$$\frac{6\pi\mu r_p U_v}{F_p} = 1.0 - 1.7601 C_\tau^{\frac{1}{3}} + C_\tau - 1.5593 C_\tau^{\ 2} \qquad C_\tau = \frac{4\pi r_p^3}{3L^3} \tag{3.9}$$

where r_p is the sphere radius, L indicates the size of the unit cell and U_v is the volumetrically averaged fluid velocity across the periodic cell. For a given fluid velocity and drag force, equation 3.9 is solved to calculate the hydrodynamic radius.

In our simulations we use a similar calibration procedure as proposed by Ladd. We want to stress here that this calibration procedure is performed independent of the experimental conditions or results. The sole purpose of this procedure is to determined the equivalent particle diameter, given a certain viscosity. A sphere is placed in the center of a fully periodic cell and the fluid is set into motion via a pressure gradient, such that the Reynolds number remains small. The hydrodynamic radius is determined as the average of the radius at 20 sphere positions, which were taken parallel to the flow because the settling sphere also moves along a single axis. One can ask if this low Reynolds number calibration procedure is allowed when it is our objective to simulate the transient motion of a sphere moving at non-zero Reynolds numbers. Therefore, in section 3.4.4 the sensitivity of the simulations to the hydrodynamic radius is investigated.

3.3.4 Scaling

When setting up a simulation of the sedimentation experiment, the scaling of mass, length and time needs to be determined. With respect to mass, only the ratio of fluid and solid density enters the equations of motion of the system. At a constant ratio, the actual values can be chosen arbitrarily without influencing the simulation result. Their numerical values were set identical to the experimental values. Length and time are scaled by using the low Reynolds number calibration procedure. A first estimate for the length scale is based on the input radius of the sphere. A first estimate for the time scale is then determined by setting u_∞ to 0.01 lu/ts [1]. With these first estimates, all parameters are scaled from the physical experiment into lattice units. Based on this first scaling, a calibration simulation is carried out to determine the hydrodynamic radius. Finally, in the sedimentation simulations, length is scaled on the basis of the hydrodynamic radius and time is scaled via the kinematic viscosity. In section 3.4, calibration results of input radii between 2 and 8 lattice units will be presented, and the sensitivity of the simulations to a variation or inaccuracy in the hydrodynamic radius will be discussed.

3.3.5 Sub-grid lubrication force

When simulating a sphere approaching a fixed wall, at some moment in time the grid lacks resolution to resolve the flow in the gap between the sphere and the wall. The interpolation scheme breaks down at the gap between the first grid node and the position of the no-slip condition at the wall and the repulsive forces that occur due to the squeezing motion of the fluid in the gap can no longer be computed accurately. This problem was noticed by Ladd (1997), who proposed to include an explicit expression for the leading order lubrication forces, calculated with lubrication theory (Crowe *et al.* (1997); Kim & Karrila (1991)). In our simulations, when the gap has become smaller than Δ_0 (set to 1 grid spacing), the force acting on the sphere due to the flow in the unresolved gap is calculated explicitly. The additional lubrication force at gap distance

[1] In lattice-Boltzmann simulations, $u_{max} << c_s$ (the speed of sound, $c_s = \frac{1}{2}\sqrt{2}$) is required to assure incompressible flow conditions

h is calculated with

$$\vec{F}_w = -6\pi\mu r_p u_\perp \left(\frac{r_p}{h} - \frac{r_p}{\Delta_0}\right) \tag{3.10}$$

where h is the gap between the wall and the sphere and $u_\perp$ is the velocity component of the sphere perpendicular to the wall. The total force that acts on the particle is taken as the sum of the force calculated via this equation and the sum of forces that are obtained from the flow simulation. In the following section, the validity of this approach will be tested by comparing simulation results with experimental data.

3.4 Results and discussion

3.4.1 Overview of simulations

In table 3.2, an overview of the simulations is given. Cases $S1$ to $S4$ were chosen as base settings for the simulations. In the following two sections, these simulations will be used to discuss various aspects of the flow field and sedimentation trajectory and will be compared to experimental results. In cases $S5$ to $S8$, the input radius was varied between 2 and 8 grid nodes to study the influence of resolution on the accuracy and performance of the simulation. Simulations $S9$ to $S15$ were done to study the sensitivity of the simulations to the hydrodynamic radius. Finally, in simulations $S18$ and $S19$, the lubrication force was applied to explore its usefulness for representing the bottom approach of the sphere. All simulations were executed for a physical time of approximately 4 seconds.

3.4.2 Sedimentation trajectory

In this paragraph, a physical interpretation of the sedimenting sphere is given based on the results of simulations $S1$ and $S4$, to demonstrate the characteristic differences in behaviour of the particle sedimentation between both cases and to provide physical insight in the different flow cases. In Fig. 3.6 the flow field is plotted at four different stages during settling. In Fig. 3.7, the development of the kinetic energy of the sphere and the fluid is given. The intermediate results at Reynolds numbers of 4.1 and 11.6 have been left out.

The velocity field of the particle settling at $Re = 1.5$ is not symmetric in the direction of motion (fig. 3.6 (a2)), demonstrating that the flow field is not in the Stokes regime. In Fig. 3.6 (a1), the sphere has moved one diameter below the point of release. At this moment, the sphere has almost reached its steady-state velocity. The rate at which the flow field develops is demonstrated in Fig. 3.7(a), by the evolution of the kinetic energy of the fluid, which keeps pace with the kinetic energy of the sphere. As the sphere approaches the bottom, the kinetic energy of the wake again reduces in pace with the decay of kinetic energy of the particle, which decelerates because of the squeezing of the liquid between the sphere and the bottom wall (fig. 3.6 (a3)). This causes the flow field in front of the sphere to deform and generates outward fluid motion across the bottom. Very quickly after the sphere has come to a halt, the fluid also comes to rest.

Table 3.2: Overview of sedimentation simulations. The table contains the input radius and calibrated radius of the sphere, with corresponding length ($L.S.$) and time ($T.S.$) scaling factors. $L.F.$ indicates the use of lubrication theory at bottom approach. u_{max}/u_∞ is the ratio of the maximum sedimentation velocity and the theoretical steady state velocity of a freely moving sphere in an infinite medium. At the bottom of the table, the experimentally obtained velocity ratio is included for comparison.

Case	r_0 $[lu]$	r_h $[lu]$	Re $[-]$	$L.S.$ $10^{-3}m/lu$	$T.S.$ $10^{-4}s/ts$	$L.F.$ $[-]$	u_{max}/u_∞ $[-]$
S 1	4	4.487	1.5	1.671	3.891	-	0.894
S 2	4	4.562	4.1	1.645	2.410	-	0.950
S 3	4	4.657	11.6	1.610	1.526	-	0.955
S 4	4	4.810	31.9	1.559	1.010	-	0.947
S 5	8	8.084	1.5	0.928	2.398	-	0.857
S 6	8	8.689	31.9	0.863	0.619	-	0.947
S 7	2	2.698	1.5	2.780	5.381	-	0.889
S 8	2	3.003	31.9	2.497	1.295	-	0.921
S 9	4	4.000	1.5	1.875	4.897	-	0.768
S 10	4	4.400	1.5	1.705	4.047	-	0.871
S 11	4	4.600	1.5	1.630	3.703	-	0.924
S 12	4	5.000	1.5	1.500	3.134	-	1.009
S 13	4	4.000	31.9	1.875	1.460	-	0.757
S 14	4	4.600	31.9	1.630	1.104	-	0.891
S 15	4	5.000	31.9	1.500	0.935	-	0.969
S 16	3	3.559	1.5	2.107	4.639	-	0.897
S 17	3	3.650	4.1	2.055	2.818	-	0.948
S 18	3	3.559	1.5	2.107	4.639	$\surd$	0.897
S 19	3	3.650	4.1	2.055	2.818	$\surd$	0.948
E 1	-	-	1.5	-	-	-	0.947
E 2	-	-	4.1	-	-	-	0.953
E 3	-	-	11.6	-	-	-	0.959
E 4	-	-	31.9	-	-	-	0.955

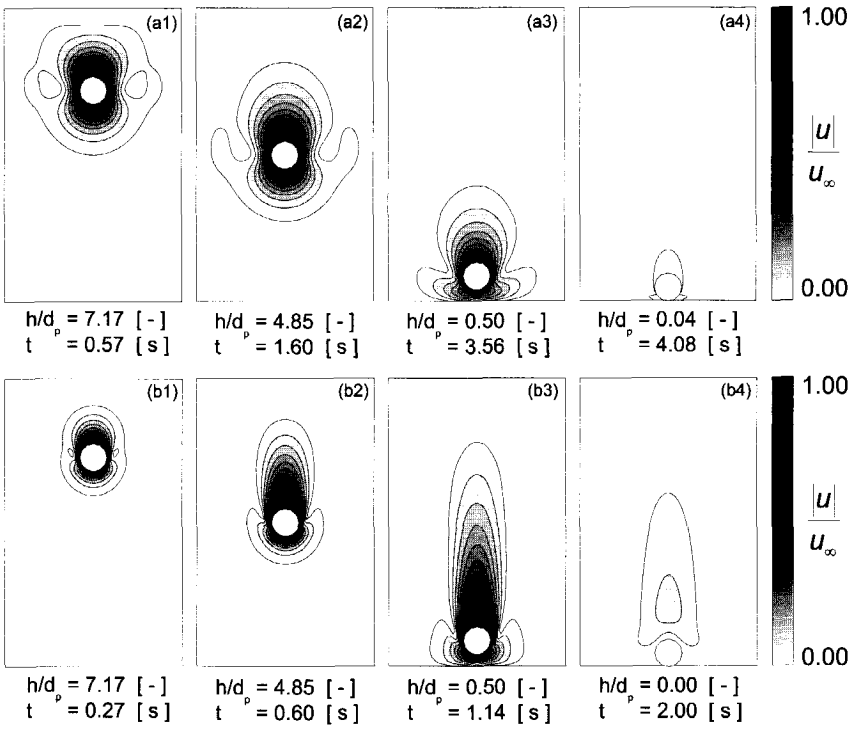

Figure 3.6: Comparison of the flow field of the sedimenting sphere at (a), $Re = 1.5$ (top, case $S1$) and (b), $Re = 31.9$ (bottom,case $S4$). The contours indicate the normalised velocity magnitude. h/d_p indicates the dimensionless gap between the bottom apex of the sphere and the tank bottom wall, t indicates time.

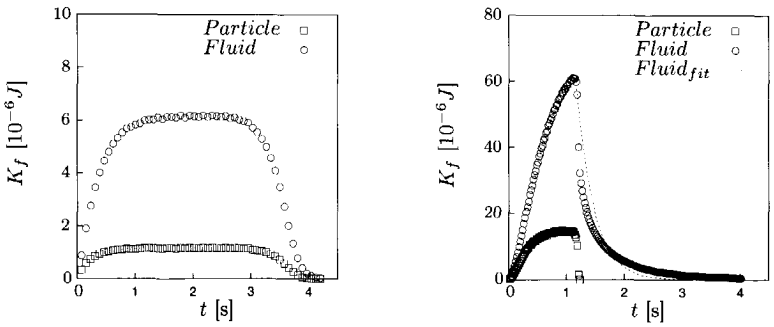

(a) (b)

Figure 3.7: Simulated result of the kinetic energy of sphere and fluid *vs.* time at $Re = 1.5$, case $S1$, (a) and $Re = 31.9$, case $S4$, (b). The dashed line in (b) is an exponential fit to the decay of the fluid kinetic energy.

The particle settling at a Reynolds number of 31.9 shows distinctively different behaviour. Compared to the case of $Re = 1.5$ a much larger, elongated wake develops. In Fig. 3.6 (b3), the deflected front of the flow field at bottom approach is again clearly visible. Another distinctive feature is that while both the kinetic energy of the particle and the fluid increase at the same pace initially, the particle reaches a plateau while the wake keeps on picking up kinetic energy until the particle reaches the tank bottom. At this stage, the kinetic energy of the fluid has not reached a steady state. Notice that the level of kinetic energy of both the fluid and the particle at the high Reynolds number are about one order of magnitude larger than that of the $Re = 1.5$ case. Figure 3.7(b) further demonstrates that the sphere abruptly comes to a halt when the sphere hits the bottom wall, which is in contrast with the more gentle deceleration of the sphere at $Re = 1.5$. After the sphere has come to a halt, the wake still contains a considerable amount of kinetic energy that slowly decays. An empirical time constant related to this process can be estimated by assuming an exponential function,

$$K_f(t) = K_{f,max} \exp\left(\frac{-t}{\tau_d}\right) \tag{3.11}$$

which is plotted in Fig. 3.7(b) with $\tau_d = 0.3$ [s].

A remark can be made on the distribution of the kinetic energy over the particle and the fluid. During settling the potential energy of the particle is transferred to the fluid and dissipated. At maximum settling velocity, the kinetic energy of the fluid is much larger than that of the particle. The volume of the moving fluid is much larger than the volume of the particle (see also Fig. 3.6) and since the solid/liquid density ratio is small, the fluid can easily contain much more kinetic energy than the particle.

Three physical time scales can be used to interpret the flow field and transient behaviour of the sedimenting sphere. The first time scale is the particle advection time

($\tau_{p,a} \simeq d_p/u_\infty$), which is a measure for the time it takes the particle to travel one sphere diameter. The second time scale is the particle relaxation time, ($\tau_{p,r} \simeq \rho_p d_p^2/18\rho_f\nu$) which is a measure for the time it takes for a particle to respond to an acceleration. The third time scale is the momentum diffusion time ($\tau_\nu \simeq {d_p}^2/\nu$), which is a measure for diffusion of momentum into the fluid over a distance of one particle diameter. These three groups determine two independent dimensionless numbers, the Reynolds and Stokes number.

The different shapes of the flow field in the high and low Reynolds number cases can be interpreted by regarding the Reynolds numbers as the ratio of τ_ν and $\tau_{p,a}$. At $Re = 1.5$, τ_ν is 0.59 s and $\tau_{p,a}$ is 0.39 s. The time it takes for the particle to travel one diameter is almost the same as the time it takes for momentum to diffuse one diameter into the fluid. This explains the penetration of the flow field into the fluid in front of the sphere and sideways to the sphere over a length comparable to the size of the wake. In contrast to this, the shape of the wake at $Re = 31.9$ is completely different. The characteristic time scales are $\tau_\nu = 3.72$ s and $\tau_{p,a} = 0.12$ s. Thus, momentum diffusion goes at a much slower rate than particle advection, resulting in an elongated wake and a very limited extension of the flow field in front of the sphere.

The time scale for momentum diffusion can also be used to interpret Fig. 3.7. At $Re = 1.5$, the diffusion time scale is much shorter than the time it takes for the particle to reach the bottom, thus allowing the wake to develop into a steady state. At $Re = 31.9$, the particle reaches the bottom after approximately 1.3 seconds while τ_ν is 3.72 seconds, which explains why the wake was not fully developed before the bottom was reached. It is interesting to note that the time constant for decay of the kinetic energy is much shorter than the time constant for momentum diffusion. The decay of kinetic energy is associated with the dissipation due to viscous effects that originate from gradients in the fluid. This process is apparently much faster than the momentum diffusion.

The second dimensionless number is the Stokes number ($St = (1/9)\rho_p d_p u_\infty/\rho_f\nu = (1/9)Re\rho_p/\rho_f \sim \tau_{p,r}/\tau_{p,a}$), which is a measure for the ratio of particle inertia to viscous forces. With a practically constant density ratio throughout the experiment, the Stokes number is proportional to the Reynolds number and was not varied independently. The Stokes number characterises the transient behaviour of the particle at acceleration and bottom approach. At the low Reynolds number, the particle starts to decelerate at some distance from the bottom while at high Reynolds number, the particle hardly decelerates prior to contact.

3.4.3 Comparison of numerical and experimental results

A first comparison is made in terms of the maximum velocity of the particle during sedimentation. In table 3.2, the ratios u_{max}/u_∞ from the experiments and simulations are given. The experimental results demonstrate that the particle reaches a maximum velocity of approximately 95 % of the steady state value in an infinite medium. The experimental data indicate a maximum of the velocity ratio value for case $E3$. An explanation for this observation is that the sphere moving at the lowest Reynolds number experiences the largest resistance due to the container wall. At increasing Reynolds number, the lateral extension of the sphere induced flow reduces, thus reducing the wall

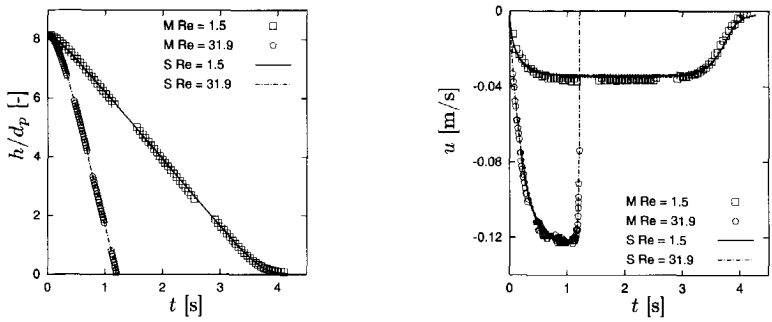

(a) (b)

Figure 3.8: Comparison between measured (M) and simulated (S) sphere trajectory (a), represented by the dimensionless gap height h/d_p, and sedimentation velocity (b) at two Reynolds numbers (simulation data from $S1$ and $S4$).

hindrance effect on the sphere. The lower u_{max}/u_∞ ratio at the highest Reynolds number (*i.e.* case $E4$) is likely caused by the fact that the sphere was still accelerating when it arrived at the bottom. This trend is also observed in the simulated results, although more pronounced. The maximum sedimentation velocity predicted by the simulations is generally within 1 % of the experimental result, except at the lowest Reynolds number, where the difference is approximately 5 %. Increased resolution does not result in an improvement. The calibration procedure has a strong impact on the terminal velocity. Its sensitivity will be further discussed in section 3.4.4.

For comparison of numerical and experimental findings as to the dynamic behaviour of the sphere, the trajectory and velocity of the sphere versus time have been plotted in Figs. 3.8 (a) and (b). At the lowest Reynolds number, the sphere decelerates at a larger distance from the bottom than at the higher Reynolds number. Along with the results at $Re = 4.1$ and $Re = 11.6$ (not shown), these results demonstrate that the complete trajectory of the sphere is captured accurately by the simulation procedure.

The simulated fluid motion has been compared in detail with the flow fields from the PIV experiment. With the use of a continuous camera, not only the spatial structure of the flow field is obtained but also the temporal behaviour. Figure 3.9 shows the flow field of the sphere at position $h/d_p = 0.5$ at the four Reynolds numbers considered. (Notice that Figs. 3.9 (c) and (d) are at a higher resolution than (a) and (b)). At the sphere position in question, the flow in front of the sphere interferes with the bottom surface, while the wake is still seemingly undisturbed. The correspondence in position of the velocity magnitude contours is indicative of a good agreement between the numerical and experimental flow field. At the side of the sphere a clear vortex is found that changes shape and position with an increase in Reynolds number. The center of this vortex is found at the same position for the numerical and experimental result.

Another (quantitative) assessment is obtained by comparing the time series of the

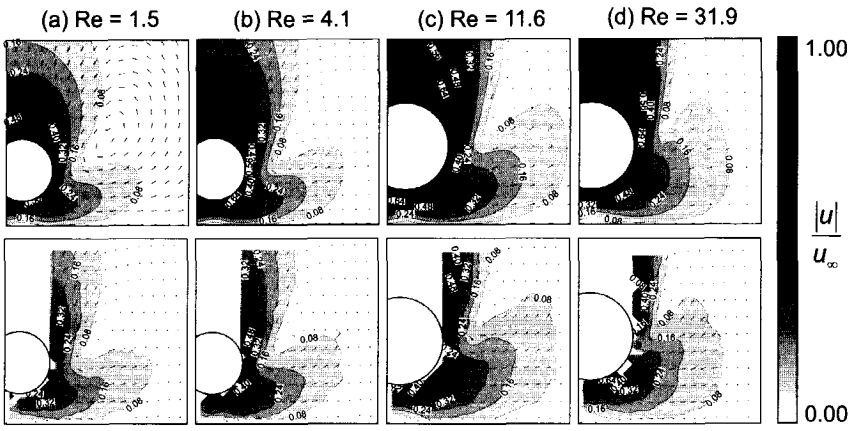

Figure 3.9: Comparison of the simulated (top, cases $S1$ to $S4$) and measured (bottom, $E1$ to $E4$) flow field of the sphere at a dimensionless gap height of $h/d_p = 0.5$. Contours indicate the normalised velocity magnitude, the vectors indicate the direction of the fluid flow only.

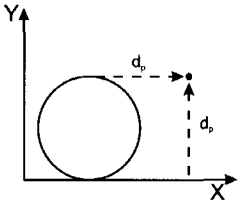

Figure 3.10: Measurement position of the time series of fluid flow.

fluid velocity in a particular point in the flow domain. As monitor point we chose a point fixed in place, positioned one diameter from the bottom of the tank and one diameter out of the center of the sphere (see Fig. 3.10).

Time series of the fluid velocity in this point are given for $Re = 1.5$ (fig. 3.11) and $Re = 31.9$ (fig. 3.12). At the low Reynolds number, the fluid flow in the x-direction is mainly effected by the squeezing action of the sphere. A distinctive positive peak is observed, due to the outward motion of the fluid. The fluid velocity drops almost back to zero at the moment the sphere touches the bottom of the container. At $Re = 31.9$, the sphere settling velocity is much higher; as a result, the x-velocity starts rising much earlier in time. After the vortex has passed the monitor point, the velocity decreases again. As the sphere comes to rest, the fluid motion in the wake still contains a considerable amount of inertia and passes over the sphere, giving rise to the slight increase in x-velocity, followed by the decay to zero.

At $Re = 1.5$, the flow in the y-direction is directed downwards, indicated by the negative value of the velocity component. The experimental data shows a steep decay to a minimum y-velocity, after which the velocity rises again. With careful observation, a

second, smaller decay can be observed in the data before returning to zero, although this decay is barely visible since the magnitude of the decay is comparable to the noise in the data. This behaviour is related to both the position of the vortex centre relative to the monitor point and the decreasing velocity of the sphere. At this Reynolds number the flow field extends the furthest sideways into the fluid and the monitor point is positioned between the sphere and the vortex centre. As a result, the y-velocity does not change sign. Since the y-velocity is smaller near the core of the vortex, an increase in velocity may be found as the centre passes the monitor point, after which a velocity decrease is anticipated. However, since the particle decelerates, the magnitude of this decrease is smaller than the main negative peak.

At $Re = 31.9$ the monitor point is positioned on the right side of the vortex. Thus, the y-velocity initially gets negative, but as the vortex passes the monitor point, the y-velocity changes sign because the flow on the right side of the vortex centre is directed upward. Eventually the vortex has passed and what follows is the wake of the sphere, resulting in a downward velocity that again slowly decays after the sphere has come to rest.

At $Re = 1.5$, the y-velocity shows the largest difference between simulation and experimental result. At low resolution of the simulation, a clear mismatch is observed between the numerical and experimental curve. Apparently, at lower Reynolds number, the position of the vortex is very sensitive to the resolution. The fluid velocity becomes positive, which is indicative of the monitor point being at the outer side of the vortex. As the resolution is increased, the position of the vortex is predicted more accurately and the simulated time series of the y-velocity is in much better agreement with the experimental result. The simulations at the high Reynolds number are in good agreement with the experimental data, although at this Reynolds number too, an increase in resolution improves the predictions. The curves that represent the velocity magnitude vs. time demonstrate that at the low Reynolds number, the fluid velocity is underpredicted by a few percent only, which is in agreement with the contour plots of Fig. 3.9.

3.4.4 Hydrodynamic radius dependency

In simulations $S9$ to $S15$, the hydrodynamic radius was varied deliberately (*i.e.* without applying the calibration procedure) to study its impact on u_{max}/u_∞. The hydrodynamic radius is used as the measure to determine length scaling. Therefore, by varying the hydrodynamic radius the scaling constants for time and length scale will change. In order to keep the ratio of particle to domain size the same, also the computational domain will vary with varying hydrodynamic radius. The input radius of the sphere, however, remains constant. Without calibration the velocity ratio is underpredicted some 20 %. The simulations further show that the velocity ratio u_{max}/u_∞ is strongly dependent on the hydrodynamic radius. When varying the hydrodynamic radius on purpose, both u_{max} and u_∞ change, as can be seen in table 3.3.

Firstly, increasing the hydrodynamic radius may increase u_{max}. The force $F_{d,input}$ drives the sphere during sedimentation and is determined from the balance between drag

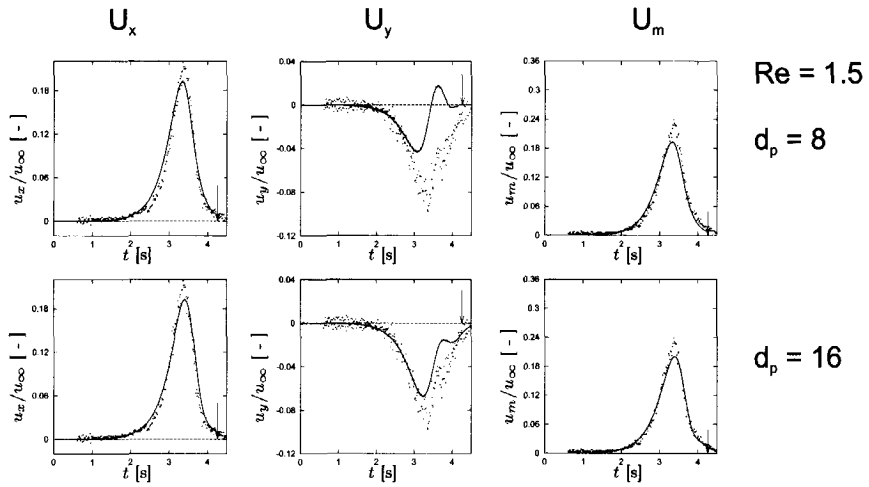

Figure 3.11: Time series of the fluid velocity in a point at $Re = 1.5$. The lines indicate the normalised velocity in x and y-direction and velocity magnitude of simulations $S1$ (top) and $S5$ (bottom). The dots indicate the experimental result of $E1$. The arrow indicates the moment the sphere comes to rest at the bottom.

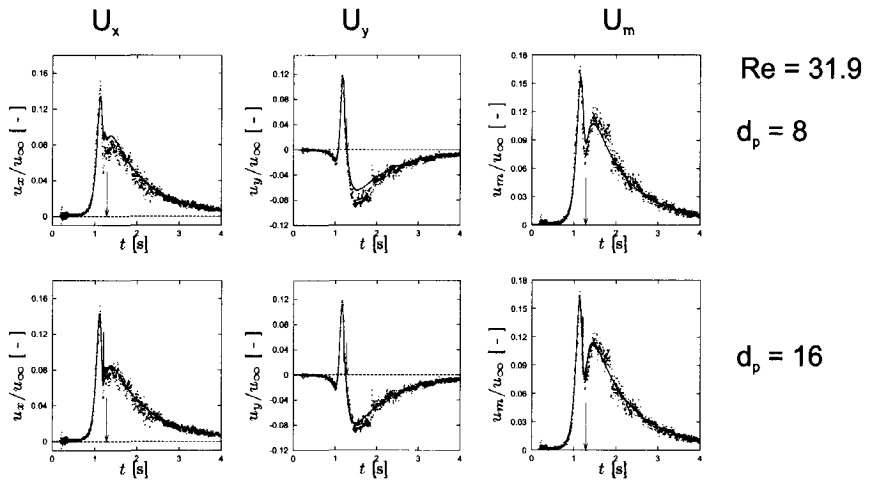

Figure 3.12: Same as Fig. 3.11, now for $Re = 31.9$.

Table 3.3: Influence of the hydrodynamic radius on the maximum sedimentation velocity.

Case	r_0 $[lu]$	r_h $[lu]$	Re [-]	u_{max} $[10^{-3}lu/ts]$	u_∞ $[10^{-3}lu/ts]$
S 9	4	4.000	1.5	7.678	10.000
S 10	4	4.400	1.5	7.920	9.091
S 1	4	4.487	1.5	7.968	8.914
S 11	4	4.600	1.5	8.034	8.696
S 12	4	5.000	1.5	8.074	8.000
S 13	4	4.000	31.9	7.573	10.000
S 14	4	4.600	31.9	7.749	8.696
S 4	4	4.810	31.9	7.877	8.315
S 15	4	5.000	31.9	7.754	8.000

force, gravity and buoyancy;

$$F_{d,input} = \frac{4}{3}\pi {r_h}^3(\rho_f - \rho_p)g \tag{3.12}$$

When the sphere moves at u_{max}, this force is balanced by the hydrodynamic forces that act on the sphere and which are obtained from the simulation. $F_{d,input}$ is independent of the hydrodynamic radius. With a changing hydrodynamic radius, length scales proportional to L, while time scales with the length squared, L^2, because time is scaled via the kinematic viscosity. Thus, when scaling equation 3.12 from physical quantities to simulation quantities, the equation is independent of the scaling factors, because ρ is kept constant, ${r_h}^3$ scales as L^3 while g scales as $1/L^3$. At the same time, the input radius of the sphere and the viscosity are kept constant. Therefore, u_{max} can only vary because a change in the container geometry occurs. By increasing the hydrodynamic radius, the scaling factor for length decreases and the container geometry is represented by a larger number of grid nodes. Consequently, because of the larger domain, the sphere experiences a smaller resistance due to the parallel walls and u_{max} increases. The sensitivity of this effect depends on the Reynolds number at which sphere settles, as can be observed in table 3.3. At $Re = 1.5$, u_{max} increases by 5.2 % when varying the hydrodynamic radius from 4 to 5 grid units while at $Re = 31.9$, u_{max} increases by 2.4 % only.

Secondly, when increasing the hydrodynamic radius, u_∞ decreases as $1/L$, which can be observed in table 3.3 where u_∞ is recalculated to lattice units. Thus, u_∞ decreases by 20 % for both the low and the high Reynolds number when increasing the hydrodynamic radius from 4 to 5 lattice units.

For the cases studied, these dependencies show that a variation in radius of the order of one lattice unit mainly affects the reference state u_∞. In our base cases (with $r_0 = 4\ lu$), increasing the hydrodynamic radius with 1 lattice unit resulted in a variation of the ratio u_{max}/u_∞ of approximately 30 %. Increasing the resolution may decrease this sensitivity. A variation of one lattice unit on an input radius of *e.g.* 8 lattice nodes causes u_∞ to vary by 11% while the relative increase in u_{max} is expected to be smaller.

The calibration procedure proposed in section 3.3 is used to determine the hydrodynamic radius *a priori*. Table 3.2 demonstrates that using this calibration method

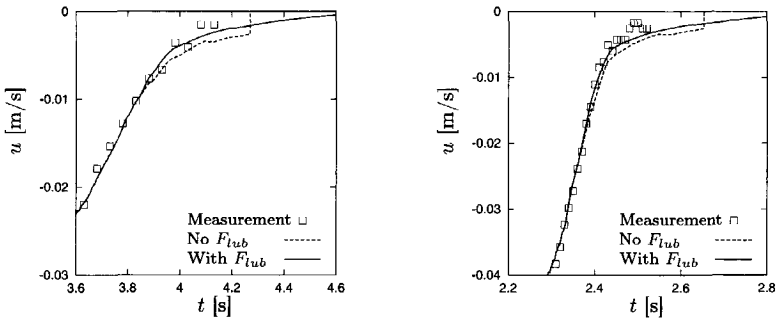

Figure 3.13: The use of a lubrication force (F_{lub}) on the particle sedimentation velocity at near wall approach at (a) $Re = 1.5$, cases $S16$ and $S18$, and (b) $Re = 4.1$, cases $S17$ and $S19$.

results in a 1% accurate match between the numerical and experimental values of the velocity ratio is found for the simulations at $Re \geq 4.1$. At the lowest Reynolds number, a systematic underprediction of the velocity ratio of approximately 5% is found. This difference corresponds to the deviations observed in Fig. 3.8. These deviations are considered acceptable, since without calibration an underprediction of more than 20 % is obtained. However, the systematic deviation at the lowest Reynolds number is striking for two reasons. One, the deviation is independent of the resolution (see table 3.2). If the deviation decreases with an increase in resolution, one would anticipate the simulations to eventually match the experimental data at high resolution, which is not the case. Two, one would expect that the calibration procedure would work best at the lowest Reynolds number, since it is based on creeping flow conditions. The simulation at $Re = 1.5$ comes closest to this situation.

3.4.5 Lubrication force

When the sphere approaches the bottom wall, the gap between the sphere and the bottom may become too narrow for a proper resolution of the flow on the original grid. As a result, the hydrodynamic force on the sphere will be underpredicted. In Fig. 3.13, the sedimentation velocities of the sphere at Reynolds numbers of 1.5 and 4.1, respectively, are given at the final stage of bottom approach. In the simulations, the particle velocity is set to zero at the moment of bottom contact. This moment is clearly visible in both figures, where the dotted line indicates the sedimentation velocity of the sphere in simulations $S16$ and $S17$. This abrupt stop indicates that the sphere velocity was not reduced to zero at the moment contact was established between the sphere and the bottom wall. The dotted line further shows unphysical fluctuations in the velocity of the sphere when the bottom of the sphere passes the first nodes above the bottom

wall. Simulations at higher resolution showed that an increase in resolution reduces the fluctuations but the abrupt stop remains.

When applying the sub-grid scale lubrication force according to equation 3.10, the velocity of the sphere reduces more gradually although some fluctuations are still observed. The use of the lubrication force improves the velocity decay initially, which is demonstrated by an improved correspondence between the experimental and numerical data. Due to the dissipative action of the lubrication force, however, at a small separation from the bottom the settling velocity has almost reached zero (of the order of the numerical accuracy) and the sedimentation time series extends further for an unrealistically long time (not in the figure). Application of a force based on lubrication theory is valid for separations that exceed either the molecular mean free path length of the molecules of the fluid (Sundararajakumar & Koch (1996)) (although this effect is negligible for solid-liquid suspensions) or that exceed the surface roughness (Joseph *et al.* (2001)) of the particle and the tank wall. For detailed simulations or experiments either of the two limits can be used as a cutoff measure for the final separation at which an apparent contact is established. In the current study, both effects are of the order of 0.1 to 1 μm or smaller, which is of a much greater detail than provided by either our experimental observations or numerical simulations. The application of a lubrication force improves the simulation result in that it provides a measure for a lacking sub-grid scale repulsive force at bottom approach. At the same time it raises a difficulty in establishing the exact moment of contact between the particle and the container wall.

3.5 Conclusion

We investigated the motion of a single sphere settling in a box filled with silicon oil. By keeping the ratio of the box dimensions to the sphere radius relatively small, we were able to perform simulations of the full flow field with incorporation of the no-slip boundary conditions due to the tank wall. We were able to validate the transient behaviour of the sphere over the whole time span of the sedimentation from release via steady fall to deceleration at bottom approach. Time series of the particle trajectory and particle settling velocity were measured and detailed snapshots of the flow field were produced by using PIV. The data could also be represented as time series of the fluid velocity in monitor points. Lattice-Boltzmann simulations of cases identical to the experiments were performed. The boundary conditions for the solid sphere were imposed using the adaptive force-field technique. This technique requires the sphere to have internal fluid that contributes to the sphere's inertia. A correction method has been proposed to compensate for this inertial effect. The simulations also require a correction for the hydrodynamic radius. The data demonstrated that the simulations are in agreement with measurements over a range of resolutions between 2 and 8 grid nodes per sphere radius. The transient behaviour of both the sphere and fluid motion is captured accurately, as demonstrated by a comparison between experimental and numerical results in terms of particle trajectory and velocity as well as of fluid velocity. The hydrodynamic radius was found to affect the sedimentation velocity in two ways. First, a change in hydrodynamic radius causes a change in domain size, which varies

the sedimentation velocity by 2 to 5 %, depending on the Reynolds number. Second, a change in radius causes a change in time scaling, resulting in a variation of the velocity up to 20 % for a sphere with an input radius of 4 lattice units. A calibration procedure was used for *a priori* determining the hydrodynamic radius of the sphere. For the cases of $Re = 4.1$ to $Re = 31.9$, this calibration procedure predicts the maximum sedimentation velocity within 1% accuracy. At $Re = 1.5$, the sedimentation velocity was underpredicted by approximately 5% (independent of resolution). At approach of the bottom wall, resolution lacks to resolve the flow in the gap. Lubrication theory was used to provide the lacking hydrodynamic interactive force at bottom approach, but this apparently overpredicts the time to contact with the bottom.

List of Symbols

Symbol	description	unit
c_s	speed of sound	lu/ts
d_p	particle diameter	m
$\vec{d_i}$	velocity deviation	lu/ts
$\vec{F_j}$	body force acting on gird node j	N or Mlu/ts^2
$\vec{F_p}$	force acting on particle	N or Mlu/ts^2
$\vec{F_w}$	force acting on particle due to wall	N or Mlu/ts^2
h	sphere-tank wall gap height	m
$I(r_{ij})$	interpolation coefficient	–
K_f	fluid kinetic energy	J
r_p	particle radius	m or lu
r_0	input radius	m or lu
r_h	hydrodynamic radius	m or lu
$\vec{r_i}$	surface point to particle center	lu
$\vec{r_i}j$	surface point to surrounding grid nodes	lu
t	time	s
$\vec{T_p}$	torque acting on particle	Nm or Mlu^2/ts^2
u_∞	sedimentation velocity in infinite medium	m/s
u_{max}	maximum velocity in simulation	lu/ts
$u_\perp$	perpendicular particle velocity component	lu/ts
U_v	volumetric averaged relative velocity	m/s or lu/ts
$\vec{u_i}$	velocity of particle surface	lu/ts
$\vec{u_j}$	velocity grid node j	lu/ts
$\vec{u_p}$	particle translation velocity	m/s or lu/ts
$\vec{x_i}$	position of control point I	lu
$\vec{x_c}$	position of center of mass of particle	lu

Greek	description	unit
Δ_0	threshold separation	lu
μ_f	dynamic viscosity	$Ns\,m^2$
ν	kinematic viscosity	$m^2\,s^{-1}$
ρ	fluid density	lu
ρ_f	fluid density	$kg\,m^{-3}$
ρ_p	particle density	$kg\,m^{-3}$
$\vec{\Omega}_p$	particle angular velocity	s^{-1} or ts^{-1}

Dim. numbers

C_d	Drag coefficient
C_τ	Volume fraction
Re	Reynolds number
St	Stokes number

Acronyms

PIV	Particle Image Velocimetry

Chapter 4

Application of spectral forcing in lattice-Boltzmann simulations of homogeneous turbulence

In this chapter it is demonstrated that by combining a spectral forcing scheme for the generation of a sustained homogeneous turbulent with a lattice-Boltzmann method for solution of the continuity and Navier–Stokes equations, turbulent conditions are generated with an accurate recovery of *a priori* set properties such as the Kolmogorov length scale, the integral length scale and the integral time scale. A specific feature of the forcing scheme is that it allows control of the power input by eliminating the force-velocity correlation. This feature has also been incorporated into the lattice-Boltzmann simulations. Furthermore, the forcing scheme also enables forcing of anisotropic turbulence.

Key words: turbulence, lattice-Boltzmann, forcing, anisotropic turbulence

4.1 Introduction

In turbulent flows, energy production takes place at large length scales ($\mathcal{O}(\Lambda)$, the integral length scale) whereas energy dissipation occurs at the microscopic length scales ($\mathcal{O}(\eta)$, around the Kolmogorov length scale). The transfer of kinetic energy from the large to the small scales is characterised by a cascade process which can be described by the well-known universal power-law spectrum (*e.g.* Tennekes & Lumley (1973))

$$E(k) = c_K \epsilon^{2/3} k^{-5/3}. \tag{4.1}$$

The property that turbulent flows obey a universal spectrum has been exploited in numerical studies of forced turbulence. In this approach, an artificial force is defined that sets the fluid in motion at the large scales (see figure 4.1). By solving all occurring length scales in a direct numerical simulation of the Navier–Stokes equations, the microscopic scales will evolve naturally. This approach is in clear contrast with conventional $k-\epsilon$ and

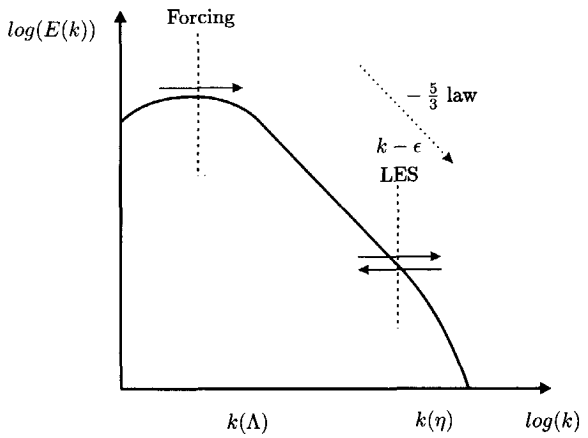

Figure 4.1: Typical representation of the power spectrum of kinetic energy in a turbulent flow. 'LES' indicates the filtering position of LES in the power spectrum, 'Forcing' indicates the wavenumber position of the spectral forcing scheme.

LES type turbulence modeling, where the large scale motion is resolved while the small scale behaviour of the turbulent flow field is modeled. By performing direct simulations of forced turbulent flow, universal microscopic properties of the turbulent flow field can be studied that hold no relation to a physical source for power input.

For this purpose, different types of forcing schemes have been developed. Typical examples of such forcing schemes are given by *e.g.* Eswaran & Pope (1988), and more recently by Overholt & Pope (1998) or Alvelius (1999). In these approaches, a body force is defined in a spherical shell at low wavenumbers. Using a pseudo-spectral method for solution of the Navier-Stokes equations is the natural choice for forcing turbulence. In this type of schemes the computational domain is (partially) solved in wavenumber space. Introducing spectral forcing to the flow field is then straightforward since both methods are defined in the Fourier domain. Nevertheless, spectral forcing only represents a means to impose an artificial momentum source term in the Navier-Stokes equations, which is essentially independent of the numerical solution method.

The objective is eventually to perform direct numerical simulations of turbulent suspensions (*i.e.* solid-liquid systems) at high resolution, which requires an efficient numerical method for solution of the Navier-Stokes equations. Successful application of the lattice-Boltzmann method to resolved suspension simulations (*e.g.*Ladd (1997)) and high resolution bubbly flow (Sankaranarayanan *et al.* (2002)) has proven that this method is suited for such applications.

This requires a method to generate turbulent conditions in the lattice-Boltzmann scheme. For this purpose, we use the forcing method of Alvelius (1999). His method offers the possibility to reduce large scale fluctuations that occur in forced turbulence due to force-velocity correlation. In the following sections the theoretical background of the forcing method is briefly reproduced. Simulation results are presented in which the

specific features of the forcing method, as applied to single-phase flow, are assessed.

4.2 Spectral Forcing

In this section, the forcing method developed by Alvelius (1999) is presented. The forcing that drives the flow field is defined in wavenumber space. The random force is active in a spherical shell at small wavenumbers where the forcing intensity is given by a prescribed distribution over the wavenumbers. Alvelius (1999) recognised that for such a force, the power input in the Navier-Stokes equations contains two contributions. Consider the force to be constant for the duration of one timestep. The discretised power input for the duration of one time step Δt (*i.e.* $n \rightarrow n+1$) becomes

$$\frac{K^{n+1}-K^n}{\Delta t} = \frac{1}{2}\overline{f_\alpha^n f_\alpha^n}\Delta t + \overline{u_\alpha^n f_\alpha^n} = P_1 + P_2. \tag{4.2}$$

where the overbar indicates spatial averaging of the force vector f_α (the summation convention is implied on repeated greek subscripts). Thus, P_1 gives the constant power input due to the force-force correlation, while P_2 represents an uncontrolled fluctuating quantity that is due to the force-velocity correlation. As will be demonstrated, the force can be chosen in such a way that (by construction) the term P_2 is set to zero each time step.

Firstly, the force is defined such that it is divergence free. In Fourier space [1] this gives:

$$k_\alpha \hat{f}_\alpha = 0 \tag{4.3}$$

which is obeyed by choosing

$$\hat{f}_\alpha(\mathbf{k},t) = A_{ran}(\mathbf{k},t)e_{1\alpha}(\mathbf{k}) + B_{ran}(\mathbf{k},t)e_{2\alpha}(\mathbf{k}) \tag{4.4}$$

where $\mathbf{e}_1$ and $\mathbf{e}_2$ are two orthogonal unit vectors, normal to $\mathbf{k}$. A_{ran} and B_{ran} are terms that distribute the power input randomly in the directions $\mathbf{e}_1$ and $\mathbf{e}_2$. The choice of Alvelius (1999) for the unit vectors $\mathbf{e}_1$ and $\mathbf{e}_2$ are

$$e_{1x} = \frac{k_y}{(k_x^2+k_y^2)^{1/2}}, \quad e_{1y} = -\frac{k_x}{(k_x^2+k_y^2)^{1/2}}, \quad e_{1z} = 0 \tag{4.5}$$

and

$$e_{2x} = \frac{k_x k_z}{k(k_x^2+k_y^2)^{1/2}}, \quad e_{2y} = \frac{k_y k_z}{k(k_x^2+k_y^2)^{1/2}}, \quad e_{2z} = -\frac{(k_x^2+k_y^2)^{1/2}}{k} \tag{4.6}$$

where $k = |\mathbf{k}|$.

The power input of the force-force correlation in spectral space is then given by

$$\frac{P_1}{\Delta t} = \frac{1}{2}\overline{f_\alpha^n f_\alpha^n} = 2\pi \int_0^\infty k^2 \langle \hat{f}_\alpha \hat{f}_\alpha^* \rangle dk \equiv \int_0^\infty F(k)dk \tag{4.7}$$

[1] The superscript '^' indicates the Fourier transform of a variable

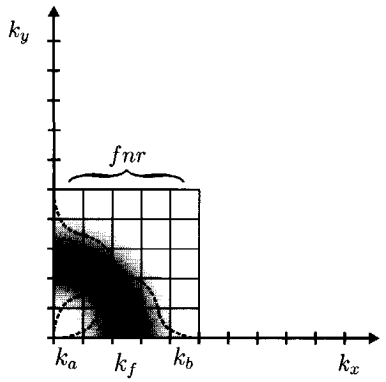

Figure 4.2: 2D representation of the placement of the forcing distribution in the Fourier domain. The dotted curves indicate the placement of the Gaussian distribution of the force signal along the x and y axis, the greyscale contour indicates the position of the Gaussian distribution in the 2D plane.

where $F(k)$ is the function that defines the distribution of the forcing spectrum in wavenumber space. The form for A_{ran} and B_{ran} was chosen as

$$A_{ran} = \left(\frac{F(k)}{2\pi k^2}\right)^{1/2} \exp(i\theta_1) g_A(\phi) \tag{4.8}$$

$$B_{ran} = \left(\frac{F(k)}{2\pi k^2}\right)^{1/2} \exp(i\theta_2) g_B(\phi) \tag{4.9}$$

where g_A and g_B are random factors that determine the direction of the forcing vector at each wavenumber and that obey $g_A^2 + g_B^2 = 1$. This is done by choosing the angles $\phi \in [0, \pi]$, and θ_1,$\theta_2 \in [0, 2\pi]$ as uniformly distributed random numbers, which are chosen at each discrete wavenumber for each time step.

The distribution of the power input over the wavenumbers is determined by the definition of $F(k)$. In order to determine the power input *a priori*, a Gaussian distribution of the spectrum function $F(k)$ is chosen, which is schematically represented in figure 4.2. The force distribution is active in the wavenumber range $k \in [k_a, k_b]$, with a forcing maximum at k_f,

$$F(k) = A \exp\left(-\frac{(k - k_f)^2}{c}\right) \tag{4.10}$$

and where c is a parameter that determines the width of the distribution. The power input is determined by the amplitude A according to

$$A = \frac{P_1}{\Delta t} \frac{1}{\int_{k_a}^{k_b} \exp\left(-\frac{(k-k_f)^2}{c}\right) dk}. \tag{4.11}$$

To control the power input, a constraint needs to be determined for ensuring that P_2 remains zero for each time step. The force-velocity correlation is given by

$$P_2 = \overline{\hat{u}_\alpha^n \hat{f}_\alpha^n} = \iiint_V \hat{u}_\alpha(\mathbf{k},t)\hat{f}_\alpha^*(\mathbf{k},t)dk_x dk_y dk_z \tag{4.12}$$

which is generally non-zero on the interval $[k_a, k_b]$ and is zero by definition outside this range. P_2 is set to zero by making $\hat{u}_\alpha(\mathbf{k},t)\hat{f}_\alpha^*(\mathbf{k},t) = 0$ ($*$ indicates the added complex of f_α) at each of the active wavenumbers. This gives the condition:

$$\text{Real}[A_{ran}^* \xi_1 + B_{ran}^* \xi_2] = 0 \tag{4.13}$$

with $\xi_1 = \hat{u}_\alpha e_{1\alpha}$ and $\xi_2 = \hat{u}_\alpha e_{2\alpha}$. Using this constraint, equations 4.8 and 4.9 lose one degree of freedom and θ_1 can be determined from

$$\tan\theta_1 = \frac{g_A(\phi)\text{Real}[\xi_1] + g_B(\phi)(\sin\psi\text{Imag}[\xi_2] + \cos\psi\text{Real}[\xi_2])}{-g_A(\phi)\text{Imag}[\xi_1] + g_B(\phi)(\sin\psi\text{Real}[\xi_2] - \cos\psi\text{Imag}[\xi_2])} \tag{4.14}$$

after choosing randomly for each wavenumber at each time step the angle ψ, which is defined as $\psi = \theta_2 - \theta_1$, on the interval $[0, 2\pi]$.

A choice for the functions g_A and g_B needs to be made to determine the mean orientation of the power input. This is determined by the product of $g_A e_{1\alpha}$ and the product of $g_B e_{2\alpha}$. With the choice for the $e-$vectors of equations 4.5 and 4.6, the power input specified for the different directions becomes,

$$\langle P_x \rangle = \langle P_y \rangle = P_1(\tfrac{1}{6} + \tfrac{1}{3}\langle g_A^2 \rangle) \tag{4.15}$$

$$\langle P_z \rangle = P_1 \tfrac{2}{3}(1 - \langle g_A^2 \rangle) \tag{4.16}$$

and the ratio of the power input, r_f, in the different $x-z$ or $y-z$ direction becomes

$$r_f = \frac{\langle P_x \rangle}{\langle P_z \rangle} = \frac{1 + 2\langle g_A^2 \rangle}{4(1 - \langle g_A^2 \rangle)}. \tag{4.17}$$

which is determined by the choice of $g_A(\phi)$. By choosing $g_A = \sin(2\phi)$ and $g_B = \cos(2\phi)$, $r_f = 1$ and the forcing becomes isotropic. Choosing g_A in the form

$$g_A(\phi) = -\frac{\tanh(b(\phi - \pi/2))}{\tanh(b\pi/2)} \tag{4.18}$$

results in

$$\langle g_A^2(\phi) \rangle = \frac{1}{\tanh(b\pi/2)}\left(\frac{1}{\tanh(b\pi/2)} - \frac{2}{b\pi}\right) \tag{4.19}$$

where b determines the degree of anisotropy. With this choice of e-vectors, axisymmetric anisotropic turbulence is obtained.

4.3 Simulations

For solving the continuity and the Navier-Stokes equations, the lattice-Boltzmann method is used. This method has been presented in more detail in section 2.2 of chapter 2. In the simulations presented here, the lattice-Boltzmann scheme of Eggels & Somers ((1995) was used. The continuity and momentum equations for the fluid motion are given by

$$\frac{\partial \rho}{\partial t} + \frac{\partial \rho u_\alpha}{\partial x_\alpha} = 0 \tag{4.20}$$

and

$$\frac{\partial \rho u_\alpha}{\partial t} + \frac{\partial \rho u_\alpha u_\beta}{\partial x_\beta} = -\frac{\partial p}{\partial x_\alpha} + \frac{\partial}{\partial x_\beta}\left[\nu\rho\left(\frac{\partial u_\beta}{\partial x_\alpha} + \frac{\partial u_\alpha}{\partial x_\beta}\right)\right] - \frac{1}{2}\frac{\partial}{\partial x_\alpha}\left(\nu\rho\frac{\partial u_\beta}{\partial x_\beta}\right) + \rho f_\alpha \tag{4.21}$$

where ρ is the fluid density, ν is the kinematic fluid viscosity, p is the pressure and f_α is the body force that acts on the fluid. These equations satisfy the continuity and Navier-Stokes equations for incompressible flow in the limit of low Mach numbers (*i.e.* when the fluid velocity remains well below the speed of sound, $c_s = \sqrt{\frac{1}{2}}$ $[lu/ts]$).

Turbulent conditions are generated by manipulating the force field $f_\alpha(\mathbf{x}, t)$. The forcing scheme discussed in the previous section defines the force field ($\hat{f}_\alpha(\mathbf{k}, t)$) in Fourier space. Since the lattice-Boltzmann method is defined in physical space, the force must be transformed to the physical domain before being applied. This is achieved via an inverse Fourier transform, after which the force is straightforwardly imposed on the flow domain. Implementation of the controlled version of the forcing scheme requires the Fourier transform of the velocity field, $\hat{u}_\alpha(\mathbf{k}, t)$. As a result, application of the forcing scheme in three dimensions requires three inverse Fourier transforms for the generation of the force field, while the controlled version of the forcing scheme requires an additional three forward Fourier transforms for the velocity field.

A number of parameters defines the conditions of the simulations. The first parameter is the domain size; $nx \times ny \times nz$ grid points. The forcing parameters are closely related to the grid dimensions. The forcing is defined on the wavenumber interval $[k_a, k_b]$ by the number of discrete Fourier modes f_{nr} in this range and the wavenumber of maximum forcing amplitude k_f. The smallest wave number that can be represented on the grid is defined by the domain size and follows $k_0 = k_a = 2\pi/nx$. The discrete wavenumbers in the Fourier domain are integer multiplications of k_0. The largest forced wavenumber is determined as $k_b = f_{nr} \times k_a$, while the forcing maximum is chosen as the central value in the range $[k_a, k_b]$. An integral forcing length scale is defined as $l_* = 2\pi/k_f$.

The next parameter that needs to be defined is a characteristic velocity u_*. To assure that the simulations obey the incompressibility restriction, this characteristic velocity is chosen typically one order of magnitude smaller than the speed of sound c_s. The velocity u_* is used as a way to determine the power input via the scaling law for energy dissipation $\epsilon \simeq \mathcal{U}^3/\mathcal{L}$ and the assumption that statistical equilibrium is achieved between dissipation and production, $\epsilon = P$. The power input is now set according to $P = {u_*}^3/l_*$.

The final parameter is the Kolmogorov length scale η. This length scale is a measure for the smallest distance over which gradients in the flow field can exist. In terms of lattice-Boltzmann units, a Kolmogorov length of 1 [lu] corresponds to one grid spacing.

Table 4.1: Parameter settings of forced turbulence simulations F_1 to F_7.

Run	η [lu]	$k_{max}\eta$ [-]	f_{nr} [-]	l_* [lu]	Re_{force} [-]	Remark
F_1	0.5	1.571	7	32	256	
F_2	0.5	1.571	7	32	256	uncontrolled
F_3	1	3.142	7	32	102	
F_4	0.1	0.314	7	32	2189	
F_5	1	3.142	3	64	256	
F_6	0.5	1.571	7	32	256	force from file
F_7	1	3.142	7	32	102	anisotropic, b= 10

In spectral simulations, the resolution is often defined in terms of $k_{max} \times \eta$ where k_{max} is the largest resolved wavenumber, which is given by $k_{max} = nx/2 \times k_0 = \pi$. A criterion for proper resolution of a DNS of turbulent flow is given by $k_{max} \times \eta > 1$. Accordingly, the Kolmogorov length scale should obey $\eta > 0.318$ [lu]. By choosing a Kolmogorov length, the kinematic viscosity of the fluid is fixed via the definition of the Kolmogorov length and the equilibrium assumption between production and dissipation: $\nu = (P\,\eta^4)^{1/3}$.

With the definition of l_*, u_* and the viscosity, a forcing Reynolds number is obtained that characterises the simulation conditions,

$$Re_{force} = \frac{u_* l_*}{\nu} = \left(\frac{l_*}{\eta}\right)^{4/3}. \tag{4.22}$$

This Reynolds number is a measure of the ratio between the largest and the smallest scales of the simulation. The parameter settings of the simulations discussed in this chapter are presented in table 4.1.

The parameter settings for the various simulations presented in this chapter is given in table 4.1. A number of parameters were identical for simulations F_1 to F_7. The domain size was $nx \times ny \times nz \sim 128^3$ and $u_* = 0.05$ [lu/ts]. The simulations were executed for 15000 [ts], corresponding to 11.7 forcing timescales l_*/u_* for simulation F_5 and 23.4 l_*/u_* for the other simulations. All simulations have controlled power input unless stated differently. The concentration parameter c of equation 4.10 was chosen 1.0 for all simulations. In the work of Alvelius (1999), the value for this parameter is chosen 0.01. This concentrates the input spectrum at a single wavenumber, rather than on the interval $[k_a, k_b]$. The current value was chosen such that the Gaussian distribution of the force spectrum influences all discrete wavenumbers on the interval $[k_a, k_b]$.

In simulations F_1 and F_2, the implementation of the forcing scheme into the lattice-Boltzmann framework is demonstrated and the difference between controlled and uncontrolled forcing is tested. In cases F_3, F_1 and F_4, the forcing Reynolds number is varied in increasing order to investigate the behaviour at decreasing Kolmogorov length. In simulation F_4 the resolution-constraint $k_{max}\eta > 1$ is violated to observe its impact on the numerical stability and physical validity of the simulations. In simulation F_5, the impact of the number of forcing Fourier modes on the flow field is investigated. In simulation F_6 forcing conditions were imposed using a set of 120 force fields $f_\alpha(\mathbf{x}, t)$. These fields were

Table 4.2: Simulation results. Properties indicated with a $*$ were nondimensionalised with u_* and l_*.

Run	$k_{max}\eta$	Re_λ	$u'*$	$\Lambda*$	Λ_s*	T_0*	$(\epsilon/P)_{lB}$	$(\epsilon/P)_s$	S_g
F_1	1.56	39.8	0.80	0.51	0.34	0.42	1.02	0.95	-0.40
F_2	1.56	39.9	0.81	0.51	0.34	0.43	1.02	0.94	-0.40
F_3	3.14	19.9	0.72	0.36	0.40	0.55	1.01	1.00	-0.43
F_4	0.36	171.6	0.86	1.05	0.28	0.32	0.60	0.41	-0.18
F_5	3.02	41.7	0.85	0.53	0.33	0.38	1.17	1.21	-0.38
F_6	1.58	39.4	0.79	0.51	0.34	0.43	0.98	0.93	-0.41
F_7	3.12	25.2	0.81	0.51	0.34	0.42	1.02	0.96	-0.40

prepared and stored prior to execution of the simulation, to increase the computational speed. As a result, the white noise forcing signal is mimicked by a limited set of force field realisations. The resulting flow field and time series are compared with simulations F_1 and F_2. Finally, run F_7 was carried out to test the feature of anisotropic forcing in the lattice-Boltzmann simulations.

4.4 Results and Discussion

4.4.1 Statistical quantities

A number of dimensionless statistical quantities that characterise the turbulent flow are given in table 4.2.

To characterise the large scales of the turbulent flow, an integral length scale Λ is given. This scale is determined both via the scaling law $\Lambda = u'^3/\epsilon$ (u' is the rms fluid velocity) and via the energy spectrum,

$$\Lambda_s = \frac{\pi}{2u'^2} \int_0^{k_{max}} \frac{E(k)}{k} dk. \tag{4.23}$$

These two integral scales have a different physical meaning. The integral scale Λ represents the large scale of the flow field based on the energy dissipation whereas Λ_s is a measure for the distance over which the velocity correlation drops to zero (Pope (2000)). Λ_s depends on the spatial structure of the flow field, which is determined by the size of the computational grid and the spectral forcing.

A Reynolds number often used to characterise simulations of isotropic turbulence is the Reynolds number based on the Taylor microscale, given by

$$\lambda = \left(\frac{15\nu u'^2}{\epsilon} \right)^{\frac{1}{2}}. \tag{4.24}$$

The table shows that the Taylor Reynolds number is about one order of magnitude smaller than the forcing Reynolds number. It is also noticed that Re_λ is practically constant for simulations with the same forcing Reynolds number.

The integral time scale given in the table is associated with the motion of the large scales in the fluid flow, and is defined by

$$T_0 = \Lambda_s / u'. \tag{4.25}$$

Two properties given in the table that are directly linked to the resolution of the small scales in the flow field are the rate of energy dissipation,

$$\epsilon \equiv \nu \overline{\left(\frac{\partial u_i}{\partial x_j} + \frac{\partial u_j}{\partial x_i}\right) \frac{\partial \mathbf{u}_j}{\partial \mathbf{x}_i}} \equiv \int_0^{k_{max}} D(k) dk \equiv 2\nu \int_0^{k_{max}} k^2 E(k) dk \tag{4.26}$$

and the velocity derivative skewness,

$$S_g = \frac{\left\langle \left(\frac{\partial u}{\partial x}\right)^3 \right\rangle}{\left\langle \left(\frac{\partial u}{\partial x}\right)^2 \right\rangle^{3/2}}. \tag{4.27}$$

At an increasing turbulent Reynolds number, motion is generated at smaller length scales. In a DNS, the smallest length scales have to be captured accurately on the computational grid. Both the rate of energy dissipation and the velocity derivative skewness give an indication of the accurate representation of the velocity gradients and consequently indicate the quality of the simulations.

The lattice-Boltzmann scheme inherently contains the deformation rate of the flow field (Eggels & Somers ((1995)), and consequently the rate of energy dissipation can be computed directly from the numerical scheme, *i.e.* without the need to determine spatial derivatives. The rate of energy dissipation can also be calculated from the energy spectrum (equation 4.26), which is directly related to the velocity field. In steady turbulent flows, the rate of energy dissipation and the power input should be in statistical equilibrium, and the ratio of power input over energy dissipation should be 1. Table 4.2 shows that ϵ_s as well as ϵ_{lB} in the different simulations are in good agreement, which demonstrates that the velocity field and the gradients in the simulations are calculated in a consistent manner. Apart from simulation F_4, the ratios ϵ/P are close to 1.0. The somewhat lower rate of energy dissipation obtained via the energy spectrum may be a result of the discretisation of the 1D energy spectrum obtained from the 3D velocity field.

In simulation F_4, the Kolmogorov length scale was set to 0.1 grid spacing. This violates the rule of thumb for accurate DNS. The rate of energy dissipation obtained from the simulations indicates that only 60 % of the power input is recovered, and the small scales of the flow field are not captured accurately by the simulations. This will be further discussed in a later section.

The velocity derivative skewness S_g is the normalized third order moment of the distribution of the velocity gradients, and can be associated with the time evolution of the longitudinal velocity correlation functions (Hinze (1975),Pope (2000)). It is a measure for the shape of the pdf of the velocity gradients. This parameter obtains a negative value which varies with the Reynolds number, and for DNS simulations is reported in the range -0.4 to -0.5 for both decaying and sustained isotropic turbulence

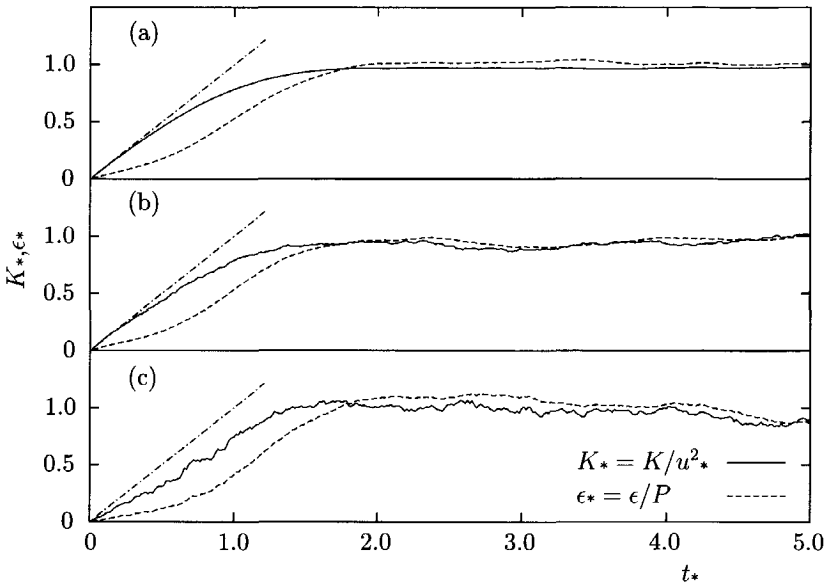

Figure 4.3: Timeseries of kinetic energy and rate of energy dissipation of simulations F_1 (a), F_2 (b) and F_6 (c).

(*e.g.* Alvelius (1999),Wang *et al.* (2000)). The values in the table indicate that for well resolved turbulent conditions a value is observed in the same range, whereas for simulation F_4, the reported value is found outside this range.

4.4.2 Transient behaviour

A comparison of the evolution of the kinetic energy and the rate of energy dissipation of simulations F_1, F_2 and F_6 is given in figure 4.3. This figure shows the difference between controlled and uncontrolled forcing and the influence of forcing while using a true white noise forcing signal compared to a signal generated by using a limited number of forcing fields. At the start of the simulations the fluid was at rest. The initial slope of the simulations should therefore be equal to the power input P, since in the absence of dissipation, $dK/dt = P$ holds. This is indicated by the tangent line through the origin of the time series.

Figure 4.3 (c) shows that the initial slope of the kinetic energy is below the expected value while for the two other cases the initial energy increase has the expected behaviour. Using a limited number of force fields (F_6) results in a reduced power input. This is clear from the time series and from the somewhat lower rms velocity u'_*, given in table 4.2. Figure 4.3 further shows that the fluctuations in the kinetic energy and the rate of energy dissipation increase for simulations F_2 and F_6. The standard deviation in K

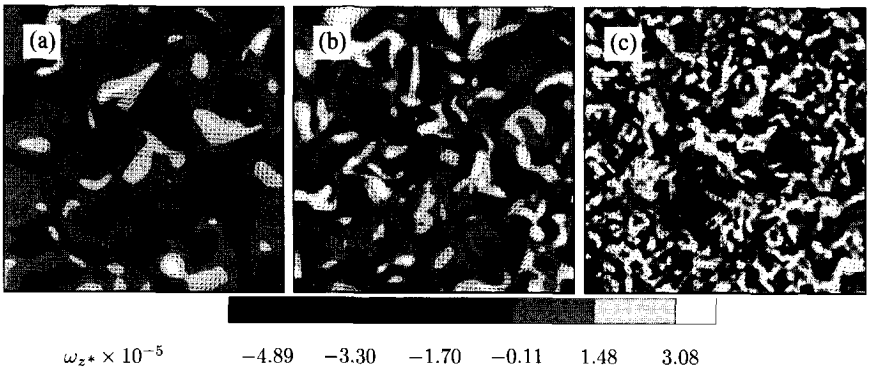

Figure 4.4: Cross section of the flow fields of simulations F_3 (a), F_1 (b) and F_4 (c). The contours indicate the vorticity component ω_z, perpendicular to the plotted plane.

(determined from the steady-state part of the time series) for these three simulations was 0.6, 3.2 and 4.8 % respectively.

One phenomenon that can be observed in figure 4.3 is that the evolution of the rate of energy dissipation follows that of the kinetic energy. Most kinetic energy is contained at the large scales. The turbulent flow field needs to develop before fluid motion reaches the length scales where dissipation takes place. The increase of the rate of energy dissipation therefore lags the development of the kinetic energy. An appropriate time scale for the transfer of kinetic energy (Pope (2000)) is $\frac{1}{10}T_e$ ($T_e = K/\epsilon$, the eddy turnover timescale). For the cases in figure 4.3, this time is $t_* = 0.1$.

4.4.3 Flow field and energy spectra

The energy spectra of figure 4.5 (a) show that with a decrease in Kolmogorov length scale (simulations F_3, F_1 and F_4), fluid motion is generated up to higher wavenumbers. This is also visible in the flow fields in figure 4.4. The spectra clearly indicate the appearance of an inertial subrange, characterised by the $-5/3$ slope (see equation 4.1).

In simulation F_4, the Kolmogorov length was smaller than the rule of thumb minimal value of 0.318 [lu]. The energy spectrum of simulation F_4 demonstrates that the energy content at the smallest scales has risen approximately 6 orders of magnitude. As a result, the gradients at the small length scales become too steep and although on the large scales the fluid motion still exhibits a physical behaviour, the fluid motion at the smallest scales is not accurately resolved, as can be observed from the spurious behaviour of the velocity vectors in the flow field. Although the simulation remains stable, the flow field of figure 4.4 (c) demonstrates that the numerical method breaks down at the small scales (also indicated by the value of ϵ/P and S_g in table 4.2).

The dissipation spectrum (figure 4.5 (b)) shows the shift of dissipation towards higher wave numbers when the Reynolds number is increased. For simulations F_3, F_1 and F_4, the power input and hence the total energy dissipation is identical. As a consequence, the

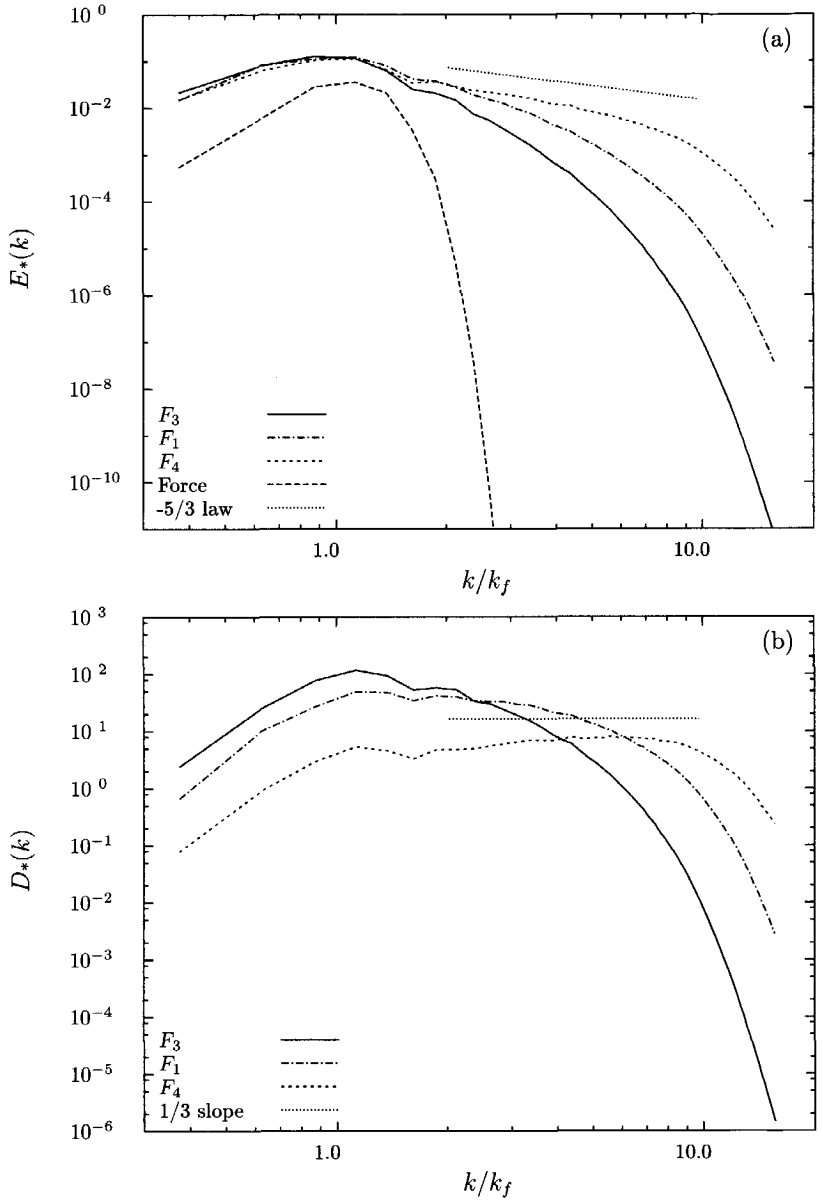

Figure 4.5: Normalised energy spectrum (a) and dissipation spectrum (b) for simulations F_3, F_1 and F_4 at increasing order of Reynolds number. ($E_*(k) = E(k)/({u_*}^2 l_*), D_*(k) = D(k) \times {l_*}^2/{u_*}^3$).

integrated value of the dissipation spectrum should be equal for these three simulations. For simulation F_3, the dissipation mainly occurs around $k/k_f = 1.0$, whereas for simulation F_4 dissipation extends to $k/k_f = 10.0$. Equation 4.26 contains the relation between ϵ, the dissipation spectrum and the energy spectrum. This relation indicates that the energy is weigthed with k^2, which stresses the constribution of the energy spectrum at larger wavenumbers in the resulting dissipation spectrum. In the inertial subrange, the dissipation spectrum should obtain a positive slope of $2 - 5/3 = 1/3$, which is indicated in the figure.

The influence of the forcing is clearly visible in the energy and the dissipation spectra. On the one hand, the use of 7 Fourier modes for forcing gives an accurate representation of the Gaussian distribution of the forcing intensity (see equation 4.10) which allows for the use of a large concentration parameter ($f_{nr} = 7, c = 1.0$). On the other hand, the effect is that the forcing dominates the energy spectrum and therefore the fluid motion over a larger range of wavenumbers. To overcome this behaviour, Alvelius (1999) uses a much smaller concentration parameter ($\mathcal{O}$ (0.01)), to concentrate the forcing spectrum around a single wavenumber k_f. In his results, the energy spectrum therefore exhibits a much more pronounced peak.

By using a larger number of discrete forcing wavenumbers and a larger concentration parameter, the power input is distributed more evenly over a wider range of wavenumbers than by choosing a small concentration parameter. The advantage of this is that the overall contribution of P_2 will decrease. The value of the fluctuating force $f_\alpha(\mathbf{k})$ will have a lower value at each discrete wavenumber, and hence the product of $u_\alpha(\mathbf{k})f_\alpha(\mathbf{k})$ will be smaller. If one intends to use the forcing scheme for uncontrolled simulations of turbulence, then in this way the contribution P_2 can also be suppressed. The disadvantage of this is that at the large wavenumbers, the energy spectrum of the turbulent flow is controlled over a wide range of wavenumbers, rather then being concetrated closely around the forcing wavenumber k_f.

The influence of the number of Fourier modes on the turbulent flow field is tested in simulation F_5 (see figure 4.6). This figure allows for a comparison between simulations F_5 and F_3, for which the same Kolmogorov length scale was set, and between F_5 and F_1, for which the same forcing Reynolds number was chosen. Table 4.2 indicates that the Taylor Reynolds number for simulations F_5 and F_1 are indeed of the same order. Since the Reynolds number is a measure for the ratio between the microscopic and macroscopic length scales, one would anticipate that the integral length scale between both simulations differs by a factor 2 (since $\eta_{F_1} = 0.5 \times \eta_{F_5}$), which is indeed the case (notice that the integral length scale in table 4.2 is normalised with $l*$ which also differs a factor 2).

A comparison of the recovered energy dissipation with the pre-defined power input indicates remarkably that $\epsilon/P > 1.0$ (see table 4.2). This is due to the poor representation of the Gaussian distribution of $F(k)$ over a limited range of 3 wave numbers. Due to the discretisation, the resulting power input P_1 was considerably larger than the desired power input ($P_1 = 1.154 \times P_{input}$). This discretisation error was negligible for all other simulations. An increase of 15 % in powerinput results only in a 4 % decrease in Kolmogorov length ($\eta \sim \epsilon^{-1/4}$). As a result, the small scale structure of the flow field of simulations F_3 and F_5 is comparable. This is consistent with the correspondence

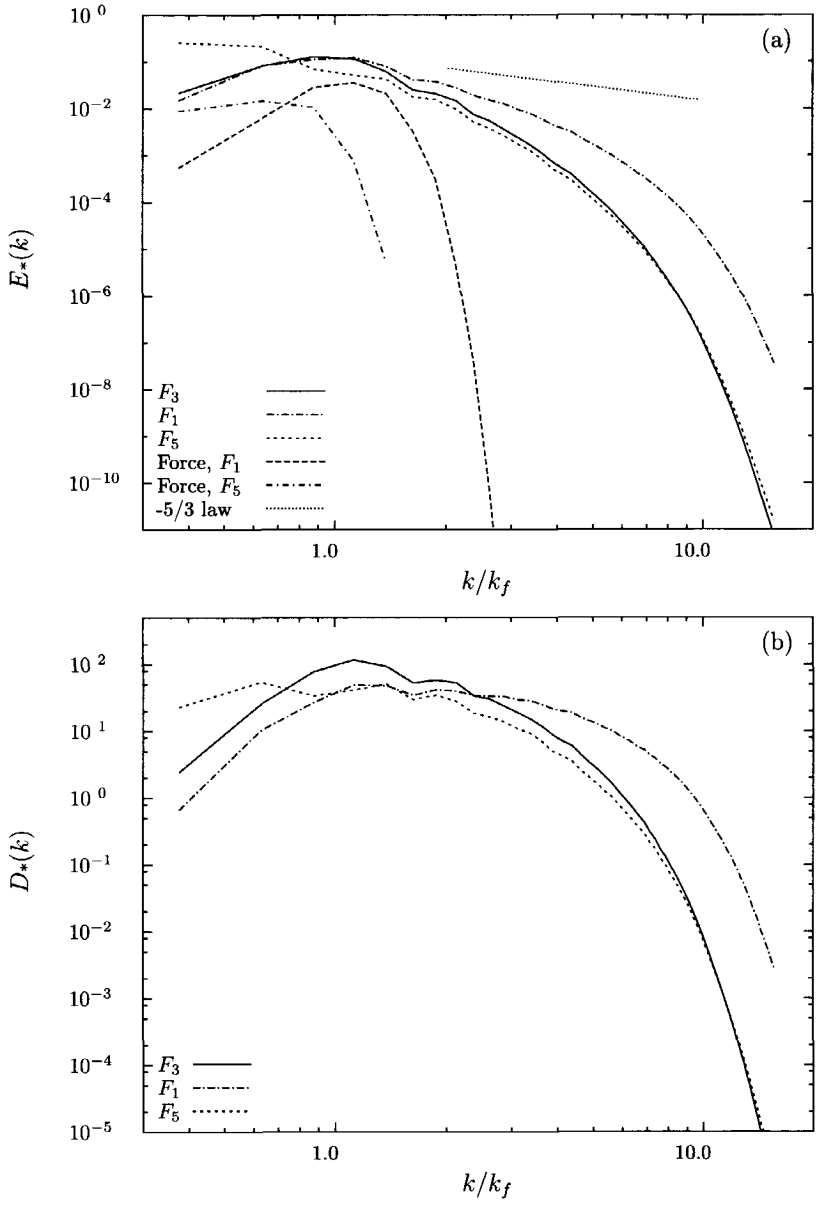

Figure 4.6: Normalised energy spectrum (a) and dissipation spectrum (b) for simulations F_3, F_1 and F_5 at order of increasing Reynolds number. ($E_*(k) = E(k)/(u_*{}^2 l_*), D_*(k) = D(k) \times l_*{}^2/u_*{}^3$).

between the two spectra at large wavenumber (figure 4.6): At large wave numbers both the energy and dissipation spectra of simulations F_3 and F_5 practically collapse.

4.4.4 Grid anisotropy and the correlation functions

For simulations F_1 and F_7, the longitudinal and transverse correlation functions, $f(r)$ and $g(r)$ respectively, are given in figure 4.7. The correlation functions are a measure for the velocity correlation over a separation r, parallel or perpendicular to the velocity component (see equations 5.21). In figure 4.7(a), these functions are plotted for simulation F_1 where the isotropic property of the simulation is tested by calculating the functions in two different ways, explained below.

Since the simulations are carried out on a cubic grid, the flow field and consequently the forcing is carried out in an inherently anisotropic domain. To test if this has any consequences for the directional character of the resulting flow field, the correlation functions were determined (i), through the Fourier transform of the velocity field and (ii) through sampling of the flow field via a large number of randomly placed sample points.

When determining the correlation functions via the Fourier transform, the velocity field is automatically aligned with the grid and anisotropic properties that may be present due to the grid are contained in the resulting correlation functions. For the second method, the velocity field was sampled with a large number of (100,000 per field) randomly placed points. The fluid velocity was computed at these points via first order interpolation. The correlation functions were then determined by calculating the correlation between all pairs of sample points. The orientation was based on an internal coordinate system, determined by the axis connecting each pair and two axes that are perpendicular to the connecting axis and to each other (see also section 5.5.3). By using random pairs of particles the orientation of the coordinate system is randomised for each pair. For a truly isotropic field and ideal interpolation, both methods should give the same $f(r)$ and $g(r)$.

For the major part the correlation functions of both approaches coincide which demonstrates that no gross anisotropy is present in the simulations. The deviations in the randomly determined correlation function at short separations may be a result of either the accuracy of the interpolation procedure or of the discretisation effect, since the correlation near zero separation was calculated from particle pairs that were separated at a distance on the order of the grid spacing or less. The longitudinal correlation reduces to zero and remains uncorrelated over large separations, as expected for turbulent flows. The interpolated transverse velocity correlation $g(r)$ obtains non-zero values at larger separation distances. This results from lack of statistical convergence, since the correlation function was only determined for a single flow field realisation. Ensemble averaging a number of independent flow field realisations should result in a convergence to zero.

The correlation functions presented in figure 4.7 (b) give the longitudinal and transverse correlation of the anisotropically forced simulation F_7. In this simulation the anisotropic forcing parameter b was set to a value of 10, indicating that the power input in the x- and y-directions was 11.2 times that of the z-direction. The longitudinal

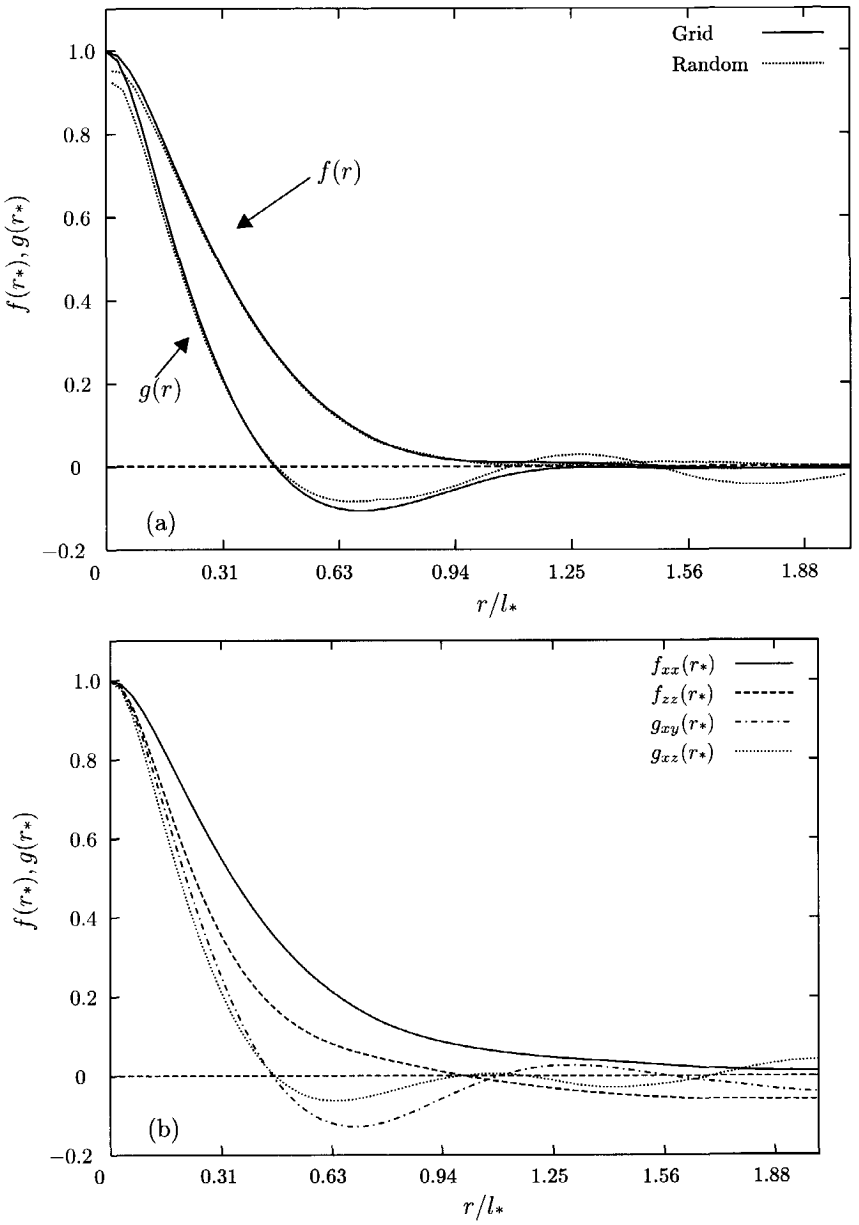

Figure 4.7: Normalised autocorrelation functions $f(r)$ and $g(r)$ of; (a) simulation F_1, where the correlation functions were determined via the Fourier transform of the velocity field (grid) and via random sample points (random); (b) simulation F_7, where the flow field is anisotropic. The correlation functions were determined from a single flow field realisation.

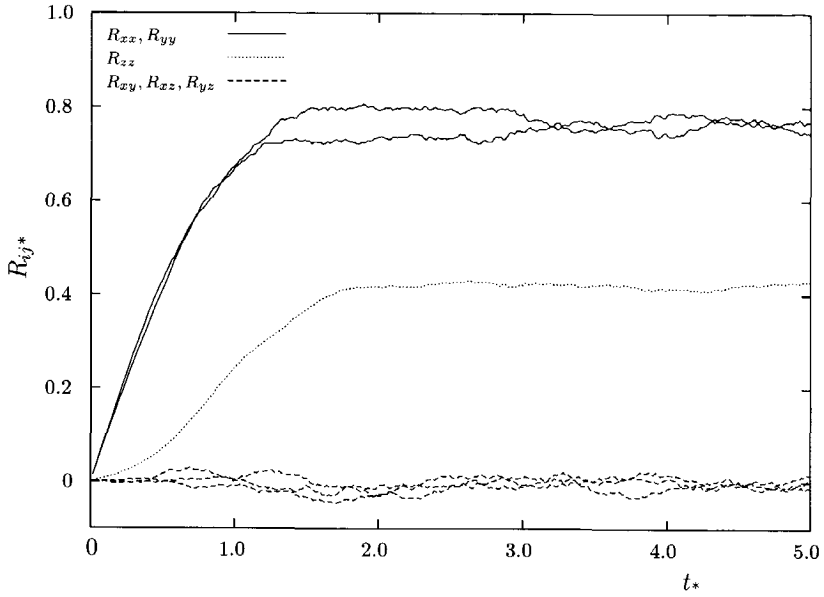

Figure 4.8: Timeseries of the normalised Reynolds stresses of simulation F_7.

correlation function f_{xx} describes the correlation of the x velocity component over a separation in the x direction while the transverse correlation function g_{xy} presents the correlation of the x velocity component over a separation in the y direction. The figure demonstrates that the f_{zz} correlation decays faster than f_{xx}. The correlation length scale Λ_{*f} gives a measure for the integral length scale over which the correlation drops to zero, comparable to the integral length scale Λ_{s^*}. It is anticipated that Λ_{*f} will be smaller in the z-direction than in the x- or y-direction since the integral length scales with u'^3 and u'_x or u'_y are larger than u'_z. This was confirmed by the values determined for $\Lambda_{*f_{xx}}$ as 0.459 and for $\Lambda_{*f_{zz}}$ as 0.274. No firm conclusions can be drawn with respect to g_{xy} and g_{xz}, since the correlation functions were obtained from a single flow field realization.

4.4.5 Axisymmetric anisotropic turbulence

The time-series of the Reynolds stresses $R_{ij}(= \overline{u_i u_j})$ of simulation F_7 (figure 4.8) show the evolution of the flow field of anisotropic forced turbulence. At startup, the value of the x- and y-components increase much faster than the z-component, as is anticipated. The fluid motion in the z direction gains momentum out of the $x-y$ plane once steady state is achieved, since the forcing is 11.3 times larger in the x-y plane, which should be compared to the steady-state ratio of a factor two, between R_{zz} and R_{xx} or R_{yy}. The off-diagonal components of R_{ij} fluctuate around zero.

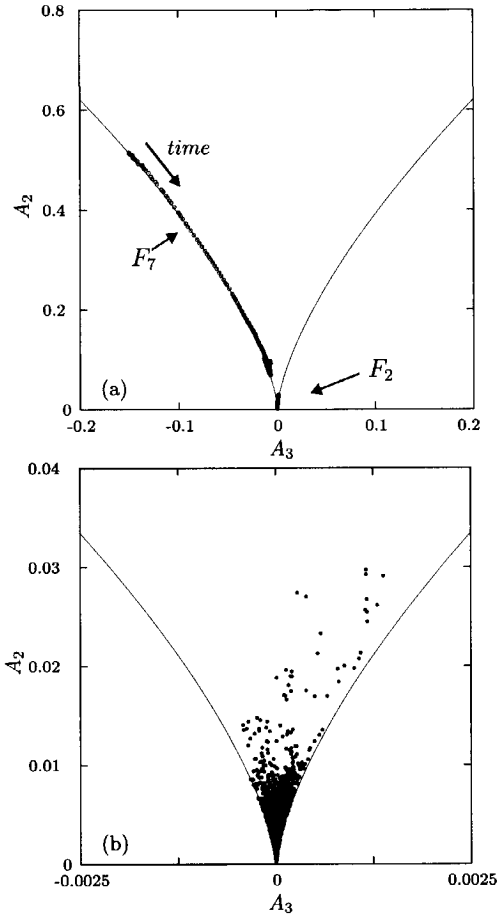

Figure 4.9: Invariants A_2 and A_3 calculated from the time series of the Reynolds stresses of simulations F_2 and F_7 (a). The lines indicate the position of the Lumley triangle. F_2 fluctuates close to zero, as indicated in the enlargement (b).

The anisotropy of a flow field is characterised by the anisotropy tensor a_{ij} that can be derived from the Reynolds stresses,

$$a_{ij} = \frac{R_{ij}}{K} - \frac{2}{3}\delta_{ij} \tag{4.28}$$

and its invariants. The first invariant of this tensor is zero by definition while the second and third invariant of this tensor are $A_2 = a_{ij}a_{ji}$ and $A_3 = a_{ij}a_{jk}a_{ki}$. For 3D isotropic flow, both invariants will also become zero. In figure 4.9, the values of the anisotropy invariants are plotted for the duration of simulations F_2 and F_7. Figure 4.9 (b) gives a detail of figure (a) which demonstrates that the invariants are indeed practically zero in the case of isotropic forcing.

With the definition of the anisotropic forcing parameters, P_x and P_y are defined equal and much larger than P_z. The resulting anisotropic flow is called axisymmetric turbulence. For this type of flow, the anisotropy tensor can be written as

$$a_{ij} = \begin{pmatrix} \alpha/2 & 0 & 0 \\ 0 & \alpha/2 & 0 \\ 0 & 0 & -\alpha \end{pmatrix}. \tag{4.29}$$

and the corresponding invariants can be expressed in terms of the parameter α. For $\alpha > 0$, the relation is given by $A_3 = -6(A_2/6)^{3/2}$, indicating that the kinetic energy in the symmetry plane exceeds that of the out-of-plane direction, while $A_3 = 6(A_2/6)^{3/2}$ is valid when the opposite holds, *i.e.* when $\alpha < 0$. These curves are plotted in the A_2 - A_3 plane of figure 4.9. The curves pose a limiting case for anisotropic conditions and represent the bottom corner of the so-called Lumley triangle (see also Lumley (1978) or Derksen *et al.* (1999)). Figure 4.9 (b) demonstrates that the invariants of the isotropic simulation F_2 are indeed bounded by the two branches of the Lumley triangle and are close to isotropy.

With R_{zz} being lower than R_{xx} or R_{yy} for simulation F_7, $\alpha > 0$ and the points in the $A_2 - A_3$ plane are accordingly found near or at the left branch of the Lumley triangle. This demonstrates that axisymmetric turbulence is obtained throughout the timeseries of the simulations. The average value of α was 0.237. The dots near the left line show the evolution of the anisotropy in the $A_2 - A_3$ plane. As already noticed, from startup of the simulation R_{zz} lags the steep increase of R_{xx} and R_{yy}. Consequently, the invariant A_3 starts at an initial value of -0.15 and proceeds in time to a steady state value of approximately -0.01.

4.5 Conclusion

In this chapter the application of a forcing scheme for the generation of sustained homogeneous turbulent conditions to a lattice-Boltzmann scheme was demonstrated. Using this forcing scheme, a turbulent flow field can be obtained with *a priori* defined turbulent conditions. The scheme describes the generation of a homogeneous body force that fluctuates as a white noise signal in time and on large length scales in space. The scheme contains a specifically advantageous feature which enables the control of the

power input by elimination of undesired fluctuations due to the velocity-force correlation. It is demonstrated that the scheme can also be used to obtain anisotropic turbulent conditions. It was further demonstrated that by straightforward implementation of the forcing scheme in the lattice-Boltzmann framework all specific features of the forcing scheme are recovered. The lattice-Boltzmann scheme proves to be an efficient method for precise direct numerical simulations of turbulence.

List of Symbols

Symbol	description	unit
a_{ij}	anisotropy tensor	–
A_{ran},B_{ran}	random forcing terms	$m\,s^{-2}$ or $lu\,ts^{-2}$
A_2,A_3	invariants of the anisotropy tensor	–
b	anisotropy control parameter	–
c_s	speed of sound	$lu,\ ts^{-1}$
$D(k)$	dissipation spectrum	$m^{-1},\ s^{-2}$ or $lu^{-1},\ ts^{-2}$
$e_{1\alpha},\ e_{2\alpha}$	orthogonal unit vectors	–
$E(k)$	kinetic energy spectrum	$m,\ s^{-2}$ or $lu,\ ts^{-2}$
f_α	body force vector	$m\,s^{-2}$ or $lu\,ts^{-2}$
f_{nr}	number of used Fourier modes	#
$f_ij(r)$, $g_ij(r)$	velocity autocorrelation functions	–
$F(k)$	power density function	$m\,s^{-2}$ or $lu\,ts^{-2}$
g_A,g_B	random functions	–
k	wave number	m^{-1} or lu^{-1}
k_a, k_b, k_f	forcing interval and max. wavenumber	m^{-1} or lu^{-1}
K	turbulent kinetic energy	$m^2\,s^{-2}$ or $lu^2\,ts^{-2}$
$l*$	forcing length scale	m or lu
$\mathcal{L}$	integral length scale	m or lu
n_x, n_y, n_z	number of gridpoints domain size	#
p	pressure	$kg\,m^{-1}\,s^{-2}$ or $M\,lu^{-1}\,ts^{-2}$
P	power input	$m^2\,s^{-3}$ or $lu^2\,ts^{-3}$
r	separation distance	m or lu
R_ij	Reynolds stresses	–
S_g	velocity derivative skewness	–
T_0	integral time scale	s or ts
T_e	eddy turnover time scale	s or ts
u	velocity	$m,\ s^{-1}$ or $lu,\ ts^{-1}$
u'	rms velocity of turbulent flow	lu/ts
$u*$	forcing velocity scale	$m,\ s^{-1}$ or $lu,\ ts^{-1}$
$\mathcal{U}$	integral velocity scale	$m,\ s^{-1}$ or $lu,\ ts^{-1}$

Greek	**description**	**unit**
Δt	time step	s or ts
ϵ	rate of energy dissipation	$m^2\,s^{-3}$ or $lu^2\,ts^{-3}$
$\phi,\ \theta_1,\ \theta_2$	random angles	–
η	Kolmogorov length scale	m or lu
Λ	integral length scale	m or lu
ν	kinematic viscosity	$m^2\,s^{-1}$ or $lu^2\,ts^{-1}$
ω	vorticity	s^{-1} or ts^{-1}
ρ	fluid density	kg/m^3 or M/lu^3

Dim. numbers	
Re_{force}	forcing Reynolds number
Re_λ	Taylor scale Reynolds number

Acronyms	
LES	Large Eddy Simulation

Chapter 5

Fully resolved simulations of colliding monodisperse spheres in forced isotropic turbulence

Fully resolved simulations of particles suspended in a sustained turbulent flow field are presented. For solution of the Navier-Stokes equation a lattice-Boltzmann scheme was used. A spectral forcing scheme is applied to maintain turbulent conditions at a Taylor Reynolds number of 61, based on the Taylor microscale. The parameter space ranged from 2 % to 10 % solids volume fraction and for the solid to fluid density ratio between 1.15 and 1.73. A lubrication force is used to account for sub-grid hydrodynamic interaction between approaching particles. Results are presented on the influence of the particle phase on the turbulence spectrum and on particle collisions.

The simulations show that the presence of the particles reduces the kinetic energy by facilitating the energy dissipation. Fluid motion is generated at length scales equal or smaller than the particle size, which results in a strong increase in the rate of energy dissipation at these length scales.

Collision data indicates that two separate collision mechanisms occur in the simulations. Collisions due to uncorrelated particle motion are observed (primary collisions), and collision frequencies are in agreement with theory on inertial particle collisions. In addition to this, also a large amount of collisions at high frequencies is encountered. These secondary collisions are due to the correlated motion of particles resulting from short range hydrodynamic interactions and due to spatial correlation of the turbulent velocity field at short distances. This view is supported by the distribution of relative particle velocities, the particle velocity correlation functions and the particle radial distribution function.

Key words: lattice-Boltzmann, suspensions, collisions, turbulence, DNS

This chapter has been submitted to J. Fluid Mech.

5.1 Introduction

In industrial processes where solid materials are produced or handled, often dense slurries are processed under highly turbulent conditions. Turbulence is required to maintain the slurry suspended and well mixed. While operating under such conditions, phenomena such as breakage, agglomeration and segregation can occur; they can be either desired or form potential problems in the operation of these processes (Zwietering (1958), Wibowo & Ng (2001)).

One example is industrial crystallisation, which deals with the production of solid crystals from a supersaturated liquid. In industrial crystallisation processes, the suspension typically contains between 5 and 20 vol % solids with an average particle size in the range of 100 to 1000 μm, with a solid to liquid density ratio in the range of 1 to 2.5. This class of processes is generally operated under highly turbulent conditions. The turbulence microscopic scale can be as small as 10 μm, which is typically one order of magnitude smaller than the mean crystal size (Ten Cate *et al.* (2001)). Phenomena occurring in crystallisation processes that are strongly dependent on the interaction between the particle phase and the turbulent flow field are agglomeration (Hollander *et al.* (2001)), abrasion and fracture (Gahn & Mersmann (1999*a*)). These phenomena have a strong influence on the performance of the crystallisation process and therefore on the product quality.

Since the particles are significantly larger than the Kolmogorov length scale and since the particle volume concentration in crystallisation systems is considerable, strong hydrodynamic interactions between particles and fluid motion and strong particle-particle interactions are anticipated. To gain insight into the behaviour of such suspensions, a simulation approach has been developed in which a number of freely moving particles is placed in a fully periodic domain. The flow field around each particle is resolved and predefined turbulent conditions are imposed by means of a spectral forcing technique. In this way simulations of a sustained turbulent suspension can be performed where full hydrodynamic coupling between the fluid and particle motion is obtained.

Direct simulations of suspensions have been pursued by a number of authors (see *e.g.* the review by Koch & Hill (2001)). Recent literature indicates that a versatile approach is based on the lattice-Boltzmann method (Chen & Doolen (1998)), which is a numerical method for solution of the Navier-Stokes equations on an equidistant cubic grid. In this type of simulations, a particle diameter occupies typically between 2 and 20 grid cells. The method was established and validated by Ladd (1994*a*,*b*). The method has been used in recent studies to simulate suspension problems for particles moving in the Stokes regime or at low but non-zero particle Reynolds numbers (*e.g.* sedimentation of large numbers of particles Ladd (1997, 2002), motion of spherical and non-spherical particles (Qi (1999), Aidun *et al.* (1998*a*), Ding & Aidun (2000)). Because of these promising results it was decided to use the lattice-Boltzmann method for our current study. However, the approach presented in this paper differs from the methods used by these authors on a number of points.

Firstly, a major difference is that in our approach the particles are moving in a fully turbulent flow field. To obtain meaningful statistical data, transient simulations are required that cover a sufficiently long time span with statistically stationary conditions.

A forcing scheme, developed by Alvelius (1999), is applied to the lattice-Boltzmann scheme to obtain a turbulent flow field with accurately defined conditions (turbulent kinetic energy K, turbulent Reynolds number, rate of energy dissipation ϵ).

Secondly, both the type of lattice-Boltzmann scheme and method to implement the no-slip particle boundary condition are different. The lattice-Boltzmann scheme used here is based on Eggels & Somers ((1995). Their approach explicitly treats the higher order terms of the lattice-Boltzmann equation, which improves the numerical stability of the scheme and allows the use of lower kinematic viscosities as compared to the standard BGK scheme, which is a desired feature for performing turbulent simulations. The technique to impose the boundary conditions is called the adaptive force-field technique. This method is used by Derksen & Van den Akker ((1999, 2000) in LES studies of the turbulent flow field in various applications. To our knowledge this approach has not yet been applied for simulating freely moving particles. However, based on the good results obtained with the LES, we had confidence that the adaptive force-field method could be used for suspension simulations at a relatively low spatial resolution per particle. Our previous study where simulations and PIV experiments of a single sphere settling under gravity were compared demonstrated that an accurate representation of the sphere's motion and the flow field it induced was obtained at relatively low resolutions (Ten Cate *et al.* (2002*b*)).

Thirdly, particles moving in a turbulent flow field can collide. In our simulations a collision detection algorithm (Chen *et al.* (1998*b*)) is used that deals with the fully elastic collisions. Further, as particles approach, a moment will occur where the separation becomes smaller than the grid spacing. The computational grid then lacks resolution to capture the details of the fluid motion in the gap between the particles and the repulsive force acting on the approaching particles will be under predicted. An analytical expression of the lubrication force is used, similar to Ladd (1997), to account for the lacking hydrodynamic forces. In the next section our numerical approach is presented in detail.

Our first results on turbulent suspension simulations have been reported in a previous study (Ten Cate *et al.* (2002*a*)). In that study the periodic domain consisted of 128^3 grid nodes. In the current study, the domain size spans 256^3 grid nodes to increase the separation of wavenumbers related to the integral length scale of turbulence, the particle diameter and the Kolmogorov length scale, and further to increase the number of particles per simulation to increase the quality of the statistical data.

A vast body of literature exists that discusses the interactions between suspended particles and a turbulent flow field. The main issues treated in these studies are the motion and collisions of particles due to the turbulent flow field and the modification of turbulence due to the presence of a second phase.

A theoretical basis for the collision rate of small particles (*i.e.* $d_p << \eta$, where d_p is the particle diameter and η the Kolmogorov length scale) suspended in a turbulent flow is provided by Saffman & Turner (1956), for the purpose of describing agglomeration of droplets in atmospheric flows. Theoretical extensions of this work were proposed by Yuu (1984) and Kruis & Kusters (1997) to improve the description of the particle motion in turbulent flow fields. Abrahamson (1975) presented a model to predict collision rates of particles with considerable inertia.

These models have been used to interpret the phenomena observed in a wide range of numerical studies on turbulent suspensions, where the particle phase is represented by particles that are much smaller than the resolution of the computational grid, and where Stokes drag is assumed to dominate the motion of the particles. Based on this approach, the collision rate of small particles in isotropic turbulence is studied extensively by Sundaram & Collins (1997) and later by Reade & Collins (2000) and Wang *et al.* (1998, 2000).

Theoretical models that describe the modification of the turbulent flow field due to the presence of particles have been presented by *e.g.* Felderhof & Ooms (1989); Ooms & Jansen (2000); Yuan & Michaelides (1992); Crowe (2000). Turbulence modification has also been studied via direct numerical simulations of isotropic turbulence where a two-way coupling between the fluid and the particle phase was present, examples of which are given by *e.g.* Squires & Eaton (1990), Elghobashi & Truesdell (1993) and Boivin *et al.* (1998).

We would like to stress that due to the application (*i.e.* industrial crystallisation), our focus has been on a different regime compared to the above citations. Our simulations were performed to study the behaviour of dense turbulent solid-liquid suspensions, where particles exhibit strong hydrodynamic interactions, while the particle size is larger than the Kolmogorov scale and the volume fraction amounted to 2 to 10 %. This requires that in our simulations the flow field associated with the particles is fully resolved.

In contrast with our approach, the above mentioned studies focus on systems where the particle size is much smaller than the Kolmogorov length while the volume fraction is of the order of 10^{-4} to 10^{-6}. In spite of the low volume fraction in these latter studies, the mass loading was considerable due to a relatively high particle to fluid density ratio. In our simulations, the density ratio was kept between 1.15 and 1.73. As a result, the mass loading in our simulations is of the same order as in the above mentioned studies.

Although the regime in our simulation is much different from that in the above studies, some of the concepts used in or obtained from these studies are used in this paper for qualitative comparison and discussion of the trends in our results. The objectives of this paper are;

- presentation of our method for simulation of fully resolved dense suspensions
- demonstration of the use of a spectral forcing scheme in lattice-Boltzmann simulations for generation of sustained turbulence with pre-defined conditions
- discussion of the modification of the turbulent energy spectrum under influence of suspended particles
- interpretation of the collision behaviour and the relative particle motion observed in dense turbulent solid-liquid suspensions

These objectives are reflected in the organisation of the paper; after the presentation of our numerical approach, the settings and results on a single phase isotropic turbulent simulation are presented in section 5.3. The same turbulent conditions are used the suspension simulations presented in section 5.4, where the influence of the particle phase on the turbulent fluid kinetic energy spectra is discussed, and in section 5.5, where a

detailed discussion is given on the behaviour of the particle phase in our simulations. The latter discussion is based on the theoretical framework presented by Wang *et al.* (2000) and Reade & Collins (2000) and focusses on phenomena such as the influence of the turbulent flow field and the short range hydrodynamic interactions on the distribution of relative velocities, particle accumulation effects and particle collision rates. The paper ends with conclusions in section 5.6.

5.2 Setup of the Direct Numerical Simulation

5.2.1 The lattice-Boltzmann method

A lattice-Boltzmann scheme has been used for simulation of the fluid flow. This scheme is based on a microscopic model for fluid behaviour. where the rules for the update of the fluid velocities are handled locally on the grid nodes. An advantageous property of the lattice-Boltzmann scheme is that it performs excellent on parallel computers, since it only involves localized operations.

The fluid is represented by mass that propagates at discrete time steps on an equidistant grid (lattice). Collision rules that guarantee conservation of mass and momentum are applied on the mass arriving at a grid node. This process is represented by the lattice-Boltzmann equation (LBE)

$$n_i(\mathbf{x}+\mathbf{c}_i, t+1) = n_i(\mathbf{x}, t) + \Gamma_i(\mathbf{n}). \tag{5.1}$$

Due to collision an amount mass n_i, aligned in the direction $\mathbf{c}_i$ (with $i = 1, M$) at position $\mathbf{x}$ and time t, is updated with an amount Γ_i after which it propagates to the position $\mathbf{x}+\mathbf{c}_i$ at the next time step. Here, $\mathbf{c}_i$ is the set of discrete velocities with which mass moves on the grid, and Γ_i is the collision operator that depends on all masses, *i.e.* the vector $\mathbf{n}$, involved in the collision step. In the lattice-Boltzmann scheme all properties are defined in lattice units for length $[lu]$, time steps $[ts]$ and arbitrary units of mass $[m]$.

Different approaches have been employed to solve equation 5.1 (see *e.g.* Ladd (1994*a*), Chen & Doolen (1998), Rothman & Zaleski (1997)). In this work we use a scheme developed by Eggels & Somers ((1995). With this scheme the following continuity and momentum equation for the fluid are recovered

$$\frac{\partial \rho}{\partial t} + \nabla \cdot \rho \mathbf{u} = 0 \tag{5.2}$$

$$\frac{\partial \rho \mathbf{u}}{\partial t} + \nabla \cdot \rho \mathbf{u}\mathbf{u} = -\nabla p + \nabla \cdot \rho\nu[\nabla \mathbf{u} + (\nabla \mathbf{u})^T] - \nabla(\frac{1}{2}\rho\nu\nabla \cdot \mathbf{u}) + \mathbf{F} \tag{5.3}$$

where $p(\mathbf{x}, t)$ is the pressure and ν is the kinematic fluid viscosity. In the limit of low Mach numbers (*i.e.* $\mathbf{u} << c_s$, the speed of sound of the lattice-Boltzmann scheme), the above set of equations represents the continuity and Navier-Stokes equations for incompressible flow. The body force $\mathbf{F}(\mathbf{x}, t)$ in equation 5.3 is used in our simulations for two goals. Firstly, it is used for the generation of sustained turbulent conditions and secondly, it is used for the implementation of the particle boundary conditions.

5.2.2 Turbulence Forcing

In a typical turbulent flow, kinetic energy is produced at large scales, and dissipated at the small scales. By forcing the fluid at small wave numbers, the fluid is set in motion at large length scales. At sufficiently large Reynolds numbers, *i.e.* at a sufficiently large separation between production and dissipation scales, the small scale structure exhibits universal characteristics of turbulent fluid motion independently of the means of power input. Schemes for forcing turbulent conditions have been developed by a number of authors, *e.g.* Eswaran & Pope (1988), and more recently by Overholt & Pope (1998) and Alvelius (1999).

For application of these schemes in numerical simulations, (pseudo) spectral methods for the solution of the Navier-Stokes equations are the natural choice, since such numerical schemes are defined in wavenumber space, as is the forcing scheme. However, the forcing scheme is not necessarily associated with spectral methods. In our work we use the algorithm developed by Alvelius (1999) for forcing the flow in the lattice-Boltzmann scheme. The turbulent forcing signal is generated in Fourier space and, after computing the inverse Fourier transform, is applied in the physical domain (*i.e.* in equation 5.3 via the body force $\mathbf{F}(\mathbf{x}, t)$). The force is defined as a divergence free white noise signal, fluctuating randomly in time and space. The white noise character assures that the forcing signal is uncorrelated with any time scale of the turbulent flow field. Alvelius shows that during one discrete time step, the volume averaged power input P is the sum of two contributions,

$$P = P_1 + P_2 = \frac{1}{2}\overline{f_k f_k}\ \Delta t + \overline{f_k u_k} \tag{5.4}$$

($F_k \equiv \rho f_k$) which are the force-force correlation and the velocity-force correlation respectively, and where the overbar indicates volume-averaging. The force is placed in the discrete Fourier space in a cubic cell with sides f_{nr}. The forcing intensity is distributed over the wavenumbers as a Gaussian distribution, active on the interval $[k_a, k_b]$, with the maximum intensity at a desired wavenumber k_f (see figure 5.1).

The power input P_1 is fixed via the Gaussian distribution of the force in Fourier space. P_2 introduces an uncontrolled power input that influences the turbulent kinetic energy and can generate substantial fluctuations. The method of Alvelius (1999) allows to choose the force such that the contribution of P_2 is zero at each time step. This results in a much smoother time development of the turbulent kinetic energy. Using this option requires the Fourier transform of the velocity field every time step. It was not used in the study because of this additional computational cost.

Alvelius chose the distribution of the power input to be narrowly concentrated around the forcing wavenumber k_f, which can cause the total power input to rise up to 1.5 times P_1. In the simulations presented in this chapter we chose to distribute the power input more evenly over the wavenumbers in the forcing interval $[k_a, k_b]$ by increasing variance of the Gaussian distribution. This is controlled by a concentration parameter c, which was set to 1.0 in our current simulation, as opposed to the value of 0.01 that is used by Alvelius (1999) (also see equation 4.10). In this way we found that the large increase in power input due to P_2 could be effectively suppressed.

For a further enhancement of the computational efficiency, rather than generating a

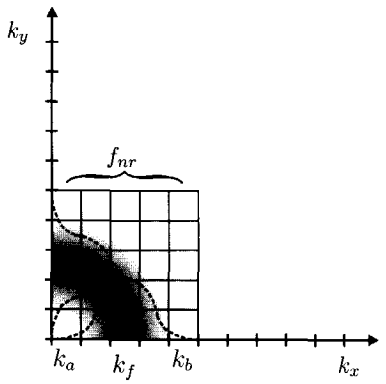

Figure 5.1: 2D representation of the forcing distribution in the Fourier domain. Dotted curves indicate the Gaussian distribution along the x and y axis, the contour indicates the Gaussian distribution in the 2D plane.

new force field each time step, 120 force fields were generated prior to the simulations. These were imposed on the fluid domain in random order during the simulations. In this way, a forcing signal that sufficiently resembled a white noise signal was generated.

5.2.3 Solid particle boundary conditions

Development of accurate (moving) boundary condition methods is an ongoing field of research in lattice-Boltzmann techniques. In the work presented by Ladd (1994*a*), a bounce-back approach is applied for the moving no-slip boundary condition at the surface of solid particles. In this approach fluid mass that propagates on a link that crosses the surface of the particle bounces back halfway between the grid nodes and returns towards the bulk fluid domain. The momentum change at bounce-back is associated with the hydrodynamic force acting on the particle. With this type of boundary conditions, curved objects will become staircase shaped, due to the discrete cut of the links between nodes on the cubic grid. A number of adaptations of the bounce back technique have been suggested to improve the representation of curved boundaries (*e.g.* Chen *et al.* (1998*a*); Rohde *et al.* (2002); Mei *et al.* (1999); Verberg & Ladd (2002); Bouzidi *et al.* (2001)).

The bounce back type boundary condition is applied in most lattice-Boltzmann studies of suspended particles (*e.g.* Ladd (1994*a*,*b*), Behrend (1995), Qi (1999), Aidun *et al.* (1998*a*)). In contrast to these studies, we use a forcing scheme to implement the moving no-slip boundary condition. Our approach is derived from a forcing scheme that was originally applied in spectral codes (Goldstein *et al.* (1993)) and was adapted for the lattice-Boltzmann method (Derksen & Van den Akker ((1999)).

The sphere surface is represented by a set of control points, placed at the sphere's surface, evenly spaced at a distance, somewhat smaller than the grid spacing (see figure 5.2). At each control point, the surrounding fluid velocity is forced to the surface velocity

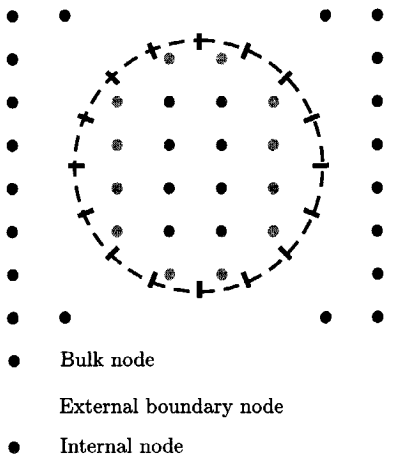

Figure 5.2: Representation of a sphere on a cubic grid. The cross-hairs indicate control points at the sphere surface.

of the sphere. The fluid velocity at a control point is determined via first-order Lagrange interpolation of the velocity from the surrounding grid nodes. For a freely moving sphere, the surface velocity ($\mathbf{u}_s$) is given by sum of the translational and rotational velocity components

$$\mathbf{u}_s = \mathbf{u}_p + \mathbf{\Omega}_p \times \mathbf{r}_p \tag{5.5}$$

where $\mathbf{u}_p$ is the translational velocity of the control point, which is identical to that of the particle, $\mathbf{r}_p$ is the position of the control point relative to the center of the sphere ($\mathbf{r}_p = \mathbf{x}_p - \mathbf{x}_c$) and $\mathbf{\Omega}_p$ is the angular velocity of the particle. The deviation between the desired surface velocity $\mathbf{u}_s$ and the interpolated fluid velocity $\mathbf{u}$ is used to update the force that is applied to the fluid. This deviation is calculated by

$$\mathbf{d} = \mathbf{u}_s - \sum_j I(\mathbf{r}_j)\mathbf{u}_j \tag{5.6}$$

where $\mathbf{u}_j$ is the fluid velocity at grid node j and $I(\mathbf{r}_j)$ is the set of interpolation coefficients, which is a function of the position $\mathbf{r}_j$ of the control point with respect to the surrounding grid nodes. The same interpolation coefficients are used for projecting the force from the control point onto the surrounding grid nodes, where the forces $\mathbf{F}_j$ acting at grid node j are updated through a relaxation scheme

$$\mathbf{F}_j(\mathbf{x}, t) = \alpha \mathbf{F}_j(\mathbf{x}, t-1) + \beta I(\mathbf{r}_j)\rho \mathbf{d}. \tag{5.7}$$

The scheme of equation 5.7 that imposes locally the desired boundary condition is a control scheme that is characterised by the relaxation parameters α and β. The scheme adjusts the imposed body force $\vec{F}_j(\mathbf{x}, t)$ proportional to the deviation of the local velocity. The dynamic action, accuracy, and stability of the control scheme are determined by the

relaxation parameters and the topology of the control points. The parameters α and β were determined empirically as 0.95 and 1.8 respectively.

After updating the forces at the grid nodes, the hydrodynamic force and torque on the sphere are calculated with

$$\mathbf{F}_p = \sum_j \mathbf{F}_j(\mathbf{x}, t) \tag{5.8}$$

$$\mathbf{T}_p = \sum_j \mathbf{r}_p \times \mathbf{F}_j(\mathbf{x}, t) \tag{5.9}$$

The summation is over all boundary nodes, both inside and outside of the sphere.

5.2.4 Internal fluid nodes

The adaptive force-field scheme requires fluid mass on the grid nodes occupied by the solid object (also indicated in figure 5.2). An advantage of this is that when a node shifts from the inside of an object into the exterior, it already contains fluid mass and the state of the node does not need to be changed. As a result, the scheme will be inherently mass-conservative. For these reasons Ladd (1994*b*) also keeps internal fluid in the particles. One drawback is that the internal fluid inertia influences the motion of the sphere via a contribution to $\mathbf{F}_p$ and $\mathbf{T}_p$ (see Eqs. 5.8 and 5.9), which requires a correction procedure.

This problem has been recognised by a number of authors who have suggested different approaches to solve it. Ladd (1994*b*) suggests to integrate the equation of motion with an effective particle mass. This is a fair approximation for systems with large solid/fluid density ratios but for solid particles in liquid with a density ratio typically between 1 and 2, numerical instabilities may occur when integrating the equation of motion this way. Other authors have proposed methods to remove the internal mass, *e.g.* Aidun & Lu (1995), Aidun *et al.* (1998*a*) and Heemels (1999), but these can not be applied in combination with the adaptive force-field technique. Qi (1999) allows particles to have internal mass but adds a force term (similar to Aidun *et al.* (1998*a*)) when computing the hydrodynamic force on the particle, to compensate for non-physical fluctuations in the hydrodynamic force $\mathbf{F}_p$ that arise from nodes entering or leaving the interior of a particle.

We propose the following straightforward correction procedure to compensate for the contribution of the inertia of the internal fluid. The force applied to the fluid nodes for implementation of the boundary condition influences the fluid both on the inside and the outside of the sphere. Hence, the total force that acts on the sphere, as calculated with equation 5.8, is a sum of the internal and external contribution to the force:

$$\mathbf{F}_{p,tot} = \mathbf{F}_{p,int} + \mathbf{F}_{p,ext} \tag{5.10}$$

When integrating the equation of motion, the only physical contribution to the sphere's motion is due to $\mathbf{F}_{p,ext}$. To estimate the internal contribution $\mathbf{F}_{p,int}$, we calculate the change in momentum of the internal fluid between two successive time steps,

$$\mathbf{F}(t)_{p,int} = \iiint_{V_{sphere}} \{\rho \mathbf{u}_{int}(\mathbf{x}, t) - \rho \mathbf{u}_{int}(\mathbf{x}, t-1)\}\ dV. \tag{5.11}$$

$\mathbf{F}_{p,ext}$ is then determined by subtracting $\mathbf{F}_{p,int}$ from the total force $\mathbf{F}_{p,tot}$. A similar procedure is applied for the torque. With this approach, the correct physical behaviour is obtained. This has been demonstrated in a study on the sedimentation of a single sphere in a closed container (Ten Cate *et al.* (2002*b*)).

5.2.5 Hydrodynamic radius

The next important issue that should be addressed when performing suspension simulations is the effective radius at which a particle is implemented. By placing a sphere on a cubic grid, the shape is approximated by imposing the boundary condition of the sphere surface on the grid. When applying the bounce back method, the no-slip condition is assumed to be present half way between two grid nodes and the sphere becomes staircase shaped. The resulting drag force that acts on the sphere is different from the drag force on a perfectly smooth sphere. In the adaptive force-field approach a similar effect occurs. The boundary is imposed by placing a force on the grid nodes via an interpolation-extrapolation procedure that extends outside of the exact location of the sphere surface and here the measured drag force also differs from the force on an ideal sphere.

Ladd (1994*b*) compared simulations on a sphere in a fully periodic array of spheres with the analytical solution of this problem (Hasimoto (1959)). Ladd (1994*b*) suggested to use the analytical solution as a calibration method, by calculating an effective sphere radius (hereafter called *hydrodynamic radius*) based on the drag force obtained from simulation. This approach demonstrated that the hydrodynamic radius varies with viscosity in a non-physical manner, on the order of 0.5 to 1 lattice spacing.

This non-physical dependency of the drag force is also reported by Rohde *et al.* (2002), who performed simulations with an improved bounce back boundary scheme. A reason for this dependency may be given by He *et al.* (1997), who demonstrated analytically that in bounce back methods for lattice-Boltzmann schemes, the exact location of the no-slip condition is a function of viscosity. However, it is not only an artifact of bounce back type boundary conditions, since a similar dependency is also observed with our adaptive force-field approach.

For particles with large input radii, a variation in the effective radius of the order of 0.5 to 1.0 grid spacing is not of great importance. However, if one seeks to perform simulations at a relatively low resolution, a calibration of the hydrodynamic radius is required. This has been demonstrated in our previous study where the simulated motion of a single settling sphere was compared with experimental data (Ten Cate *et al.* (2002*b*)). We found that by calibrating the particle radius via the analytical expression of Hasimoto (1959), the transient settling behaviour of a single sphere settling in a closed tank could be predicted at an accuracy of approximately 1 to 5 %. Although the calibration is performed in the creeping flow regime, as required by the analytical expression, the sedimentation experiment was done at Reynolds numbers between 1.5 and 32. We therefore view that the calibration procedure offers a reasonable method to estimate the inaccuracy of the boundary condition, even when the particles in the actual case are simulated at non-zero Reynolds numbers.

5.2.6 Short range interactions

An important situation occurs when two suspended particles approach towards close proximity. For real suspended particles, the fluid that is squeezed out of the gap between approaching particles will induce a strong repulsive hydrodynamic force on the particles. Conversely, as the particles separate, the gap must be filled with fluid again and the force will become attractive. These hydrodynamic effects can have a strong influence on the behaviour of solid/liquid suspensions and require an accurate treatment in suspension simulations.

In our simulations the flow field surrounding the particles is simulated explicitly and hydrodynamic interactions between particles are inherently present. However, as two particles approach, one should guarantee that hydrodynamic effects at short distances are present, and one should take care that particles may collide. For the latter we use an efficient collision detection algorithm in our simulations according to Chen *et al.* (1998*b*) to prevent that particles will overlap and to detect and registrate particle-particle collisions.

The application of a collision detection algorithm alone is not sufficient. For two approaching particles moving on a cubic grid, a moment will occur where the gap s between the particles becomes too small to be resolved by the computational grid. As a result, the hydrodynamic force that acts on the particles due to the squeezing of the interstitial fluid will be under predicted. This effect was recognised by Ladd (1997), who proposed to calculate the hydrodynamic forces explicitly, using the leading order term of the analytic expression for the lubrication force (*e.g.* Kim & Karrila (1991); Crowe *et al.* (1997)). This force is calculated for particles that have reached a distance smaller than Δ_0 (set to two lattice spacings in our simulations), as given by

$$\mathbf{F}_{ij}^{lub} = \frac{-3\pi\rho\nu r_p^2}{2}\left(\frac{1}{s} - \frac{1}{\Delta_0}\right)\widehat{\mathbf{x}}_{ij}\widehat{\mathbf{x}}_{ij}\cdot(\mathbf{u}_i - \mathbf{u}_j) \tag{5.12}$$

where s is the width of the gap between particles i and j, $\mathbf{u}_i$ and $\mathbf{u}_j$ are the particle velocities and $\widehat{\mathbf{x}}_{\mathbf{ij}} = (\mathbf{x}_i - \mathbf{x}_j)/\mid \mathbf{x}_i - \mathbf{x}_j \mid$ is the vector with unit length connecting the centers of the two particles.

Ladd & Verberg (2001) chose to implement the lubrication force according to equation 5.12 on a particle pair-wise basis. In our simulations the implementation of this force was done in the following way. First, the force acting on grid nodes where particle boundary force contributions overlap is treated. The adaptive force-field method for the boundary conditions extrapolates forces to the grid extending outside of the particle. When two particles approach, both particles may impose forces on the same grid nodes inbetween the particles. Since the resulting force on these grid nodes can not be identified with any of the two particles in particular, the force acting on these grid nodes is set to zero.

Second, the lubrication force acting on each particle is calculated by means of equation 5.12. In suspensions at high volume concentrations a particle may have multiple interactions with a number of surrounding particles. Therefore, the lubrication forces are calculated for the interaction between each particle and all of its neighbouring particles each time step.

Third, combining lubrication forces with the collision algorithm requires special attention. When both are active, particle pairs can become trapped in an unphysical pair-wise oscillating motion. This behaviour is an artifact due to time discretisation. At collision, the axial velocity component of the colliding spheres is reversed and the spheres are separated by the remaining part of their post collision trajectory. At high temporal resolution, this will be a small separation, which in the following time step may give rise to a very large lubrication force, that has becomes attractive instead of repulsive, because of the reversed axial velocity component. The attractive force can become so large that it reverses the particle velocities and brings them together again. In the following time step the particles will collide again and so on.

This is prevented in our simulations by setting the lubrication force to zero for particles that can travel the gap s between the particle pair in one time step and are about to collide (notice that in lattice-Boltzmann simulations the time step has a value 1),

$$\begin{array}{ll} \mathbf{F}_{ij} = \mathbf{F}_{ij}^{lub} & s > |(\mathbf{u}_i - \mathbf{u}_j)| \\ \mathbf{F}_{ij} = 0 & s \leq |(\mathbf{u}_i - \mathbf{u}_j)| \end{array} \tag{5.13}$$

In this way, the lubrication is also turned on again after collision, when particles are separated a distance that is comparable to their separating velocity.

One should also realise that application of the analytical expression of the lubrication force has its limitations. According to this theory (Eq. 5.12) the motion of two particle approaching at a certain initial velocity will be fully dissipated and particles will always come to a halt at a finite separation. Experiments, however, indicate that particles suspended in a liquid will rebound when bouncing with a bottom (Gondret *et al.* (1999, 2002)) or with a vertical wall (Joseph *et al.* (2001)). The limitations of lubrication theory are owed to the break down of the lubrication model when the gap becomes of the order of the particle surface roughness or of the order of the molecular mean free path (Sundararajakumar & Koch (1996)). Furthermore, in a true suspension, inertial particles may collide because forces may act on the suspended particles due to *e.g.* gravity or velocity gradients in the flow field that can push particles together and enforce contact. In previous work on the simulation of a single settling sphere (Ten Cate *et al.* (2002*b*)) it was observed that application of a lubrication force adds a repulsive force which improves the description of the wall approach, but postpones the moment of contact between the particle and the bottom wall for an unrealistically long time.

5.3 Single phase isotropic forced turbulence

5.3.1 Definition of turbulent conditions

Homogeneous, isotropic turbulent conditions are imposed on a computational grid with a size of 256^3 nodes and periodic boundary conditions. The turbulent flow field is characterised by a number of *a priori* defined input parameters which are given in table 5.1 together with a number of turbulence characteristics. The forcing is defined by setting a characteristic root mean square velocity (v'_*) and a characteristic forcing length scale l_*. The rms velocity was chosen as 0.02 because the lattice-Boltzmann scheme requires

Input parameters	Value
n_x, n_y, n_z	256
n_t	40000
v'_*	0.02
l_*	128
f_{nr}	3
k_f	0.049
$P_{input} \times 10^8$	6.25
$P_1 \times 10^8$	7.19
η	1.2
$\nu \times 10^3$	5.06

Table 5.1: Parameter settings for the single phase turbulent simulations

velocities to remain well below the speed of sound ($c_s = \frac{1}{2}\sqrt{2}$ in the scheme used) to obey the demand of low Mach numbers for incompressible flow. The central forcing wavenumber determines the forcing length scale: $k_f = 2\pi/l_*$. The forcing length scale was set to $l_* = n_x/2$. The power input is determined by the equilibrium between production and dissipation, resulting in $P_{input} = v'^3_*/l_*$. In table 5.1 P_{input} is given, together with the effective power input P_1, as calculated with equation 5.4. The deviation results from the error made in discretising the power input on a cube in the Fourier domain with sides of three points.

The chioce for the Kolmogorov length scale determines the value of the kinematic viscosity. In a statistical equilibrium, the rate of energy dissipation balances the power input, *i.e.* $P = \epsilon$ and the Kolmogorov length and time scales are set *a priori* via; $\eta = (\nu^3/\epsilon)^{\frac{1}{4}}$ and $\tau_k = (\nu/\epsilon)^{\frac{1}{2}}$. The Kolmogorov length scale was carefully chosen as 1.2 $\lceil lu \rceil$ after a number of considerations: (i) we would like to obtain a clear separation of length scales between the microscopic length scale η, the particle size d_p and the integral scale of the turbulence Λ, (ii) in a DNS of turbulence the rule-of-thumb $k_{max}\eta > 1$ warrants sufficient resolution, where k_{max} is the maximum resolved wavenumber ($k_{max} = \pi/\Delta$, with $\Delta = 1$, the lattice spacing), and (iii) the uncontrolled contribution of P_2 to the power input can result in strong local velocity fluctuations or velocity gradients. Therefore, $\eta = 1.2$ was a conservative choice to stay well away from the minimum resolution demand and assure full resolution of the turbulent suspension simulations.

5.3.2 Results of single phase turbulence

In table 5.2, a number of properties is presented that characterise the turbulent flow simulations. The parameters are presented in two columns to distinguish between values calculated directly from the velocity field and values obtained via the energy spectrum $E(k)$, which is computed by means of the Fourier transform of the velocity field. Flow field data was stored every 4000 time steps (approximately 2 integral time scales) and the figures in the table were determined by averaging over 10 independent flow field realisations.

Property	Flow field	Via $E(k)$
$K \times 10^4$	4.28	4.28
u'	0.017	0.017
$\epsilon \times 10^8$	6.48	6.42
η	1.19	1.20
η_{min}	0.45	
τ_k	279	283
λ	18.27	18.38
Re_λ	60.98	61.22
Scale	Λ_i	T_i
Λ_K,T_K	74.28	6598
Λ_E,T_E	37.71	2245
Λ_f,T_f	42.47	2515
Λ_g,T_g	22.17	1313

Table 5.2: Turbulence properties from the single phase simulation.

The volume and time averaged turbulent kinetic energy K and turbulence intensity u' are calculated from the flow field and the energy spectrum $E(k)$ with

$$K = \frac{3}{2}u'^2 \equiv \frac{1}{2}\overline{\mathbf{u}\cdot\mathbf{u}} \equiv \int_0^{k_{max}} E(k)dk. \tag{5.14}$$

The values, obtained from the velocity field and the energy spectrum, are equal by definition.

Since the deformation rate tensor is inherently contained in the lattice-Boltzmann scheme (Eggels & Somers ((1995)), the rate of energy dissipation can be determined directly using this tensor (*i.e.* no spatial differentiation of the velocity field is required). Alternatively, the rate of energy dissipation can be calculated from the dissipation spectrum:

$$\epsilon \equiv \nu\overline{\left(\frac{\partial u_i}{\partial x_j} + \frac{\partial u_j}{\partial x_i}\right)\frac{\partial u_j}{\partial x_i}} \equiv 2\nu\int_0^{k_{max}} k^2 E(k)dk \tag{5.15}$$

The two values for the rate of energy dissipation in the table only differ 1 %, indicating that the deformation rate contained in the lattice-Boltzmann scheme is consistent with the velocity field. The values of η indicate that the input Kolmogorov length scale is recovered well. The minimum Kolmogorov length as encountered in instantaneous realisations of the flow field can be regarded as a measure for the lowest resolution in the simulations. This parameter still satisfies the $k_{max}\eta > 1$ constraint, which warrants the quality of the DNS.

In isotropic turbulence simulations, the flow is often characterised using the Taylor microscale and the corresponding Reynolds number,

$$\lambda \equiv \left(\frac{15\nu u'^2}{\epsilon}\right)^{\frac{1}{2}} \tag{5.16}$$

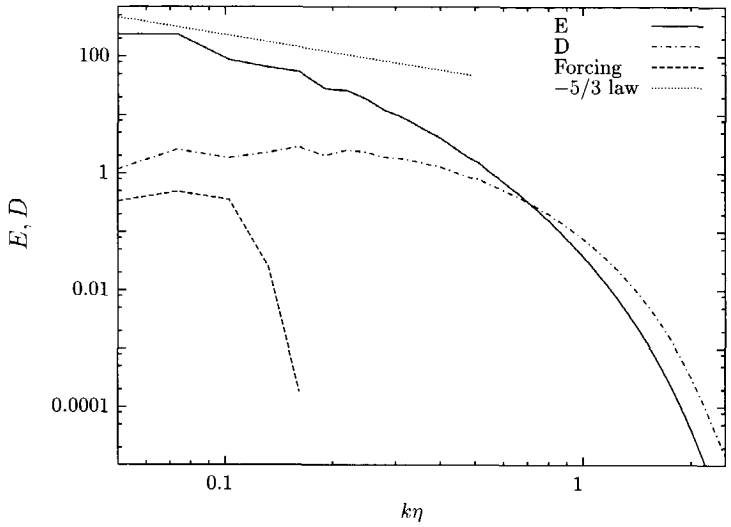

Figure 5.3: Scaled turbulent kinetic energy ($E = E(k)/(\epsilon^{2/3}\eta^{5/3})$) and dissipation ($D = 2\nu k^2 E(k)/(\epsilon\eta)$) spectra. 'Forcing' indicates the position of the forcing spectrum and is not on scale. $-5/3$ law indicates the spectral decay associated with the inertial subrange.

and

$$Re_\lambda \equiv \frac{u'\lambda}{\nu}. \tag{5.17}$$

$Re_\lambda \simeq 61$, as found in our simulation, has been applied in a number of DNS simulations by various authors, on grids of the order of 64^3 to 96^3 points (*e.g.* Eswaran & Pope (1988); Overholt & Pope (1998); Boivin *et al.* (1998); Reade & Collins (2000)) while Reynolds numbers of approximately 200 have been reported in simulations with grids of 256^3 points (Yeung & Zhou (1997)). The Taylor Reynolds number in our simulations remains relatively low with respect to the grid size. This is the result of the pre-defined Kolmogorov length of 1.2 grid spacing. The Reynolds number is a measure of the ratio between the largest and the smallest scale in the simulation; by choosing a 'large' Kolmogorov length scale the Reynolds number will be low.

In figure 5.3 the normalised energy spectrum and the dissipation spectrum of the single phase simulation are given. The initial decay of the energy spectrum shows a $-5/3$ slope associated with the inertial subrange. The figure also contains the forcing spectrum to indicate its position in wavenumber space. The forcing dominates the turbulent motion at the largest scales, which is visible in the shape of the energy spectrum at the low wave numbers. The shape of the normalised dissipation spectrum indicates that dissipation takes place throughout the whole spectrum, but extends further into larger wave numbers (the smaller scales) than the energy spectrum. The spectra are comparable to those presented by *e.g.* Eswaran & Pope (1988), Sundaram & Collins (1997) or Alvelius (1999).

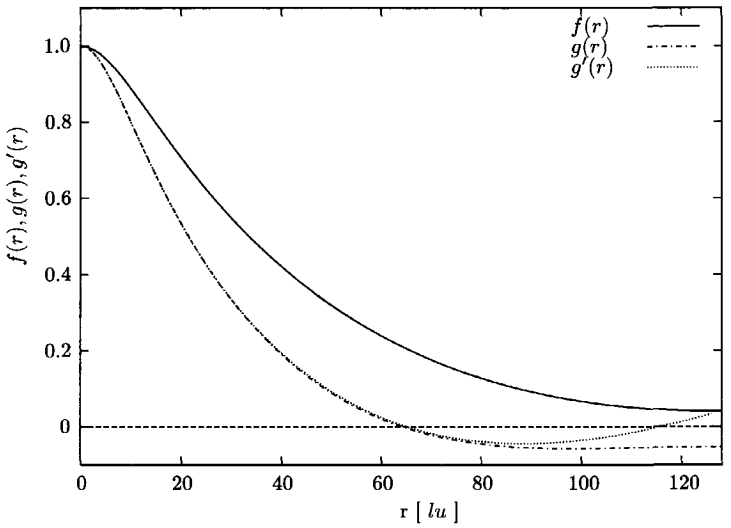

Figure 5.4: Longitudinal $f(r)$ and lateral $g(r)$ correlation functions of the turbulent simulation. $g'(r)$ is the value of $g(r)$ as computed from $f(r)$ with relation 5.22.

Four different integral length scales of the turbulence are presented in table 5.2. The integral length scale Λ_K is calculated from the turbulence intensity and the rate of energy dissipation with the scaling law,

$$\Lambda_K = \frac{u'^3}{\epsilon} \tag{5.18}$$

A second integral length scale is computed from the energy spectrum:

$$\Lambda_E = \frac{\pi}{2u'^2} \int_0^{k_{max}} \frac{E(k)}{k} dk \tag{5.19}$$

which is the length scale derived from the integration of the velocity correlation function. For reference, also the longitudinal and transverse integral length scales Λ_f and Λ_g, obtained from integration of the longitudinal and transverse velocity correlation functions $f(r)$ and $g(r)$ (see below) are given. In isotropic turbulence their ratio is approximately 2, which is the case here (Hinze (1975)).

Based on these length scales, integral time scales can be calculated, using

$$T_i \equiv \frac{\Lambda}{u'} \tag{5.20}$$

The integral time scale T_K, calculated from the kinetic energy is the eddy turnover time or eddy lifetime and is identical to K/ϵ.

In figure 5.4, the longitudinal ($f(r)$) and lateral or transverse ($g(r)$) velocity correlation functions have been plotted. For the longitudinal correlation function the separation

r is in the same direction as the velocity component, for the transverse correlation function, r is perpendicular to the velocity component. The functions are given by

$$f(r) = \frac{\overline{u_1(\mathbf{x})u_1(\mathbf{x}+r\mathbf{e}_1)}}{u'^2} \qquad g(r_2) = \frac{\overline{u_1(\mathbf{x})u_1(\mathbf{x}+r\mathbf{e}_2)}}{u'^2} \tag{5.21}$$

where the subscript i indicates the direction of the axis in an arbitrary orthogonal coordinate system. The average is taken in space as well as in time.

The correlation functions $f(r)$ and $g(r)$ in figure 5.4 show the typical behaviour for turbulent flow. A deviation from natural turbulent flows is that at larger separations the correlation functions do not reduce to zero. This is a result of the periodic domain as well as of the forcing scheme. Comparable correlations functions were obtained by Eswaran & Pope (1988) and Overholt & Pope (1998), who used a different numerical method for solving the Navier-Stokes equations as well as for generating the turbulence forcing.

A relation between the longitudinal and lateral correlation functions $f(r)$ and $g(r)$ for homogeneous isotropic turbulence is given by Hinze (1975) (pp. 185),

$$g(r) = f(r) + \frac{r}{2}\frac{\partial f(r)}{\partial r}. \tag{5.22}$$

In figure 5.4, $g'(r)$ denotes $g(r)$ based on $f(r)$ and equation 5.22. The excellent agreement at the shorter length scales indicates that indeed isotropic incompressible turbulent flow is simulated. The deviations at larger separations may differ because the correlation functions do not drop to zero.

5.4 Two Phase Direct Numerical Simulations

5.4.1 Particle phase definition

Five simulations were performed (see table 5.3) where the volume fraction ($\Phi_v = V_p/V_{tot}$) was varied at a constant density ratio (simulations S_1 to S_3), and the particle density was varied at a constant volume fraction (simulations S_4, S_2 and S_5 in increasing order). In simulations S_4, S_2 and S_5, the particle densities were chosen such that the *total* mass of the system ($m_{tot} = m_p + m_f$, while $\Phi_m = m_p/m_f$) of S_4 corresponds to that of S_1 and S_5 to that of S_3.

Particle inertia is characterised by the particle Stokes number, which for particles suspended in a turbulent flow field can be defined as the ratio of the particle relaxation time ($\tau_p = \rho_p d_p^2/18\mu$) and a relevant turbulent time scale,

$$St_i = \frac{\tau_p}{T_i}. \tag{5.23}$$

For the turbulent time scale often the Kolmogorov time scale is chosen (see *e.g.* Sundaram & Collins (1997),Sommerfeld (2001)), but as table 5.2 already indicates, at least 5 different time scales can be determined for our simulations. Three different Stokes numbers are given in table 5.3. St_K and St_E are based on the integral time scales while

Parameter	Volume fraction			Density ratio	
	S_1	S_2	S_3	S_4	S_5
N_p	773	2200	3868	2200	2200
Φ_v	0.020	0.057	0.100	0.057	0.057
ρ_p/ρ_f	1.414	1.414	1.414	1.146	1.728
Φ_m	0.029	0.085	0.157	0.069	0.104
$m_{tot} \times 10^6$	16.92	17.17	17.47	16.92	17.47
τ_p	1369	1369	1369	1109	1673
St_K	0.207	0.207	0.207	0.168	0.254
St_E	0.610	0.610	0.610	0.494	0.745
St_η	4.845	4.845	4.845	3.926	5.921

Table 5.3: Definition and properties of the particle phase for suspension simulations S_1 to S_5. The particle input radius was set to 4 lattice units for all simulations, the corresponding hydrodynamic radius was 4.696 $[lu]$.

St_η is based on the Kolmogorov time scale. The Stokes numbers indicate that the time scale of particle inertia is approximately 5 times larger than the Kolmogorov time scale and about half the integral time scale.

At the start of a simulation, the particles were placed randomly and without contact in a fully developed single phase turbulent flow field. The initial flow field was identical for every simulation and the particles initially had zero velocity. The order in which the precalculated force fields were exposed was identical for all simulations, in order to have identical time series of the forcing signal. Obviously, the evolution of the flow fields differed per case due to changes in the flow field that originate from the presence of the particle phase. The motion of the particles modifies the flow field directly, which furthermore results in a change of the uncontrolled contribution P_2 (see also section 5.2.2).

5.4.2 Kinetic energy distribution in the turbulent suspension simulations

In figures 5.5 (A) to (D), cross sections of the flow field are given at increasing particle concentration. In the single phase simulation of figure 5.5 (A), a number of vortical structures can be seen, typical of a turbulent flow field. At increasing particle concentration, the pattern of the rate of energy dissipation is altered. An increase of the rate of energy dissipation close to the particle surfaces can be observed.

The presence of particles changes the distribution of kinetic energy and rate of energy dissipation over the different length scales, as can be seen in the spectra of figure 5.6. The spectra were determined by averaging 10 realisations of the full fluid domain and contain the contribution of all grid nodes, from those both in the bulk fluid domain as well as from those inside the particles.

The particle volume only covers up to 10 vol % of the domain. The kinetic en-

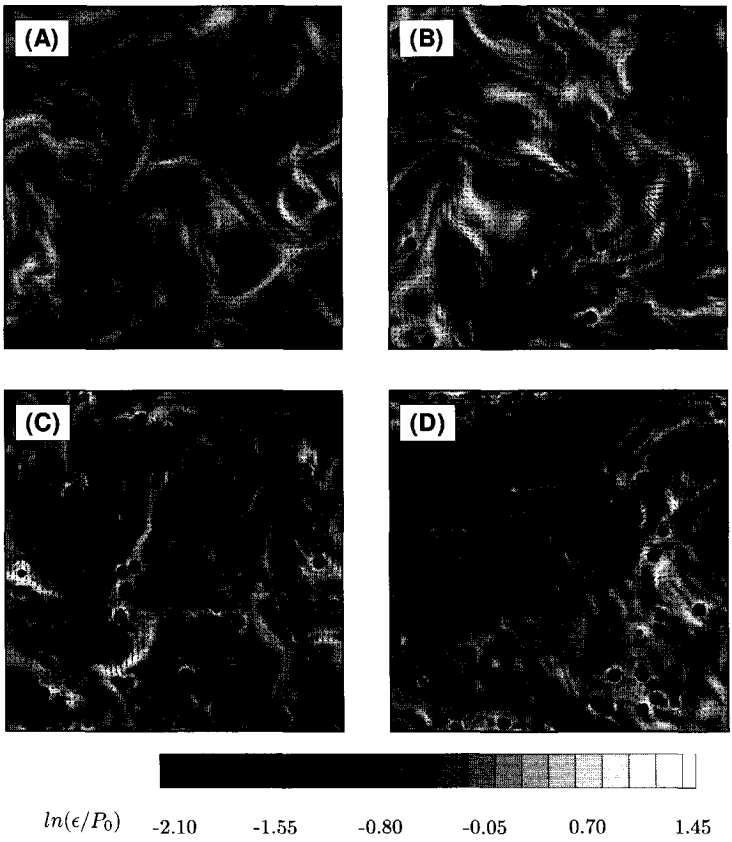

Figure 5.5: Cross sections of single realisations of the flow field of the single phase simulation (A), S_1 (B), S_2 (C) and S_3 (D) respectively. The particles are plotted at their position, intersected by the plane of view. The contours indicate the logarithmic value of the rate of energy dissipation. The vectors represent the velocity in the fluid and have been plotted at a linear interval of 1 out of 3.

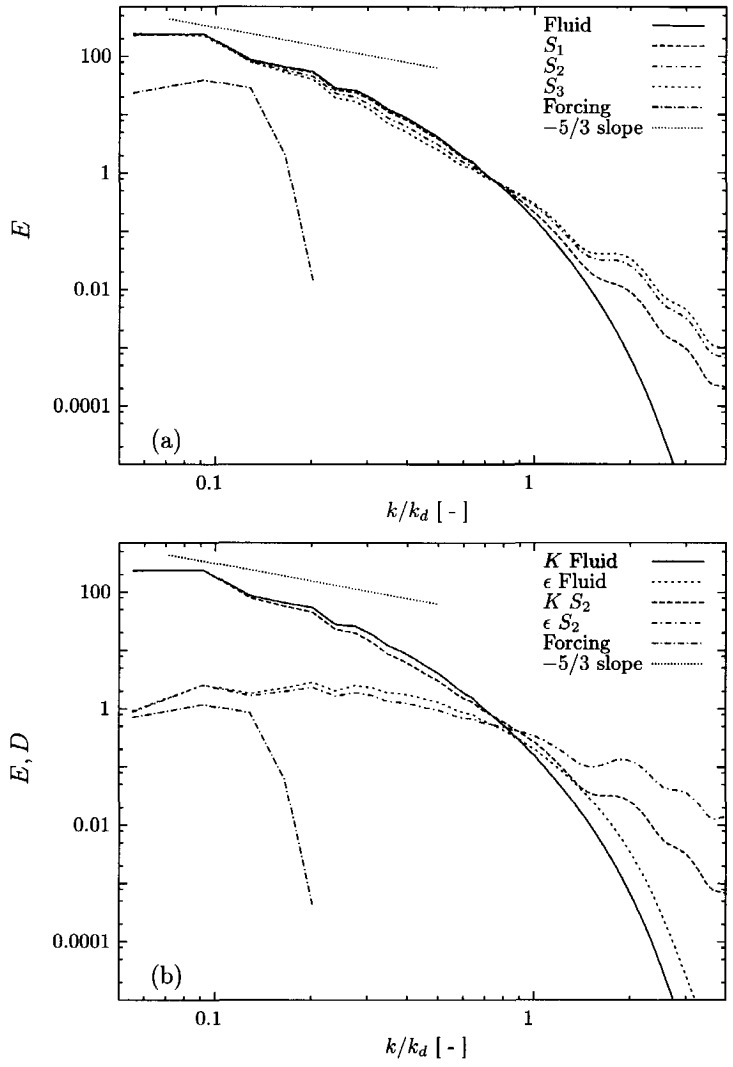

Figure 5.6: Scaled energy spectra ($E = E(k)/(\epsilon^{2/3}\eta^{5/3})$) of the single phase simulations and simulations S_1 to S_3 (a) and energy and dissipation spectra ($D = 2\nu k^2 E(k)/(\epsilon\eta)$) of single phase simulation and suspension simulation S_2. The forcing spectrum and $-5/3$ slope are included (see also fig. 5.3). The wave number axis is scaled with the particle diameter wave number $k_d = 2\pi/d_p$.

	1. $k < k_{piv}$				2. $k > k_{piv}$	
	K/K_{tot}	ϵ/ϵ_{tot}	$K/K_{F,1}$	$\epsilon/\epsilon_{F,1}$	$K/K_{F,2}$	$\epsilon/\epsilon_{F,2}$
Fluid	0.996	0.885	1.000	1.000	1.000	1.000
S_1	0.994	0.823	0.974	0.946	1.237	1.560
S_2	0.992	0.712	0.927	0.816	1.570	2.535
S_3	0.992	0.646	0.884	0.705	1.683	2.973
S_4	0.993	0.721	0.967	0.838	1.574	2.488
S_5	0.993	0.717	0.948	0.817	1.581	2.477

Table 5.4: Distribution of kinetic energy and rate of energy dissipation over wavenumbers smaller (1.) or larger (2.) than the pivot wavenumber k_{piv}. K/K_{tot} and ϵ/ϵ_{tot} indicate the kinetic energy and rate of energy dissipation contained at wavenumbers smaller than k_{piv}, relative to the *total* amount in the respective simulation. The other columns indicate the change in distribution of kinetic energy and rate of energy dissipation relative to that of the *single phase* simulation on the same wavenumber interval.

ergy spectrum in the suspension simulations presented in figure 5.6 exhibits a smooth behaviour up to wave numbers around $k/k_d = 1.5$, which is likely associated with the fluid motion in the flow field near the particle surface. At larger wave numbers, for $k/k_d > 1.5$, the energy spectrum contains a fluctuating contribution due to the presence of the discrete particle boundaries in the continuous fluid domain. For the energy spectrum, this contribution can be considered negligble compared to the overall kinetic energy content. For the dissipation spectrum this fluctuating behaviour of the energy spectrum, which is partly due to the change in fluid motion near the particle surface and partly due to the discrete particle boundary, increases energy dissipation at the smallest scales significantly. Since one can not distinguish between both contributions, careful consideration of the dissipation spectrum is required. However, the particle motion is determined by the interaction with their surrounding external flow field. Therefore, the change in the spectra at the larger scales will likely be a result from this interaction rather than from the discrete nature of the boundary condition.

At the largest scales, the fluid motion is strongly dominated by the turbulent forcing. As a result, little difference exists between the spectra of the various simulations for $k/k_d \leq 0.1$. As the wavenumbers increase, the fluid spectrum is influenced less by the force and the impact of the particles on the kinetic energy can be clearly distinguished. Figure 5.6 (a) shows that an increase in particle volume concentration reduces the fluid kinetic energy at intermediate wave numbers ($0.15 < k/k_d < 0.7$). At larger wavenumbers the spectra cross at a clear pivot point at wavenumber k_{piv} ($k_{piv}/k_d \simeq 0.72$). The particles generate fluid motion beyond this point, at length scales on the order of the particle diameter and smaller. As compared to the single phase simulation, the increase in volume fraction particles increases the kinetic energy at this wave number range. It is striking that the energy spectra of all suspension simulations exhibit a pivot point around the same wavenumber. This is probably due to the fact that the length scales

in the simulations are kept constant. The simulations have been performed with one particle size and at one turbulent Reynolds number.

In figure 5.6 (b) the influence of the particles on both the energy and the dissipation spectrum are compared. It is clear that the increased motion at larger wavenumbers, generated by the particles, strongly increases the rate of energy dissipation at larger wavenumbers. Our interpretation is that due to the difference in velocity between the particles and the bulk fluid, gradients arise at and near the particle surface that increase the rate of energy dissipation at higher wavenumbers.

The trends in the spectra are quantified in table 5.4. In this table the total kinetic energy content and the total rate of energy dissipation are divided in a part smaller and a part larger than k_{piv} . The table indicates on the one hand that about 99.4 % of the kinetic energy within each simulation is contained at wavenumbers less than k_{piv}, and this varies little under the influence of the particles. On the other hand, the rate of energy dissipation is strongly redistributed by the action of the particles. A decrease from 89 % for single phase to 65 % for S_3 is observed.

The table also quantifies the influence of the particle parameters on the evolving flow field. Changing the particle volume fraction reduces the kinetic energy of the flow field much stronger than changing the particle inertia. Velocity gradients (and hence dissipation of kinetic energy) are generated at the boundary of the solid particles by the slip-velocity. By increasing the number of particles, the total amount of particle surface is increased, resulting in an increase of the rate of energy dissipation. Increasing the particle inertia will reduce the response of particles to the turbulent flow field, resulting in an increasing slip velocity of the particles (*see e.g.* Abrahamson (1975),Kruis & Kusters (1997) for a discussion on the response of particles to a turbulent flow field). This effect will increase the gradients at the surface of the particle, but apparently this effect is less strong than the effect of volume fraction. Table 5.4 demonstrates that the kinetic energy and rate of energy dissipation in simulations S_4, S_2 and S_5 are reduced by approximately 6 %. The standard deviation of the fluctuations in kinetic energy is of the order of 10 % which may cause the lack of a clear trend in these (S_4, S_2 and S_5) simulation results.

Modulation of the kinetic energy spectrum by presence of particles has been studied via direct numerical simulations by a number of authors (*e.g.* particles in forced isotropic turbulence by Squires & Eaton (1990) and Boivin *et al.* (1998) and in decaying isotropic turbulence by Elghobashi & Truesdell (1993)). In the work of these authors, the particles were very much smaller than the numerical grid, the volume fraction was on the order of 10^{-4}, while the mass loading was considerable (Φ_m up to 1.0). The particle inertia was characterised by the particle relaxation time while Stokes drag was assumed to calculate the particle motion. In these two-way coupled simulations the interaction between the particles and the fluid phase was imposed by projecting the force acting on the particles back to the fluid grid.

Clearly, large differences exist between this approach and our simulations. In our simulations all scales of the fluid motion are resolved, whereas details of the flow field near the particle are not captured in the work presented by the authors mentioned above. Still, for a mass loading of approximately 10 %, the work of these authors indicates a decrease in turbulent kinetic energy of approximately 10 %, which is comparable to the

decrease observed in simulations S_2 and S_3 in table 5.4.

In the work of Boivin *et al.* (1998), simulations are presented where both the particle mass loading and the particle Stokes numbers are in the same range as in our simulations. In that work, a decrease of the rate of energy dissipation in the fluid phase of approximately 20 % was observed. Due to their two-way coupling approach, the decrease of the energy dissipation is caused by the particle drag, given by the Stokes drag relation. In our simulations the total energy dissipation in the fluid phase is conserved. Due to the turbulent forcing in our simulations, a practically constant power input is warranted and an equilibrium between power input and dissipation requires a constant rate of dissipation. On the other hand, our simulations indicate a decrease of the rate of energy dissipation at large scales (table 5.4, $k < k_{piv}$) by 5 to 30 %, which is of a comparable order as what is found by the above authors. This demonstrates that, although the simulation approach of the above mentioned authors lacks the detail of the small scale phenomena as present in our simulations, the large scale phenomena of both simulation approaches are consistent.

5.5 Analysis of particle phase behaviour

In this section, the motion of the particle phase in our simulations is studied in detail to characterise the particle collision behaviour observed in the simulations and to characterise the relation between the particle motion and the turbulent flow field. As stated in the introduction, particle collisions in turbulent suspensions have been studied by a large number of authors and a considerable theoretical framework exists to describe and model particle motion in turbulent flow fields. In the following paragraphs we will first give a short review of the collision theory as presented by Wang *et al.* (2000). This theoretical basis will subsequently be used to discuss characteristic features of our suspension simulations such as the distribution of relative particle velocities.

5.5.1 A short review on the formulation of the collision kernel

Two limiting cases of turbulent suspension flows are dilute flows, where the particle motion is dominated by hydrodynamic transport effects, and dense flows, where the motion of the particles is dominated by inter-particle collisions (Sommerfeld (2001)). Based on their high volume fraction one may expect that the suspensions here studied are well in the dense regime. However, the two regimes are not only characterised by the volume fraction. The ratio of the particle relaxation time and the average time between two collisions (τ_c) gives a more precise indication of the regime of the suspension. In the dilute flow limit: $\tau_p << \tau_c$; the dense flow limit: $\tau_p >> \tau_c$. In dense two phase flows, particles are not able to respond to the fluid flow between successive collisions. This applies to heavy particles in low volume concentrations or for light particles at higher volume concentrations.

We are interested in the behaviour of turbulent slurries at moderate to high volume fractions, that consist of large particles ($d_p > \eta$). The average time between particle collisions is $\tau_c = 1/f_c$, the inverse of the collision frequency f_c, which is equal to the

collision rate per unit volume divided by the particle number density. For a mono disperse system of N_p particles in a volume Ω, the collision frequency is given by

$$f_c = \frac{1}{\tau_c} = \frac{\dot{\mathcal{N}}_c}{n_0} = \frac{n_0}{2}\Gamma \tag{5.24}$$

where $\dot{\mathcal{N}}_c$ is the rate of collisions per unit volume, $n_0 = N_p/\Omega$ is the particle number concentration. In equation 5.24 the average collision kernel Γ is defined. In order to estimate the regime we are in, an upper bound estimate for Γ is approximated by (Abrahamson (1975)):

$$\Gamma = \sqrt{\frac{16\pi}{3}} R^2 u_p' \tag{5.25}$$

where u_p' is the particle rms velocity and $R = d_p$. Based on this approximation the ratio τ_p/τ_c ranges from 0.2 to 0.8 in our simulations. As a result, collisions as well as hydrodynamic forces will contribute to the overall motion of the particles.

An expression for the collision kernel Γ can be derived based on two different approaches, known as the *cylindrical* and the *spherical* approach. Wang *et al.* (1998) give an analysis of both formulations and demonstrate that the spherical formulation is the more appropriate way to describe the collision process. We will restrict ourselves to the spherical formulation. According to the original concept of Saffman & Turner (1956), a collision sphere is defined as a central sphere with a radius $R = r_i + r_j$ which for mono disperse systems is $R = 2r_p$. In the center of this collision sphere, a particle is placed. The collision kernel is given by the mean inward velocity w_r^-, times the probability P to observe this velocity,

$$\Gamma_c = 4\pi R^2 P w_r^- \tag{5.26}$$

where w_r is the radial component of the relative velocity $\mathbf{w}_{ij} = \mathbf{u}_{p,i} - \mathbf{u}_{p,j}$ and P is the probability to observe $w_r < 0$. If radial influx and outflux are in equilibrium, the collision kernel can be rewritten in terms of the absolute mean radial velocity $\langle |w_r| \rangle$, which is given by

$$\langle |w_r| \rangle = \int_{-\infty}^{0} -wP(w)dw + \int_{0}^{\infty} wP(w)dw = Pw_r^- + (1-P)w_r^+ \tag{5.27}$$

where the angle brackets denote ensemble averaging over all directions in space and time-averaging. The ratio of net inward to net outward flux is given by

$$C_p \equiv \frac{Pw_r^-}{(1-P)w_r^+} \tag{5.28}$$

which should be equal to 1 for a system in equilibrium. Wang *et al.* (2000) indicate that the ratio w_r^-/w_r^+ can be viewed as a rough measure for the compressibility of the particle velocity field. Both C_p and w_r^-/w_r^+ will be discussed for our simulations in a later section. When substituting equations 5.27 and 5.28 into equation 5.26, while assuming equilibrium between in- and outflux, the spherical formulation is obtained

$$\Gamma^{sph} = 2\pi R^2 \langle |w_r| \rangle. \tag{5.29}$$

The collision kernel is thus estimated as half the surface area of the collision sphere times the average magnitude of the radial relative velocity.

If one assumes the particle velocity to be Gaussian distributed, then the relative velocity magnitude $\langle|w_r|\rangle$ can be related to the variance of the distribution as $\langle|w_r|\rangle = \sqrt{2/\pi}\sigma_w$ with σ_w given by

$$\sigma_w = \sqrt{w_r^2} = [2(u_p')^2 - 2\langle u_{r,1}u_{r,2}\rangle]^{0.5} \tag{5.30}$$

with $u_{r,i}$ the radial velocity component of particle i. The relative velocity magnitude of the particles therefore is a function of the velocity correlation of the particles at contact. For isotropic turbulence, the correlation $\langle u_{r,1}u_{r,2}\rangle$ of the radial velocity of the fluid is given by the longitudinal velocity correlation function $f(r)$ as was discussed earlier. An equivalent expression for the particle transverse relative velocity is given by

$$\sigma_w = \sqrt{w_t^2} = [2(u_p')^2 - 2\langle u_{t,1}u_{t,2}\rangle]^{0.5} \tag{5.31}$$

where $\langle u_{t,1}u_{t,2}\rangle$ can be compared with the fluid lateral correlation function $g(r)$.

The velocity correlation functions of the particles describe the relative velocity at contact and depend on the particle-turbulence interaction. The particle properties and particle-turbulence interaction simultaneously determine the particle correlation functions which in general deviates from the fluid correlation functions.

The effect of the particle size on the collision rate is demonstrated by evaluating the longitudinal correlation function $f(r)$ at contact. In our simulations, the separation R of the centers of mass of two particles at contact is about 8 times the Kolmogorov length. At this separation, the fluid correlation functions $f(r)$ and $g(r)$ have dropped already considerably (see figure 5.4). If one assumes that the particle velocity correlation is equal to $f(r)$, then $\sqrt{w_r^2}$ is given by

$$\sqrt{w_r^2} = [2(u_p')^2(1 - f(R))]^{0.5}. \tag{5.32}$$

Since $f(R) < 1$, the relative velocity is larger at contact as R becomes larger and as a result, an increase in particle size increases the collision rate. In the following section, we will discuss the lateral and transverse relative velocities of the particles as a function of their separation.

The formulation of equation 5.29 holds for particles that exhibit a homogeneous, random spatial distribution. Finite-inertia particles in turbulent flows, however, have a tendency to collect in regions with low vorticity and high strain rate. As demonstrated by Sundaram & Collins (1997), the impact of this 'preferential concentration' effect can be separated from the turbulent transport effect via the radial distribution function at contact, $g_r(R)$. This function is defined as the probability to observe a particle pair at separation R divided by the probability to observe a particle pair at this separation in a uniform, random cluster of particles. By including this term, the spherical formulation of the collision kernel becomes

$$\Gamma^{sph} = 2\pi R^2 \langle|w_r|\rangle g_r(R). \tag{5.33}$$

The radial distribution function $g_r(r)$ will be discussed to demonstrate the presence of particle accumulation and preferential concentration in our suspension simulations.

5.5.2 Collision frequencies

In our simulations two collision mechanisms are observed. These two types of collisions are designated primary collisions, which are a result of uncorrelated particle motion, and secondary collisions, which are a result of correlated particle motion. Correlation of the particle motion arises due to the short range hydrodynamic interactions between two particles at short separation, due to the spatial correlation present in the turbulent flow field, and may also be influenced by the numerical treatment of the collision process in the simulations.

The typical behaviour of approaching particle pairs as observed in the simulations is that for approaching particles the relative velocity reduces due to the structure of the turbulent flow field. As they come close and make contact, the hydrodynamic forces acting in the gap between the particles may cause the particle pair to capture each other and stay in each others vicinity for some time, until the particles are separated again by the external flow field.

We study the probability density function (pdf) of the time between two collisions. Uncorrelated particles move randomly and behave as a kinetic gas. The distribution of collision times for such random processes is described by an exponential distribution,

$$P_c(t_c) = \frac{1}{\tau_c} exp(-\frac{t_c}{\tau_c}) \tag{5.34}$$

where τ_c is the average time between two collisions (see also equation 5.24).

In figure 5.7, the distribution of the time interval between two collisions of a single particle with another particle is given, obtained from all particles during the run of a simulation. The pdf shows an exponential decay at long collision times. A particle that moves freely in the fluid bulk until a collision with another particle takes place. After such a collision, the probability that a second collision occurs increases strongly since the relative velocity is reduced. This behaviour is also observed in the distribution of the relative velocity, which will be discussed in section 5.5.3. After a number of collisions closely spaced in time, the particles are separated again and move freely until a new uncorrelated collision occurs. If more than two particles form a cluster, also three or more neighbour particles can collide with each other collectively, which further enhances the high frequency collision rates.

This conceptual image is supported by the collision events registered during the simulations. The collisions show that two particles that form a collision pair often stay in each others vicinity and have many collisions during the run of a simulation (see also Ten Cate *et al.* (2002*a*)). Three particle collisions are also observed, where inbetween two collisions of particles A and B, a collision between a particle A and C can occur. Sundaram & Collins (1996) demonstrate that similar behaviour can occur for particles in a simple shear flow, even when lubrication forces are not present. They show that two particles in a shear flow will have multiple collisions, because their post collision trajectories coincide.

To quantify the two different collision mechanisms, we propose the following form for the probability density function,

$$P_c(t_c) = \alpha_c P_{c,1}(t_c) + (1 - \alpha_c) P_{c,2}(t_c) \tag{5.35}$$

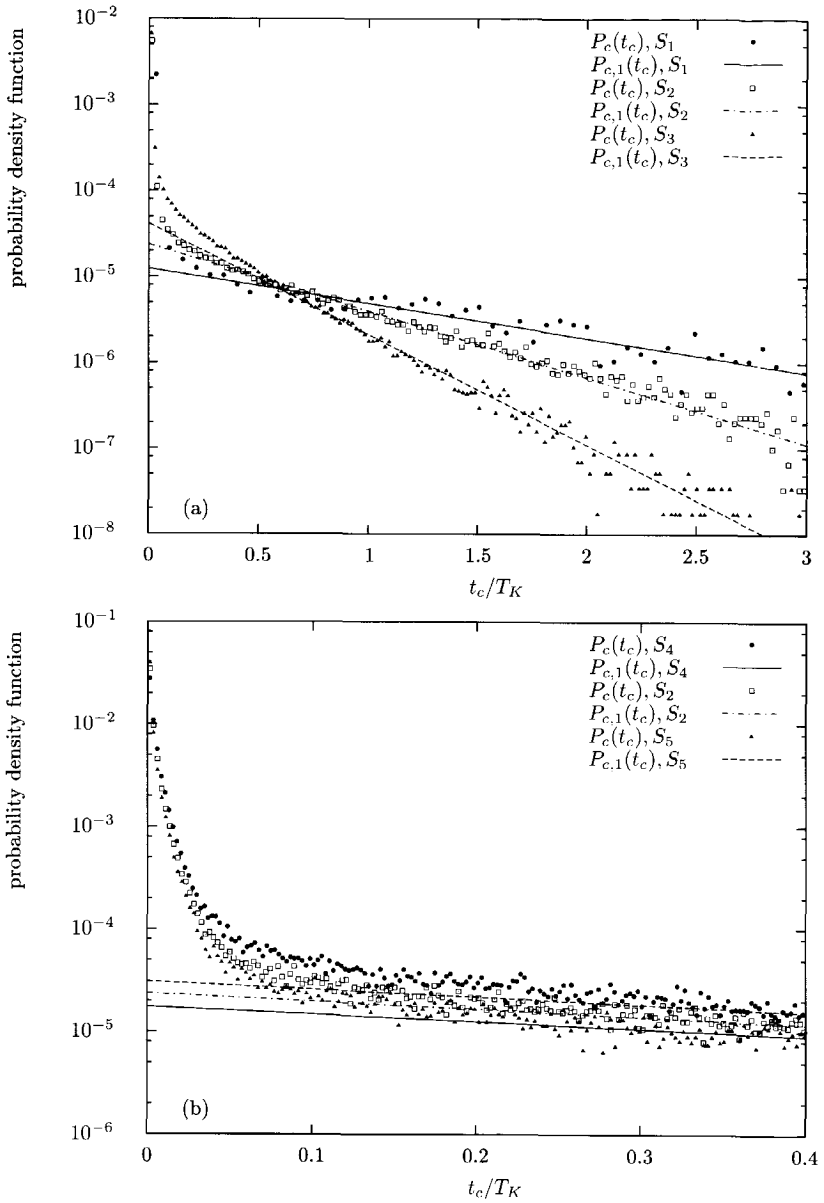

Figure 5.7: Probability density function of collision times. Simulations S_1 to S_3 (a) indicate the influence of volume concentration and simulations S_4, S_2 and S_5 (b) demonstrate the influence of particle to fluid density ratio on the collision time pdf. The lines of $P_{c,1}(t_c)$ relate to equations 5.34 and 5.35.

	$\alpha_c(\%)$	$\tau_{c,1}/T_K$	$\tau_{c,Ab}/T_K$	$\tau_{c,2}/T_K$	$\Gamma_{c,1}$	$\Gamma_{c,Ab}$
S_1	8.80 ± 0.54	1.08 ± 0.07	1.15	0.028	6.11	5.71
S_2	8.79 ± 0.44	0.56 ± 0.01	0.41	0.025	4.12	5.58
S_3	9.21 ± 0.60	0.34 ± 0.01	0.25	0.026	3.90	5.36
S_4	6.95 ± 0.30	0.60 ± 0.01	0.40	0.025	3.85	5.73
S_5	11.71 ± 0.44	0.57 ± 0.01	0.41	0.026	4.04	5.64

Table 5.5: Characteristic collision time scales τ_c of suspension simulations S_1 to S_5.

where $P_{c,1}$ is the probability to observe primary collisions, and $P_{c,2}$ the probability for secondary collisions. $P_{c,1}$ is a result of uncorrelated particle motion and may therefore be described by equation 5.34. In this formulation, the collision process is characterised by three parameters: α_c is the fraction of primary collisions, $\tau_{c,1}$ is the collision time of primary collisions and $\tau_{c,2}$ is the average time for secondary collisions. The parameters α_c and $\tau_{c,1}$ can be determined by fitting the long-time tail of the distributions. After determination of these two parameters, $\tau_{c,2}$ can be determined from $P_{c,2}$ via

$$\tau_{c,2} = \int_0^\infty t_c P_{c,2}(t_c) dt_c = \int_0^\infty t_c \left(\frac{P_c(t_c) - \alpha P_{c,1}(t_c)}{(1-\alpha)} \right) dt_c. \tag{5.36}$$

The curve fits of $P_{c,1}$ are presented in figure 5.7 while the parameter values are given in table 5.5.

The results indicate that by describing the collision process according to equation 5.35, the influence of particle volume concentration can be separated from that of particle inertia. At increasing particle concentration, the collision time $\tau_{c,1}$ decreases, which corresponds to a decrease in mean free path of the particles. This is clearly demonstrated in figure 5.7 (a), where the slope of the tail is a function of the particle volume concentration. Table 5.5 indicates that α_c remains practically constant. When the particle density is varied at constant volume concentration (see figure 5.7 (b)), the particle collision time is practically constant while α_c increases. As particle density increases, the particles become less sensitive to the details of the collision process (lubrication force, velocity correlation or the numerical collision procedure), which favors the occurrence of primary collisions.

In table 5.5, the time inbetween primary collisions is compared with the theory of Abrahamson (1975), where the collision rate is calculated via equations 5.24 and 5.25, with u_p' determined from the particle kinetic energy. For low volume concentrations $\tau_{c,1}$ corresponds well with Abrahamson's result, but as the volume concentration increases, the simulations show a systematically larger collision time. According to Abrahamson (1975) (equation 5.25), the collision kernel is a function of the particle rms velocity, and not of volume concentration. Table 5.5 however suggests that this is not the complete picture and a correction on the collision kernel for primary collisions is required.

5.5.3 Fluid and particle relative velocities

The radial relative velocity of a particle pair plays a dominant role in the collision kernel. In this section we present the distribution of the relative velocities of the particles in the simulations. This distribution is compared to the distribution of the relative velocity in the fluid phase. We demonstrate the change of the distribution at different separations, and present the relationship with the longitudinal and transverse correlation functions.

Radial and transverse relative velocity components of the fluid single phase simulation have been plotted in figure 5.8. The relative velocities in these figures are determined from $w_i = u_i(x + r) - u_i(x)$, where the separation distance r had values of 1, 8 and 32 lattice units. At $r = 1$, the radial relative velocity reduces to the velocity gradient $\partial u/\partial x$ while the transverse relative velocity reduces to $\partial u/\partial y$. The figure demonstrates clearly how the distribution of the relative velocity changes with distance. As a reference, a normalised exponential and Gaussian distribution are given.

At a separation of 1, we see that the radial relative velocity distribution is negatively skewed with a skewness value of -0.5. This skewness is a typical characteristic of isotropic turbulence, also reported by *e.g.* Alvelius (1999) and Wang *et al.* (2000). It is further noticed that, for a separation of $r = 1$, the tail of the distribution follows the exponential curve at negative relative velocities, while at positive values the distribution has a Gaussian shape.

As the separation increases to 8 lu, the skewness decreases and the shape of the distribution tends to the Gaussian curve. When the separation further increases to 32 lu, the correlation decreases (see figure 5.4) and the distribution of the radial relative velocity becomes Gaussian. The relative velocity magnitude and the velocity correlation values corresponding to the data in figure 5.8 are given in table 5.6. The tendency of the relative velocities towards a Gaussian distribution is expected since the relative velocity of two uncorrelated Gaussian distributed velocity components is Gaussian distributed (see equations 5.30 and 5.31).

The transverse relative velocity is also given in figure 5.8. In an isotropic flow field no directional distinction can be made regarding the velocities in the plane perpendicular to the radial direction. The sign of the transverse relative velocity indicates velocities relative to an arbitrarily chosen coordinate system. The distribution must then be symmetric by definition. The distribution of the transverse relative velocities exhibits an exponential shape at short separation distances and changes into a Gaussian distribution at larger separations. The Gaussian distribution can be anticipated for the transverse velocity based on the same argument that was given for the radial relative velocities (see equation 5.31).

In table 5.6, the standard deviation or rms value of the radial and transverse relative velocity at the three separations distances is presented. Transverse rms velocities are larger than the radial components. Equations 5.30 and 5.31 show that the radial and transverse velocity standard deviation depend on the velocity correlation. In isotropic turbulence $g(r)$ has a stronger decrease than $f(r)$ and thus, the rms value of w_t must be larger than that of w_r.

For the computation of the radial and transverse velocity distributions of the particle phase, the radial and transverse velocity component need to be defined. The radial

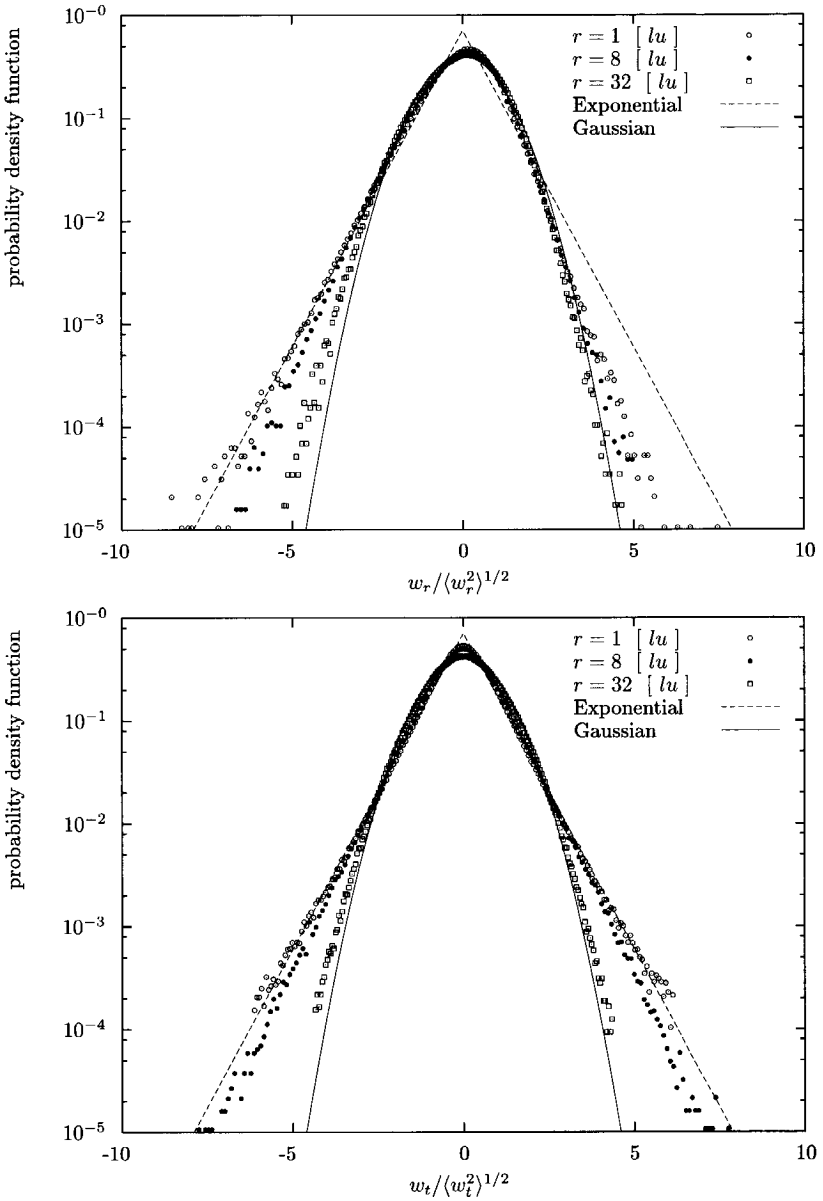

Figure 5.8: Distributions of the radial and transverse relative velocity components of the single phase simulation. The relative velocities were determined at separation distances $r = 1$, $r = 8$ and $r = 32$ $[lu]$.

	Fluid			S_2		
	r	$(w_i^2)^{1/2}$ $\times 10^3$	$\langle u_{i,1}u_{i,2}\rangle/u'^2$	s	$(w_i^2)^{1/2}$ $\times 10^3$	$\langle u_{ip,1}u_{ip,2}\rangle/u_p'^2$
Radial	1	0.91	0.998	0.5	3.12	0.979
	8	6.63	0.918	2.5	6.90	0.895
	32	16.49	0.494	31.5	16.20	0.423
Transverse	1	1.28	0.997	0.5	7.20	0.886
	8	8.98	0.850	2.5	9.17	0.815
	32	19.91	0.262	31.5	19.26	0.184

Table 5.6: Standard deviation of the relative velocities of the fluid for the single phase simulation and for the particle phase in simulation S_2, both determined at three different separation distances r or s.

velocity is defined by $w_r = \mathbf{w} \cdot \mathbf{R}/R$, where $\mathbf{R}$ is the vector connecting the centers of any two particles. A definition for the transverse component is given by $w_t = |\mathbf{w} \times \mathbf{R}|/|R|$ (Wang *et al.* (2000)). The transverse velocity vectors, projected in the plane perpendicular to $\mathbf{R}$, are not necessarily aligned. Therefore, the velocity vectors need to be decomposed in two orthogonal components in the plane perpendicular to the connecting axis. In our analysis, the transverse velocity distribution and transverse velocity correlation functions are calculated for the particle phase via the orthogonal coordinate system defined by Alvelius (1999). The principal axis is given by $\mathbf{e_0} = \mathbf{R}/R$. The two axes orthogonal to $\mathbf{e_0}$ and to each other that define the new coordinate system are given by the unit vectors $\mathbf{e_1}$ and $\mathbf{e_2}$, defined as

$$e_{1,x} = \frac{e_{0,y}}{(e_{0,x}^2 + e_{0,y}^2)^{1/2}}, \quad e_{1,y} = -\frac{e_{0,x}}{(e_{0,x}^2 + e_{0,y}^2)^{1/2}}, \quad e_{1,z} = 0 \tag{5.37}$$

$$e_{2,x} = \frac{e_{0,x}e_{0,z}}{e_0(e_{0,x}^2 + e_{0,y}^2)^{1/2}}, \quad e_{2,y} = \frac{e_{0,y}e_{0,z}}{e_0(e_{0,x}^2 + e_{0,y}^2)^{1/2}}, \quad e_{2,z} = -\frac{(e_{0,x}^2 + e_{0,y}^2)^{1/2}}{e_0}. \tag{5.38}$$

By using this coordinate system, the particle velocities can be decomposed in a longitudinal and two parallel velocities from which one radial and two transverse relative velocity components can be determined. Since the turbulent flow field is isotropic, all quantities should be recovered regardless of the orientation of the coordinate system.

In figure 5.10 the relative velocity distributions of the particle phase of simulation S_2 are given at three different separations. The separation s refers to the gap between the two sphere surfaces, *i.e.* $s = r - R$. For each realisation statistical data was obtained on $1/2N_p(N_p - 1)$ particle pairs. The velocity distribution at a given separation s was determined from all particles in the flow field that were separated at $s \pm 0.5\ lu$, and data was obtained over 75 realisations of the particle field at a time spacing of 470 time steps.

The distribution of the radial relative velocity component at $s = 0.5\ lu$ exhibits a number of peculiar characteristics. The distribution is strongly asymmetric and is much more negatively skewed (-2.43) than the distribution of the fluid velocity at a separation of 1 lu in the single phase simulation (see figure 5.8). The negative relative velocity (*i.e.*

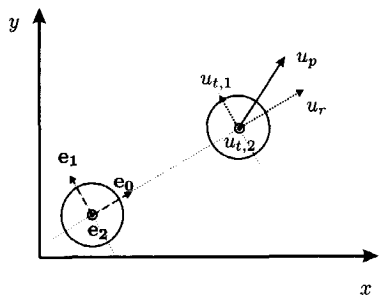

Figure 5.9: 2D representation of the axial and transverse vector decomposition for a particle pair.

approach velocity) contains a strongly stretched tail, while the positive relative velocity (separation) is found within the Gaussian distribution. As the separation increases, the skewness reduces and the tail in the distribution disappears. At $s = 2.5$, the skewness has become -0.94.

The strong negative skewness as well as the stretched tails in the distribution are also observed in the results of Wang *et al.* (2000), who studied collision characteristics of small particles ($d_p < \eta$) in one-way coupled simulations carried out in frozen flow fields. As the particle relaxation time in their simulations was increased from $\tau_p/\tau_k = 0$ to $\tau_p/\tau_k = 1$, the skewness in the distribution decreased to a minimum of -2.03. In their results tails were observed in both the positive and the negative direction of the radial relative velocity distributions. Clearly the tails in the distribution in their work are a result of the response of the particles to the turbulent flow field, controlled by the particle inertia.

The shape of the distribution of the radial relative velocity reflects the collision behaviour in terms of primary and secondary collisions. At the approach of two particles, the relative velocity of the particles decreases due to the dissipative action of the lubrication force and due to the velocity correlation in the turbulent flow field. Further, for separating particles at close proximity, the lubrication force becomes attractive. Sufficient inertia is required for the particles to escape from the attractive force after a collision: else, the local external flow field might bring the particles together again and a next collision at low relative velocity takes place.

As a consequence, approaching particles are found in a wide range of negative relative velocities. The shape of the distribution is caused by two separate contributions; (i) the distribution contains the relative velocities of particles that were initially separated over larger distances with uncorrelated velocities. The relative velocity of such particles can have larger values than particles that are in each others vicinty, contributing to the relatively long tail in the velocity distribution; (ii) the distribution contains contributions of particle pairs that were already in each other's vicinity and remain there, increasing the pdf at low relative velocities (secondary collisions). The dissipative effect of the lubrication force may suppress the presence of large positive relative velocities, which

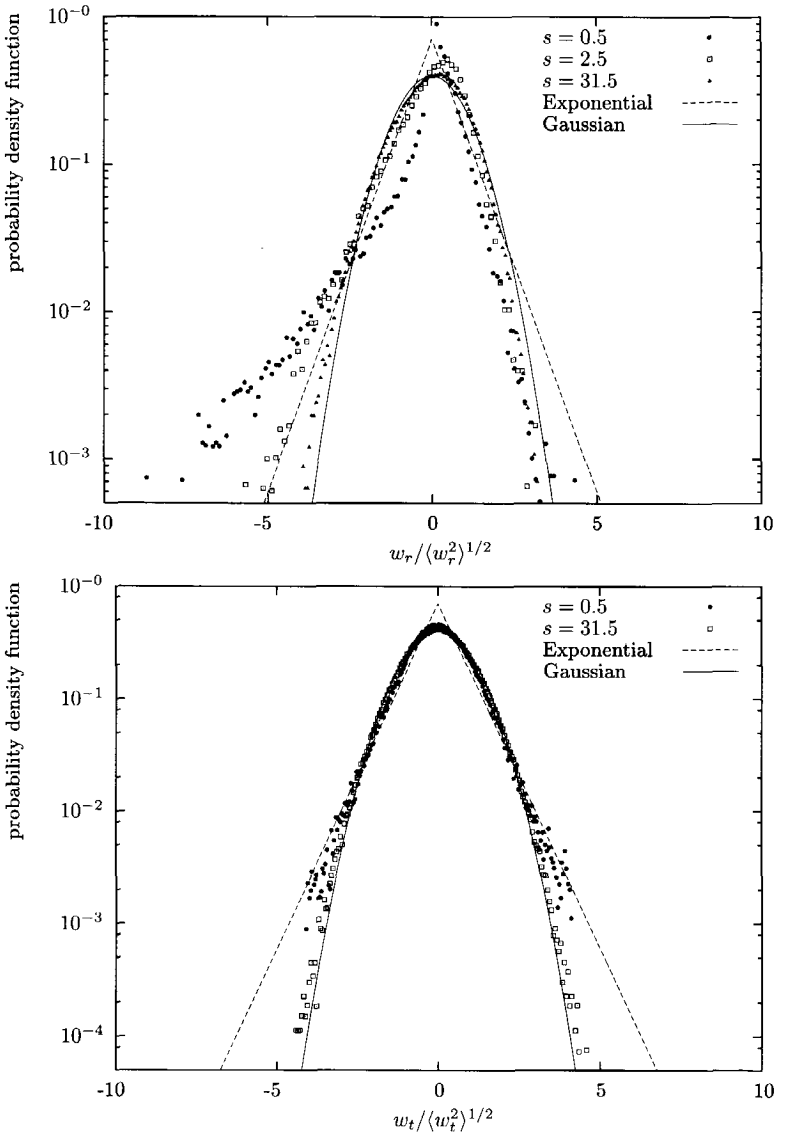

Figure 5.10: Distribution of the radial and transverse relative velocity components of simulation S_2. The relative velocities were determined from particles that were separated $s = 0.5 \pm 0.5$,$s = 2.5 \pm 0.5$ and $s = 31.5 \pm 0.5$ $[lu]$, where s indicates the separation gap between two spheres.

results in the steep decay of the tail of the distribution at the positive side. At higher values of s, the shape of the distribution changes rapidly. When s increases from 0.5 to 2.5, the short range hydrodynamic interactions decay strongly, which results in a change of the pdf towards a Gaussian distribution. At further separation, the distribuiton becomes practically Gaussian in a similar way as the distribution of the radial fluid velocity distribution.

The transverse relative velocity shows a symmetric and practically Gaussian distribution, even at the closest separation. The symmetric shape is due to the isotropic nature of the turbulent flow field. The Gaussian shape of the particle phase is a striking feature, bearing in mind the almost exponential shape of the distribution of the fluid transverse velocity at a separation of 8 lu.

The difference between transverse velocity distribution of the fluid in the single phase and that of the particles in the suspension may be caused by two effects. In the first place, the effect can be caused by the particle inertia. At increasing inertia, particles will respond to the larger scales in the fluid motion which are Gaussian distributed. In the second place, the effect may be a result of the size of the particles. Particles are larger than the Kolmogorov scale and therefore pick up hydrodynamic forces at their surface from all directions. The fluctuating flow field at the particle surface averages out the forces that act on the particle. This effect evens out the fluctuations in the fluid velocity over the size of the particle, leading to a Gaussian transverse velocity distribution.

A large difference can also be seen between the radial and the transverse relative velocity magnitude in the particle phase (see table 5.6). The lubrication force is active in the radial direction. In the transverse direction only shearing forces are active which are orders of magnitude smaller and consequently have a negligible effect on the particle motion. As a result, the transverse velocity only reduces 20 % as the separation reduces from 2.5 to 0.5 [lu], while for the radial velocity a decrease of 55 % is observed (table 5.6).

In figure 5.11 the radial relative velocity distribution is given for simulations S_4, S_2 and S_5, *i.e.* in the order of increasing particle density. At close examination, the data hints towards a widening of the tails in the distribution at increase of the particle relaxation time. This would be in agreement with the results on the particle collisions presented in section 5.5.2 (*i.e.* more primary collisions for heavier particles). Due to the scatter in the data no definitive distinction can be made to determine the influence of the particle relaxation time on the shape of the distribution. The transverse relative velocity distributions also practically collapse (not shown). The window in which the particle properties were varied was rather small and further work should be performed to study the effect of the particle inertia on the relative velocity distributions.

The normalised velocity variance of the radial and the transverse velocity components for the fluid and the particle phase are given in figure 5.12 as a function of the separation r. For the fluid phase one can recognise the shape of the curves as $1 - f(r)$ and $1 - g(r)$ (see also fig. 5.4), the longitudinal and transverse correlation functions (see equations 5.30 and 5.31). At decreasing separation, the particle relative velocity reduces faster than the fluid relative velocity due to a stronger correlation of the particle motion as compared to the fluid motion. As the particles mainly respond to the larger scale structures in the fluid, their velocity will become stronger correlated over intermediate separations

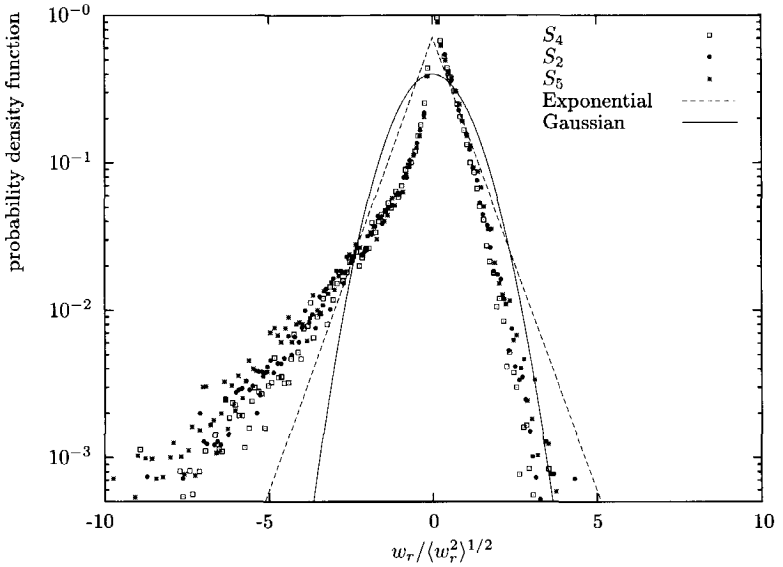

Figure 5.11: Pdf of the radial relative velocity components of simulation S_2, S_4 and S_5. The relative velocities were determined at $s = 0.5 \pm 0.5$ $[lu]$.

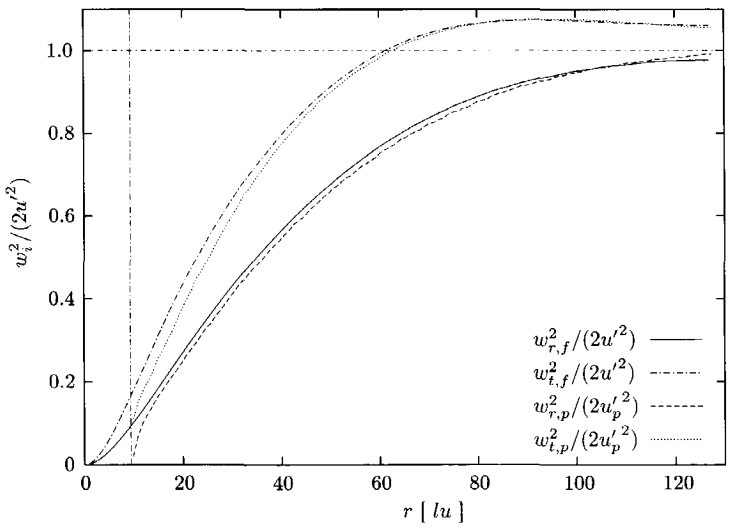

Figure 5.12: Normalised variance of radial and transverse relative velocity $(w_i{}^2/(2u_i'^2))$ of the fluid and particle phase of simulation S_2, as a function of separation r. The vertical line indicates the separation R at which there is contact between two particles.

than the fluid velocity. At closest approach, the short range hydrodynamic interactions dominate the relative radial velocity, causing a steep decay. The transverse velocity of the particles near contact is also reduced much stronger than the fluid transverse velocity.

The flux-balance coefficient C_p of equation 5.28 is given in figure 5.13(a) as a function of the separation r. This figure demonstrates that the flux balance assumption is valid for the fluid phase, as should be the case, and also for the particle phase, where the scatter in the data is only 3 %. The particle flux in the simulations therefore has reached a steady-state.

The ratio w_r^-/w_r^+ of figure 5.13(b) exhibits a monotonous increase at decreasing separation. According to Wang *et al.* (2000) this ratio is a measure for the compressibility of the (particle) velocity field. However, if C_p equals 1, as is practically the case for both the solid phase and the fluid phase in our simulations, w_r^-/w_r^+ equals $(1-P)/P$. Therefore, the latter is mainly a measure for the asymmetry of the relative velocity distributions. One can relate the curves of figure 5.13 (b) with the distributions of figures 5.8 and 5.10. The ratio $(1-P)/P$ merely represents the ratio of the probability to have negative and positive relative velocities. Therefore, the shape of the curves in figure 5.13(b) can be considered as a characteristic feature of the turbulent (particle) velocity field. The strong increase of the ratio for the particle phase at close approach is then caused by the increased asymmetry of the particle phase relative velocity pdf.

5.5.4 Accumulation and preferential concentration of particles

In direct numerical simulations of turbulent suspensions with the point particle approach, accumulation of inertial particles in regions of low vorticity and high strain rates has been observed by a number of authors (Squires & Eaton (1990), Sundaram & Collins (1997)) and was studied in more detail by *e.g.* Reade & Collins (2000) and Wang *et al.* (2000). This accumulation effect can have a large impact on the rate of collisions of particles. The above authors used the radial distribution function at contact, $g_r(R)$ (see also equation 5.33), to quantify the accumulation effect as a function of physical properties such as the flow Reynolds number and the particle relaxation time.

The radial distribution function $g_r(r)$ indicates the probability of observing a particle pair separated at a distance r, with respect to the probability of observing a particle pair in a uniformly distributed field. A residual radial distribution function is defined as

$$h_r(r) \equiv g_r(r) - 1. \tag{5.39}$$

In figure 5.5, this accumulation effect can be observed, especially in figures (C) and (D), *i.e.* at 5 and 10 vol% particles respectively. In figure 5.14, a 3D representation of an instantaneous particle field at 2 vol% is given. In this figure, the spatial distribution of the particles also suggests the presence of regions where particles have accumulated and regions with less particles.

In figure 5.15, the residual radial distribution function of simulation S_2 is given. The figure indicates that particle accumulation occurs at particle separations smaller than 4 [lu]. The radial distribution function increases strongly when the separation s goes to 0. The radial distribution function has been determined from the simulation by counting

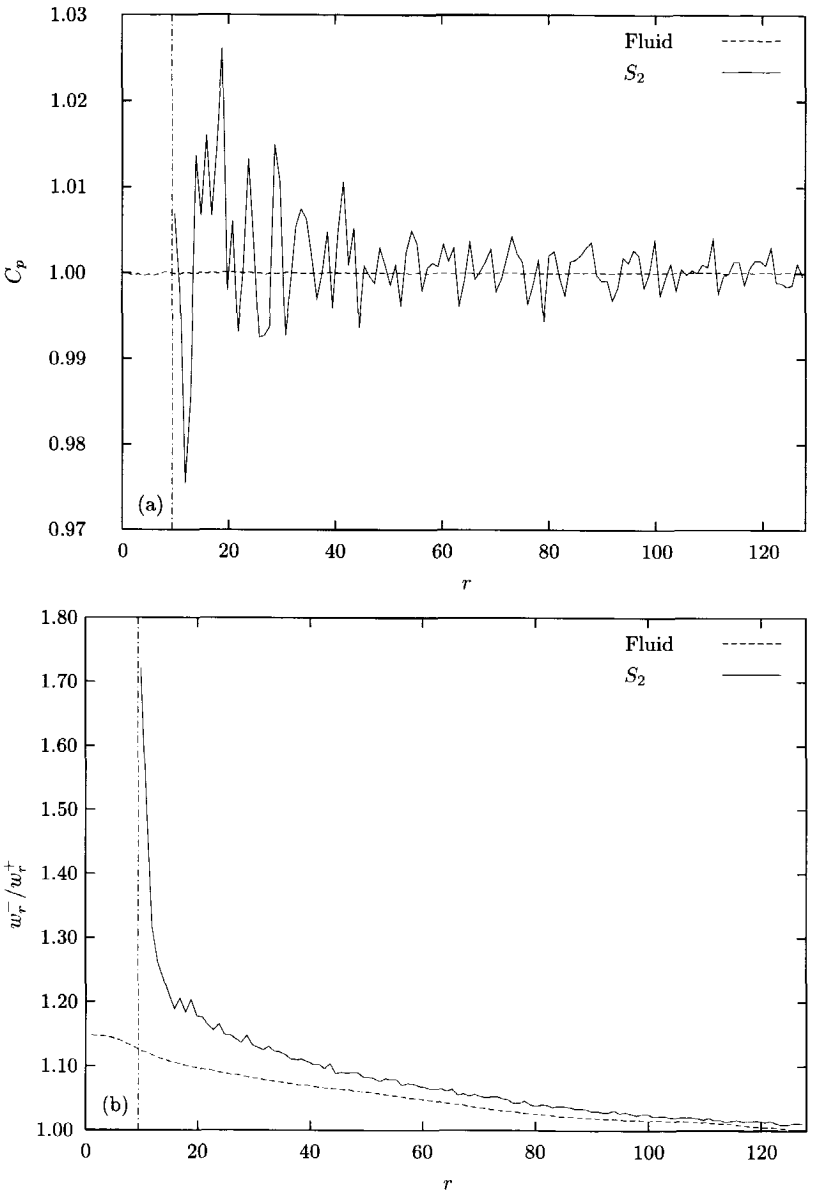

Figure 5.13: The flux balance coefficient C_p (a) and the ratio of w_r^-/w_r^+ as a function of distance r. 'Fluid' indicates the single phase simulation.

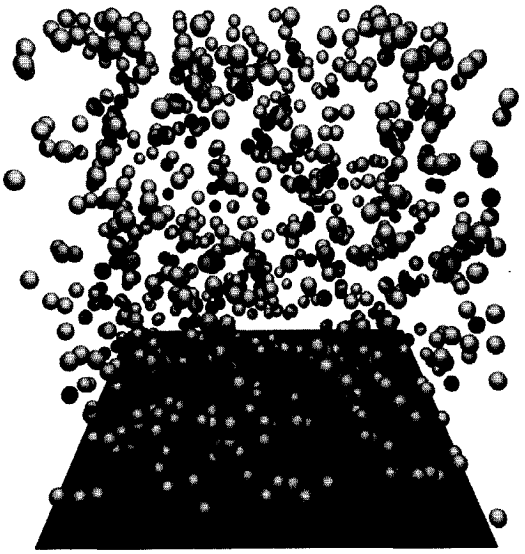

Figure 5.14: 3D snapshot of the particle field of simulation S_1 (2 vol% particles). The square at the bottom indicates the dimensions of the computational domain.

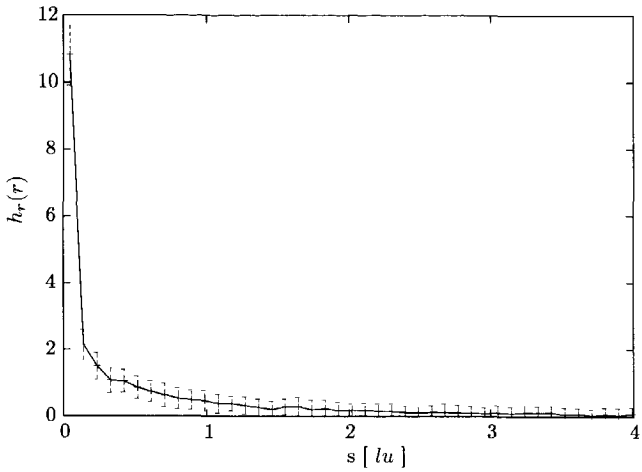

Figure 5.15: $h_r(r)$ of simulation S_2. s indicates the gap between the sphere surfaces ($s = r - R$). The error bars indicate the standard deviation, determined over 75 realisations of the particle field. $\delta = 0.094$ (δ explained in text), corresponding to 0.01 r_p.

the number of particle pairs in a realisation of the flow field, the centers of mass of which lie between $r - \delta/2$ and $r + \delta/2$,

$$g_r(r) = \frac{(N_{pairs})}{V_s} \times \frac{V_{domain}}{N_p(N_p - 1)/2} \tag{5.40}$$

which is normalised by the average number of particle pairs in a shell volume $V_s = 4\pi[(r + \delta/2)^3 - (r - \delta/2)^3]/3$.

Determination of this function requires the choice of a bin width δ. With a relatively large contact radius R, V_s becomes proportional to δ via $V_s \simeq 4\pi R^2\delta$ and g_r becomes proportional to $1/\delta$. The choice of δ is delicate since it implies a compromise between the resolution of g_r and statistical convergence. With a relatively low number of particles per simulation, and only a limited number of independent realisations, the accuracy at which $g_r(R + \delta/2)$ can be determined is limited, which is indicated by the error bars plotted in figure 5.15. This is also expressed in the second column of table 5.7, which contains the average number of pairs counted in a single realisation of the particle field, where δ was 1 [lu], similar to the interval at which the relative velocity distributions in section 5.5.3 were determined.

The usual explanation for the increase of $g_r(R)$ is that vortical structures in the flow field collect particles at their edge. It is likely that this mechanism is also present in our simulations, but since the separation of scales between the particle size and the integral length scale of the turbulence is only a factor 4, this effect probably plays a weak role in our simulations.

A second mechanism for the increase in particle concentrations at short separations can be attributed to the influence of the short range hydrodynamic interactions. In a

Simulation	$g_r(R+\delta/2)$	$\langle N_{pairs} \rangle$
S_1	2.70 ± 0.36	59.18
S_2	2.80 ± 0.14	497.23
S_3	2.98 ± 0.10	1634.13
S_4	2.69 ± 0.13	476.53
S_5	2.88 ± 0.16	510.52

Table 5.7: $g_r(R)$ and its standard deviation, at $r = R + 0.5$ and shell width $\delta = 1$. The function value was obtained from 75 particle field realisations. $\langle N_{pairs} \rangle$ indicates the average number of pairs per realisation.

study of Ladd (1997) on fully resolved settling spheres, also a strong increase in the radial distribution function at short separations is observed. In that study a similar approach for taking into account the lubrication force was used. As observed in the previous section, the relative radial velocity is reduced upon approach and a capturing mechanism occurs for particles with low relative velocities. This may give rise to the increase in particle concentration at small separations.

In table 5.7, also trends in the dependency of g_r on the simulation parameters can be observed. Both an increase in particle concentration and an increase in particle inertia appear to enhance the accumulation effect, although these effects are smaller than the statistical accuracy. In previous studies of Sundaram & Collins (1997) the radial distribution function was found to be practically independent of the volume fraction in the limit of low volume concentrations. The increase in the radial distribution function with increasing volume fraction and particle inertia is therefore possibly the result of the high volume concentration of particles in these simulations.

5.6 Summary and conclusions

A simulation approach was developed for the study of dense turbulent solid-liquid suspensions. Fully resolved simulations were performed of a sustained isotropic turbulent flow, using a lattice-Boltzmann scheme for the fluid flow simulation with a spectral forcing scheme for the generation of turbulent conditions. The suspension contained up to 3900 freely moving particles. The particle diameter spanned approximately 8 grid points, assuring that the flow field around the particles was fully resolved. For particles approaching contact, a collision detection algorithm was used. This was combined with a sub-grid model based on lubrication theory to compensate for the lack of resolution to compute the flow in the gap between two particles separated at less than the grid spacing. Five turbulent suspension simulations were carried out at a Taylor Reynolds number of 61, where the volume fraction of particles was chosen between 2 and 10 % and where the particle to fluid density ratio was varied between 1.15 and 1.73. The results of these simulations were characterised in two ways. First, the interaction between the particle phase and the turbulent flow field was studied. Second, the behaviour of the particle phase was characterised by studying particle collisions and particle relative

velocity distributions.

The influence of the particles on the energy spectrum showed that particles generate fluid motion at scales of the order of the particle size. This is reflected by an increase in the kinetic energy contained in the wavenumbers of the order of or larger than the particle wavenumber. Due to the relative motion between the particles and the fluid, gradients are generated near the particle surface which enhance the rate of energy dissipation at large wave numbers and consequently suppress the kinetic energy in the spectrum at smaller wavenumbers. The decrease of kinetic energy and energy dissipation at small wavenumbers are in quantitative agreement with results obtained from numerical studies on two-way coupled suspensions where the solid phase was treated as point particles. It was demonstrated that at a constant mass loading, the changes in the spectrum are much more sensitive to the volume fraction of particles than to the particle inertia.

The characteristics of the particle phase were further analysed using a number of concepts that originate from theory to describe particle collisions in turbulent flow fields. The collision behaviour of the particles in the suspension simulations was studied based on the collision time, *i.e.* the time that particles travel between successive collisions. Other properties that were studied are, the radial and transverse relative velocity distribution near contact, the flux-balance assumption, particle and fluid velocity correlation functions, and particle accumulation effects.

The collision time distribution steeply rises for short collision times and decays exponentially for longer times, indicating the presence of two separate collision mechanisms. An exponential decay corresponds to a random collision process for particles that exhibit uncorrelated motion, comparable to the behaviour of a kinetic gas. The peak for short collision times corresponds to repetitive contacts between particles in correlated motion. Collisions due to uncorrelated particle motion were designated primary collisions, collisions due to correlated motion were designated secondary collisions. The latter originates from a number of aspects such as short range hydrodynamic interactions, spatial correlation in the turbulent flow field at short separations, and the numerical treatment of the lubrication forces and particle collisions in the simulations. In this respect there is room for improvement, since the choices made in the sub-grid forces and collision modeling may significantly influence the short range suspension behaviour.

From a decomposition of the collision time pdf-s, two parameters were obtained to characterise primary collisions, *viz.* the average collision time ($\tau_{c,1}$), and the ratio of primary collisions to the total number of collisions (α_c). An increase of the particle volume fraction decreased the average time between primary collisions. At low volume concentration, the mean time compared well with kinetic theory for inertial particles at low volume concentrations (Abrahamson (1975)) whereas at higher volume fraction, the average collision time proved to be longer than predicted by kinetic theory. By increasing the particle inertia, the fraction of primary collisions α_c was found to increase, leaving τ_c practically unaffected.

The radial relative velocity distribution near contact showed a large tail for negative velocities and a strong increase at small velocities, while the distribution was strongly suppressed at larger positive velocities. This pdf supports the image of primary and secondary collisions where particles may approach at large velocities, but at close range reduce their relative velocties due to the action of lubrication forces and velocity corre-

lation in the turbulent flow field. As particles separate, the lubrication force becomes attractive. This may explain the strong decay at positive values of the radial velocity distribution. As separation increases, the pdf of the radial relative velocity becomes Gaussian.

The transverse relative velocity distribution remained practically Gaussian even at close separations, although the distribution of transverse velocities of the fluid phase follows an exponential distribution. Particle size effects cause this different behaviour of solid and liquid phase.

The magnitude of the radial and transverse relative velocities respectively show a $1 - f(r)$ and $1 - g(r)$ like dependency of the separation r, where $f(r)$ and $g(r)$ are the longitudinal and transverse velocity correlation functions. This demonstrates that the particle motion is strongly linked to the turbulent flow field. The particle relative velocity shows a stronger decay than that of the fluid phase as the separation reduces to zero. A check of the flux-balance assumption demonstrated that the particle field reaches a dynamic steady state since the ratio of inward to outward particle flux practically equals 1.

The spatial distribution of the particles was further characterised by the radial distribution function, which indicates that an increase in particle concentration at short separations occurs. This increase in concentration is caused by both the familiar 'preferential concentration' effect and by the short-range hydrodynamic interactions.

Our method proves to be an efficient tool to obtain detailed insight in the behaviour of turbulent suspensions with a full recovery of the two-way interactions between the particle and the fluid phase. This simulation approach can be used to gain insight in *e.g.* the collision behaviour of crystals in dense turbulent suspensions as encountered in industrial crysallisation processes. In these processes, crystal collisions occurring at sufficiently high impact velocity may lead to fragmentation. Our simulations offer possibilities to study for instance the rate of fragmentation of crystals in dense turbulent suspensions, based on *e.g.* the radial velocity distribution near impact.

List of Symbols

Symbol	description	unit
c_s	speed of sound	$lu,\ ts^{-1}$
C_p	velocity ratio	–
d	velocity deviation	lu/ts
d_p	particle diameter	lu
$e_{1\alpha},\ e_{2\alpha}$	orthogonal unit vectors	–
f	specific body force vector	$lu\,ts^{-2}$
f_c	particle collision frequency	$\#\,ts^{-1}$
f_{nr}	number of used Fourier modes	$\#$
$f(r),\ g(r)$	velocity autocorrelation functions	–
F	body force vector	$M\,lu^{-2}\,ts^{-2}$
g_r	radial distribution function	–
h_r	reduced radial distribution function	–
k	wave number	lu^{-1}
k_a, k_b, k_f	forcing interval and max. wavenumber	lu^{-1}
K	turbulent kinetic energy	$lu^2\,ts^{-2}$
l_*	forcing length scale	lu
m	mass	M
n_0	particle number density	$\#\,lu^{-3}$
n_i	fluid mass density	$M\,lu^{-3}$
n_x, n_y, n_z, n_t	grid dimensions and timesteps	lu and ts
N_p	number of particles	$\#$
$\dot{\mathcal{N}}_c$	particle collision rate	$\#\,ts^{-1}\,lu^{-3}$
p	pressure	$M\,lu^{-1}\,ts^{-2}$
P	power input	$lu^2\,ts^{-3}$
P	probability	$\#$
r_p	particle radius	lu
R	collision sphere radius	lu
T	macroscopic turbulent time scale	ts
T_p	torque acting on particle	Mlu^2/ts^2
u	velocity	$lu,\ ts^{-1}$
u'	rms velocity of turbulent flow	lu/ts
u'_p	rms particle velocity	lu/ts
v'_*	forcing velocity scale	$lu,\ ts^{-1}$
V_s	spherical shell volume	lu^3
w	relative particle velocity	lu/ts

Greek	**description**	**unit**
δ	bin width	lu
Δ	grid spacing	lu
ϵ	rate of energy dissipation	$lu^2\,ts^{-3}$
Phi_m	mass fraction particles	$-$
Phi_v	volume fraction particles	$-$
Γ	particle collision kernel	$lu^3\,ts$
Γ_i	lattice-Boltzmann collision operator	$M\,ts$
η	Kolmogorov length scale	lu
Λ	integral length scale	lu
λ	Taylor micro length scale	lu
μ_f	dynamic viscosity	$M\,lu^{-1}\,ts^{-1}$
ν	kinematic viscosity	$lu^2\,ts^{-1}$
Ω_p	particle angular velocity	ts^{-1}
ρ	fluid density	M/lu^3
σ_w	relative velocity variance	lu/ts
τ_c	collision time	ts
τ_k	Kolmogorov time scale	ts
τ_p	particle relaxation time	ts

Dim. numbers	
Re_λ	Taylor scale Reynolds number
St	Stokes number

Acronyms	
LES	large eddy simulation
PIV	particle imaging velocimetry
pdf	probability density functio

Chapter 6

An assessment of fragmentation due to crystal-crystal collisions

The crystal-crystal collisions that are observed in the turbulent suspension simulations of the previous chapter are evaluated to determine whether crystal-crystal collisions may lead to fragmentation and to obtain a measure for the rate of fragmentation of ammonium sulphate crystals. Since particle collisions are strongly dependent on the short range hydrodynamic interactions between the particles, a model for lubrication forces is given, that contains contributions of the advective and accelerative terms from the Navier-Stokes equations. An effective particle impact velocity was calculated when particles reach a separation comparable to their surface roughness. Evaluation of the impact velocities showed that incorporating additional terms in the models makes little difference. Impact velocities of the particles in the suspension simulations are evaluated based on the radial velocity distributions near contact, while incorporating lubrication theory. The minimum fragmentation velocity depends on the particle size, since fragmentation is based on a minimum impact energy. Values of the fragmentation kernel obtained via this theoretical route correspond well to the values obtained from the collisions registered during the simulations.

Key words: lubrication, collisions, fragmentation, ammonium sulphate

6.1 Introduction

In industrial crystallisation processes, the phenomena of fragmentation and erosion of crystals may have a large impact on the behaviour of the crystallisation process and on the quality of the resulting product. Fragmentation leads to secondary nucleation, the formation of new crystals from fragments, which may strongly influence the dynamics of the crystallisation process. Fine particles in a crystalliser may also lead to undesired properties of the produced solid compound such as a large content of fines. Fragmentation occurs when a crystal collides with an internal part of the crystalliser or with other

particles at a sufficiently high impact velocity. Throughout this thesis, particle motion in a turbulent suspension has therefore been studied from different perspectives.

As a first exercise, the flow field of a pilot scale DTB crystalliser was studied. A detailed LES simulation was carried out where the fluid phase was approximated as a pseudo single phase with average properties of the crystal slurry. This study demonstrated the inhomogeneous distribution of hydrodynamic conditions in the crystalliser, which opposes the assumption that the behaviour of a crystalliser can be described effectively by a single ideally mixed stirred vessel, as in the often used MSMPR concept.

Describing the fluid phase as a pseudo single phase is questionable. Many ill-understood phenomena occur in turbulent suspensions that strongly influence the overall behaviour of the flow field. Particle-turbulence interactions can strongly alter the characteristics of a turbulent flow field, particle-particle collisions may lead to agglomeration or fragmentation, gravity causes sedimentation of particles, preferential concentration effects may increase or decrease the local accumulation of particles and turbulent dispersion enhances mixing properties or transport of particles.

To gain a better understanding of the interactions in turbulent suspension flow, numerical studies of one-way and two-way coupled turbulent suspensions are presented in literature (*e.g.* Sundaram & Collins (1997), Reade & Collins (2000)), in which the particle size is assumed to be much smaller than the microscopic scales of turbulence. In this type of simulations, most properties occur at sub-grid level and the particle interactions in the flow field can only be effectively modelled at very low volume concentrations of particles. Slurries in crystallisation processes often contain 10 to 20 vol % of solids. Further, due to the highly turbulent conditions, particle size and turbulent microscopic length scales in this type of processes are in the same range, leading to strong interactions between the turbulence and the particle phase. For numerical studies of this type of slurries, a much more detailed type of simulations is required.

In this thesis, a simulation approach is presented, where the flow field of the particles was fully resolved and where turbulent conditions were generated with accurately defined characteristics. Simulations of a single particle settling under gravity have been compared to experimental data to assess the accuracy of the simulation procedure (chapter 3). The turbulent flow field was generated by using a spectral forcing technique (chapter 4). Finally, by combining the various techniques, fully resolved simulations of turbulent suspensions have been carried out, containing up to 3900 particles. The results of these simulations have been presented in chapter 5.

In the current chapter, we return to the industrial crystallisation processes of chapter 2. A number of important questions remain to be answered. The main question addressed in this section is whether particle-particle collisions in a turbulent flow can lead to fragmentation. The simulation results of chapter 5 will be used as a basis to answer this question. The collision rate of particles in a turbulent flow field is given by

$$\dot{\mathcal{N}}_c = \Gamma \frac{n_0^2}{2} \tag{6.1}$$

where n_0 is the particle number density and Γ is the collision rate constant. This constant is a complex function of the many parameters that determine the flow field conditions and the particle properties. In section 5.5, a theoretical approach to determine this rate

constant is presented. Although large differences exist between the conditions for which this approach was originally derived and the regime in which our simulations have been carried out, it provided a useful basis for analysing our results.

This analysis demonstrated that the inertial particles in our numerical simulations exhibit two types of collisions. The first type of collisions was designated primary collisions, related to the uncorrelated particle motion of randomly moving particles. Many collisions were observed at relatively high collision frequencies, that arise due to the short range hydrodynamic interactions and due to the correlation of velocities at short separations. These collisions were designated secondary collisions.

It is the objective of this chapter to establish whether the submerged particles in the turbulent flow field can collide at sufficient impact velocity for fragmentation to occur and if so, to determine a rate constant of fragmentation based on the simulation results of chapter 5. The radial relative velocity distributions of particles near contact (see figure 5.10) that were obtained from the turbulent suspension simulations demonstrate that for a random pair of particles at close separation, a wide range of approaching velocities can be observed. For an actual collision to occur, only the higher approach velocities will be sufficient to overcome the repulsive action of lubrication forces and result in subsequent collision. Once particles are at contact, fragmentation will only occur when the kinetic energy of the particle impact exceeds the minimum impact energy required for fragmentation.

To assess this process of approach, collision and possible fragmentation, we will first take a closer look at the lubrication force model in the first part of this chapter. This model dictates the motion of two approaching spherical particles in a fluid separated at a short distance. The original model for lubrication forces has been derived based on the assumption that the flow in the gap is in the creeping flow regime. A feature of this model is that particles essentially will never touch, regardless of their initial velocity. Zenit & Hunt (1999) derived a variation of the lubrication model that contained also the transient and advective terms of the Navier-Stokes equations, and concluded that collision may occur when these terms are included. Their derivation was unfortunately incorrect and therefore we revisit this model in the next section, with the correct derivation.

In practice however, when the separation of two approaching particles becomes very small, it will come close to the molecular path length or to the surface roughnesses of the particles. In both situations the model description breaks down (Sundararajakumar & Koch (1996) and Joseph *et al.* (2001)). Using either form of the lubrication model, an effective impact velocity can be estimated by defining a cutoff separation, related to *e.g.* the surface roughness of the particles, as a threshold at which contact is established. Both classical lubrication theory and the full transient model are evaluated to study their prediction of the resulting impact velocity.

In the second part of this chapter, the particle radial velocity distribution obtained from the suspension simulations is evaluated to see whether it is likely that fragmentation occurs. It is assumed that the approach velocity of two particles is dominated by the lubrication force and the lubrication force model is used to predict the impact velocity of a particle pair, when their initial separation is chosen as the average separation at which the relative velocity distribution of figure 5.10 was determined. This impact velocity is then compared to the minimum impact velocity that is required for fragmentation. The

latter velocity is predicted by a theoretical model of Gahn & Mersmann (1997).

Finally, the conditions of our isotropic suspension simulation are compared to the conditions encountered in the LES simulation of the internal crystalliser flow in chapter 2 and a kinetic constant for the rate of fragmentation is determined, based on both a theoretical approach and on the collisions registered in the turbulent suspension simulations. This chapter is concluded with a number of remarks regarding crystal collisions in a true turbulent flow field as found in industrial equipment.

6.2 Lubrication forces

6.2.1 Formulation of lubrication forces

An analytical expression for the force acting on two approaching particles is given by standard lubrication theory (*e.g.* Crowe *et al.* (1997) or Kim & Karrila (1991)). This theory assumes creeping flow in the gap between the particles. A more extensive analysis of this force was presented by Zenit & Hunt (1999), who incorporated next to the viscous term, the advective and the accelerative terms of the Navier-Stokes equations in their analysis. For particles in a transient turbulent flow field, these terms may contribute to the particle motion. The derivation of Zenit & Hunt (1999) is revisited in appendix A, where also an analysis of the various terms in the full model[1] is given. In their analysis, several terms were ignored which resulted in an erroneous formulation.

The geometry of two approaching particles, along with the cylindrical coordinate system (r, θ, z) is given in figure 6.1. The relative velocity of the two particles at separation h_0 is w. The approaching particles induce transverse fluid motion in the gap, which will be a function of r.

The starting point for our derivation of the full model is the momentum equation for the flow in the gap, given by the Navier-Stokes equation in cylindrical coordinates (Bird *et al.* (1960)), with the assumption that the velocity components u_θ and u_z are negligible and the pressure is assumed only to be a function of r,

$$\frac{\partial u_r}{\partial t} + u_r \frac{\partial u_r}{\partial r} = -\frac{1}{\rho_f}\frac{\partial p}{\partial r} + \frac{\eta}{\rho_f}\frac{\partial^2 u_r}{\partial z^2} \tag{6.2}$$

When using only the rhs terms of this equation, the expression for repulsive force according to the lubrication theory can be derived (Crowe *et al.* (1997)).

By using the continuity equation, while assuming an approximation for the particle geometry, and by assuming Poiseuille flow in the gap, the following expression for the repulsive force can be obtained,

$$\widehat{F}(\widehat{t}) = A(\widehat{H})\frac{d\widehat{V}}{dt} + B(\widehat{H})\widehat{V}^2 + C(\widehat{H})\frac{1}{Re_0}\widehat{V} \tag{6.3}$$

where all dimensionless properties are indicated by carets, $\widehat{H}$ is the dimensionless gap h_0/a and $\widehat{V}$ is the dimensionless relative velocity $w/|w_0|$. Expressions for Re_0, the sphere

[1]The creeping flow approximation will be referred to as *(classical) lubrication theory* while the extensive model will be referred to as *full model.*

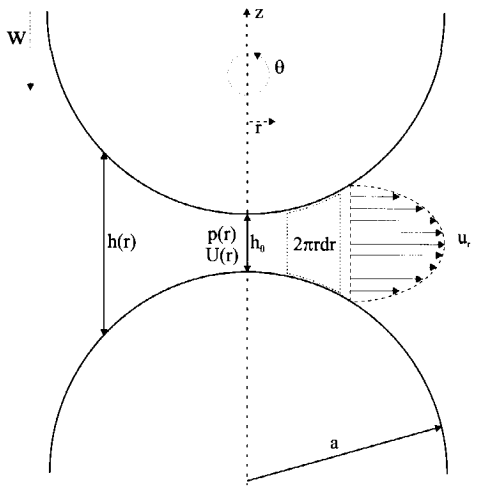

Figure 6.1: Schematic representation of the flow between two approaching spheres.

Reynolds number at the initial velocity w_0, and the dimensionless groups A, B and C are given by

$$Re_0 = \frac{\rho_f 2a|w_0|}{\eta} \tag{6.4}$$

$$A(\widehat{H}) = \frac{3}{16}\left[\widehat{H} ln\left(\frac{\widehat{H}+1}{\widehat{H}}\right) - 1\right] \tag{6.5}$$

$$B(\widehat{H}) = \frac{3}{32}\left[ln\Big(\frac{\widehat{H}+1}{\widehat{H}}\Big) - \frac{1}{\widehat{H}+1} + \frac{1}{(\widehat{H}+1)^2}\right] \tag{6.6}$$

$$C(\widehat{H}) = -\frac{9}{4}\left[\frac{1}{\left(\widehat{H}+1\right)^2\widehat{H}}\right] \tag{6.7}$$

In expression 6.3, one can clearly recognize the contribution of the terms for acceleration (A), momentum advection (B) and viscous flow (C). Term (C) is identical to the result for the leading order lubrication force approximation at small separations (for $\widehat{H} \to 0$),

$$\widehat{F} = \frac{-9}{4Re_0\widehat{H}}\widehat{V}. \tag{6.8}$$

The influence of each of the terms A, B, C and Re_0 in expression 6.3 can be determined by integrating the equations of motion of two approaching freely moving spheres. The equations of motion are given by

$$\Gamma\frac{d\widehat{V}}{dt} = 2\widehat{F} \tag{6.9}$$

and

$$\frac{d\widehat{H}}{dt} = \widehat{V}, \tag{6.10}$$

where Γ is the density ratio ρ_p/ρ_f which is a dimensionless measure for mass.

6.2.2 Impact velocity

The viscous term of equation 6.7, also present in equation 6.8 is proportional to $1/\widehat{H}$. When the gap between two particles reduces to zero, the repulsive force will go to infinity. As a result, when integrating the equations of motion of two approaching particles, the particles always come to rest before contact is established. As, in reality, collisions between suspended particles do occur, lubrication theory proves to be inadequate for predicting the collision process. Two phenomena that may cause the lubrication approximation to break down are that the gap becomes of the order of the free path length of the molecules of the fluid ($\mathcal{O}(10nm)$ for liquids, Sundararajakumar & Koch (1996)), or of the order of the surface roughness of the particles($\mathcal{O}(0.1\mu m)$, Joseph *et al.* (2001)).

For the calculation of a finite impact velocity, a minimum separation distance of the order of the surface roughness is defined up to which the lubrication formulation is assumed to be applicable. The particles are assumed to make contact at this threshold separation. The impact velocity w_i is calculated by integrating the trajectory of the particles from an initial separation to the point of contact. For lubrication theory, the impact velocity can be calculated analytically;

$$\widehat{V}_i = \frac{w_i}{w_0} = 1 + \frac{18}{4Re_0\Gamma} ln\left(\frac{\widehat{H}_i}{\widehat{H}_0}\right) = 1 + \frac{1}{2St_0} ln\left(\frac{h_i}{h_0}\right) \tag{6.11}$$

in which St_0 is the particle Stokes number at initial relative velocity w_0 while h_i is the collision length that indicates the integration limit. This equation demonstrates that the collision velocity is a weak function of h_i. By plotting the impact velocity w_i as a function of the initial velocity w_0, a straight line with slope 1 is obtained, since the Reynolds number is proportional to w_0 (see figure 6.2). The critical initial velocity w_c, where particles just touch at zero impact velocity, corresponds to the position where the line crosses the x-axis.

Figure 6.2 also presents the characteristics of the full model. A first striking feature is that it also predicts a linear relation between w_i and w_0. One can observe that the slope of the line in this case is slightly less than 1. As a result, the lines intersect at a velocity of approximately 0.07 [lu/ts] while the full model predicts a lower w_c. A second property in the figure is the sensitivity of the full model to the final separation h_i. It is noticed that upon variation of h_i, the slope of the margin lines, calculated with the full model, remains constant.

A quantitative comparison between the two models is made in table 6.1. Both models exhibit a weak dependency of w_c on h_i, as w_c varies just by 40 % when h_i is varied one order of magnitude. The table indicates that in the current regime, the full model exhibits an identical relative behaviour as the classic lubrication formulation. Lubrication theory is used for predicting the impact velocity of colliding particles in

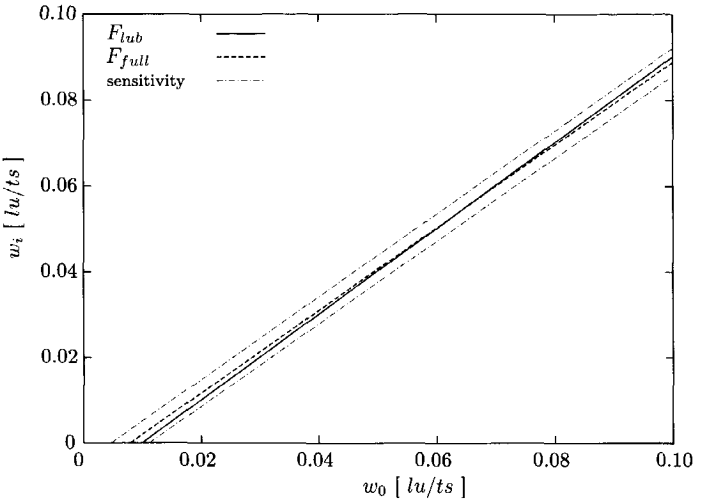

Figure 6.2: Impact velocity as a function of initial approach velocity, calculated for both models. The margins indicate the influence of the integration endpoint in the full model, which is varied by a factor of 5.($\Gamma = 1.414$, $\eta = 5.06\ 10^{-3}$ [$M\ lu/ts$],$a = 4.696$ [lu], $\widehat{H}_0 = 0.5/a = 0.106$ [-]).

Table 6.1: Sensitivity of critical velocity w_c to h_i. h_i Is varied relative to the reference length $h_{i,ref}$ which was chosen as 0.1 μm.(Conditions according to figure 6.2.)

	Lubrication		Full model	
$h_i/h_{i,ref}$	w_c	w_c relative	w_c	w_c relative
[–]	$[lu/ts]$	[%]	$[lu/ts]$	[%]
0.1	0.0138	140	0.0110	140
0.2	0.0127	128	0.0101	128
0.5	0.0111	112	0.0089	113
1	0.0099	100	0.0079	100
2	0.0087	88	0.0070	89
5	0.0071	72	0.0057	72
10	0.0059	60	0.0047	60

the following section, since both models exhibit a comparable behaviour at the same accuracy.

6.3 Crystal fragmentation

6.3.1 Crystal fracture modeling

In the recent study of Gahn & Mersmann (1997), a physical model is developed for the fracture process of crystals. This model predicts the formation of a volume of crystal fragments upon the impact of a crystal with a second material, based on the mechanical properties of the crystalline material. For the theoretical fracture model a number of simplifying assumptions regarding *e.g.* the geometry of the fracture region of the crystal and the fracture process are made. One important assumption of the fracture model is that *only the contact of a crystal corner with another flat and much harder object* is considered. This assumption is not applicable to colliding monodisperse spherical particles. The current excercise illustrates how the results of the turbulent suspension simulations in principle can be used to estimate the contribution of particle-particle collisions to abrasion and fragmentation of crystals and therefore it is assumed that the theoretical fracture model is applicable.

An important feature of the fracture model of Gahn & Mersmann (1997) is the prediction of a minimum impact energy E_{min} that must be exceeded for fragmentation to occur. Based on this result, one can easily determine the relation between particle size and minimum impact velocity $w_{f,min}$, required for fragmentation,

$$w_{f,min} = \sqrt{\frac{12E_{min}}{\pi d_p^3 \rho_p}}. \tag{6.12}$$

Througout this thesis, ammonium sulphate has been used as a model compound. The minimum impact energy for this compound, E_{min}, is 1.87 10^{-9} [J] (Gahn & Mersmann (1997)). The velocity $w_{f,min}$ is given in figure 6.3 as a function of crystal size, which is varied from 100 to 2000 μm, which is the range of crystal sizes encountered in the production of ammonium sulphate crystals.

6.3.2 Fragmentation impact velocity

Before presenting a rate of fragmentation one would first like to know if sufficiently large velocities are encountered in the turbulent suspension for collision and subsequent fragmentation to take place. From the simulations presented in chapter 5, a distribution of radial relative velocities as a function of the separation distance was obtained (figure 5.10). In this section, the distribution at closest particle separation (0.5 [lu] $\sim \widehat{H} =$ 0.11) is used to evaluate the collision process. A fragmentation velocity can be estimated under the assumptions that

- the crystal suspension consists of monodisperse spheres at a constant volume fraction

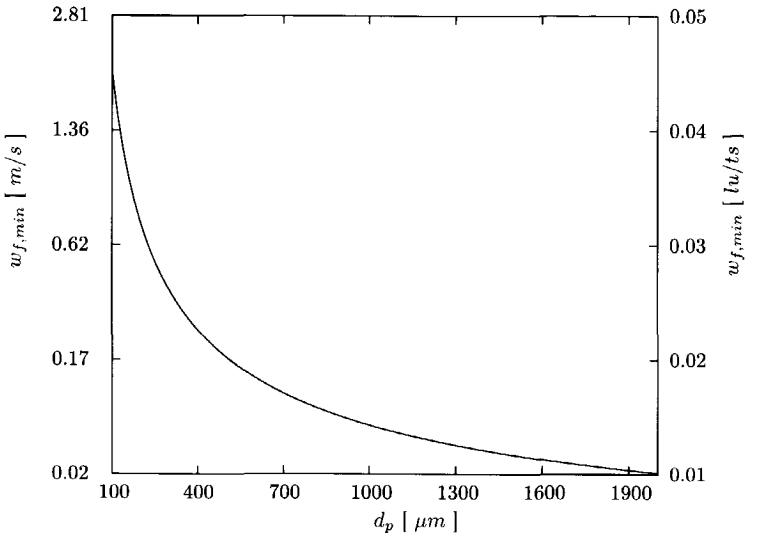

Figure 6.3: Minimum fracture velocity $w_{f,min}$ both in [m/s] and [lu/ts], as a function of crystal size in μm.

- the fragmentation behaviour is predicted correctly by the fragmentation model of Gahn & Mersmann (1997)
- the motion of non-spherical particles can be approximated by spherical particles
- the main force acting on the approaching particles is the lubrication force of the fluid in the gap between the spheres
- the collision process is much faster than the change in local hydrodynamic conditions of the turbulent flow field.

As a starting point, let's consider two particles at an initial separation of 0.5 [lu], approaching at an initial velocity w_0. Assuming that the particle approach in the final stage of the collision trajectory is dominated by the repulsive action of the lubrication force, a sufficiently large initial velocity is required for the particles to touch, as indicated by the critical velocity w_c from the previous section. Below w_c, approaching particles may have come to a halt before the gap has reduced to zero, while above this velocity particles may collide at a finite impact velocity, as given in figure 6.2[2]. The velocity w_c is indicated by a vertical line in the relative velocity distribution of figure 6.4.

Fragmentation may occur if the impact velocity exceeds the minimum fracture velocity $w_{f,min}$. In contrast to w_c, which is determined from a dimensionless relation, the fragmentation velocity $w_{f,min}$ depends on particle size (see figure 6.3). The minimal

[2]The relative velocity is defined such that an *increase* in *approaching* velocity corresponds to a more negative value of w

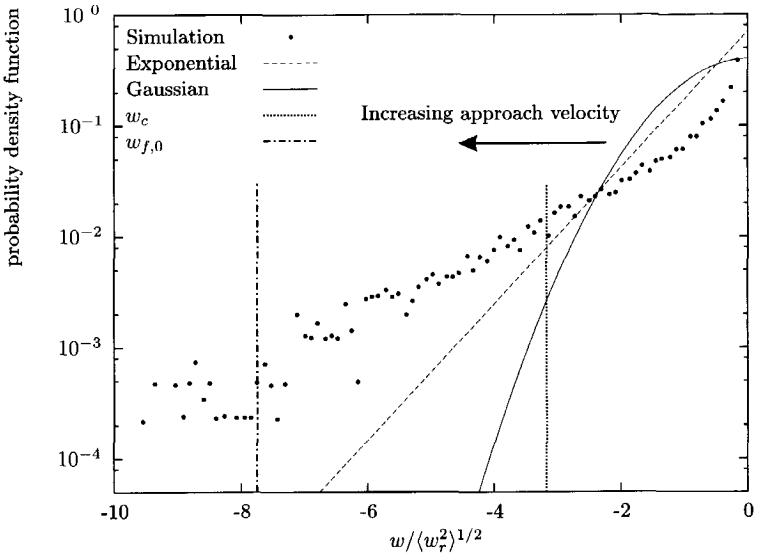

Figure 6.4: Pdf of approach velocities (*i.e.* negative w) of simulation S_2 at $\Delta = 0.5$ [lu]. The vertical lines indicate w_c and $w_{f,0}$ for ammonium sulphate particles of 1000 μm.

velocity that a pair of particles upon approach must exceed for fragmentation to occur is now simply given by $w_{f,0} = w_c + w_{f,min}$. As an example, $w_{f,0}$ is plotted in figure 6.4 for a particle diameter of 1000 μm. For particles of 1000 μm, the probability that collisions which result in fragmentation are observed is now given by that part of the relative velocity distribution that is left of the $w_{f,0}$ line. In table 6.2, the fracture velocity $w_{f,min}$ and threshold velocity $w_{f,0}$ are given for a range of crystal sizes.

Since fragmentation of smaller particles requires a larger impact velocity, the largest approach velocity for which data was obtained from simulation S_2 corresponds to a particle size of 520 μm. This size is the smallest crystal size for which the probability of fragmentation could be determined based on the pdf. Larger velocities may occur, but the probability of such events becomes negligibly small.

Table 6.2: Variation of fragmentation velocity and suspension simulation properties with particle size.

d_p [μm]	$w_{f,min}/\langle w_r^2 \rangle^{1/2}$ [-]	$w_{f,0}/\langle w_r^2 \rangle^{1/2}$ [-]	Box size [mm]	$E \times 10^3$ [m^2/s^2]	$\epsilon \times 10^2$ [m^2/s^3]	$log_{10}(\epsilon/\epsilon_{av})$ [-]
520	6.38	9.55	14	30.67	78.00	-0.35
1000	4.58	7.75	27	8.29	5.70	-1.48
1500	3.74	6.91	41	3.69	1.13	-2.19
2000	3.24	6.41	55	2.07	0.36	-2.69

To place the turbulent box simulations into perspective, the rescaled box dimensions are mentioned in table 6.2. If one compares the domain size to the length scales in the crystalliser flow (see also table 2.3), one can see a difference of about one order of magnitude between the large-scale turbulent structures that may exists in the crystalliser flow field and the size of the box simulations. Since the integral length scales in the box simulations cover a fraction of the domain size, a direct comparison between the crystalliser conditions and the box simulations is difficult. The Reynolds number of the turbulent flow in the crystalliser is also orders of magnitude larger than in the box simulations and the kinetic energy content in the large-scale structures of the crystalliser flow is orders of magnitude larger than that observed in the microscopic box simulations.

On the other hand, the ratio between the Kolmogorov scale and the particle size is comparable and the level of kinetic energy at the sub-grid scale of the crystalliser simulation is of the same order of magnitude as in the box simulations. For an interpretation of the simulation results in the light of the crystallisation process, the box simulations are therefore best regarded to represent a part of the macroscopic flow field that moves along in a frame of reference with coherent large-scale turbulent structures. The collisions that are then registered in our suspension simulations are collisions due to turbulent motion originating from the smaller scales of the crystalliser flow field. One important assumption one needs to make when relating the particle collisions from the box simulations to the crystalliser behaviour in this way is that the cascade of the turbulent energy spectrum in a turbulent suspension still exists and the microscopic structure of the turbulent flow field remains practically the same. This is highly unlikely, as it is demonstrated that the energy spectrum of the turbulent box simulations already changes considerably under the action of the particle phase.

Nevertheless, let us at least make an attempt to give an interpretation of the collisions observed in our suspension simulations. The relative proportions of microscopic scales observed in our box simulations are consistent with that of the crystalliser flow field. We therefore interpretate the simulations based on the rate of energy dissipation. The rate of energy dissipation is based on the gradients in the flow field and is thus related to the small-scale properties such as the Kolmogorov length. The rate of energy dissipation of the turbulent box simulations in table 6.2 scales with particle size. As a consequence the turbulent box simulation will represent different local turbulent conditions for different particle sizes.

The volume averaged power input of the crystalliser (table 2.2) exceeds the rates of energy dissipation in table 6.2 by almost an order of magnitude. In the crystalliser, the power input is concentrated at the impeller, where due to the impeller action, also the strongest turbulent conditions can be found. In the impeller region relative particle velocities may be present that may lead to fragmentation as a result of particle-particle collisions.

To determine whether particle collisions play a role in other regions of the crystalliser geometry, a comparison can be made with the contour plots of figure 2.5. For this purpose, the logarithmic value of the rate of energy dissipation in table 6.2 was rescaled with the volume averaged power input obtained from the crystalliser simulation. The contour plots indicate that a considerable part of the crystalliser volume contains levels of energy dissipation that exceed a value of $10^{-0.35}$ (obtained for particles of 520 μm).

Table 6.3: Fragmentation rate kernels for particles of $1000\mu m$. For results S_1 to S_3, the particle to fluid density ratio corresponds to that of ammonium sulphate in supersaturated fluid, while for S_4 and S_5 the density ratio was chosen differently (see chapter 5).

	$\Gamma_{f,1}$ $[\times 10^{-9} m^3/s\ ]$	N_c [-]	$\Gamma_{f,2}(w_{f,0})$ $[\times 10^{-9} m^3/s\ ]$	$\Gamma_{f,2}(w_{f,min})$ $[\times 10^{-9} m^3/s\ ]$
S_1	10.94	147	2.51	27.63
S_2	10.42	1131	2.00	24.56
S_3	14.29	4795	2.97	27.18
S_4	7.33	796	1.78	22.96
S_5	11.79	1280	3.99	30.42

This indicates that, given all the assumptions, the range of the rate of energy dissipation represented by the rescaled microscopic box simulations is within the range of energy dissipation levels encountered in the crystallisation process, and fragmentation due to crystal-crystal collisions may occur throughout large sections of the crystalliser volume.

6.3.3 Rate of fragmentation

In section 5.5, a discussion has been presented on the collision rate of particles in the turbulent flow field and a theoretical model for the collision rate constante Γ was presented. As an extension to that discussion, in this section an approach to determine the rate constant for fragmentation, Γ_f, is discussed.

Two routes can be travelled to determine Γ_f. The first route is simply to count collisions during the course of a simulation, of which the impact velocity exceeds $w_{f,min}$, assuming that the collision process is accurately captured in the suspension simulations. By using equation 6.1, a collision rate and consequently a collision kernel for fragmentation can then be determined. This value is given in table 6.3 as $\Gamma_{f,1}$, together with the number of collisions from which this value was determined.

For the second route, a collision rate can be determined by using the pdf of the relative radial velocity (figure 6.4) and the formal definition of the collision kernel from equation 5.26. According to this equation, the rate of collisions is proportional to the flux of particles through a reference sphere of size $R = 2 \times r_p$. To apply this model to the simulation data, it must be adapted to capture the flux of particles through a reference sphere $R = 2 \times r_p + \delta$, where δ is the average particle pair separation at which the pdf of figure 6.4 was determined, and thus reads,

$$\Gamma_{f,2} = 4\pi(R+\delta)^2 g_r(R+\delta)\alpha_f w_{f,m}. \tag{6.13}$$

In this equation, the flux of particles that leads to fragmentation is determined from figure 6.4 by the integral

$$\alpha_f w_{f,m} = -\int_{-\infty}^{w_f} wP(w)dw \tag{6.14}$$

i.e. for particles that approach at a sufficiently large velocity to overcome the lubrication forces and collide. The velocity $w_{f,m}$ represents the mean relative velocity over the

integration region. The parameter α_f in this equation represents the probability to observe a particle pair (at a separation of 0.5 [lu]) with an approach velocity that exceeds w_f,

$$\alpha_f = \int_{-\infty}^{w_f} P(w)dw. \tag{6.15}$$

To determine the collision rate kernel via this route, an upper integration boundary w_f must be chosen. If one assumes that the collision process is dominated by the lubrication forces, then based on the appraoch presented in section 6.3.2, $w_{f,0}$ should be chosen as upper boundary. As justification for this approach one can claim that most of the repulsive action of the lubrication force takes place when the gap between the two particles becomes of the order of 0.02 times the particle radius, which is in the range where the lubrication force is turned off in the simulations, and one needs to account for that.

However, other effects are also likely to increase the value of the collision kernel. It has been demonstrated that at close approach, the radial distribution function $g_r(R)$ may be much larger than $g_r(R+\delta)$ (see Reade & Collins (2000) and figure 5.15 versus table 5.7), thus increasing the collision kernel. Furthermore, the distribution in figure 6.4 is a statistically averaged result of the simulations that already contain at least partly the effect of lubrication forces. As an alternative, an upper limit value for the collision kernel can be estimated using $w_{f,min}$ as the upper integration boundary in stead of $w_{f,0}$.

Values for $\Gamma_{f,2}$, determined via these two approaches, are given in table 6.3 for particles of $1000\mu m$, based on the pdf results of simulation S_1 to S_5. The table shows a number of trends. First of all, as anticipated, the collision rate constant $\Gamma_{f,1}$ lies between $\Gamma_{f,2}(w_{f,0})$ and $\Gamma_{f,2}(w_{f,min})$ for all simulations. The effective collision rate in the simulations decreases due to the many different hydrodynamic interactions , whereas a theoretical prediction that accounts for lubrication forces tends to overestimate the reduction of the collision rate roughly by a factor 4.

Two other trends present in the fragmentation kernel are that (i) an increase in volume concentration appears to increase the rate constant and (ii), an increase in particle-fluid density ratio also tends to increase the rate constant. As to (i), one should notice that especially for simulation S_1, the values are based on a relatively small number of collisions. $\Gamma_{f,2}$ is also calculated from the tail of the relative velocity distribution, which is also based on a small number of observations. It is also striking that the trend in these kernels appears to contradict the trend in the collision kernels for primary collisions (table 5.5). For (ii) the trend corresponds better to the observations in table 5.5. Nevertheless, what is important is that the trends are consistent from simulations S_1 to S_5, irrespective of the method in which the different collision kernels have been determined. This shows that the different sorts of data (collision data and relative velocity distributions) obtained from the simulations exhibit consistency.

6.3.4 Some remarks on fragmentation in turbulent crystal slurries

In the previous sections, fragmentation of crystals due to particle-particle collisions was evaluated. The main issue of that section was that a demonstration is given on how

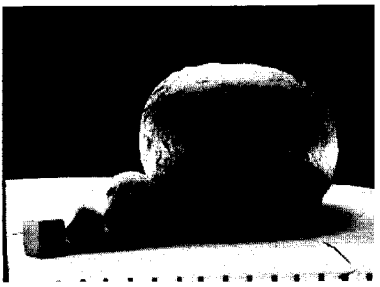

Figure 6.5: NaCl crystals from an industrial crystalliser.

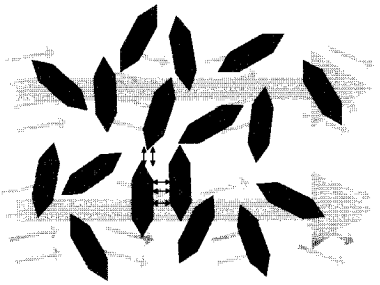

Figure 6.6: Schematic representation of the motion of irregular shaped crystals in a turublent flow field.

the data obtained from the numerical simulations of chapter 5 may be interpreted for estimating a rate of fragmentation. Off course, this analysis has limited applicability. One limitation for instance is that only the impact energy due to motion along the radial axis is considered. Since the particles move freely in a turbulent flow field, they can also rotate and exhibit transverse velocity components which may result in an enhancement of the mechanical wear of crystals. Therefore, a number of remarks need to be made to place the previous analysis in perspective with true crystallisation processes and to form a more complete image of particle behaviour in a turbulent suspension.

- When computing the particle relative velocity based on lubrication theory, the relative velocity of approaching particles may reduce to zero before the particles touch. One should realise, however, that this process is only valid for two particles in a stagnant fluid. Two particles in a turbulent flow field may experience a force due to the external flow field that may be aligned along their connecting axis and push the particles together. In such a case, the particle trajectory may be altered since the equation of motion contains the force due to the external flow field. Thus, larger values for w may be observed than predicted if only lubrication forces were active. A further analysis of simulation data with respect to the external forces that act on the particles is therefore required, to obtain further insight in the

characteristics and dynamics of the collision process.

- Next to a radial velocity component, the particles also have a transverse velocity. The simulation data indicate that the transverse velocity components are Gaussian distributed and that the rms value of the transverse velocity is two times larger than the radial velocity component (see figure 5.8 and table 5.6). Lubrication forces acting on a pair of approaching particles have a repulsive action that keeps the particles separated. In analogy to the lubrication forces, hydrodynamic shear forces may exist, that have an action that opposes particle rotation and transverse velocity. As these forces were estimated to be much smaller ($\mathcal{O}(10^{-3})$ times), they may offer little resistance to the particle transverse motion and the particles maintain large transverse velocities even at close separations. A contribution of shear forces to mechanical wear is therefore also unlikely.

- Due to the relatively large transverse velocities of particles, even at close separations, abrasion of the particle surface by lateral motion may occur. This effect may have a large contribution to the final shape of the crystals produced in industrial crystallisation equipment. An example is presented in figure 6.5, where sodium chloride crystals are shown that were taken from an industrial process. The figure shows that, although the original sodium chloride lattice is cubic, the particles become ball shaped due to abrasion during the crystallisation process.

- In addition to the transverse motion, rotation of the particles near contact also may contribute to the abrasion of the particle surface. Since shear forces at the particle surface are relatively small, rotation may occur in the suspensions. Although particle rotation is captured in the simulations, it has currently not been analysed.

- In crystallisation processes, particles usually have a nonspherical shape with many surface irregularities. In general, the edges and corners of a crystal are most sensitive to fragmentation and breakage, since the load of the collision energy is concentrated in a small volume of the crystal. The shape of the crystals may have two effects on colliding particles in a turbulent suspension;

  In the first place, the irregular shape may have an impact on the orientation of the particles in the flow field. Nonspherical particles that move in a range roughly indicated by $0.05 < Re < 100$ have a natural tendency to rotate towards highest drag force, because this orientation is the most stable (Lund & Trees (2001)). To assess the influence of the irregular shape of particles on their orientation and collision behaviour, detailed lattice-Boltzmann simulations can be done similar to the suspension simulations presented in this thesis. Recent examples of three-dimensional lattice-Boltzmann simulations are given by Aidun *et al.* (1998*b*) for one or two sedimenting spheroids and by Qi (2001) who presents results on the suspension behaviour of 16 cylindrical particles at $Re = 16.7$. The findings of the latter indeed indicate that the particles are mostly oriented perpendicular to their direction of motion and that cylindrical particles tend to form T-shaped pairs. This perpendicular orientation towards the main flow is schematically represented in figure 6.6. If particles become aligned in the flow field, a side to side collision of

their respective planes seems unlikely due to the stronger repulsive forces that act in the gap between the particles. However, aligned particles may also suffer from head to tail collisions which can cause particle edges to fragment.

In the second place, the impact that occurs at protruding edges or corners of non-spherical particles can occur at a higher impact velocity because a lower repulsive lubrication force may act on this type of shapes. This may again contribute to an increased wear of particle edges and corners.

6.4 Conclusion

To study the influence of the transient motion of approaching particles on the repulsive force that acts on approaching particles, a formulation of lubrication forces is presented that includes the advective and accelerative terms of the Navier-Stokes equation. This formulation was compared to classic lubrication theory (in which Stokes flow is assumed) for prediction of the impact velocity.

As particles approach contact, the lubrication force will reach an infinite value and according to theory particles will never touch. In practice this theoretical approach breaks down either because the gap width reaches the mean free path length of the gas or liquid molecules, or the gap becomes of the order of the surface roughness of the approaching particles. In evaluating the lubrication models, contact between particles is assumed by choosing an endpoint separation of the order of the estimated particle surface roughness. The impact velocity is defined as the velocity at the endpoint separation. It was shown that this velocity is a weak function of the chosen endpoint and that both models exhibit comparable behaviour.

Crystal fragmentation occurs whenever particles collide at an impact velocity which exceeds the minimum impact energy. In the second part of this chapter, an analysis of the approach and collision behaviour of particles in a turbulent flow field is given, to determine whether collisions at sufficiently large impact velocity can occur and to determine an effective rate of fragmentation. The analysis was based on the simulation results of chapter 5.

The distribution of the radial velocity components for particles near contact demonstrates that a wide range of approach velocities occurs. The approach velocity can be related to the minimum impact energy by choosing a specific particle size. By doing so, all properties of the suspension simulations are fixed. The fragmentation velocity $w_{f,0}$ indicates the approach velocity above which particles may collide at such impact that fragmentation may occur. This velocity was calculated, while assuming lubrication forces to dominate the relative particle motion. The analysis demonstrated that the impact velocity required for fragmentation decreases with an increasing particle size. Correspondingly, the probability to observe a particle pair at impact velocity $w_{f,0}$ increases with increasing particle sizes. Collision rates could be estimated for particles larger than 520 μm.

A comparison of the volume averaged rate of energy dissipation of the suspension simulations and the crystalliser simulations presented in chapter 2 of this thesis demonstrates that the microscopic turbulent conditions of the suspension simulations are com-

parable to the microscopic properties of the crysalliser flow field, whereas the large scale properties of the crystalliser flow field could not be captured.

For the box simulations, a rate of fragmentation was determined in two ways. First, the collision rate constant was based on the collisions registered during the simulations. Second, the rate constant was based on a theoretical evaluation of the relative velocity distribution near contact. In the latter case, the impact of the lubrication force on the prediction of the rate of fragmentation was evaluated.

The fragmentation rate constant determined by counting collisions was found to lie inbetween the values determined theoretically with and without the influence of lubrication theory, where the use of lubrication theory seems to lead to an underprediction. This may be due to the effect of local particle accumulation, as well as by the limited accuracy with which lubrication forces are implemented in the suspension simulations. The data demonstrated that the rate of fragmentation increases with an increase in particle to fluid density ratio.

List of Symbols

Symbol	description	unit
a	particle radius	m or lu
d_p	particle diameter	m or lu
E	(kinetic) energy	J or $Mlu^2\,ts^{-2}$
$\widehat{F}$	dimensionless force	–
h	gap width	m or lu
$\widehat{H}$	dimensionless gap width	–
n_0	particle number density	$\#m^{-3}$ or $\#\,lu^{-3}$
N_c	number of collisions	#
$\dot{\mathcal{N}}_c$	particle collision rate	$\#\,s^{-1}\,m^{-3}$ or $\#\,ts^{-1}\,lu^{-3}$
U	mean fluid velocity	$m,\ s^{-1}$ or $lu,\ ts^{-1}$
$\widehat{V}$	dimensionless relative velocity	–
w	relative particle velocity	m/s or lu/ts

Greek	description	unit
Δ	initial separation	m or lu
ϵ	rate of energy dissipation	$m^2\,s^{-3}$ or $lu^2\,ts^{-3}$
Γ	particle/fluid density ratio	–
Γ	particle collision kernel	$m^3\,s^{-1}$
μ	dynamic viscosity	$Pa\,s$
ν	kinematic viscosity	$lu^2\,ts^{-1}$
ρ_f	fluid density	$kg\,m^{-3}$ or M/lu^3

Dim. numbers

St_0	approach velocity Stokes number
Re_0	approach velocity Reynolds number

Acronyms

LES	large-eddy simulation

Chapter 7

Conclusions and perspectives

7.1 Conclusions

At the start of the project described in this thesis, little knowledge was present in the industrial crystallisation community on the precise interactions between hydrodynamics and the properties of products produced in industrial crystallisation processes. It was recognised that hydrodynamics play a crucial role in the dynamics of the crystallisation proces, and that crystal-crystal collisions may have a large impact on design and scale-up of crystallisation processes. Quantification of phenomena such as secondary nucleation due to crystal-crystal collisions, however, appeared virtually impossible. In this thesis, a step forward has been made in quantifying particle collision phenomena in dense turbulent solid-liquid suspensions such as those encountered in industrial crystallisation processes.

A procedure was proposed to assess crystal-crystal collisions that starts by investigating the properties of the turbulent flow field of a typical crystallisation process using large-eddy simulations. From these simulations, the conditions for performing direct numerical simulations of turbulent suspensions were estimated.

The next step was to develop a method for the direct simulation of suspended solid particles in liquid. For this purpose, a lattice-Boltzmann scheme was used, where the no-slip particle boundary conditions were implemented using the adaptive force-field technique. Since this approach has not been used previously for the simulation of freely moving particles, validation was necessary.

For this purpose, a comparison between simulations and PIV experiments on a single sphere settling in a container was made. This demonstrated that the transient motion of particles could be simulated sufficiently accurate at non-zero Reynolds numbers at a relatively low resolution.

For generation of sustained isotropic turbulent conditions, a spectral forcing scheme, originally developed for (pseudo-) spectral simulation methods, was applied to the lattice-Boltzmann scheme. It was demonstrated that all properties of the forcing scheme were accurately recovered in our lattice-Boltzmann framework.

Simulations of a forced turbulent suspension were performed by combining the particle simulations with the turbulence forcing scheme. Results were reported on five turbulent suspension simulations where volume fraction and particle-fluid density ratio

were varied. From these simulations, both the influence of the particles on the turbulent energy spectrum and the turbulence induced collisions were studied. The energy spectra showed that particles generate fluid motion at the scales of the particle size. This small-scale motion enhances energy dissipation and suppresses the development of turbulent kinetic energy at larger scales. Our numerical results agreed well with two-way coupled simulations on turbulent suspensions presented in literature.

A study of the motion of the particle phase showed complex particle-particle interactions. As particles approach one another, their relative velocity may decrease due to an increased spatial correlation of the turbulent flow field at shorter separations. Particles in solid-liquid suspensions also exhibit strong hydrodynamic interactions, which may further reduce their relative velocity. Upon separation, the hydrodynamic forces become attractive, causing particles to stay in each other's vicinity for a long time, until they are separated by *e.g.* external turbulent action. In line with the above picture, the distribution of the time between collisions showed that two types of collision mechanisms were present, *viz.* due to uncorrelated particle motion (primary collisions) and due to correlated particle motion (secondary collisions). The rate constant obtained for primary collisions corresponded well with theoretical models.

Finally, our simulation results were interpreted in the light of fragmentation of crystals due to crystal-crystal collisions, based on a mechanical model for crystal fragmentation. This analysis demonstrated that larger particles are more likely to exhibit fragmentation. The impact velocity required for fragmentation to occur depends on the crystal size and larger particles therefore require a lower impact velocity. Since lower particle approaching velocities are more likely to occur, larger particles are more likely to exhibit fragmentation. Based on these results, a fragmentation rate constant was determined, that depends on both the particle volume fraction and particle-to-fluid density ratio.

7.2 Direct Numerical Simulations

In this thesis, the main focus has been on performing detailed numerical simulations of turbulent suspensions. First results were obtained on domain sizes of 128^3 grid points (Ten Cate *et al.* (2002*a*)), which was later increased to 256^3 grid nodes (chapter 5), to increase the separation between integral, particle and Kolmogorov length scales. Still, in the current simulations, the integral length scale of turbulence was only 5 times larger than the particle diameter. In the 128^3 simulations, the particle field appeared practically homogeneous. Preferential concentration effects could be observed in the 256^3 simulations, but they still do not seem significant. For a further increase of the integral length scale, simulations at larger computational grids are required.

Another important issue is the resolution at which the particles are resolved. Simulation results were presented on turbulent suspensions with particles that had an input diameter of 8 grid nodes. For dense suspensions, the resolution of the flow around the particle can play an important role in the resulting particle suspension behaviour. A resolution study of the current type of simulations can be performed by increasing the particle input diameter. This also requires larger computational domains to maintain a constant ratio of the integral, particle and Kolmogorov length scale.

Clearly, for both reasons, there is a need for larger computational domains which implies larger computational efforts. The simulations performed on 256^3 computational grids were done on only 6 processors in parallel and took about 3 GB computer memory and 3 weeks of computation on a Linux cluster with 500 MHz processors. By increasing the computational grid two times in each direction, *i.e.* move to 512^3 computational grids, roughly 8 times more computer memory and 16 times more computational power would be required to perform the simulations in three weeks time (time discretisation scales linear in lattice-Boltzmann simulations). This would mean a computational effort of roughly 24 GB computer memory and 96 processors at 500 MHz. If one would move to 1024^3 grids, 192 GB computer memory would be required and 1536 processors are needed.

These numbers seem ridiculously large. Nevertheless, the development of cluster computing has boomed during the last 5 years and simulations with $\mathcal{O}(100)$ processors are currently performed on a routine basis in supercomputer centers. A good example of the development of parallel computing is given by the developments at the Kramers Laboratorium. At the start of this project the Laboratory owned a 4 processor HP Convex computer, which was outclassed by a simple set of two dual pentium 450 MHz PC's about two years after the Convex had been installed. During this project it became apparent that parallel computing on off-the-shelf PC's was very rewarding and soon the two dual machines were upgraded to a cluster of 6 machines, which later again was extended with a second cluster of 10 dual pentium 500 MHz machines. The most recent cluster installed at the Kramers Laboratorium consists of 20 machines of dual 1600 MHz Athlon processors, which comes close to the demand for 512^3 simulations. Computer systems with of the order of 1000 processors are found in the top 500 supercomputers currently present in the world, and for research purposes, such computations are currently achieveable.

Other aspects of moving into larger simulations are the parallelisation of the computer code, and the need to handle very large data files. For simulations with, say, 100 processors, domain decomposition in one direction, as is currently done, will be insufficient, since the overhead on communication will strongly increase in this way. Parallelisation in more than one direction sets new challenges. For instance, a drawback of parallelisation in more directions is that fast Fourier transforms, needed for the generation of turbulent forcing, become highly inefficient and alternative approaches are needed. Also, post-processing the large datasets generated in this type of simulations requires efficient handling of the data files and computer memory.

Clearly, going to larger simulations is on the one hand challenging, looks promising from a research perspective and practically inevitable. On the other hand, it poses a number of practical difficulties that should be solved. With the high pace of the developments in computer power, the time is currently ready to get experience in this type of simulations and move into this direction.

7.3 Perspectives for modeling industrial crystallisation processes

After all these complex excersises of a fundamental nature, what perspective does the approach presented in this thesis offer to crystallisation processes? Bear in mind that a real industrial crystallisation process is typically of the order of 100 m^3, contains a dense suspension of crystals with a continuous crystal size distribution, is operated under highly turbulent conditions, often placed under vacuum, and boiling to generate supersaturation. The process spans a tremendous range of length scales, from meters for the equipment size to nanometers for the size of nuclei, and spans a wide range of time scales, of the order of hours for the process dynamics up to microseconds for the turbulence and particle response time scales. With the currently available numerical methods and computational power, an approach is suggested to study the influence of secondary nucleation on the dynamics of crystallisation processes.

A common way of modeling crystallisation processes is by means of population balances that describe the evolution of crystal size in time. A description of a crystallisation process that accurately represents the full process can not be achieved in models, simply because the many relations that connect local conditions and population balance kinetics are unknown. Based on the here presented simulation approach, one can at least start to evaluate for instance the role of secondary nucleation due to crystal-crystal collisions in the overall behaviour of the crystallisation process.

Let us assume, for the sake of simplicity, that the internal flow of a crystalliser is accurately predictable via LES computations. Let us further assume that the microscopic suspension simulations presented in this thesis provide an accurate method to obtain fragmentation constants Γ_f as a function of the rate of energy dissipation, particle to fluid density ratio and solids volume fraction, that can be straigthforwardly applied to describe fragmentation processes in crystallisers due to crystal-crystal collisions.

Our simulations showed that Γ_f was a function of volume fraction and density ratio. When studying a single model compound, the density ratio can be taken as a constant. The simulations were done at a single turbulent Reynolds number, and the rate of energy dissipation was constant. From a study in which volume fraction and turbulent conditions are varied, a model relation should be obtained for $\Gamma_f(K, \epsilon, \Phi_v, d_p)$.

This rate constant can then be used straightforwardly in a population balance model. The one problem with the regular approach to population balances is that homogeneous conditions throughout the crystalliser vessel are assumed. As an example, for the rate of energy dissipation often the volume averaged specific power input is chosen. This value is orders of magnitude larger than the levels of energy dissipation encountered in large parts of the crystalliser. Therefore, prediction of a rate of secondary nucleation based on this result will be orders of magnitude too large, compared to the rate present in the crystalliser volume (see also Hollander *et al.* (2001)). To incorporate inhomogeneous properties such as the rate of energy dissipation, a compartmental discretisation of the population balance has been proposed (Bermingham *et al.* (1998)). This raises new difficulties, since choosing control volumes is often arbitrary. To overcome this, the compartment structure of the population balance model should contain a resolution

comparable to the resolution of the flow field, which is virtually impossible due to its computational demand.

Monte Carlo (MC) approaches for solving population balances (Smith & Matsoukas (1998)) offer an alternative opportunity to tackle this problem. In such an approach, a large number of particles is taken where each particle has a given particle size, such that the ensemble of particles represents a continuous particle size distribution. These particles can be tracked through the flow field of a crystalliser. The kinetic parameter Γ_f can then be determined in each cell of the flow field, based on the local volume concentration of particles and the local rate of energy dissipation. A stochastic simulation of the kinetic processes then determines which particles of the group of particles residing in each cell have collided at such impact that secondary nuclei have been formed.

The advantages of such an approach are that the physical properties of the flow field, which determine, *e.g.* the local residence time and circulation of the particles, are inherently present, and that collisions of particles with, *e.g.* the internal parts of the crystalliser can also be incorporated. Another advantage is that MC simulations can be extended easily to describe other kinetic phenomena such as agglomeration or growth, and to include other particle properties such as morphology or internal stress of the particles. The latter is especially difficult to model in a conventional discretised population balance approach, since it requires discretisation of the population in additional dimensions. A drawback of MC simulations is that a dynamic simulation of the flow field at high resolution takes a number of hours per impeller revolution to compute. Simulations of a crystalliser the dynamic response of which is on the order of hours is therefore not feasible. To overcome this problem one should revert to an approach using time averaged or frozen flow fields.

To compute collisions between particles on a statistical basis, each cell in a MC simulation should contain a sufficient number of particles. An estimate of the required number of particles depends on the specific approach. For MC simulations of mixing processes, a rule-of-thumb of 50 particles per cell is used. For a detailed simulation of the crystalliser flow field as presented in chapter 2, 10 particles per grid cell corresponds to approximately 106 million particles in total; such a number would occupy about 3 GB computer memory and may currently be regarded feasible.

On the basis of the type of simulations proposed, the impact of the rate of secondary nucleation on scale-up can be studied numerically. Furthermore, by incorporating other kinetic mechanisms such as agglomeration, crystal growth, crystal fragmentation due to crystal-impeller collisions and crystal growth rate dispersion, a more complete model for crystallisation processes with full incorporation of the crystalliser hydrodynamics may be obtained.

Appendix A

Derivation of the full lubrication model

The starting point for the derivation of the full model for the lubrication force is given by the Navier-Stokes equation in the cylindrical coordinate system (equation 6.2) and the geometry of two approaching semi-spheres as given in figure 6.1. In accordance with lubrication theory, the velocity profile for u_r is assumed parabolic, where the second derivative of the velocity profile can be expressed as a function of the mean flow U,

$$\frac{\partial^2 u_r}{\partial z^2} = \frac{-12U}{h^2}. \tag{A.1}$$

Using the continuity equation, a relation between the mean velocity U and the relative particle velocity w is obtained,

$$Uh = -\frac{r}{2}w \tag{A.2}$$

which can be used to rewrite the momentum balance such that an equation for the pressure distribution in the gap is obtained,

$$p(r) - p(a) = \underbrace{\int_a^r \rho_f \frac{\partial}{\partial t}\left(\frac{rw}{2h}\right) dr}_{I} + \underbrace{\int_a^r \frac{\rho_f rw}{2h}\frac{\partial}{\partial r}\left(\frac{-rw}{2h}\right) dr}_{II} + \underbrace{\int_a^r \frac{6\mu rw}{h^3} dr}_{III} \tag{A.3}$$

which contains the contributions of I. fluid acceleration, II. advection and III. viscous forces. This expression for the pressure drop needs to be integrated over the surface of the sphere to obtain an expression for the forces acting on the spheres;

$$F = \int_0^{2\pi}\int_0^a p(r) r d\theta dr \tag{A.4}$$

which requires an approximation of the gap $h(r)$ between the spheres. The leading order term of the force is obtained by taking the first and second order terms of the Taylor expansion on the double sphere geometry

$$h(r) = h_0 + 2a - 2\sqrt{a^2 - r^2} \approx h_0 + \frac{r^2}{a} + ...\mathcal{O}(3) \tag{A.5}$$

where a is the sphere radius. Rewriting and integrating terms I, II and III will give the following expressions for the different contributions to the force on the sphere;

$$F_I = 2\pi \int_0^a \int_a^r \frac{\rho_f r}{2} \Big(\underbrace{\frac{1}{h}\frac{\partial w}{\partial t}}_{a} - \underbrace{\frac{w^2}{h^2}}_{b} \Big) dr\ r dr \tag{A.6}$$

$$F_{I,a} = \pi \rho_f \dot{w} \frac{1}{4} a^3 \left[\frac{h_0}{a} ln \left(\frac{h_0 + a}{h_0} \right) - 1 \right] \tag{A.7}$$

$$F_{I,b} = \pi \rho_f w^2 \frac{1}{4} a^2 \left[ln\Big(\frac{h_0 + a}{h_0} \Big) - \frac{a}{h_0 + a} \right] \tag{A.8}$$

$$\begin{aligned} F_{II} &= 2\pi \int_0^a \int_a^r \frac{\rho_f r w}{2h} \frac{\partial}{\partial r} \left(\frac{-rw}{2h} \right) dr\ r dr \\ &= -\pi \rho_f w^2 \frac{1}{8} a^2 \left[ln \left(\frac{h_0 + a}{h_0} \right) - \frac{a}{(h_0 + a)} - \frac{a^2}{(h_0 + a)^2} \right] \end{aligned} \tag{A.9}$$

$$F_{III} = 2\pi \int_0^a \int_a^r \frac{6\mu r w}{h^3} dr\ r dr = -\pi \mu w \frac{12}{8} \left[\frac{a^4}{(h_0 + a)^2 h_0} \right] \tag{A.10}$$

Time and length scales are made dimensionless using the particle radius a and the initial approaching velocity w_0. The force is made dimensionless by dividing both the lhs and rhs of the equations with the following group,

$$\frac{4}{3} \pi a^3 \rho_f \frac{\dot{h}_0^2}{a} \tag{A.11}$$

and by defining a Reynolds number according to equation 6.4 and the dimensionless distance, velocity and acceleration of the spheres as

$$\widehat{H} = \frac{h_0}{a} \tag{A.12}$$

$$\widehat{V} = \frac{w}{|w_0|} \tag{A.13}$$

$$\frac{d\widehat{V}}{dt} = \frac{a\dot{w}}{{w_0}^2} \tag{A.14}$$

which results in the dimensionless groups for the force,

$$\widehat{F}_{I,a} = \frac{d\widehat{V}}{dt} \frac{3}{16} \left[\widehat{H} ln \left(\frac{\widehat{H} + 1}{\widehat{H}} \right) - 1 \right] \tag{A.15}$$

$$\widehat{F}_{I,b} = \widehat{V}^2 \frac{3}{16} \left[ln\Big(\frac{\widehat{H} + 1}{\widehat{H}} \Big) - \frac{1}{\widehat{H} + 1} \right] \tag{A.16}$$

$$\widehat{F}_{II} = -\widehat{V}^2 \frac{3}{32} \left[ln \left(\frac{\widehat{H}+1}{\widehat{H}} \right) - \frac{1}{\widehat{H}+1} - \frac{1}{(\widehat{H}+1)^2} \right] \tag{A.17}$$

and

$$\widehat{F}_{III} = -\widehat{V} \frac{1}{Re_0} \frac{9}{4} \left[\frac{1}{(\widehat{H}+1)^2 \widehat{H}} \right] \tag{A.18}$$

Samenvatting

In de chemische industrie worden veel vaste produkten geproduceerd in industriële kristallisatie processen. Een typisch kristallisatie process bevat rond de 20 vol% kristallen waarbij de kristal grootte verdeling varieert tussen de 100 en 2000 μm. Om een homogene suspensie te verkrijgen wordt de kristal slurrie rondgepompt onder hoog turbulente condities. In deze turbulente stroming kunnen botsingen tussen kritallen en de apparatuur of kristal-kristal botsingen tot secundaire nucleatie leiden. Met de term nucleatie wordt de vorming van nieuwe kristallen aangeduid. In grootschalige industriële processen vormt secundaire nucleatie, het ontstaan van nieuwe kristallen uit fragmenten die afbreken wanneer kristallen botsen, de belangrijkste bron van nieuwe kristallen. Aangezien bij opschaling van kristallisatie processen de turbulente eigenschappen van het stromingsveld sterk kunnen veranderen kan secundaire nucleatie het dynamisch gedrag, en dientengevolge de kwaliteit van het beoogde produkt, sterk beinvloeden.

De doelstelling van dit proefschrift was om secundaire nucleatie door kristal-kristal botsingen in een turbulent stromingsveld te bestuderen. Hiertoe werd een methode ontwikkeld voor de direkte numerieke simulatie van deeltjes die vrijelijk in een turbulente stroming bewegen.

Daarvoor werd allereerst onderzocht welke stromings condities voor dergelijke simulaties van toepassing zijn aan de hand van een gedetailleerde large-eddy simulatie van de stroming in een experimentele 1100 l kristallisator. Hierbij werd aangenomen dat het stromings gedrag van de kristal-slurrie benaderd kan worden met een enkele homogene fase, waarbij de invloed van de kristal slurrie word benaderd met een effectieve viscositeit. Het Reynolds getal van de LES simulatie bedroeg 240000, en werd uitgevoerd met een rooster-Boltzmann simulatie, met een Smagorinsky sub-grid schaal turbulentie model (c_s bedroeg 0.11). Uit deze simulaties werden turbulente lengteschalen afgeschat. Hierbij bleek dat deze tot een orde kleiner konden worden dan de gemiddelde kristal grootte in het kristallisatie proces.

Omdat de grootte van de kristallen overeenkomt met die van de kleinste lengteschalen van de turbulente stroming, en omdat er een sterke interactie bestaat tussen de beweging van de vloeistof en die van de vaste deeltjes in de vloeistof, is een direkte simulatie van de vloeistof rondom de deeltjes vereist wanneer men het gedrag van vaste deeltjes in een turbulente suspensie wil bestuderen. Hiertoe werd een simulatie methode ontwikkeld gebaseerd op het rooster-Boltzmann schema. Twee punten die verder onderzoek vereisten waren het testen van de methode waarmee de randvoorwaarden van de vaste deeltjes werden opgelegd, en de methode waarmee een turbulente stroming opgewekt kan worden.

De methode voor de randvoorwaarden van de vaste deeltjes zoals die in dit proefschrift beschreven wordt is gebaseerd op de 'adaptive force-field' methode. Validatie van

deze aanpak was nodig aangezien deze nog niet eerder toegepast was op vrij bewegende vaste deeltjes. Hiertoe werd er een vergelijking gemaakt tussen experimenten en simulaties aan een enkel deeltje dat bezinkt in een glazen bak. De afmetingen van de bak waren zo gekozen dat het stromings veld volledig gesimuleerd kon worden, met inbegrip van de invloed van de vaste wanden van de bak. Vier kruis-correlatie PIV metingen aan een bezinkend deeltje zijn uitgevoerd, waarbij het Reynolds getal tussen 1.5 en 31.9 is gevarieerd. Het Stokes getal varieerde hierbij tussen de 0.2 en 4 en opstuiteren van het deeltje werd hierbij niet waargenomen. De experimenten leverden gedetailleerde informatie over het stromings veld, de baan van de kogel en de snelheid van de vallende kogel tijdens optrekken, bezinken en afremmen bij het naderen van de bodem. Rooster-Boltzmann simulaties waren in staat het volledige tijdsafhankelijke gedrag van zowel de kogel als die van de vloeistof na te bootsen. De experimentele data werd gebruikt om de invloed van de ruimtelijke resolutie op de simulaties te onderzoeken, waarbij de bol radius gevarieerd werd tussen 2 en 8 rooster punten. Hieruit bleek dat de kwaliteit van de berekeningen van het Reynolds getal af hing. Tevens werd het gebruik van een analytische uitdrukking voor de smerings-kracht op het naderen van de bodemwand onderzocht. Deze kracht kan worden gebruikt wanneer er onvoldoende ruimtelijke resolutie is om de stroming tussen de bol en de bodemwand te simuleren.

Voor het opwekken van een homogeen isotroop turbulent stromingsveld werd een spectraal krachten schema toegepast op het rooster-Boltzmann schema. Met dit schema kan een turbulent stromingsveld gegenereerd worden waarvan de eigenschappen *a priori* kunnen worden vastgelegd. Een bijzondere eigenschap van het schema is dat het in staat is om de vermogens toevoer die uit de kracht-snelheids koppeling ontstaat te elimineren, waardoor de turbulente eigenschappen van het stromingsveld nauwkeurig gecontroleerd kunnen worden.

Door de deeltjes simulatie met het spetraal krachten schema te combineren konden simulaties van turbulente suspensies worden uitgevoerd. Vijf simulaties zijn er uitgevoerd waarbij de deeltjes diameter 8 gridpunten bedroeg en waarbij de volume concentratie deeltjes gevarieerd werd tussen 2 en 10 vol%, terwijl de vast/vloeistof dichtheids ratio gevarieerd werd tussen de 1.15 en 1.73. Het Taylor schaal Reynolds getal bedroeg 61 in deze simulaties. Voor elkaar naderende of zich van elkaar verwijderende deeltjes werd een analytische uitdrukking voor de smerings kracht gebruikt wanneer de deeltjes zich minder dan twee roosterpunten van elkaar bevonden. Er werden resultaten gepresenteerd die de invloed van vaste deeltjes op het turbulente energiespectrum laten zien en er werden resultaten gepresenteerd die het botsingsgedrag van de vaste deeltjes in het turbulente stromingsveld bespreken.

De simulaties laten zien dat door de aanwezigheid van vaste deeltjes de kinetische energie van het systeem wordt onderdrukt omdat vaste deeltjes de dissipatie van kinetische energie te vergemakkelijken. De vaste deeltjes genereren vloeistof beweging op lengteschalen ter grootte van de deeltjes, wat resulteert in snelheids gradienten rondom de deeltjes, die een sterke toename van energie dissipatie op de lengteschalen van de deeltjes tot gevolg heeft. De resultaten bevestigen eerdere bevindingen uit de literatuur, waarin twee-weg gekoppelde directe simulaties van turbulente suspensies met punt-deeltjes worden beschreven.

Informatie over het botsings gedrag van de deeltjes in de simulaties laat zien dat er

twee botsingsmechanismen optreden. Botsingen treden op door ongecorreleerde bewegingen van deeltjes (primaire botsingen). De botsingsfrequenties voor deze botsingen komen overeen met voorspellingen op basis van een theoretisch botsingsmodel voor trage deeltjes. Daarnaast wordt er een groot aantal botsingen met hoge frequentie waargenomen. Deze zogenaamde secundaire botsingen treden op omdat de bewegingen van twee deeltjes die zich in elkaars omgeving bevinden gecorreleerd zijn vanwege de hydrodynamische interactie tussen de deeltjes op korte afstand, vanwege ruimtelijke correlatie die optreed in het turbulente stromingsveld en vanwege de numerieke methode waarop lubricatiekrachten en botsingen in de simulaties geïmplementeerd zijn. Dit wordt ondersteund door een analyse van de deeltjes fase, gebaseerd op de verdeling van de relatieve deeltjes snelheden en de ruimtelijke deeltjes correlatie.

In het laatste gedeelte van dit proefschrift worden de deeltjesbotsingen die in de simulaties worden waargenomen gebruikt om een maat voor de breukfrequentie van ammonium sulfaat kristallen in een turbulente suspensie te bepalen. Een minimale botsings snelheid waarbij breuk optreed kan worden bepaald uit de minimale breuk energie, waardoor deze snelheid varieert met de grootte van het kristal. Uit de simulaties wordt de verdeling van de radiele relatieve snelheden bij botsing verkregen. Deze verdeling laat zien dat naar mate de snelheid groter wordt, de kans dat deze snelheid aangetroffen wordt kleiner wordt. Aangezien kleinere kristallen een hogere botsings-snelheid nodig hebben om de minimale breuk energie te overschreiden, neemt de kans dat breuk optreed af voor kleinere kristallen. Een theoretische benadering om de breuk frequentie te bepalen, gebaseerd op de relatieve snelheids verdelingen in de simulaties, komt goed overeen met de botsingsfrequenties die in de simulaties waargenomen worden. Dit laat zien dat de gepresenteerde methode consistent is en biedt een perspectief voor het opstellen van modellen voor breukgedrag van kristallen in een turbulente stroming.

Acknowledgement

I want to express my gratitude to the many special people I got to know during the period working on my PhD thesis. First and foremost there is the great support I got from my team of promotors. Thanks to the DIOC, I was never short of advisors. I thank both Gerda van Rosmalen and Johan Grievink very much for their support and for the liberty they gave me to pursue my own interests during this period. Gerda, you always made me feel you were one of my biggest fans, which is something I consider very special.

I also gratefully thank Harrie van den Akker for the opportunity he gave me to work at the Kramers Laboratorium and for the many hours he spent on scrupulous corrections of my writing. Being in the Kramers Laboratorium was a special experience in its' own right, but I'll get back to that later.

First I want to thank some very special advisors. My sincere gratitude goes out to Jos Derksen, from whom I learned the basics of numerical simulations and who always found the time to help me with simulation programs that were bothering me, with the terrible math I sometimes got stuck with, or with reading my writings. I have great respect for your continuous support and presence ever since I started this work. I also want to thank Herman Kramer for his continuous support, especially during the earlier period of my PhD studies at API, and for bearing with me during my more impatient moments. I also thank Peter Verheijen for inspiring me with the idea of discrete particle simulations.

Apart from the advisors that were connected to my project, I also got to meet and know a whole range of people that were very special to me. Being part of the DIOC put me in a position where I met probably more than the average number of people one gets to know during the period of a PhD study. This also makes it very difficult for me to start somewhere, so I'll try and make this some sort of a chronological list.

Among the first people I got to work with and spend time with in API were Sean Bermingham and Maarten de Jong. You guys are both amazing and I wish you all the best. Sean, although I enjoyed every minute of our cooperation, only little of it made it into my thesis. You understood better than anyone else what it meant to be part of two different research groups. I consider having you as a friend and former colleague a great privilege, and I hope we'll meet again in the future.

From API I want to shift my attention to the people I met in PSE and that were part of the DIOC. My thanks go out to Wouter van Winden and Michiel Meeuse. Michiel especially, for giving me the pleasure of the looks of his nonchalant orange hairdo.

During this project I tried to master the art of parallel computing. All this would probably not have been so succesfull without the great help of Gerben and the other

guys of Linvision. Thanks guys for walking with me down the early road of parallel linux-computing, it was a pleasure being your first customer. Many best wishes with your enterprise.

It is time to move to the Kramers laboratorium. There is a great number of people in that lab that I want to thank. First of all I want to thank the ladies from the secretariat. Karin and Thea, thanks for all your good care through these years, keep up the good work! Second of all, the guys from the technical support and the workshop. That were Jaap, Jaap, Jaap and Jaap, and of course, Ab, Jan and Wouter. Special thanks also to Peter, for bringing the computer system in such great shape and keeping it that way!

My PhD colleagues at the Kramers laboratorium were numerous, but the most unforgettable was of course the big lumberjack Elco Hollander. We went through a number of unforgettable experiences together. I don't know exactly which one was more stressful, the time we faced De Voogd together or the time we had to face a class of schoolkids to teach them the mystique of making shampoo! Both experiences were unforgettable! Never a dull moment 'lange'!

When I started at the laboratorium, I had the privilege to have a room of my own, when I left we were with five. The first one to join me in the room was of course Martin. Getting to know you gave me the opportunity to pass some of my lattice-Boltzmann wisdom, of which you have much more right now, on to you, while in the mean time you were able to pass some of your feng-shui tai-chi-chuan wisdom onto me. I consider you a great colleague and you and Gerty very special friends.

After Martin, also Ying and Koji joined our room, but not for long. It was if I recall correctly, about a year later, that Drona showed up. Drona, I always have and always will enjoy our discussions and hope that one day I can join you to enjoy a famous Surinam nasi meal from one of your many cousins in Paramaribo.

And then Drona left the room again, for he had to do science, and Wouter Harteveld showed up. I must be honest, Wouter and I met much earlier as being members of the DIOC, but I got to know him really when he came back to the lab after being away for more than a year. Wouter, your great sense of humour and your acupressure massages always kept me going. Thanks! Around the same time that Wouter returned, also Hugo joined our room, while the last one to join was Ruurd. All you guys in the room, many thanks, you made it a very special time for me.

Luckily, the Laboratorium extends outside of my office. Thank you Luis Portela, for your great support. I learned very much from you. Your never lacking willingness to discuss work, no matter what time of the day, has been invaluable to me.

I also want to thank Kees Nieuwstad. Kees, working with you, or not working with you, or again working with you was a very special experience! It was a privilege for me to assist you with your graduation project and a great deal of the work presented in chapter 3 of my thesis I owe to you. I'm sure you'll recognise it.

I think it is time to move closer to home. But not just yet. I first want to thank Eelco van Vliet. First of all for being a great friend. Second of all, for motivating me to spend those hours in the swimming pool. Swimming was great excersise and always was a good break from the office and most of all, it was the best way of doing field experiments for a fluid mechanics scientist. Third, your important contribution to my work! You taught me Fourier transformations and the whole turbulent forcing in my

thesis would not have been the same without you. But last, I wish you and Pauline the best in life and I thank you for being one of my paranymphs.

Which brings me to my other paranymph and very special friend, Flip Wauters. Flip, thanks for the time we shared at our home back when we studied, and thanks for the great friend you proved to be for the many years after.

I could now present a very incomplete and random list of names of friends that have been and are very special to me. I will make it a short one and apologise for anyone that I forgot. Ok, thank you, Bart, Dick, Rene, so that is Painless, John, Frank, Smaal en Petra. Furthermore, I want to thank all the friends from Frisbee for the hours on the sportstichting and all other places on earth (Obat Sakit Maag) and I want to thank Gert, Pascal and Bart 'watermelonman' Wirtz, and all other friends from 'Happy Hour' who gave me the such a special musical experience throughout the largest part of my PhD-years.

My final thougts go out to my biggest fans throughout this journey. Pa en Ma, you are my most dedicated supporters, thank you for giving me the possibility to do this thesis the way I wanted to do it, thank you for the great love and advise in life that I got from both of you.

One time, there was a sailing trip of a group of students from Delft on a old traditional ship. On this boat was also a funny strange little girl. At night she kept running and jumping up and down the quay nervously, as if something was bothering her. Of course there was. It only took me a few more weeks to collect the nerves to find out what it was. I'm very happy I did though, because ever since, she has been the biggest treasure I found during my restless search for a PhD. Jantien, thank you for giving me the pleasure of finding things out.

Bibliography

ABRAHAM, F. 1970 Functional dependence of drag coefficient of a sphere on reynolds number. *Phys. Fluids* **13**, 2194.

ABRAHAMSON, J. 1975 Collision rates of small particles in a vigorously turbulent fluid. *Chem. Eng. Sci.* **30**, 1371–1379.

AIDUN, C. K. & LU, Y. 1995 Lattice-boltzmann simulation of solid particles. *J. Stat. Phys.* **81** (1/2), 49–61.

AIDUN, C. K., LU, Y. & DING, E.-J. 1998*a* Direct analysis of particulate suspensions with inertia using the discrete boltzmann equation. *J. Fluid Mech.* **373**, 287–311.

AIDUN, C. K., LU, Y. & DING, E.-J. 1998*b* Direct ananlysis of particulate suspensions with inertia using the discrete boltzmann equation. *J. Fluid Mech.* **373**, 287–311.

ALVELIUS, K. 1999 Random forcing of three-dimensional homogeneous turbulence. *Phys. Fluids* **11** (7), 1880–1889.

BEHREND, O. 1995 Solid-fluid boundaries in partcle suspensionsimulations via the lattice boltzmann method. *Phys. Rev. E* **52** (1), 1164–1175.

BENNET, R. 1984 Advances in industrial crystallization techniques. *Chem. Eng. Prog.* **80** (3), 89–95.

BENNET, R. 1993 *Crystallizer Selection and Design*, 4th edn., chap. 5, pp. 103–130. In Myerson (1993).

BERMINGHAM, S., BRUINSMA, O. S. L., KRAMER, H. J. M., ROSMALEN, G. M. V. & WITKAMP, G. J. 1997 *Industrial Crystallisation and Precipitation*. PAON.

BERMINGHAM, S. K., KRAMER, H. J. M. & VAN ROSMALEN, G. M. 1998 Towards on-scale crystalliser design using compartmental models. *Comp. Chem. Eng.* **22**, S355–S362.

BIRD, B. R., STEWART, W. E. & LIGHTFOOT, E. N. 1960 *Transport Phenomena*, 1st edn. John Wiley and Sons.

BOIVIN, M., SIMONIN, O. & SQUIRES, K. D. 1998 Direct numerical simulation of turbulence modulation by particles in isotropic turbulence. *J. Fluid Mech.* **375**, 235–263.

BOUZIDI, M., FIRDAOUSS, M. & LALLEMAND, P. 2001 Momentum transfer of a boltzmann-lattice fluid with boudaries. *Phys. Fluids* **13** (11), 3452–3459.

BRENNER, H. 1961 The slow motion of a sphere through a viscous fluid towards a plane surface. *Chem. Eng. Sci.* **16**, 242–251.

CHEN, H., TEIXEIRA, C. & MOLVIG, K. 1998*a* Realization of fluid boundary conditions via discrete boltzmann dynamics. *Int. J. Mod. Phys. C* **9** (8), 1281–1292.

CHEN, M., KONTOMARIS, K. & MCLAUGHLIN, J. 1998*b* Direct numerical simulation of droplet collisions in a turbulent channel flow. part i: collision algorithm. *Int. J. Multiphase Flow* **24** (11), 1079–1103.

CHEN, M., KONTOMARIS, K. & MCLAUGHLIN, J. 1998*c* Direct numerical simulation of droplet collisions in a turbulent channel flow. part ii: collision rates. *Int. J. Multiphase Flow* **24** (11), 1105–1138.

CHEN, S. & DOOLEN, G. 1998 Lattice boltzmann method for fluid flows. *Annu. Rev. Fluid Mech.* **30**, 329–364.

CROWE, C., SOMMERFELD, M. & TSUJI, Y. 1997 *Multiphase Flows with droplets and particles*, 1st edn. CRC Press.

CROWE, C. C. 2000 On models for turbulence modulation in fluid-particle flows. *Int. J. Multiphase Flow* **26**, 719–727.

DERKSEN, J. & VAN DEN AKKER, H. E. A. (1999) Large eddy simulations on the flow driven by a rushton turbine. *AIChE J.* **45** (2), 209–221.

DERKSEN, J., DOELMAN, M. & VAN DEN AKKER, H. E. A. 1999 Three-dimensional lda measurements in the impeller region in a turbulently stirred tank. *Exp. Fluids* **27**, 522–532.

DERKSEN, J., KOOMAN, J. & VAN DEN AKKER, H. E. A. 1997 Parallel fluid flow simulation by means of a lattice-boltzmann scheme. *Lect. Notes Comput. Sci.* **1225**, 524.

DERKSEN, J. J. & VAN DEN AKKER, H. E. A. 2000 Simulation of vortex core precession in a reverse-flow cyclone. *AIChE J.* **46** (7), 1317–1331.

DING, E.-J. & AIDUN, C. K. 2000 The dynamics and scaling law for particles suspended in shear flow with inertia. *J. Fluid Mech.* **423**, 317–344.

EGGELS, J. G. M. 1994 Direct and large eddy simulation of turbulent flow in a cylindrical pipe geometry. PhD thesis, Laboratory for Aero- and Hydrodynamics, Delft University of Technology, The Netherlands.

EGGELS, J. G. M. 1996 Direct and large-eddy simulations of turbulent fluid flow using the lattice-boltzmann scheme. *Int. J. Heat Fluid Flow* **17**, 307.

EGGELS, J. G. M. & SOMERS, J. (1995) Numerical simulation of free convective flow using the lattice-boltzmann scheme. *Int. J. Heat and Fluid Flow* **16**, 357–364.

ELGHOBASHI, S. & TRUESDELL, G. 1993 On the two-way interaction between homogenous turbulence and dispersed solid particles. i: Turbulence modification. *Phys. Fluids* **5** (7), 1790–1801.

ESWARAN, V. & POPE, S. B. 1988 An examination of forcing in direct numerical simulations of turbulence. *Comput. Fluids* **16** (3), 257–278.

FELDERHOF, B. & OOMS, G. 1989 Effective mass density of fluid suspensions. *Phys. Fluids* **1** (7), 1091–1097.

GAHN, C. & MERSMANN, A. 1997 Theoretical prediction and experimental determination of attrition rates. *Trans. Instn. Chem. Engng.* **75 A**, 125–131.

GAHN, C. & MERSMANN, A. 1999*a* Brittle fracture in crystallization processes part a: Attrition and abrasion of brittle solids. *Chem. Eng. Sci.* **54**, 1273–1282.

GAHN, C. & MERSMANN, A. 1999*b* Brittle fracture in crystallization processes part b: Growth of fragments and scale-up of suspension crystallizers. *Chem. Eng. Sci.* **54**, 1283–1292.

GARSIDE, J. 1985 Industrial crystallisation from solution. *Chem. Eng. Sci* **40** (1), 3–26.

GOLDSTEIN, D., HANDLER, R. & SIROVICH, L. 1993 Modeling a no-slip flow boundary with external force field. *J. Comp. Phys.* **105**, 354–366.

GONDRET, P., HALLOUIN, E., LANCE, M. & PETIT, L. 1999 Experiments on the motion of a solid sphere toward a wall: From viscous dissipation to elastohydrodynamic bouncing. *Phys. Fluids* **11** (9), 2803–2805.

GONDRET, P., LANCE, M. & PETIT, L. 2002 Bouncing motion of spherical particles in fluids. *Phys. Fluids* **14** (2), 643–652.

HASIMOTO, H. 1959 On the periodic fundamental solutions of the stokes equations and their application to viscous flow past a cubic array of spheres. *J. Fluid Mech.* **5**, 317–328.

HE, X., ZOU, Q., LUO, L.-S. & DEMBO, M. 1997 Analytic solutions of simple flows and analysis of nonslip boundary conditions for the lattice boltzmann bgk model. *J. Stat. Phys.* **87** (1/2), 115–136.

HEEMELS, M. 1999 Computer simulations of colloidal suspensions using an improved lattice-boltzmann scheme. PhD thesis, Faculty of Applied Physics, Delft University of Technology, The Netherlands.

HINZE, J. 1975 *Turbulence*, 2nd edn. McGraw Hill, New York.

HOLLANDER, E., DERKSEN, J., PORTELA, L. & VAN DEN AKKER, H. E. A. 2001 Numerical scale-up study for orthokinetic agglomeration in stirred vessels. *AIChE J.* **47** (11), 2425–2440.

HOLLANDER, E. D. 2002 Shear induced agglomeration and mixing. PhD thesis, Faculty of Applied Physics, Delft University of Technology, The Netherlands.

JOSEPH, G., ZENIT, R., HUNT, M. & ROSENWINKEL, A. 2001 Particle-wall collisions in a viscous fluid. *J. Fluid Mech.* **433**, 329–346.

KAANDORP, J. A., LOWE, C. P., FRENKEL, D. & SLOOT, P. M. A. 1996 Effect of nutrient diffusion and flow on coral morphology. *Phys. Rev. Lett.* **77** (11), 2328–2331.

KIM, S. & KARRILA, S. J. 1991 *Microhydrodynamics: Principles and Selected Applications*. Butterworth-Heinemann.

KOCH, D. L. & HILL, R. J. 2001 Inertial effects in suspension and porous-media flows. *Annu. Rev. Fluid Mech.* **33**, 619–647.

KRAMER, H. J. M., BERMINGHAM, S. K. & VAN ROSMALEN, G. M. 1999 Design of industrial crystallisers for a required product quality. *J.Crystal Growth* **198/199**, 729–737.

KRUIS, F. & KUSTERS, K. 1997 The collision rate of particles in turbulent flow. *Chem. Eng. Comm.* **158**, 201–230.

LAARHOVEN, H. A. J. V. 1932 Hydreeringsverschijnselen bij vetzuren met drievoudige binding. PhD thesis, Afdeling der Scheikundige Technologie, Technische Hoogeschool Delft, Nederland.

LADD, A. J. C. 1994*a* Numerical simulations of particulate suspensions via a discrtized boltzmann equation. part 1. theoretical foundation. *J. Fluid Mech.* **271**, 285–309.

LADD, A. J. C. 1994*b* Numerical simulations of particulate suspensions via a discrtized boltzmann equation. part 2. numerical results. *J. Fluid Mech.* **271**, 311–339.

LADD, A. J. C. 1997 Sedimentation of homogeneous suspensions of non-brownian spheres. *Phys. Fluids* **9** (3), 491–499.

LADD, A. J. C. 2002 Effects of container walls on the velocity fluctuations of sedimenting spheres. *Phys. Rev. Lett.* **88** (4), 04830–1 04830–4.

LADD, A. J. C. & VERBERG, R. 2001 Lattice-boltzmann simulations of particle-fluid suspensions. *J. Stat. Phys.* **104** (5/6), 1191–1251.

LEEUWEN, M. L. J. V. 1998 Precipitation and mixing. PhD thesis, Laboratory for Process Equipment, Delft University of Technology, The Netherlands.

LIU, S. 1999 Particle dispersion for suspension flow. *Chem. Eng. Sci.* **54**, 873–891.

LUMLEY, J. 1978 Computational modeling of turbulent flows. *Adv. Appl. Mech.* **24**, 123–176.

LUND, K. O. & TREES, D. 2001 Low reynolds-number moment on asymmetric bodies. *Exp. Thermal Fluid Sci.* **24**, 61–66.

MEI, R., LUO, L.-S. & SHYY, W. 1999 An accurate curved boundary treatment in the lattice boltzmann method. *J. Comp. Phys.* **155**, 307–330.

MULLIN, J. 2001 *Crystallization*, 4th edn. Butterworth-Heinemann.

MYERSON, A. S. 1993 *Handbook of Industrial Crystallization*, 1st edn. Butterworth-Heinemann.

NEUMANN, A. M. 2001 Characterizing industrial crystallizers of different scale and type. PhD thesis, Laboratory for Process Equipment, Delft University of Technology, The Netherlands.

NEUMANN, A. M., BERMINGHAM, S. K., KRAMER, H. J. M. & ROSMALEN, G. M. V. 1999 Modeling industrial crystallizers of different scale and type. In *Proceedings of the 14th International Symposium on Industrial Crystallization*.

OOMS, G. & JANSEN, G. 2000 Particles-turbulence interaction in stationary, homogeneous, isotropic turbulence. *Int. J. Multiphase Flow* **26**, 1831–1850.

OVERHOLT, M. & POPE, S. 1998 A deterministic forcing scheme for direct numerical simulations of turbulence. *Computers & Fluids* **27** (1), 11–28.

OVERKAMP, K. M. 2002 Mitochondrial oxidation of cytosolic nadh in yeasts : physiological analysis and metbolic engineering. PhD thesis, Microbiology, Department of Biotechnology,Delft University of Technology, The Netherlands.

PICIOREANU, C. 1999 Multidimensional modeling of biofilm structure. PhD thesis, Delft University of Technology, The Netherlands.

PICIOREANU, C., LOOSDRECHT, M. C. M. V. & HEIJNEN, J. 1999 discrete-differential modelling of biofilm structure. *Wat. Sci. Tech.* **39** (7), 115–122.

POPE, S. B. 2000 *Turbulent Flows*, 1st edn. Cambridge University Press.

QI, D. 1999 Lattice-boltzmann simulation of particles in non-zero-reynolds-number flows. *J. Fluid Mech.* **385**, 41–62.

QI, D. 2001 Simulations of fluidization of cylindrical multiparticles in a three-dimensional space. *Int. J. of Multiphase flow* **27**, 107–118.

QIAN, Y., D'HUMIERES, D. & LALLEMAND, P. 1992 Lattice bgk models for navier-stokes equation. *Europhys. Lett.* **17** (6), 479–484.

RAFFEL, M., WILLERT, C. & KOMPENHANS, J. 1998 *Particle Image Velocimetry*. Springer-Verlag.

READE, W. C. & COLLINS, L. R. 2000 Effect of preferential concentration on turbulent collision rates. *Phys. Fluids* **12** (10), 2530–2540.

ROHDE, M., DERKSEN, J. & VAN DEN AKKER, H. E. A. 2002 Volumetric method for calculating the flow around moving objects in lattice-boltzmann schemes. *Phys. Rev. E* **65**, 056701.

ROTHMAN, D. H. & ZALESKI, S. 1997 *Lattice-Gas Cellular Automata*, 1st edn. Cambridge University Press.

ROUBOS, J. A. 2002 Bioprocess modeling and optimization: fed-batch clavulanic acid production by streptomyces clavuligerus. PhD thesis, Delft University of Technology, The Netherlands.

SAFFMAN, P. & TURNER, J. 1956 On the collision of drops in turbulent clouds. *J. Fluid Mech* **1** (16), 2530–2540.

SANKARANARAYANAN, K., SHAN, X., KEVREKIDIS, I. & SUNDARESAN, S. 1999 Bubble flow simulations with the lattice-boltzmann method. *Chem. Eng. Sci.* **54** (21), 4817.

SANKARANARAYANAN, K., SHAN, X., KEVREKIDIS, I. & SUNDARESAN, S. 2002 Analysis of drag and virtual mass forces in bubbly suspensions using an implicit formulation of the lattice boltzmann method. *J.Fluid Mech.* **452**, 61–96.

SCILIMAGE 1994 *Install guide, User's manual, (unix version)*. Technisch Physische Dienst, TNO-TU Delft.

SMAGORINSKY, J. (1963) General circulation experiments with the primitive equations: 1. the basic experiment. *Mon. Weather Rev.* **91**, 99–164.

SMIT, B. & FRENKEL, D. 1996 *Understanding Molecular Simulation*, 1st edn. Academic Press.

SMITH, M. & MATSOUKAS, T. 1998 Constant-number monte carlo simulation of population balances. *Chem. Eng. Sci.* **53** (9), 1777–1786.

SOMERS, J. 1993 Direct simulation of fluid flow with cellular automata and the lattice-boltzmann equation. *Appl. Sci. Res.* **51**, 127–133.

SOMMERFELD, M. 2001 Validation of stochastic lagrangian modelling approach for inter-particle collisions inhomogeneous isotropic turbulence. *Int. J. Multiphase Flow* **27**, 1829–1858.

SQUIRES, K. D. & EATON, J. K. 1990 Particle response and turbulence modification in isotropic turbulence. *Phys. Fluids* **2** (7), 1191–1203.

SUNDARAM, S. & COLLINS, L. R. 1996 Numerical considerations in simulating a turbulent suspension of finite-volume particles. *J. Comp. Phys.* **124**, 337–350.

SUNDARAM, S. & COLLINS, L. R. 1997 Collision statistics in an isotropic particle-laden turbulent suspension. part 1. direct numerical simulations. *J. Fluid Mech.* **335**, 75–109.

SUNDARARAJAKUMAR, R. R. & KOCH, D. L. 1996 Non-continuum lubrication flows between particles colliding in a gas. *J. Fluid Mech.* **313**, 283–308.

TEN CATE, A., BERMINGHAM, S., DERKSEN, J. & KRAMER, H. M. J. (2000) Compartmental modeling of an 1,100l dtb crystallizer based on large eddy flow simulation. In *10th European conference on Mixing*, pp. 255–264.

TEN CATE, A., DERKSEN, J. J. & VAN DEN AKKER, H. E. A. 2002*a* Lattice-boltzmann dns of solid particles in forced isotropic turbulence. *Int. J. Multiphase Flow, accepted* .

TEN CATE, A., DERKSEN, J. J., KRAMER, H. J. M., VAN ROSMALEN, G. M. & VAN DEN AKKER, H. E. A. 2001 The microscopic modelling of hydrodynamics in industrial crystallisers. *Chem. Eng. Sci.* **56**, 2495–2509.

TEN CATE, A., NIEUWSTAD, C. H., DERKSEN, J. J. & VAN DEN AKKER, H. E. A. 2002*b* Piv experiments and lattice-boltzmann simulations on a single sphere settling under gravity. *Phys. Fluids, accepted* .

TENNEKES, H. & LUMLEY, J. 1973 *A First Course in Turbulence*, 2nd edn. The MIT Press.

VERBERG, R. & LADD, A. J. C. 2000 Lattice-boltzmann model with sub-grid-scale boundary conditions. *Phys. Rev. Lett.* **84** (10), 2148–2151.

VERBERG, R. & LADD, A. J. C. 2002 Accuracy and stability of a lattice-boltzmann model with subgrid scale boundary conditions. *Phys. Rev. E.* **65** (1), 016701–1–16.

WANG, L.-P., WEXLER, A. S. & ZHOU, Y. 1998 Statistical mechanical descriptions of turbulent coagulation. *Phys. Fluids* **10** (10), 2647–2651.

WANG, L.-P., WEXLER, A. S. & ZHOU, Y. 2000 Statistical mechanical description and modelling of turbulent collision of inertial particles. *J.Fluid Mech.* **415**, 117–153.

WESTERWEEL, J. 1993 Digital particle image velocimetry - theory and application. PhD thesis, Laboratory for Aero- and Hydrodynamics, Delft University of Technology, The Netherlands.

WESTERWEEL, J. 1994 Efficient detection of spurious vectors in particle image velocimetry data. *Experiments in Fluids* **16**, 236–247.

WIBOWO, C. & NG, K. M. 2001 Operational issues in solids processing plants: Systems view. *AIChE J.* **47** (1), 107–125.

YEUNG, P. & ZHOU, Y. 1997 Universality of hte kolmogorov constant in numerical simulations of turbulence. *Phys. Rev. E* **56** (2), 1746–1752.

YUAN, Z. & MICHAELIDES, E. 1992 Turbulence modulation in particulate flows-a theoretical approach. *Int. J. Multiphase Flow* **18**, 779–785.

YUU, S. 1984 Collision rate of small particles in a homogeneous isotropic turbulence. *AIChE J.* **30** (5), 802–807.

ZENIT, R. & HUNT, M. L. 1999 Mechanics of immersed particle collisions. *J. Fluids Eng.* **121**, 179–184.

ZHU, W. 2001 Adsorption and diffusion in microporous materials: an experimental study with the teom. PhD thesis, Section for Industrial Catalysis, DelftChemTech, Delft University of Technology, The Netherlands.

ZWIETERING, T. N. 1958 Suspending of solid particles in liquid agitators. *Chem.Eng.Sci.* **8**, 244–253.

List of Publications

Publications in Journals

A. ten Cate, J.J. Derksen, H.J.M. Kramer, G.M. Van Rosmalen, and H.E.A. Van den Akker. The Microscopic modelling of hydrodynamics in industrial crystallisers. *Chem Eng Sci*, **56**, pp. 2495, (2001)

A. ten Cate, J.J. Derksen and H.E.A. van den Akker. Lattice-Boltzmann DNS of solid particles in forced isotropic turbulence. *Accepted for publication in Int. J. Multiphase Flow*

A. ten Cate, C. H. Nieuwstad, J.J. Derksen and H.E.A. van den Akker. PIV Measurements and lattice-Boltzmann simulations on a single sphere settling under gravity. *Accepted for publication in Phys. Fluids* , **14**(12), (2002)

A. ten Cate, J.J. Derksen and H.E.A. van den Akker. Fully resolved simulations of colliding monodisperse spheres in forced isotropic turbulence. *Submitted to J. Fluid Mech.* (2002)

Publications in Conference Proceedings

A. ten Cate, H.J.M. Kramer, J.J. Derksen, J. Grievink, and G.M. Van Rosmalen. The Microscale modelling of hydrodynamics in crystallization processes using the lattice-Boltzmann method. *Proceedings of the 14th International Symposium on Industrial Crystallisation, Cambridge*, paper 12, (1999)

A. ten Cate, S.K. Bermingham, J.J. Derksen, and H.J.M. Kramer. Compartmental modeling of an 1100 l DTB crystallizer based on large eddy simulation. *Proceedings of the 10th European conference on Mixing, Delft*, pp. 255 (2000)

A. ten Cate, J.J. Derksen and H.E.A. van den Akker. Lattice-Boltzmann DNS of solid particles in forced isotropic turbulence. *Proceedings of the 4th International Conference on Multiphase Flow, New Orleans*, (2001)

A. ten Cate, C. H. Nieuwstad, J.J. Derksen and H.E.A. van den Akker. PIV Measurements and lattice-Boltzmann simulations on a single sphere settling under gravity. *Proceedings of the 4th International Conference on Multiphase Flow, New Orleans*, (2001)

About the Author

Andreas ten Cate was born on Januari 12^{th} 1971 in Amsterdam, the Netherlands. After graduating from highschool in 1990 at the Hervormd Lyceum Zuid in Amsterdam, he began his study Chemical Engineering at Delft University of Technology in Delft, The Netherlands. As part of his study, he did practical training in the Amsterdam Medical Center and spent four months in South Africa at the Duvha Power station for his trainee ship. He did graduation research in the group of Industrial Catalysis and graduated as an MsC in Chemical Engineering in 1996. On October 15^{th} 1997 he started working on his PhD research at Delft University of Technology. This project led him through a number of diverse research groups, ranging from Industrial Crystallisation research to Proces Systems Engineering, and the Kramers Laboratorium voor Fysische Technologie, where he conducted the major part of the research presented in this thesis. Apart from research he also spent his time on the frisbee field to play ultimate frisbee and discgolf, as well as on stage for a period of three years, playing his saxophone in a three-man horn section. Currently, the author is working as a postdoc in Princeton University.

The movie in the right margin of this thesis represents the simulated flow field of a sphere settling in a closed box, comparable to those presented in chapter 3. The contours indicate the velocity magnitude of the fluid. The conditions were:
$Height/d_p = 41$, $Width/d_p = Depth/d_p = 4.1$, $Re_p = 46$.

The images on the back cover are raw PIV images of a sphere settling towards the bottom wall of a closed box, taken from the experiment as described in chapter 3, case E_1.